A WIDE FIELD ULTRASOFT X-RAY CAMERA FOR ASTRONOMY

thesis submitted by

MARTIN A. BARSTOW

for the degree of Doctor of Philosophy

December 1983

X-ray Astronomy Group

Department of Physics

University of Leicester

ProQuest LLC
789 East Eisenhower Parkway
P.O. Box 1346
Ann Arbor, MI 48106-1346

DECLARATION

I hereby declare that no part of this thesis has been previously submitted to this or any other University as part of the requirements for a higher degree. The work described here was conducted by the undersigned except for the contributions of colleagues indicated in the text.

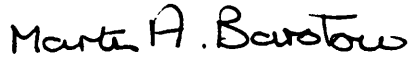

Martin A. Barstow

December 1983

ABSTRACT

In a collaboration between the University of Leicester X-ray Astronomy Group and the Center for Space Research at the Massachusetts Institute of Technology an imaging X-ray telescope has been developed to carry out a partial sky survey of the extreme-ultraviolet (EUV) region of the spectrum in the waveband 50 to 250Å. The instrument is designed to be flown on NASA Astrobee or Black Brant sounding rockets.

The history of EUV astronomy and the types of object likely to be of interest in the EUV are reviewed. The development of the WFSXC payload is described with particular emphasis on the development of the focal plane instrument, a microchannel plate detector with resistive anode image readout. The gain performance of the detector is summarised and the use of MgF_2 and CsI photocathodes to enhance its quantum efficiency is described, CsI giving efficiencies 10-20 times higher than uncoated MCPs. Also, the use of a resistive anode to provide a low distortion high resolution image readout is demonstrated. Thin film filters are used to define the instrument bandpasses and reject geocoronal background and their design and testing are described. The linear absorption coefficients of beryllium and parylene N, derived from the measured filter transmissions, are compared with theoretical predictions of the absorption in the 50-300Å waveband showing good agreement up to 300Å for beryllium and 100Å for parylene.

The WFSXC payload was flown twice experiencing technical problems on both occasions. The anaylsis and interpretation of the data from these flights is presented in the latter chapters of this thesis and the likely causes of the problems determined.

DEDICATION

To my Wife and Family

ACKNOWLEDGMENTS

Many people at a number of institutions have contributed to the WFSXC sounding rocket programme in various capacities. I am grateful to have had the opportunity of working with so many people, in both England and the USA, and have great pleasure in thanking them here.

At Leicester University:

I would like to thank Dr George Fraser whose theoretical work on photocathodes and resistive anodes contributed substantially to the project. In addition I would like to thank him for his advice and many helpful discussions during the writing of this thesis. My thanks also go to Dr Margaret Lewis under whom I worked on the first rocket flight and from whom I learned a great deal about testing and calibrating MCP detectors. I am grateful to Mark Whiteley who, on the second flight, provided valuable assistance during calibration and testing of the flight detector and later during filter tests at the National Physical Laboratory. Dave Watson and Harold Chapman provided the engineering support and technical assistance without which the development of the WSFXC detectors would not have been possible. I would also like to thank Dr Ray Hall, Dr K.D. Evans and Mr S.G. Price for calibrating the filters for the first rocket flight on the Leicester University Crystal Spectrometer.

Finally I would like to thank Professor K.A. Pounds for giving me the opportunity of studying at Leicester and Mr A.A. Wells for the management of the WFSXC project, his useful criticism of the first drafts of this thesis and advice on writing style.

At Massachusetts Institute of Technology:

It has been a pleasure collaborating with members of the Center for Space Research at MIT - Professor S. Rappaport, Mr Ed Boughan, Dr Robert Petre (now at Goddard Space Flight Center), Dr Alan Levine and Mr Fred Miller. In particular I would like to thank Rob Petre, who designed the WFSXC mirrors, instructed me in testing them and provided much of the mirror data that I have used. On the first WFSXC flight he and Ed Boughan taught me the practical aspects of flying a sounding rocket payload. Most of the work on the second flight was performed by myself and Ed Boughan and I would like to thank him for making an extended visit (3 months) to the USA a pleasant one.

I would finally like to thank the members of other institutions who also made valuable contributions to the project:

The staff of the Goddard Space Flight Center sounding rocket group and naval personnel at White Sands Missile Range, New Mexico who flew the rockets.

Dr Barry Kent of the Rutherford and Appleton Laboratory, Didcot, who manufactured the carbon/lexan filters and performed the pre-flight calibrations of them.

Mr E. Grapor of the Lebow Company, Goleta, California, who manufactured the parylene and beryllium/parylene filters.

Dr G.H.C. Freeman and Mr D. Nettleton of the National Physical Laboratory, Teddington, Middlesex, for the use of their far-UV spectrometer and their assistance in calibrating the filters after the second flight.

The staff at American Science and Engineering and at Acton Environmental Testing, where the payload was tested.

PUBLICATIONS

The following publications have arisen from work contained within this thesis.

1) M.A.Barstow, M.Lewis and R.Petre, "Linear absorption coefficient of beryllium in the 50-300Å wavelength range", Journal of the Optical Society of America, 73(1983), 1220.

2) G.W.Fraser, M.A.Barstow, M.J.Whiteley and A.Wells, "Enhanced soft X-ray detection efficiencies for imaging microchannel plate detectors", Nature, 300(1982), 509-511.

3) G.W.Fraser, M.A.Barstow, J.F.Pearson, M.J.Whiteley and M.Lewis, "The soft X-ray detection efficiency of coated microchannel plates", in preparation.

4) G.W.Fraser E.Mathieson, M.Lewis and M.Barstow, "Signal location by uniform resistive anodes (C) time-dependent performance", Nuclear Instruments and Methods in Physics Research, 190(1981), 53-65.

5) G.W.Fraser, J.F.Pearson, G.C.Smith, M.Lewis, and M.A.Barstow, "The gain characteristics of microchannel plates for X-ray photon counting", IEEE Transactions in Nuclear Science, NS-30(1983), 455.

CONTENTS

PREFACE

In a collaboration between the University of Leicester X-ray Astronomy Group and the Center for Space Research at the Massachusetts Institute of Technology (MIT) an imaging X-ray telescope has been developed to carry out a partial sky survey of the extreme-ultraviolet (EUV) region of the spectrum, in the waveband 50 to 250Å. The instrument is designed to be flown on NASA Astrobee or Black Brant sounding rockets. This thesis describes the development of instrumentation for the telescope and presents the results of the two sounding rocket flights to date.

In view of the collaborative nature of this project a summary is given below of the main contributions made by the author. All experimental work on the microchannel plates (chapters 3 and 4) and the resistive anode (chapter 5) was carried out by the author. Although the initial design and optimisation of the thin film filters was performed by MIT, detailed study of the absorption of the filter materials and the remaining work in chapter 6 was undertaken by the author.

The author participated in the integration of the payload for the first rocket flight under the supervision of Dr M.Lewis (Leicester) and Dr R.Petre (MIT) and carried out the post-flight analysis of the data. On the second flight the author, as Leicester project scientist, was responsible for most of the integration work, Ed Boughan of MIT providing engineering support. All the data analysis from this flight (chapter 11) was performed by the author, apart for some individually acknowledged contributions from MIT.

CHAPTER 1

A REVIEW OF EXTREME-ULTRAVIOLET ASTRONOMY

1.1 Introduction

Until the early 1970s, the conventional view was held that EUV astronomy, over the waveband 100Å to 1000Å, was not a practical proposition. Since most known elements have outer electron binding energies ~10 - 100eV, photons in the corresponding wavelength range will be strongly absorbed in any photon atom interaction when, if λ is the photon wavelength and V the outer electron ionisation potential,

$$eV < hc/\lambda \qquad (1.1)$$

Hence, λ lies in the range 100-1000Å when $10<V<100$eV. As a result:

i) The Earth's atmosphere is opaque to EUV radiation due to photoabsorption by N_2, O_2 and O, the 1/e depth being at ~130km for λ=100Å. Hence, ground based astronomy is inconceivable.

ii) Over astronomical distances (>1parsec) interstellar gas at low densities is also opaque to EUV radiation. For example, hydrogen as the most abundant element in the Interstellar Medium (ISM) has an estimated mean free path (MFP) of $\sim 10^{18}$cm (0.4parsec). This was estimated for an interstellar neutral hydrogen density (n_H) of 1 atom cm^{-3}, inferred from 21cm radiowave measurements, and a neutral hydrogen absorption cross-section (σ) of $\sim 10^{18} cm^{-2}$, averaged over the EUV band (equation 1.2; Aller, 1959).

$$MFP = 1/(n_H.\sigma) \qquad (1.2)$$

In contrast to this first crude estimate, Cruddace et al (1974) derived the interstellar absorption cross-section over the wavelength range 1 to 2000Å (figure 1.1) and then calculated the percentage absorption by the ISM as a function of wavelength and n_H. The results, shown in figure 1.2 as the distance at which 90% of the EUV radiation is absorbed at three values of n_H (0.03, 0.1, and 0.2 cm^{-3}), indicate real transparency in the EUV window. The calculations demonstrated the possibility of being able to "see" EUV sources out to distances of a few hundred parsecs, at short wavelengths (100-500Å) especially, if the interstellar medium should prove to be inhomogeneous with local regions of low column density.

Radio measurements give hydrogen densities that are averages of the material along columns of several kiloparsecs. In the early 1970s far-ultraviolet satellite experiments were providing sensitive localised measurements of n_H over shorter pathlengths by observing the absorption profiles of Lyman α (1216Å) and Lyman β (1026Å) radiating in the spectra of unreddened stars (ie. without the presence of dust along the line of sight). Results from these experiments - Mariner 9 (Bohlin, 1973), OAO-2 (Savage and Jenkins, 1972) and Copernicus (Rogerson et al, 1973; Spitzer et al, 1973) - and some more recent ones are summarised in table 1.1. These measurements show that the ISM is far from uniformly distributed, as had been supposed previously, and that "local" values of n_H can be very much lower than

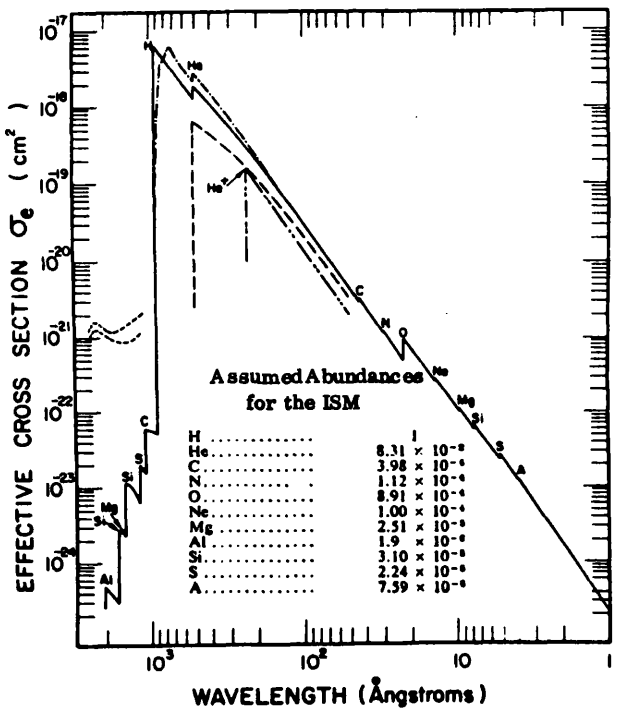

Effective cross-section (cross-section per hydrogen atom or proton) of the interstellar medium. ——— gaseous component with normal composition and temperature; -·- hydrogen, molecular form; — — H II region about a B star; — — — H II region about an O star; ---- dust.

Figure 1.1 (taken from Zombeck, 1981).

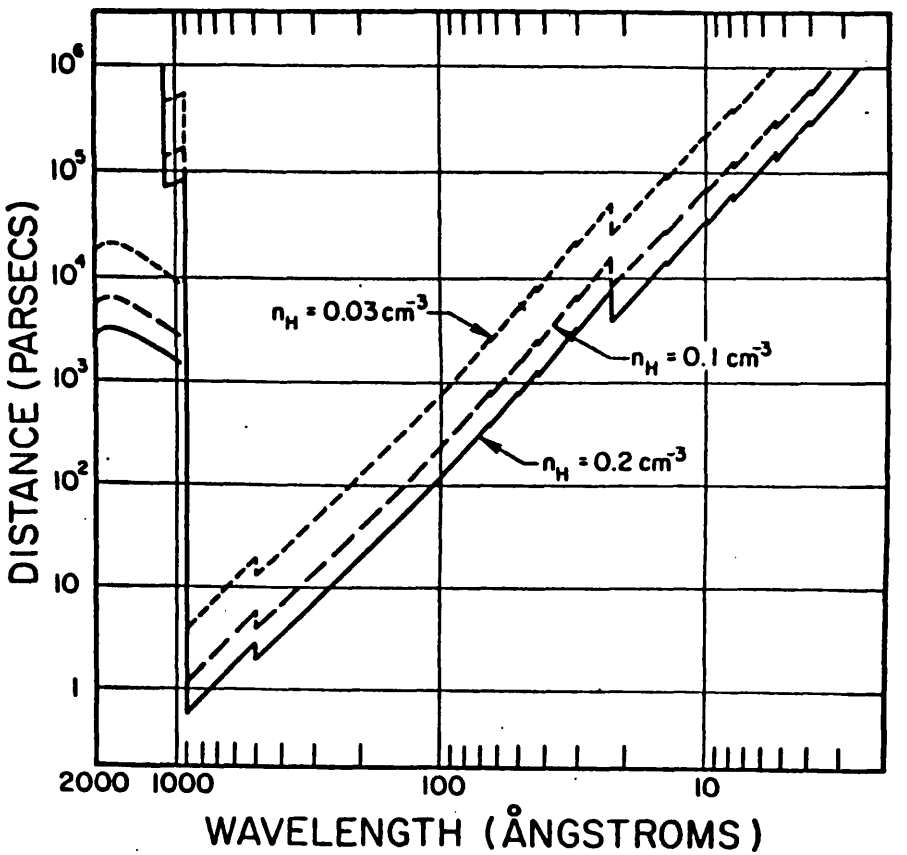

Figure 1.2 Distance at which the attenuation of the incident radiation reaches 90% as a function wavelength (from Zombeck, 1981).

Table 1.1. Neutral hydrogen densities along the lines of sight to a number of objects arranged in order of distance

OBJECT	DISTANCE (pC)	VOLUME DENSITY (cm^{-3})	COLUMN DENSITY (cm^{-2})	REFERENCE
α CMi	3.5	0.03	3.2×10^{17}	Henry et al (1976a)
β Gem	10.7	0.15	5.0×10^{18}	"
α Boo	11.0	0.10	3.4×10^{18}	"
α Aur	14.0	0.025	1.1×10^{18}	"
α Tau	20.8	0.20	1.3×10^{19}	"
α Leo	22	0.02	1.4×10^{18}	Rogerson et al (1973)
α Eri	23.8	0.07	5.1×10^{18}	"
λ And	26.0	0.075	6.0×10^{18}	Baliunas and Dupree (1979)
α Gru	28.0	1.16	1.0×10^{20}	Spitzer et al (1973)
α Pav	63	0.10	1.9×10^{19}	Henry et al (1976a)
U Gem	76	0.43	1.0×10^{20}	Fabbiano et al (1981)
α Sgr	80	0.12	3.0×10^{20}	Henry et al (1976a)
δ Per	83	0.59	1.5×10^{20}	Spitzer et al (1973)
Feige 24	90	0.01	2.7×10^{18}	Thorstensen et al (1978)
β Cen	90	0.11	3.0×10^{19}	Savage and Jenkins (1972)
AN UMa	100	0.65	2.0×10^{20}	Hearn and Marshall (1979)
α Vir	100	0.03	1.0×10^{19}	Henry et al (1976a)
2A2254-033	100	0.13	3.9×10^{19}	Griffiths et al (1980)

1 atom cm^{-3}.

With the realisation that many galactic sources could conceivably be detected in the EUV from above the earth's atmosphere, a research group at the University of California at Berkeley embarked upon a series of sounding rocket experiments, between 1972 and 1974, to look for EUV sources.

1.2 A Summary of Extreme-Ultraviolet Astronomy

1.2.1 Early Sounding Rocket Experiments

The first two sounding rockets, which were flown in 1972 and 1973 respectively, employed a set of nested gold-coated plane mirrors with a mechanical collimator to constrain the field of view to 1°x50° full width half maximum (FWHM). The collecting area was divided into five overlapping segments each covered with a channel electron multiplier (CEM) photon detector. A bandpass of 135 - 475Å was defined by filters composed of aluminium and carbon. The first flight (Henry et al, 1975b) surveyed an area of sky of approximately 1350 square degrees around the north galactic pole with a limiting sensitivity of 4.3×10^{-8} ergs $cm^{-2} s^{-1}$. A slightly improved version of the experiment (Henry et al, 1976a), on the second flight, covered a similar area of sky down to a flux limit of 2.9×10^{-8} ergs cm^{-2} s^{-1}.

The second experiment also carried two gas filled proportional counters (one argon and one propane), covering soft X-ray wavelengths (44-85Å and 44-125Å respectively), and another CEM (145-515Å), each of field of view 1°x15° (FWHM), for pointed observations of the cataclysmic variables RX Andromedae and U Geminorum (Henry et al,

1975a).

No sources were detected by either of the two surveys. The second experiment obtained 3σ upper limits of 2.7×10^{-11} ergs $cm^{-2} s^{-1}$ (44-125Å) and 6.3×10^{-7} ergs $cm^{-2} s^{-1}$ (145-515Å) for the flux from RX Andromedae, during flare. A single 3σ upper limit of 7.5×10^{-11} ergs $cm^{-1} s^{-1}$ (44-85Å) was obtained for U Geminorum, which was in its quiescent state.

A third experiment (Henry et al, 1976b) comprised a focussing collector equipped with five propane-filled proportional counters having individual fields of view approximately 2°x15° (FWHM). 3700 square degrees of sky around the south celestial pole were surveyed, resulting in the detection of a single source with a flux of 1.3×10^{-9} ergs $cm^{-2} s^{-1}$ (44 - 165Å), lying in an error box containing the cataclysmic variable VW Hydri.

A group from the California Institute of Technology performed a further sounding rocket experiment (Reigler and Garmire, 1975). A spiraltron detector was used to obtain upper limits on a number of objects in the wavelength range 140 to 430Å - α Canis Majoris, o' Canis Majoris, λ Geminorum, γ^2 Velorum and NGC 239. The 2σ upper limits lie between 1.1×10^{-8} and 6.3×10^{-8} ergs cm^{-2} s^{-1} depending upon the observing conditions for a particular target.

1.2.2 The Apollo-Soyuz Test Project

An EUV telescope was flown in 1975 as part of the Apollo-Soyuz Test Project (hereafter ASTP). This experiment, built by the group at Berkeley, obtained the data that led to the first published identification of an EUV source.

The telescope consisted of a set of four nested, concentric, confocal grazing incidence parabolic mirrors (figure 1.3) with a CEM as the focal plane detector. Thin film filters were used to determine four bandpasses : 55 - 150Å, 114 - 150Å, 170 - 620Å and 500 - 780Å (Paresce, 1977). Two modes of observation were employed, a pointing mode having a 2.3° circular field of view (FWHM) for looking at selected objects and a diffuse radiation mode of 4.3° field of view to monitor the EUV background.

Out of thirty two targets observed by ASTP, four were positively detected as EUV sources. Both HZ43 (Lampton et al, 1976), the brightest source, and Feige 24 (Margon et al, 1976) are hot DA type white dwarfs. SS Cygni (Margon et al, 1978), is a cataclysmic variable (dwarf nova type) and soft X-ray source and Proxima Centauri (Haisch et al, 1977) is a dwarf M-type flare star. SS Cygni and Proxima Centauri were both observed during flare.

One further possible detection of an EUV source was reported, in the 500 - 780Å waveband, in the constellation Pavo. An identification either with the ultraviolet intense star HD192273 or the high galactic latitude X-ray source 3U 1959-69 was suspected (Cash et al, 1978a). However an observation of HD192273 with the Voyager 1 UV spectrometer (Barry et al, 1980) placed an upper limit upon the flux from this star

Figure 1.3 Schematic diagram of the ASTP EUV telescope (from Paresce, 1977).

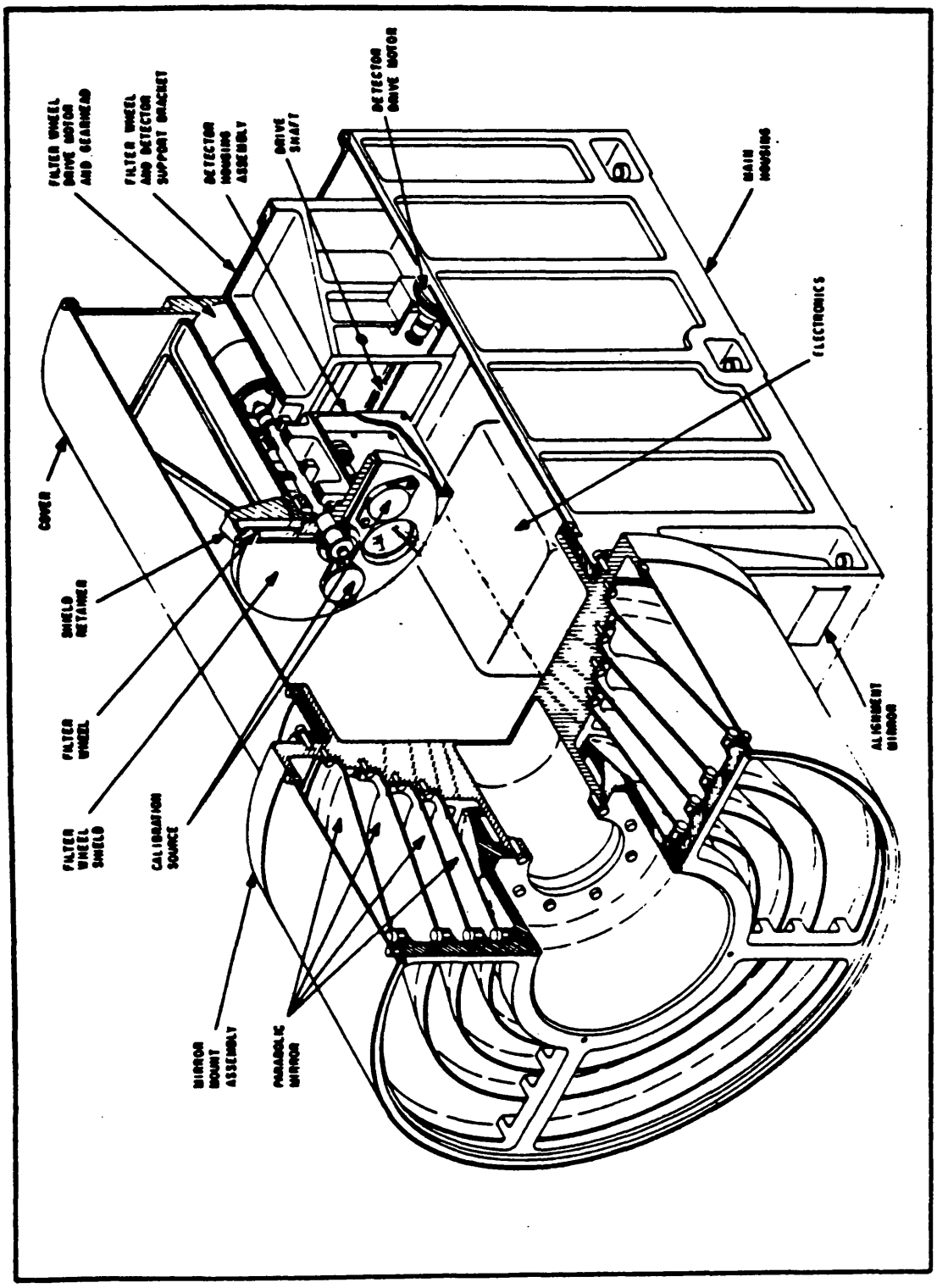

only ~1/10 of the flux reported by Cash et al.

ASTP also established upper limits on several objects including Sirius B, the hot DA white dwarf (Shipman et al, 1977), several pulsars (Greenstein et al, 1977) and catacylsmic variables (Margon et al, 1978), including VW Hydri. Since VW Hydri was optically quiescent during the ASTP observation and its activity during the earlier sounding rocket observation was unknown, VW Hydri remains unconfirmed as a candidate EUV source.

1.2.3 Other EUV Observations

Following ASTP, further attempts at observations in the EUV were made with sounding rockets, by Berkeley and a Dutch/Japanese group, both in 1976, and by further satellite borne experiments on Voyagers 1 and 2 and the Russian/French experiment on Prognoz 6.

The Berkeley experiment was the first imaging EUV telescope to be flown, comprising a Wolter-Schwarzchild Type II grazing incidence mirror and a microchannel plate (MCP) focal plane detector. Passbands were determined by two filters with responses peaking at 300Å and 500Å. An upper limit to the flux from Sirius B (5×10^{-9} ergs cm^{-2} s^{-1}, 170 - 620Å), a factor of ten below that obtained by ASTP, was established (Cash et al, 1978b). Similar upper limits were also obtained on Feige 24 and G191-B2B (Cash et al, 1979).

The Dutch/Japanese collaboration (Bleeker et al, 1978), covering a band 50 - 207Å (60 - 250eV), comprised two detection systems, a one-dimensional X-ray focussing collector with a position sensitive focal plane detector and eight large area collimated proportional counters

having a range of entrance windows. Bleeker et al obtained the first spectrum of an EUV source, observing HZ43.

Both Voyager spacecraft have similar UV spectrometers, covering a band from 500 - 1700Å, which can be used to observe stars during the interplanetary phase of the mission. Further observations of the spectrum of HZ43 were made in the 500 - 1200Å band by Voyager 2 (Holberg et al, 1980b). Many far-ultraviolet observations of hot stars have been made by Voyagers 1 and 2 (Holberg et al, 1982) but only one other object was observed to have any flux shortward of the Lyman edge, the hot white dwarf G191-B2B (Holberg et al, 1980a).

Sagdeev et al (1979) have reported the discovery of another EUV emitting hot white dwarf, Feige 4, by Prognoz 6 in the range 500 - 700Å. However International Ultraviolet Explorer (IUE) spectra of Feige 4 (Holm and Boggess, 1982) suggest a temperature too low for EUV emission and Voyager failed to detect any emission between 500 and 900Å (Holberg, private communication).

In a decade of EUV astronomy, a total of six sources have been discovered and a number of upper limits established by the experiments described in this section. These observations are summarised in table 1.2.

1.3 Likely Classes of EUV Sources

Experimental results give direct evidence of three classes of emitter, hot white dwarfs, cataclysmic variables and flare stars. Theoretical models of emission processes also give more indirect evidence of EUV emission. Within the temperature range 4×10^4K to

Table 1.2. Summary of EUV source detections and upper limits

NAME	BAND (Å)	FLUX (ergs $cm^{-2}s^{-1}$)	REFERENCES
Source Detections:			
HZ 43	55-150	$1.1x10^{-9}$	Lampton et al (1976)
	114-150		
	170-620	$4.0x10^{-9}$	"
FEIGE 24	170-620	$3.0x10^{-9}$	Margon et al (1976)
G191-B2B	500-900		Holberg et al (1980a)
SS Cygni	55-150	$9.0x10^{-11}$	Margon et al (1978)
	114-150		
VW Hydri	44-165	$1.5x10^{-9}$	Henry et al (1976b)
Proxima Centauri	55-150		Haisch et al (1977)
Upper Limits:			
Sirius B	170-620	$5.0x10^{-9}$	Shipman et al (1977)
PSR 1133+16			
PSR 1451-68			Greenstein et al (1977)
PSR 1929+10			
AE Aquarii	55-150	$2.7x10^{-10}$	
VW Hydri	55-150	$9.0x10^{-10}$	Margon et al (1978)
Z Chaemelionis	55-150	$8.3x10^{-10}$	

$4x10^5$K blackbody emission peaks in the EUV

$$kT = hc/\lambda \qquad (1.3)$$

where: k is Boltzmann's constant

h is Plancks constant

c is the velocity of light

T is the temperature

λ is the wavelength of peak emission

Hence, blackbody-like objects having such temperatures - hot white dwarfs, O-B subdwarfs, UV stars, planetary nebulae nuclei and neutron stars - are prime candidates as EUV sources. Thermal bremsstrahlung radiation from hot plasma (10^6K to 10^7K) should also extend into the EUV. Such plasmas occur in several types of object - supernova remnants, stellar coronae, flare stars and accretion driven systems such as cataclysmic variables and close binaries.

This section will discuss the theoretical and experimental evidence that exists for EUV emission from each of the above classes of object and point out the astrophysical significance of such emission.

1.3.1 Hot White Dwarfs

Observations to date (table 1.2, section 1.2) support theoretical considerations that hot white dwarfs are a major class of EUV source. EUV measurements of HZ43 (Lampton et al, 1976; Bleeker et al, 1978; Holberg et al, 1980b) show a spectrum that is a close fit to a blackbody. Lampton et al suggest an effective temperature of 1.1×10^5K while the longer wavelength data of Holberg et al indicate one of 5.5×10^4K. A temperature of 6×10^4K is estimated for Feige 24 (Margon et al, 1976). Any white dwarfs which, like HZ43 and Feige 24, have temperatures in the range 4×10^4-4×10^5K will be potential EUV sources.

The region of the H-R diagram bounded by these temperatures (figure 1.4) is relatively sparsely populated and only by stars in the later stages of their evolution - planetary nebulae nuclei, O-B subdwarfs, UV stars and white dwarfs. White dwarfs constitute the most common final stage of stellar evolution, evolving either from O-B subdwarfs (Weidemann, 1968) or along the Harman-Seaton sequence for planetary nebulae (Harman and Seaton, 1964), and are stabilised at constant radius by temperature independent electron pressure, cooling to invisibility. Determination of their total number, luminosities and effective temperatures will provide important clues as to the final evolutionary stages of the majority of stars. EUV observations provide the means of acquiring this data, obtaining luminosities and temperatures more accurate than those determined by standard methods, from optical and UV data, and thereby a better estimate of the population of these objects. HZ43 and Feige 24, whose positions in the H-R diagram are shown in figure 1.4, illustrate this statement.

1.3.2 Planetary Nebulae Nuclei and Ultraviolet Stars

The central stars of planetary nebulae have temperatures between $\sim 3\times10^4$K and 5×10^5K (Harman and Seaton, 1964; Lang, 1974). Hills (1971) suggests that hot pre-white dwarfs (UV stars) may be responsible for the measured far-UV flux from M31, which requires sources with mean temperatures in excess of 10^5K. Thus both these types of object are potential EUV sources.

It appears from theoretical calculations (Salpeter, 1971) and observations of planetary nebulae in the Magellanic clouds (Webster, 1969) that the luminosity of planetary nuclei increases with age, reaching a maximum $\sim 10L_\odot$ before declining towards the hot white dwarf regime, as postulated by Harman and Seaton (1964). The space density of planetary nebulae has been estimated, assuming lifetimes of $\sim 10^4$-3×10^4years, as $\sim 10^{-7}$pc^{-3} (ESA, 1979). Hence ~12 will be found within 300pc of the sun.

UV stars may be remnant planetary nebulae nuclei continuing the cooling process towards the white dwarf stage or, as Hills (1972) suggests, they may have evolved directly from red giants. Hills points out that the lifetime of these stars is considerably longer, $\sim 10^6$-10^7years, than that of planetary nebulae and estimates a space density which is dependent upon the rate of cooling by neutrino emission.

$$n_{UV} = 1\times10^{-5}\text{pc}^{-3}(1-\tau) \qquad (1.4)$$

where: n_{UV} is the space density of UV stars

τ is the fraction of the star's energy emitted as neutrinos

Hills estimated the lifetime of a UV star to be

$$t_{UV} = 7 \times 10^6 \text{years}(1-\tau) \qquad (1.5)$$

If the star cools without neutrino emission ($\tau=0$, $t_{UV}=7\times10^6$) $\sim10^3$ will be found within 300pc of the sun. If energy loss by neutrinos is significant ($\tau\sim0.9$ say) then $\sim10^2$ will be found within 300pc. Thus, these objects should yield a large number of EUV sources. However, none have been detected by UV surveys such as the OAO-2 or TD-1A satellites and, without the presence of a nebula, they have no a priori optical identification.

EUV observations will improve our knowledge of the evolutionary path between planetary nebulae and white dwarf stages. In particular constraints will be placed on the space density of UV stars allowing determination of their lifetime and energy loss.

1.3.3 O-B Subdwarfs (sdO and sdB stars)

An alternative pre-hot white dwarf evolutionary sequence passes through the hot O-B subdwarf class of stars (Liebert, 1980), stars possessing inert helium cores with thin hydrogen burning shells. They should have temperatures in the range 10^4 - 10^5K and several have been identified optically (Greenstein and Sargent, 1974) that may have

temperatures greater than $5x10^4$K. Greenstein and Sargent have also found many of these stars at high galactic latitude suggesting that they are old stars from an evolved stellar population. O-B subdwarfs are too hot or too low in luminosity for helium burning evolution and some have temperatures too low to fit theoretical models for non-binary contracting stars of reasonable mass ($>0.4M_\odot$). Carnochan et al (1975) suggest that many unidentified UV bright stars seen by the TD-1A satellite, which obtained stellar spectra in the far-UV (1400 - 2550Å), are sdOs implying a space density of such objects $>8x10^{-5}pc^{-3}$, or ~8000 within 300pc of the sun. This represents a population even larger than that estimated for UV stars. Superficially, it might be expected that most hot white dwarfs will have evolved along this path, but the proportion following each evolutionary track will depend upon the time spent on each as well as the relative populations. It is hoped that EUV observations will ultimately provide this information and allow determination of the "branching ratio" between subdwarf and planetary nebula paths.

1.3.4 Neutron Stars

When formed, neutron stars are exceedingly hot. Tsuruta (1974) predicts temperatures as high as ~$2-4x10^6$K for young neutron stars such as the Crab nebula and Vela supernova remnant (SNR) pulsars. However, after several million years temperatures become only several hundred to several thousand degrees. The cooling rate of a neutron star may be slowed by frictional heating (Greenstein, 1975), or heating by the accretion of material from the surrounding medium if

the star is travelling slowly enough. The competing processes make it difficult to predict the resulting cooling rate and consequently when a neutron star will be cool enough to emit in the EUV.

Tsuruta (1981) has reviewed cooling theory of neutron stars and compared predicted cooling models with measurements and upper limits of the luminosities and temperatures of neutron stars measured by the Einstein observatory (figure 1.5). These results show that substantial X-ray fluxes will be emitted by neutron stars $\sim 10^3$-10^4 years old (temperatures $\sim 10^6$-$10^{6.5}$K). All the positive detections - Crab, Vela and RCW103 SNRs - lie within the limits of Tsuruta's cooling models. Some of the upper limits suggest lower temperatures for the neutron stars but it is possible that this may be due to a complete absence of a neutron star in the case of SN1006 and Cassiopiea A SNRs. As blackbody spectra peak in the EUV between $\sim 4\times10^4$K and $\sim 4\times10^5$K (section 1.3.1), neutron stars would be expected to be EUV sources later in their life. Tsuruta's model suggests an age greater than 10^4 years.

EUV flux upper limits on the radio pulsars PSR 1133+16, PSR 1451-68 and PSR 1929+10 were obtained by ASTP (Greenstein et al, 1977). These upper limits, calculated in each band of the experiment, were used to derive upper limits to the temperature of the stars. Uncertainties in the knowledge of the line of sight column densities and the stellar radii (and therefore the masses) give a range of temperatures, corresponding in the most favourable cases to $T<1.6\times10^5$K. The ASTP upper limits all lie above temperatures predicted by the models of Tsuruta (1974) and Greenstein (1975) for

Figure 1.4 Luminosity - Effective temperature diagram for prime EUV candidates. HZ43 and Feige 24 are shown by the filled circles.

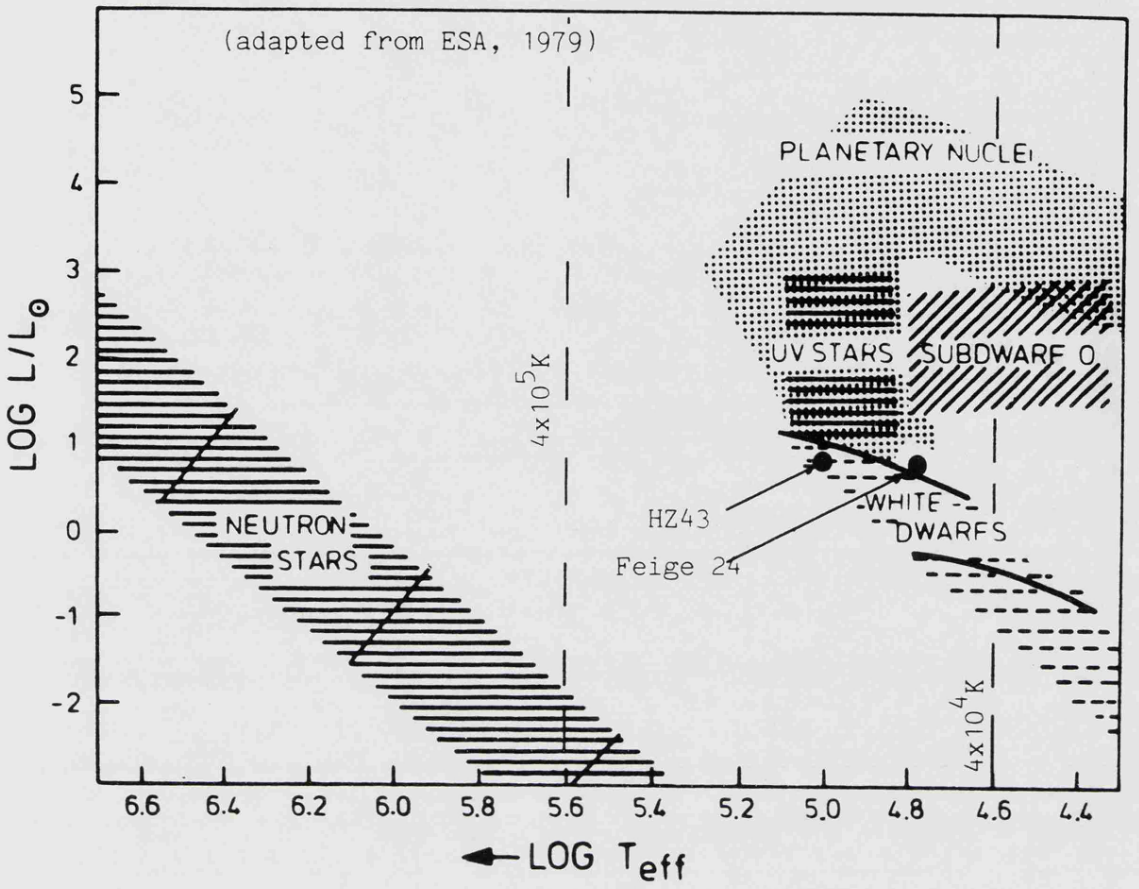

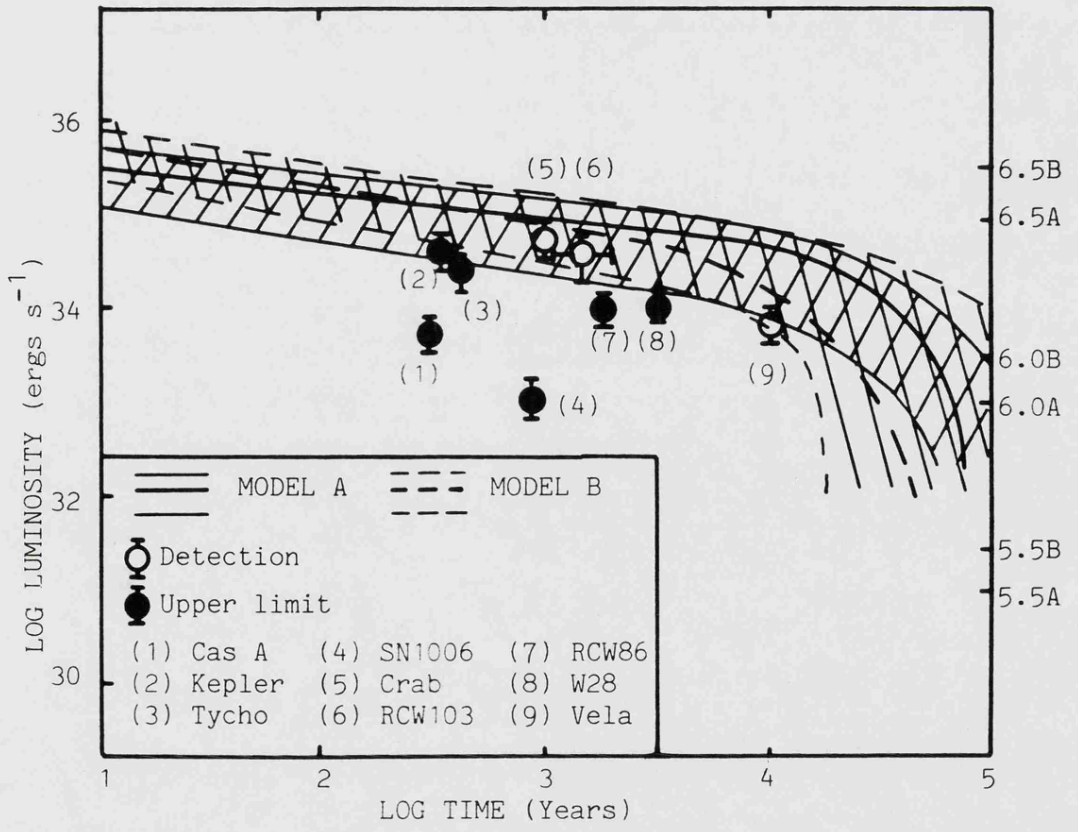

Figure 1.5 Comparison between experiment and the cooling theory of Tsuruta (1981) for neutron stars.

each pulsar, hence more sensitive EUV measurements are required to compare with these neutron star cooling theories.

1.3.5 Stars With Hot Coronae and RS Canum Venaticorum Binaries

Soft X-ray measurements (0.15 - 4.0KeV) made by the Einstein telescope (Vaiana et al, 1981) have established stars in general as a class of low luminosity soft X-ray sources. The emission is most likely derived from hot coronae which must be several orders of magnitude more active than the solar corona. To date soft X-ray emission has been reported from ~150 stars and stellar systems throughout most of the H-R diagram. The level of coronal activity may well depend strongly on the rotation rate of the star, the presence and strength of a magnetic field and presence or absence of a companion star.

RS Canum Venaticorum (RS CVn) binaries have also been observed as soft X-ray sources by both the HEAO 1 A/2 experiment (Walter et al, 1980) and Einstein (Swank et al, 1980). The results of Walter et al (1980, 0.15 - 2.8KeV) suggest thermal bremsstrahlung emission as the source of radiation with a characteristic temperature of 10^7K. Einstein solid state spectrometer (SSS) measurements (0.4 - 4KeV) suggest a two component model with temperatures $\sim 5 \times 10^6$K and $\sim 5 \times 10^7$K.

The surface temperatures of main sequence stars are generally $< 10^4$K. Hot coronal plasma ($\sim 10^7$K) must therefore be supported by cooler gas of intermediate temperature which will radiate strongly in the EUV, the strength depending upon the temperature profile of the gas with respect to height and the density of the plasma, which are

largely unknown parameters for most stars. Figure 1.6a shows the solar temperature and electron density profile as an example. The solar corona radiates quite strongly in the soft X-ray and EUV (figure 1.6b), a large fraction of the latter being emitted in lines, but is much less active than those stars observed by the Einstein telescope and HEAO 1. However, if, as Walter et al(1980) suggest, the difference between solar and RS CVn activity is only a matter of scale, RS CVns should be bright EUV as well as soft X-ray sources. Similarly the active coronae of single stars should also be EUV sources.

Study of the temperatures and emission measures of these stars will enhance understanding of stellar atmospheres, EUV observations providing information about the transition between the chromosphere and corona itself.

1.3.6 Flare Stars

Flare stars are late dMe red dwarfs some of which may be binary systems. They show characteristic rapid increases in optical flux of a few magnitudes and lasting about thirty minutes between one and ten times per day. ASTP detected one such star (Haisch et al, 1977), Proxima Centauri, in the EUV. As Proxima Centauri was only seen on one of two observations, it is likely that it was flaring when detected in the EUV. Simultaneous X-ray and optical observations of UV Ceti (Heise et al, 1975), one of the most active flare stars, show that soft X-ray and optical flares coincide.

Figure 1.6a Temperature and electron density as a function of distance from the solar surface (Zombeck, 1981).

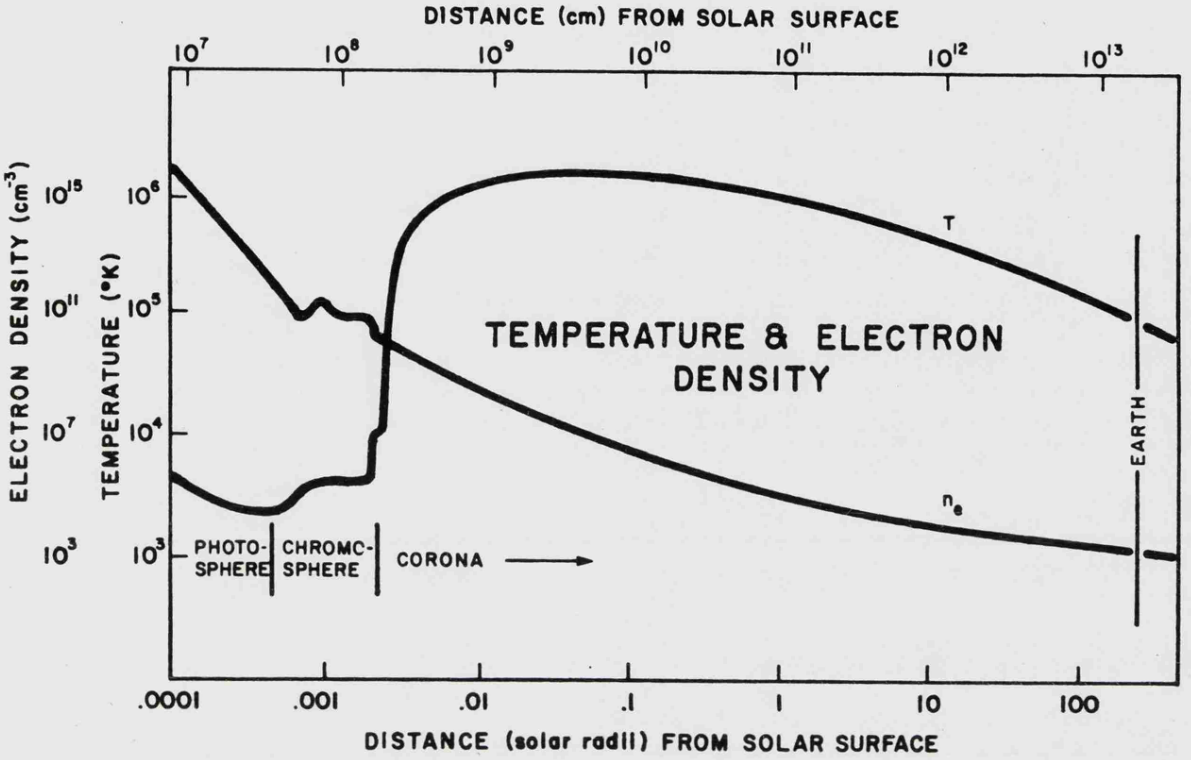

Figure 1.6b (Zombeck, 1981).

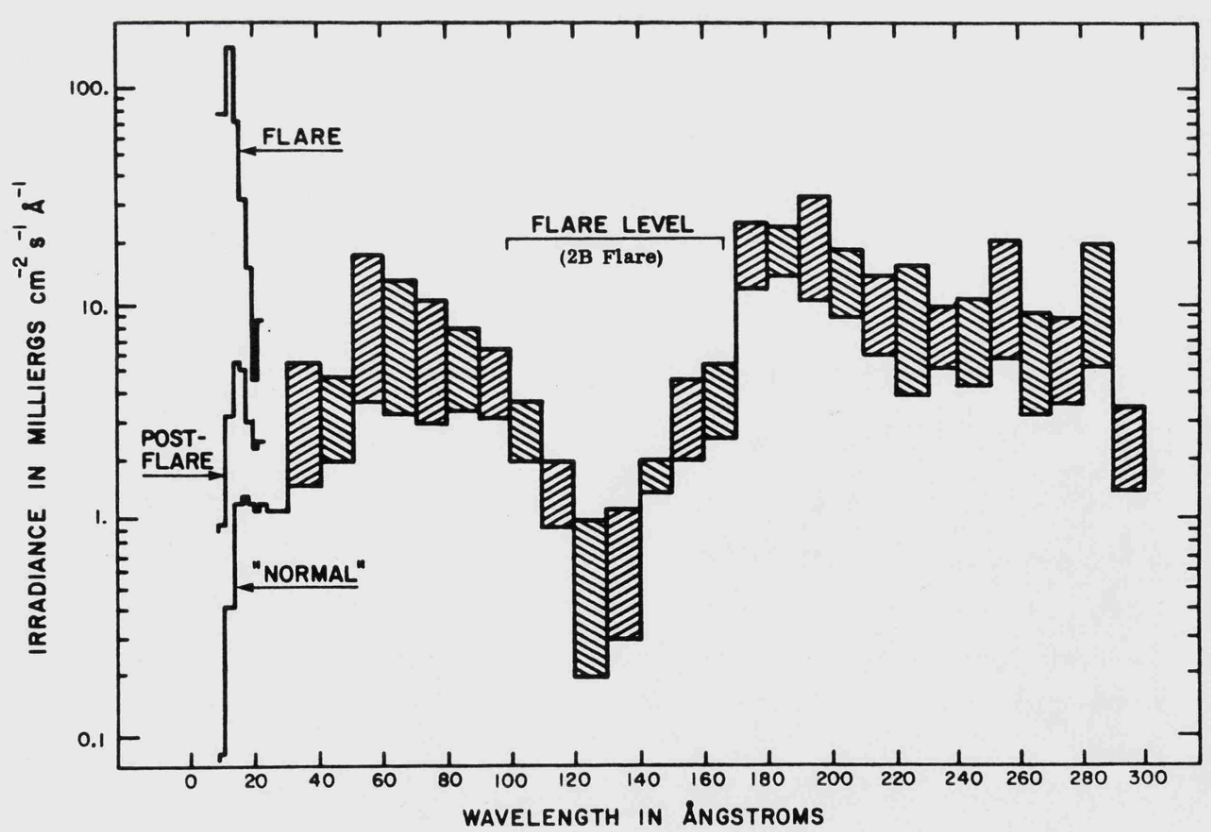

The solar spectral irradiance at 1 AU between 10 and 300 Å. Three states of solar activity are shown for the region 10–30 Å. The vertical extent of the shaded areas is representative of the variability of the spectral irradiance for changing solar conditions.

Haisch et al suggest that the source of the EUV flux is an optically thin flare plasma at a temperature of 10^6-10^8K. The X-ray emission from UV Ceti and 10^7K temperature of solar flares indicate that these temperatures are typical for flare plasma. Hence, if sufficiently active, flare stars should be EUV sources.

1.3.7 Dwarf Novae Type Cataclysmic Variables

Dwarf novae are U Geminorum type very short period binaries consisting of a red dwarf spilling matter onto a close hot white dwarf companion. They exhibit quasi-periodic optical outbursts of several magnitudes with occasional rapid optical flickering at maximum outburst. The time between outbursts is different for different objects ranging between 20 and a few hundred days. SS Cygni, observed in the EUV by ASTP (Margon et al, 1978) is a member of this class of system, which are analogous to binary X-ray emitters such as Hercules X-1 and Centaurus X-3 where the companion is a neutron star rather than a hot white dwarf.

Paresce (1977) uses this analogy to estimate the characteristic spectrum of a dwarf nova from that of an X-ray binary. The masses of the two types of system will be very similar and the ratio of the energies must therefore equal the ratio of the radii. R(white dwarf) is ~10^9cm and R(neutron star) is ~10^6cm. The characteristic spectrum of a binary X-ray source has kT~12-15KeV giving kT(white dwarf)~12-15eV with temperatures of 10^4-10^5K. Consequently as confirmed by ASTP we would expect dwarf novae to be bright in the EUV. Measurements of the EUV flux from these systems will provide valuable

insight into the physical processes occurring in these systems as do the observations of X-ray binaries.

1.3.8 Close Binaries

Another source of hot plasma, and therefore EUV radiation, is the transfer of gas between two close binary companions. Evidence for such mass transfer has been found from observations of Alpha Aurigae (Capella) in the soft X-ray (Catura et al, 1975; Mewe et al, 1975) and ultraviolet bands (Dupree, 1975). The luminosities of these objects will be determined by the rate of matter transfer, while the peak wavelength of the emission will be a complex function of the accretion mechanism, the thermalisation of the kinetic energy and the radiation transfer. Therefore, any close binary system could be a potential EUV source.

1.3.9 Supernova Remnants

The occurrence of a supernova ejects a shell of gas expanding at high velocity (up to $1\text{-}2\times10^{4}$ km s^{-1}). Investigations distinguish four phases of evolution. Initially the remnant expands at a relatively constant rate until the amount of interstellar material swept up is comparable to the mass initially ejected. Then an adiabatic blast wave develops leaving behind the original ejecta. As the velocity of the blast wave decreases the temperature of the gas behind the shock front decreases and eventually radiative cooling becomes important. At this time a cool, thin, dense shell of gas evolves. Eventually the velocity of the gas shell decreases to the random velocities of the

ISM and the remnant loses its identity.

Soft X-rays have been detected from a number of supernova remnants (SNRs) (eg. Rappaport et al, 1979; Levine et al, 1979; Pye et al, 1981; Fabian et al, 1980) and originate in plasma of temperature $>10^6$K behind the shock front. EUV emission is likely to occur in the later stages of evolution when the plasma is cooler.

In a young SNR deceleration of the ejected matter causes a shock wave to propagate inward, heating the material through which it passes - reverse shock heating. This process occurs when the SNR radius is typically less than a few parsecs (McKee, 1974). Soft X-rays are emitted at energies determined by the temperature of the reverse shock. As this shock cools it will emit in the EUV.

EUV radiation will form an important component of the net flux in either very young or quite old SNRs. Observations in this band will contribute to the understanding of the propagation of blast waves in the interstellar medium, at two different points in their evolution.

1.3.10 The Interstellar Medium

Supernovae will provide a source of hot gas in the Interstellar Medium (ISM). Evidence for the existence of this gas, of temperature 10^6K, is provided by the diffuse soft X-ray background (deKorte et al, 1976; Sanders et al, 1977; Marshall, 1982). The data offer evidence that the emission is local for a number of reasons.

- The brightness distributions are patchy, unlike the background at higher energies (>1KeV) which is highly isotropic and predominantly extra-galactic.

- The correlation of soft X-ray brightness with neutral hydrogen column density is not consistent with what might be expected from simple photoabsorption of galactic flux.

- A number of energy-dependent large scale features are discernible (eg. the North Polar Spur).

- There is emission from the galactic plane at 0.25keV which would be absorbed by intervening material if it were extra-galactic.

The presence of OVI absorption lines in the spectra of hot stars also provides evidence for material with temperatures $>10^5$K (Jenkins, 1978).

Two models exist for the disposition of the hot plasma in the ISM. Cox and Smith (1974) propose that supernovae generate and maintain a mesh of interconnected tunnels of very low density gas at 10^6K, occupying roughly half the interstellar volume. Energy from new supernova events will be efficiently propagated through the tunnel network reheating the slowly cooling plasma, hence the plasma will be isothermal. However, McKee and Ostriker (1977), considering supernovae explosions in an inhomogeneous medium, show that a two phase model is unstable. Imposing pressure equilibrium conditions, they suggest a multi-temperature model of cold clouds (T~100K) with conducting interfaces to a hot intercloud medium (T up to $\sim 5\times10^5$K).

The model of Cox and Smith finds support in the existence of extended regions of enhanced soft X-ray emission, such as the North Polar Spur, which is a gigantic supernova shell in its adiabatic phase and has $T\sim3\times10^6$K. However, temperature measurements derived from

observations in different wavebands and different regions of sky yield different values, eg. $10^5K<T<4x10^5K$ (Stern and Bowyer, 1979) and $4x10^5K<T<10^6K$ (Levine et al, 1976 and 1977), supporting McKee and Ostriker. Paresce and Stern (1981) have analysed Berkeley EUV background measurements (Stern and Bowyer, 1979; Cash et al, 1976) using isothermal and multi-temperature models, finding agreement in both cases with the suggestion from harder X-ray data that the sun is immersed in a hot ($T>10^5K$) plasma extending out to ~100pc. From the existing experimental data no choice can be made between the two models.

Clearly, from the discussion above, the ISM is complex. The temperature ranges of plasma in the ISM make EUV observations a useful tool for testing the theoretical models. Both spectrally and spatially resolved data will be important for future study.

1.4 The Extreme-Ultraviolet Background

There are two separate sources of EUV background, the cosmic sky background (arising from the ISM) and emission arising from the earth's local environment. In order to make good observations of the cosmic EUV background it is necessary to separate the two components. There are two contributions to the local background

1) The plasmasphere (geocoronal)

2) The interplanetary medium

The solar flux incident upon the earth in the 50-250Å band is about 1 erg cm^{-2} s^{-1}. Much of this flux is in line radiation which can be resonantly scattered by ions and neutral atoms in the earth's plasmasphere. The intensity of the scattered radiation will depend upon the number of atomic and ionic species present and also vary with solar activity.

Below 1000Å the helium I (584Å) and helium II (304Å) lines predominate. Weller and Meier have described, from the Space Test Program (STP) 72-1 satellite, how the intensities of HeI (Meier and Weller, 1974) and of HeII (Weller and Meier, 1974) vary with the solar zenith angle (the angle between sun, earth and satellite, figure 1.7) and magnetic latitude for two viewing directions, along the zenith and nadir. In both cases the minimum intensity occurs when the satellite is at its nadir with respect to the sun and when the view direction is along the earth shadow. The maximum HeI flux (~50 Rayleighs) occurs during the daytime (solar zenith angle <90°) and appears to be independent of the view direction. At night the flux drops by two orders of magnitude or more to a minimum, looking along the earth shadow. The night-time flux is due to the contribution from interplanetary helium (1-9 Rayleighs) (Weller, 1981). The HeII emission (5 Rayleighs maximum) is an order of magnitude below the HeI flux but shows similar variation with some differences caused by the interaction between the ions and the earth's magnetic field. The range of geocoronal fluxes outlined above are summarised in table 1.3a.

Above 1000Å the geocoronal spectrum is dominated by the emission lines of neutral hydrogen (1216Å and 1025Å) and those of neutral oxygen (1304Å and 1356Å). The lines of neutral hydrogen have been observed with satellite and sounding rocket experiments (Meier and Mange, 1970; Thomas and Anderson, 1976; Paresce et al, 1972; Young et al; 1971). At high altitude (~650Km) the intensity of the Lyman α (1216Å) radiation does not appear to vary with viewing direction but does change with solar zenith angle between a maximum of 2×10^4 Rayleighs and a minimum of 10^3 Rayleighs (Meier and Mange, 1970). The data of Thomas and Anderson (1976) support this conclusion. At rocket altitudes (~215Km) some variation with viewing angle is seen (Paresce et al, 1972). The hydrogen 1216Å and 1024Å fluxes are summarised in table 1.3b with the oxygen 1304Å data of Meier and Prinz (1971).

To date, few direct measurements of the cosmic EUV background have been made and estimates of the expected flux rely heavily on theoretical models. Grewing (1975) has derived a model of the background between 1750Å and 504Å, based on far-ultraviolet observations made by the Copernicus satellite, showing that the flux fits a blackbody of temperature $\sim 1.1 \times 10^4$K and is the result of contributions from a large number of O and B stars.

The ASTP experiment carried out an extensive survey of the EUV background between 50Å and 775Å as part of the mission (Stern and Bowyer, 1979). Although the cosmic background at the longer wavelengths was masked by geocoronal radiation an intense background was observed in the 114 to 155Å band. Using upper limits from the

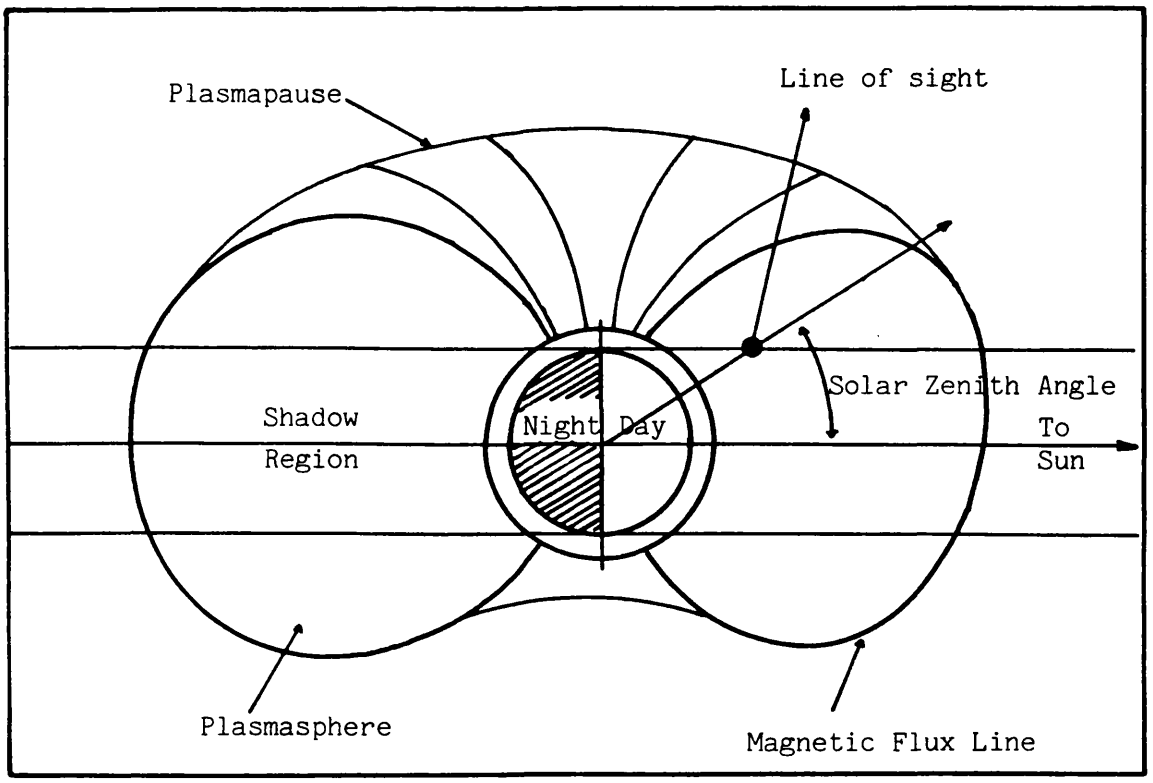

Figure 1.7 The observing geometry for a spacecraft.

Table 1.3a. Geocoronal helium line background fluxes

Line	Wavelength	Flux		
		Maximum	Mean	Earth Shadow
HeII	304Å	5R*	1R	<0.03-1R
HeI	584Å	50R	10R	1-9R

* 1R = 1Rayleigh = 7.96×10^4 photons $cm^{-2} s^{-1} ster^{-1}$

The maximum fluxes are obtained at a solar zenith angle of 0°.

Table 1.3b. Geocoronal hydrogen and oxygen line background fluxes

Line	Wavelength (Å)		Flux (R)	Solar Zenith Angle (°)	Zenith Angle (°)	Altitude (km)
HI	1025		10	night-time	44-50	230
HI	1216	maximum	2×10^4	0-180	0	~650
		minimum	1×10^3	0-180	180	~650
		maximum	9×10^3	150	80	215
		minimum	3×10^3	150	140	215
OI	1304	maximum	5×10^3	76	?	~500
		minimum	1×10^3	90	?	426-855

other bands and other experimental data in the same band (Cash, Malina and Stern, 1976; Burstein et al, 1977) Stern and Bowyer propose a single temperature model, in the range $5.1<\log T<5.6$ for the background above 44Å. The background between 44Å and 1750Å can be derived by combining the models of Grewing and Stern and Bowyer. Scaling the latter to the measurements of Cash, Malina and Stern (1976) at 124Å, where the flux predicted by Grewing's model is negligible, the two model curves can be summed and the geocoronal line fluxes added to the resultant (figure 1.8). It should be noted that other soft X-ray/EUV measurements of the background (Yentis et al, 1972) suggest that the flux may vary in scale in different parts of the sky.

1.5 Summary

The past decade has seen the development of EUV astronomy through sounding rocket experiments and satellite experiments on ASTP and Voyager. Six sources have been discovered to date from three classes of object - hot white dwarfs, cataclysmic variables and flare stars. Theoretical considerations also suggest these and other types of object as potential EUV sources, dividing them into two groups depending upon their emission mechanism;

a) Blackbody (4×10^4K - 4×10^5K)

hot white dwarfs

O-B subdwarfs

planetary nebulae nuclei

UV stars

Figure 1.8 A model of the extreme ultraviolet background.

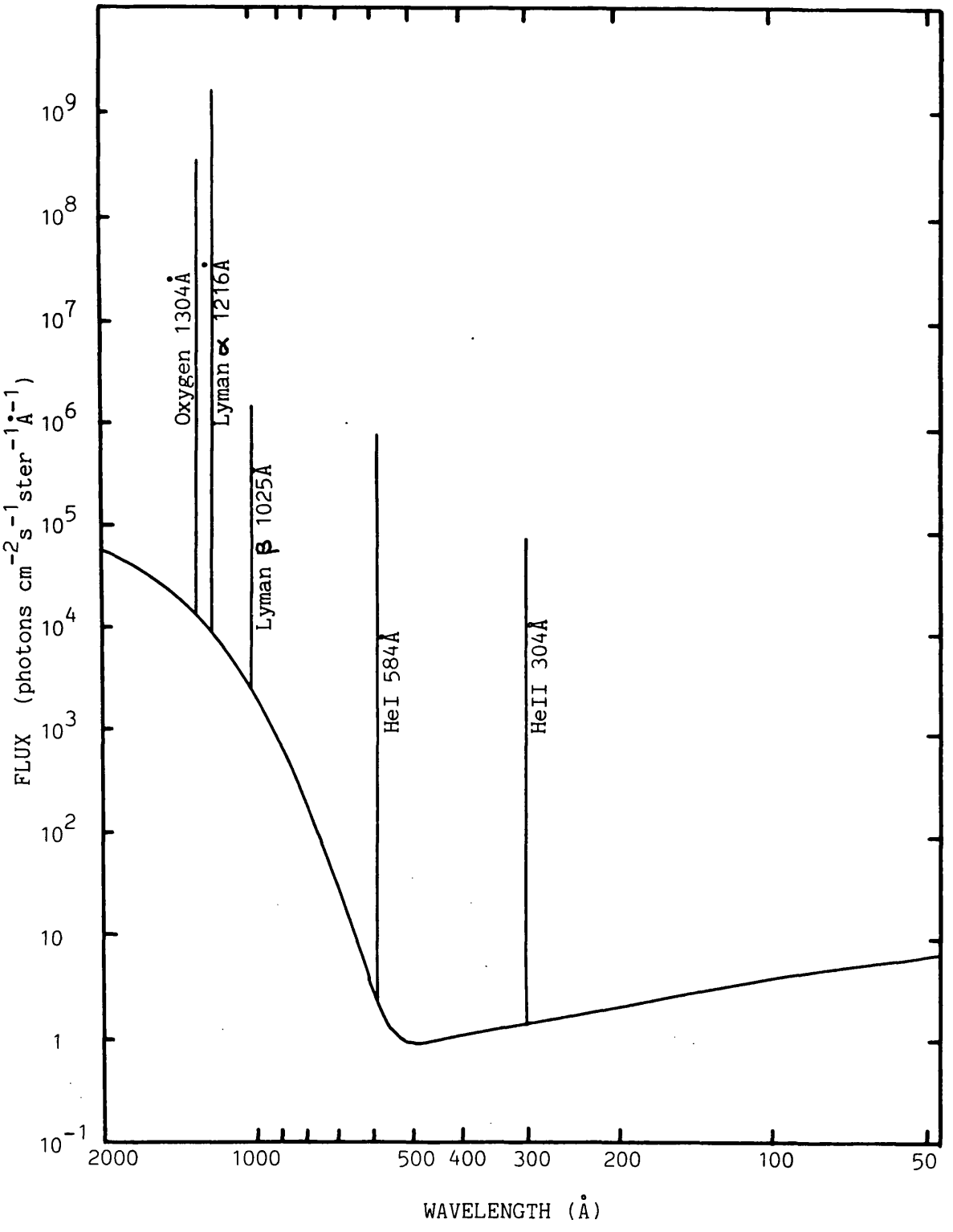

neutron stars

b) Thermal emission from hot plasma (10^6K - 10^7K)

stellar coronae

RS CVn variables

flare stars

cataclysmic variables

close binaries

supernovae remnants

interstellar medium

Further EUV observations of the first group of objects may be expected to yield information about the evolution of stars towards the end of their life, away from the main sequence. Observations of the second group will contribute to the understanding of stellar atmospheres, mass transfer systems and the physics of the interstellar medium.

Only one of the six sources, G191-B2B, has been discovered since ASTP, most experiments having concentrated on pointed observations of a few objects (eg. Cash et al, 1978b; Bleeker et al, 1978). However, in order to approach the astrophysical problems outlined in section 1.3, a much larger sample of EUV sources is required. The Wide Field Soft X-ray Camera (WFSXC) developed jointly by MIT and Leicester for flight on NASA sounding rockets has been designed with this as its principal objective. The remainder of this thesis deals with the development, test and flight of the WFSXC.

CHAPTER 2

THE WIDE FIELD SOFT X-RAY CAMERA ROCKET EXPERIMENT

2.1 Description of the payload

The Wide Field Soft X-ray Camera (WFSXC) payload (figure 2.1) is an imaging telescope with associated structural and electronic equipment which is designed to be flown on sounding rockets, to carry out partial EUV surveys of the sky or pointed observations of selected objects. The WFSXC telescope comprises a set of nested grazing-incidence mirrors with an MCP* detector at the focal plane. Thin film filters are mounted in front of the detector to define the energy bandpass (50-250Å, the XUV), and to attenuate geocoronal background radiation which would otherwise saturate the detector.

The MCP detector can only be operated in vacuum, at pressures below $\sim 5 \times 10^{-5}$ Torr, and is therefore mounted in a vacuum box to permit ground operations and to provide protection for the detector and filters during launch. The housing is evacuated by an ion pump which can attain a pressure of $\sim 10^{-7}$ Torr. It is intended that the vacuum housing should be pumped until the moment of launch when a "snatch" disconnect turns the pump off. When sufficient altitude is attained the spring loaded housing lid is released by a pyrotechnic device.

The payload skin is not structural, hence mechanical support for the payload components is provided by four parallel rails, mounted on a 17" (43cm) base plate, braced by a series of diagonal struts. The telescope mirrors are mounted on the top of the support structure

* Microchannel Plate

(figure 2.1) with the star camera in the centre of the nest, to provide aspect data. A thick (1") bulkhead mounted between the rails, ~40cm below the mirror, supports the vacuum housing, which is connected to the ion pump via a bellows attachment. The bellows ensures that any flexing of the structure does not break the vacuum connection. During flight a battery is mounted adjacent to the ion pump. Below the ion pump bulkhead are the payload electronics that handle the output pulses from the detector. The payload has a total length of 44" (1.1m).

Image readout is accomplished via a resistive anode on which charge, generated when an X-ray enters the detector, is deposited. Four preamplifiers mounted underneath the vacuum housing bulkhead collect the anode output. The signals from these are passed to the processing electronics which calculate the event coordinates and digitise the output. The individual electrode signals are also digitised. All six signals are then passed to the telemetry (TM) unit that transmits the data to the ground station. The TM unit is a standard 200kHz pulse code modulated system (PCM). It has 15 channels which are all read out once every 0.8ms, comprising one telemetry "frame". Therefore the 6 digitised outputs from the payload can be transmitted twice every frame, a maximum count rate of 2500 s^{-1}.

The TM is part of the standard NASA support provided by Goddard Space Flight Center (GSFC), which includes a Strap III gas jet attitude control system (ACS), with a pointing accuracy $\sim \pm 1°$. This accuracy can be maintained with maximum slew and roll rates of $6°s^{-1}$. A parachute recovery module is also included in the support. Figure

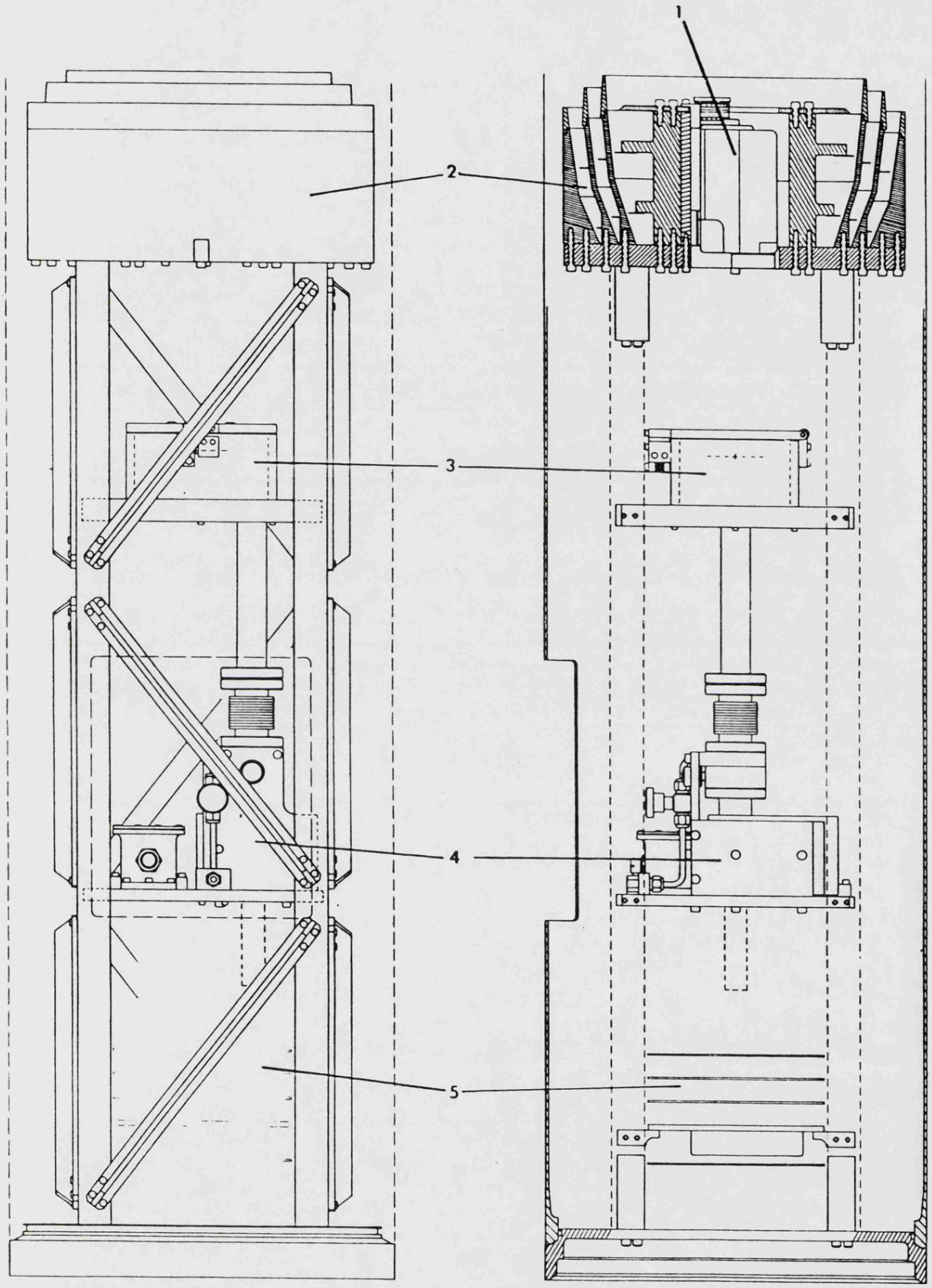

Figure 2.1

Schematic of the Wide-Field Soft X-Ray Camera payload. Key components include: (1) aspect camera, (2) nested telescopes, (3) detector vacuum housing, (4) ion pump, (5) electronics boards.

2.2 shows a line drawing of the payload with support systems.

2.2 Instrument Design Objectives

2.2.1 The Mirrors

In order to cover a large area of sky, a survey experiment requires a wide field of view and high throughput. Accurate positioning of detected sources is also required to facilitate optical identification. These objectives are most easily achieved with an imaging system. Thus a focussing collector is required that satisfies the above requirements.

For an optical system to image it must satisfy the Abbé sine condition, at least approximately. The Abbé sine condition states that an optical system will form an image of an infinitely distant source only if, for each ray from the source

$$h_r/\sin\theta_r = f \qquad (2.1)$$

where: h_r is the distance of the ray from the optical axis

θ_r is the angle of the final path of the ray relative to the optical axis

f is a constant for all rays

Any optical system satisfying this condition acts as a simple spherical lens.

Figure 2.2 Schematic of the payload and its support systems

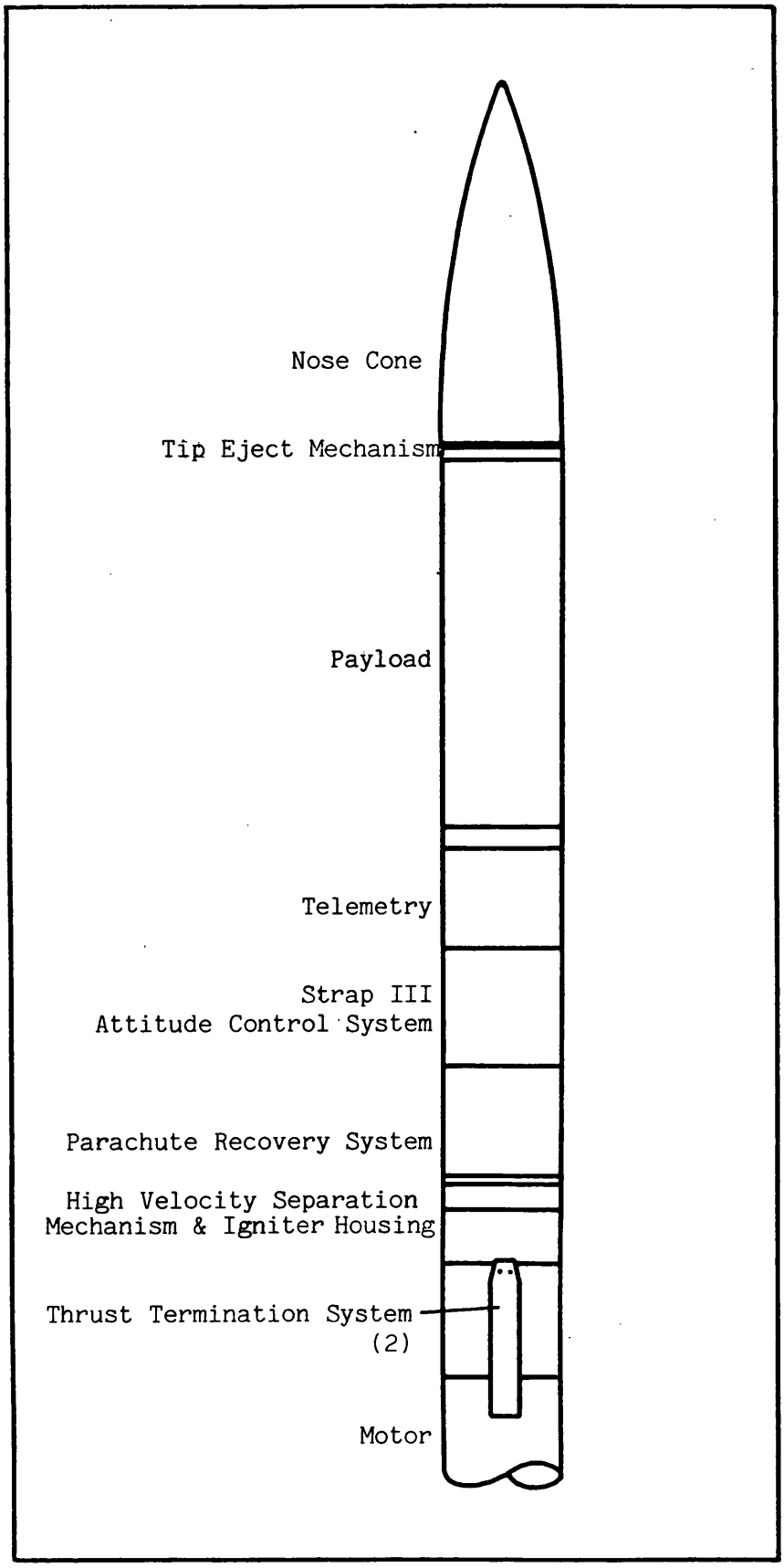

Reflection efficiencies at normal incidence are low at soft X-ray wavelengths, thus grazing incidence optics are needed. Wolter (1952a, 1952b) has discussed three different grazing-incidence telescopes comprising two elements, a parabolic surface followed by a confocal hyperboloid or ellipsoid, that nearly satisfy the Abbé sine condition, the types I, II and III (figure 2.3). In these systems each incoming ray is focussed by a double reflection. The design most commonly used is the Wolter I since it has the simplest mechanical configuration (figure 2.3a). Compared to normal incidence mirrors, grazing incidence optics have a small collecting area. The Wolter I design allows the possibility of nesting several telescopes inside one another, in order to increase the collecting area and therefore the sensitivity. The type II allows longer focal lengths and therefore higher focal plane magnifications than a type I of comparable aperture and grazing angle. All Wolter type telescopes suffer from curvature of field. As the effect is much more severe in type II systems than in type I, the type II is only useful as a narrow field imager.

The design of telescope proposed to fulfill the WFSXC requirements is the Wolter-Schwarzchild type I (Chase and VanSpeybroeck, 1973), which is based on the Wolter I but has slightly modified surfaces that exactly fulfill the Abbé sine condition. This eliminates coma near the optical axis and helps reduce off-axis aberrations. The reflectivity of the mirror surface, usually gold, restricts the maximum achievable field of view of the telescope, as the larger the X-ray grazing angle the lower the efficiency at high energies. A high energy limit $\sim$50Å is required by the experiment

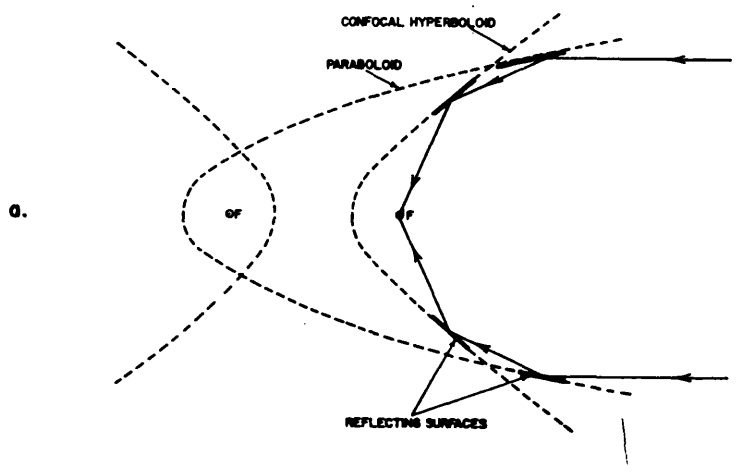

Figure 2.3 The three configurations of X-ray imaging telescopes suggested by Wolter (1952a and 1952b). (figure from Giacconi et al, 1969)

passband, allowing grazing angles (with gold) of 0-8° and therefore a field of view ~8°.

The geometric collecting area (A) of a mirror is an annulus defined by the front and rear radii of the front mirror element. A nested set of mirrors will have a total area which is the sum of the annuli for each element. Although the area subtended by the annuli decreases as a cosine function of the angle away from the optical axis, A is dominated by the vignetting of baffles in the system, designed to remove straight through and singly reflected rays, that would otherwise contribute to the instrument background.

For the WFSXC, the physical size of the mirrors, and therefore the collecting area, is restricted by the diameter of the rocket cylinder (17 inches). A nest of three mirrors has an on-axis collecting area of ~300cm^2 falling to ~200cm^2 at the edge of the field (figure 2.4). The expected mirror efficiency, shown as a function of wavelength in figure 2.5, is the square of the reflectivity of the surface as each X-ray undergoes two reflections. The effective area of the mirrors (geometric area X efficiency) is included in figure 2.4.

Since the focal surface of the Wolter-Schwarzchild mirrors is curved, a flat plane detector placed at the paraxial focus will see increasingly defocussed images with increasing off-axis angle. Off-axis aberrations contribute to the effect. The shape and size of the defocussed image, and hence the resolution of the telescope, can be determined theoretically by a ray tracing of the telescope geometry (Petre, 1982), and is characterised by the root mean square (RMS) of

Figure 2.5 The efficiency of the WFSXC telescope calculated from the reflectivity of gold.

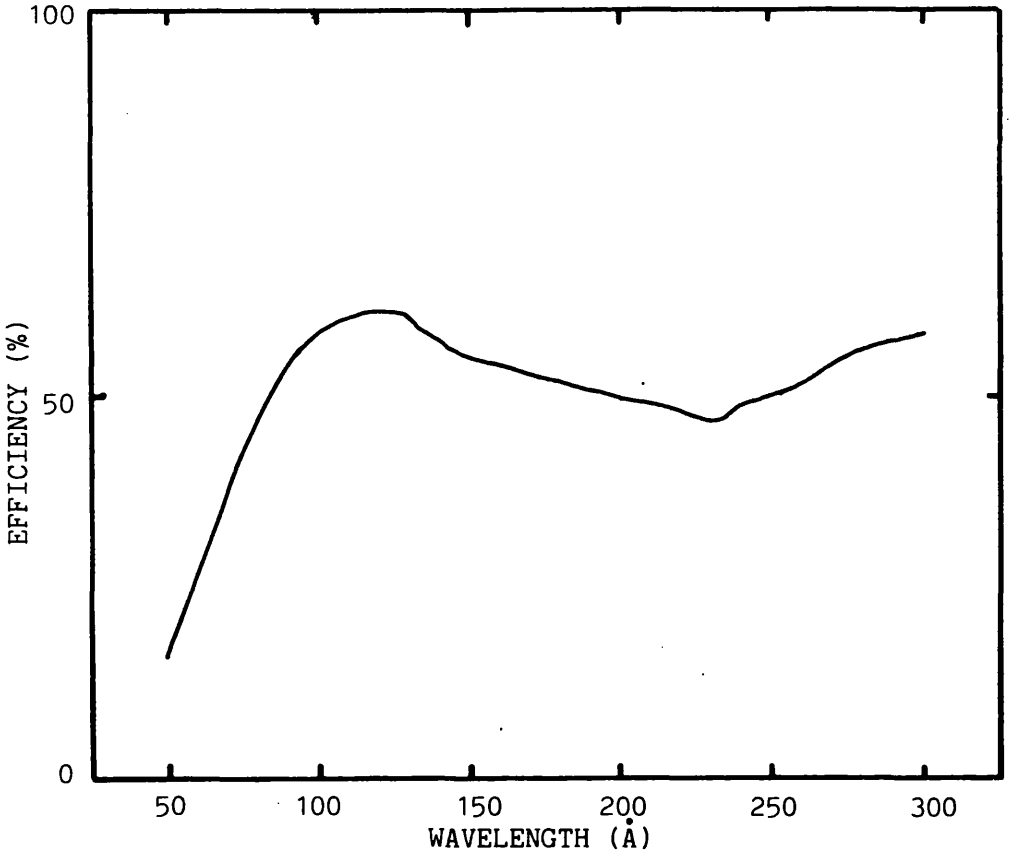

Figure 2.4 Effective area of the WFSXC telescopes as a function of off-axis angle.

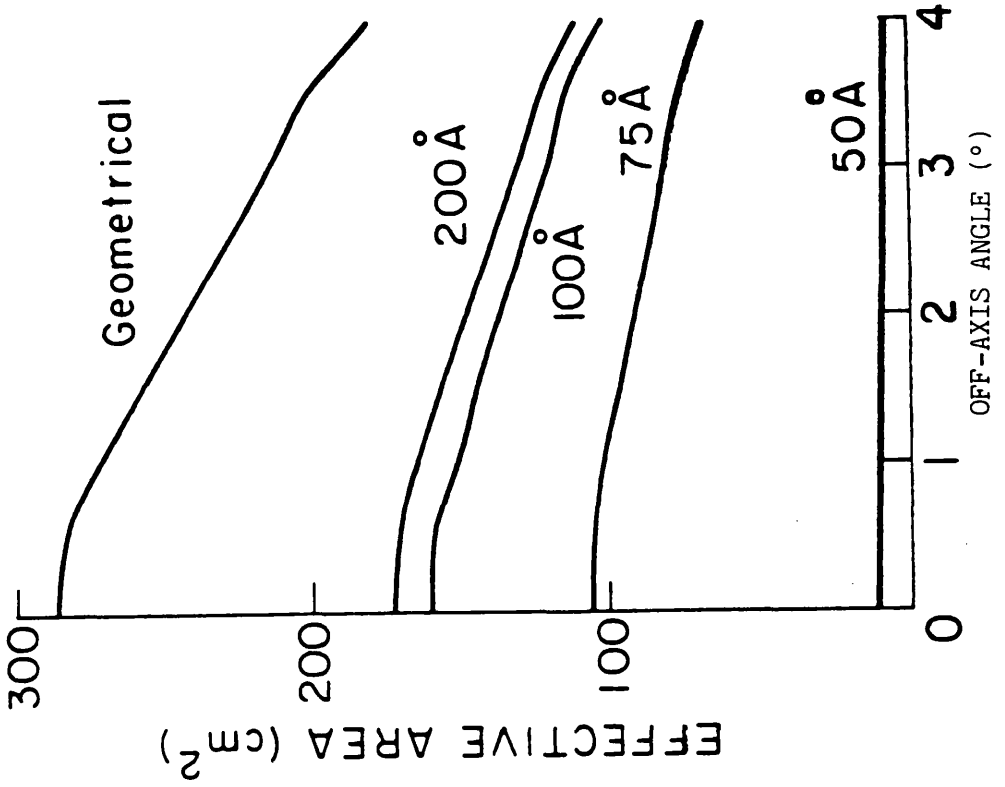

the surface brightness distribution from a point source, the RMS blur circle radius. Figure 2.6 shows the predicted blur circle response as a function of the off-axis angle.

Theoretically, the on-axis RMS blur circle radius is zero degrading to $\sim 20'$ at the edge of the field of view. Imperfections in the surface figure of the mirrors, which unavoidably occur during manufacture, degrade the final on-axis resolution to $\sim 1'$. A better average resolution can be obtained by displacing the detector from the focal plane, although the on-axis response is then degraded. With an optimum displacement of 1.25mm the WFSXC mirrors have an on-axis response of $\sim 7'$.

In conclusion, three nested Wolter-Schwarzchild type I grazing incidence mirrors were proposed for the WFSXC, to fulfill the requirement for a survey instrument. The telescope has an 8° field of view, a mean collecting area of $250cm^2$ ($300cm^2$ on-axis) and an on-axis resolution of $\sim 1'$. The focal length of each mirror is 35cm.

2.2.2 The Focal Plane Detector

The choice of a focal plane detector was an important consideration in the design of the WFSXC. Accurate determination of source positions requires high spatial resolution and that of the detector must be comparable with that of the telescope. As the detector plays an important part in determining the instrument sensitivity it should have high quantum efficiency over the WFSXC waveband. Good energy resolution is also a desirable characteristic. A microchannel plate detector was chosen as the focal plane instrument

of the WFSXC. In order to justify this choice, it is necessary to compare and contrast the properties of different types of detector in the context of the needs of the WFSXC.

Currently, there are two other types of device that could be used in the XUV, imaging proportional counters (IPCs) and charge coupled devices (CCDs).

A large field of view telescope requires a relatively large detector area

$$D_t = F_t \cdot \alpha_t \qquad (2.2)$$

where: D_t is the diameter of the detector (cm)

F_t is the focal length (cm)

α_t is the field of view (radians)

The 8° field of view and 35cm focal length required a detector diameter of 4.9cm. Thus the option of a CCD was ruled out as areas of only $\sim 1cm^2$ were available. Both MCP detectors and IPCs can provide the necessary active areas. Typical MCP sizes range from 25 to 70mm in diameter (Mullard, 1976). Eng and Landecker (1981) have used rectangular MCPs 68.5mmx58.5mm. Quite large areas can be imaged by IPCs. The Einstein telescope used one of area 7.6cmx7.6cm (Giacconi et al, 1979) and Kayat (1980) one of 6cmx6cm.

The angular resolution of the detector should be comparable to the on-axis response of the mirrors, $\sim 1\hat{}$. The 8° field covers a focal plane diameter of 4.9cm, hence the plate scale of the WFSXC is

$1\hat{\uparrow}$=102μm. Thus the detector spatial resolution must be ~100μm (RMS).

An MCP detector cannot have a resolution that is smaller than the channel pitch (p, the spacing between channel centres). As p is less than ~45μm for the largest channel diameters available, the image readout will probably determine the final resolution. Resolutions below 100μm have been measured with a number of readout systems - the coincidence anode array (Timothy and Bybee, 1975), resistive strip (Parkes et al, 1974) and the graded density cathode (Smith et al, 1982).

Basic gas physics imposes some limits on IPC resolution. A finite absorption depth exists in the filling gas which is a function of the photon energy. At the large angles of incidence determined by the telescope (20-30°) there will be an uncertainty in the photon position ($dX=X_1-X_2$) increasing as a function of increasing photon energy (figure 2.7). The effect can be controlled to a certain extent by choice of detector gas filling. For example, a heavy atom such as xenon will "stop" photons in short distances, reducing the positional uncertainty. However, IPCs used in the XUV require plastic windows, allowing diffusion of gas into the counter which contaminates Xe very quickly and, as Xe is very expensive, this contamination cannot be avoided by flowing the gas. Bleeker et al (1980) developed an Argon-Methane filled IPC with a thin lexan window, for use in the 50-250Å waveband. The full width half maximum position resolution (FWHM = 2.36 x RMS resolution) was measured at 13.34Å and 44.7Å, yielding 120μm and 230μm respectively, using an orthogonal wire grid readout method with a wire spacing of 200μm. These results, measured

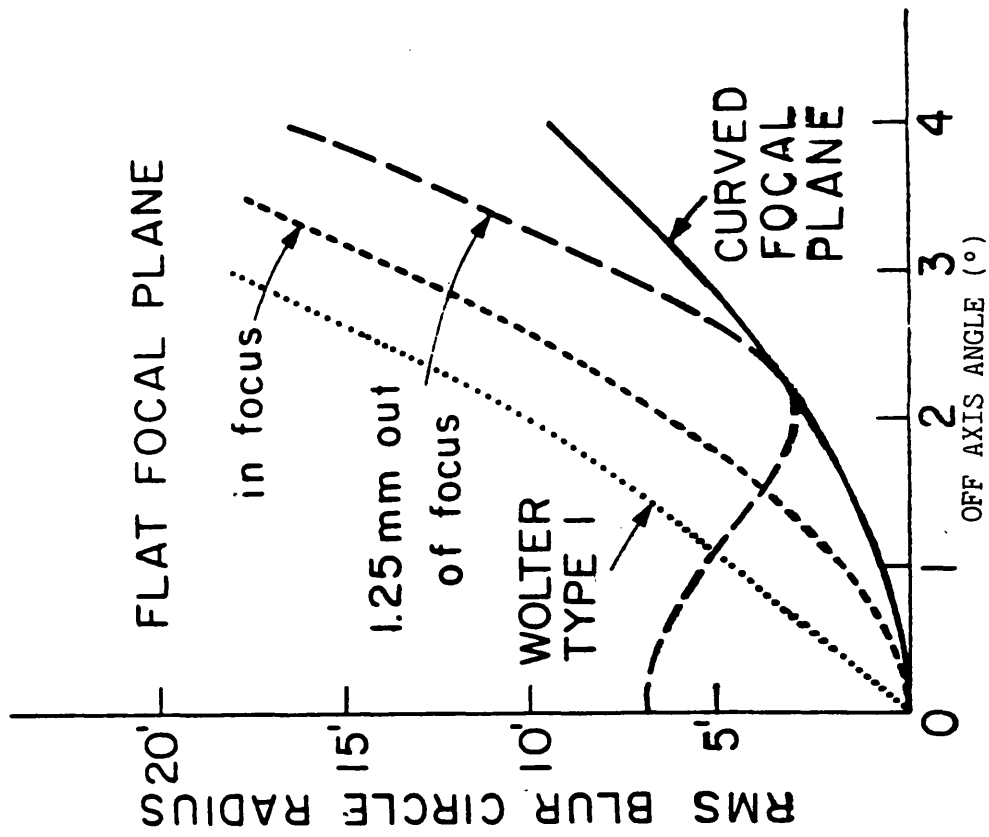

Figure 2.6 RMS blur circle radius of the WFSXC telescopes as a function of off-axis angle.

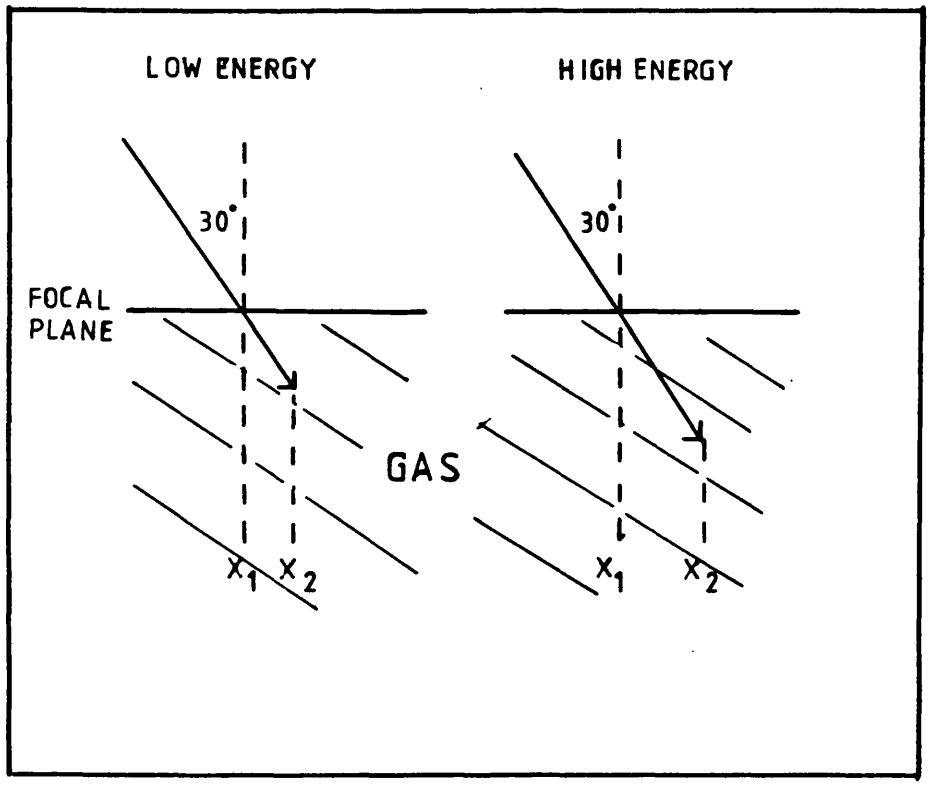

Figure 2.7 The uncertainty in the position of a photon at large angles of incidence in a proportional counter.

with a gas pressure of 0.6 atmosphere fit a theoretical curve which predicts a resolution $\gtrsim$500μm at 250Å. Resolution predictions for a gas pressure of 1 atmosphere are ~230μm at 50Å and ~350μm at 250Å.

At soft X-ray energies, peak MCP quantum detection efficiencies (Q) range from 15% to 35% (Fraser, 1982). Q is a strong function of incident angle (eg. figure 2.8) becoming quite small at the angles produced by the telescope (20-30°), eg. 0.5-1% at 44.7Å (Parkes et al, 1970) and ~5% at 304Å (Rogers, 1980; Bowyer et al, 1981). By coating the MCP with a photoemissive material such as MgF_2 or CsI, it is possible to improve Q at large angles, at energies determined by the choice of material. MgF_2 was used as a photocathode for the Einstein MCP detector (the high resolution imager or HRI). Fraser (1982, 1983a) has predicted the quantum efficiency of an MgF_2 photocathode in the range 50-300Å expecting values ~2.5-6% at 30° angle of incidence (figure 2.9). The response is maintained at this level throughout the EUV and it is only at wavelengths above ~1000Å that the efficiency begins to decrease significantly (Paresce, 1975; Martin and Bowyer, 1982). By comparison IPC efficiencies are much larger. In the XUV the gas will absorb nearly 100% of the incident radiation within typical counter volumes. The net efficiency will therefore be determined entirely by the window absorption. Huizenga et al (1980) have developed an ultra-thin lexan window for use on an IPC (figure 2.10). A peak transmission of 90% can be obtained falling to ~10% at 200Å or 250Å, depending upon the window thickness.

Figure 2.8 Typical quantum efficiency of a microchannel plate as a function of incident angle at carbon Kα (44.7Å), taken from Parkes et al (1970).

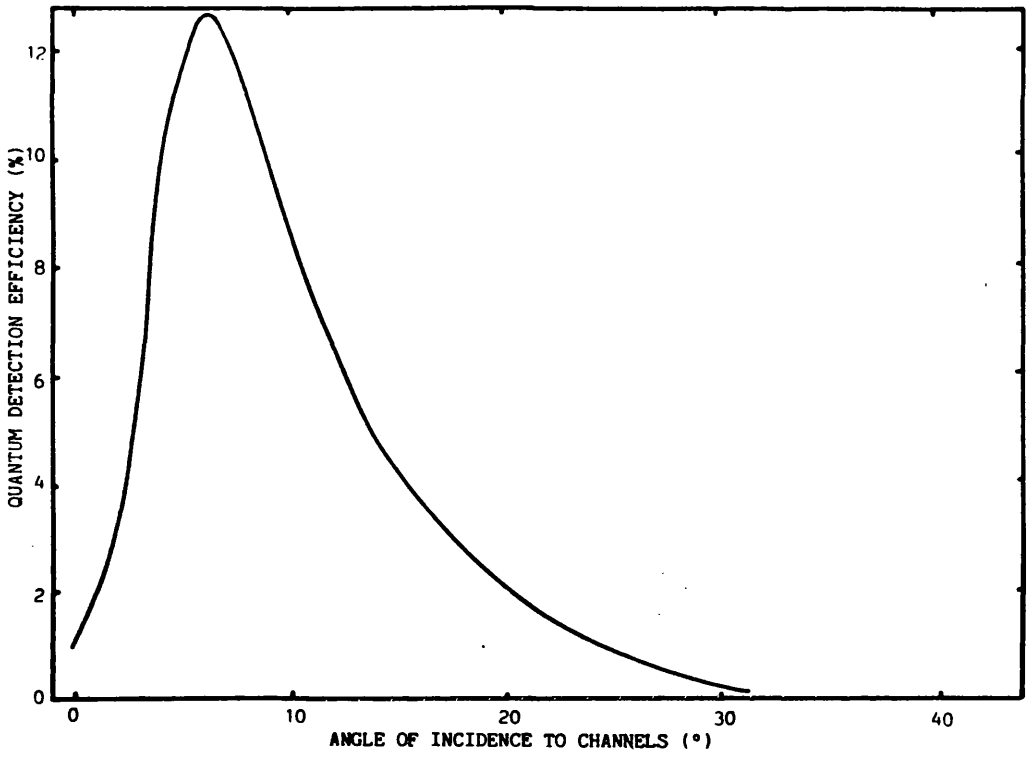

Figure 2.9 Theoretical quantum efficiency of a MgF_2 coated MCP as a function of wavelength (Fraser, 1982).

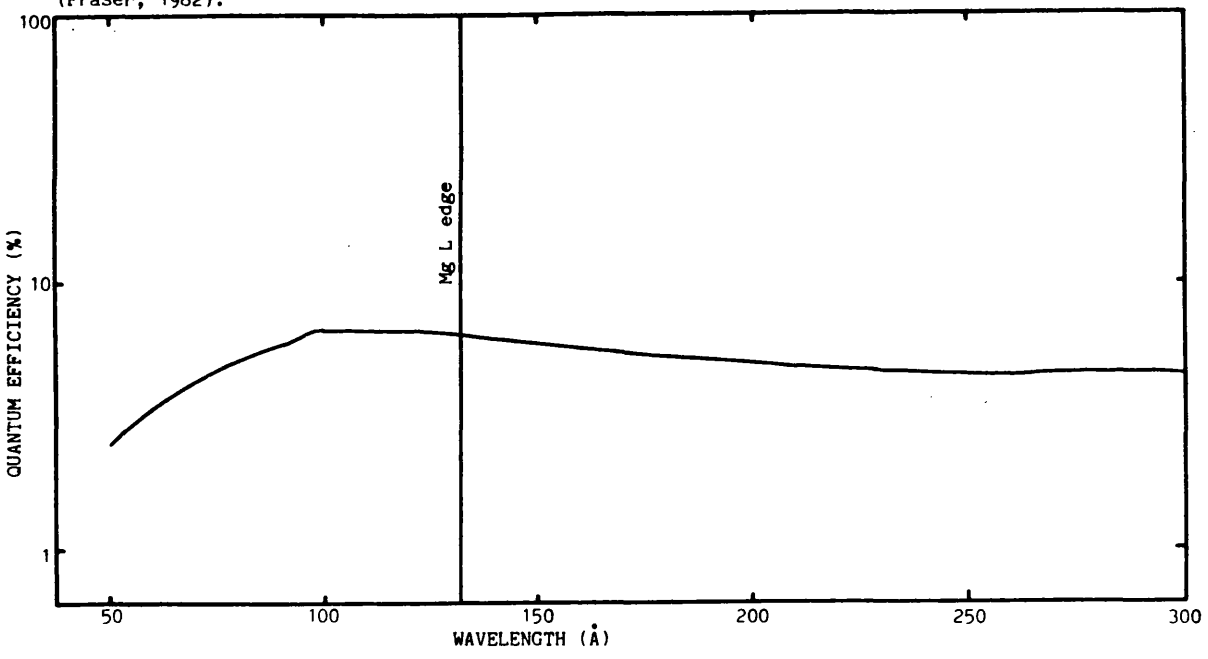

MCPs have no intrinsic energy resolution. As the photoelectric yield of MCP glass is low and not well defined, the number of photoelectrons cannot be determined from the detector gain. In an IPC the gain is proportional to the photon energy (E). An upper limit to the theoretical counter resolution (dE/E, full width half maximum) is (Sims, 1981)

$$dE/E = 2.355(1+F_f)^{1/2}W^{1/2}E^{-1/2} \qquad (2.3)$$

where: W is the energy required to create an ion pair in the gas

F_f is the fano factor of the gas mix

For argon $dE/E=0.416E^{-1/2}$ (where E is in keV). At the limits of the XUV band the expected energy resolutions will be 84% (50Å) and 187% (250Å).

Table 2.1 summarises the characteristics of both MCP detectors and IPCs. The energy resolution of the IPC is probably not much of an advantage in the XUV as it will not give much better discrimination than that provided by bandpass filters. It was necessary to decide either to sacrifice spatial resolution or sensitivity. The MCP detector was chosen for the WFSXC, as the resolution best matches that of the mirror, with the hope that the detection efficiency could be improved by photocathode development work. The MCP detector also has advantages in that such devices are smaller than the equivalent IPC and usually mechanically stronger.

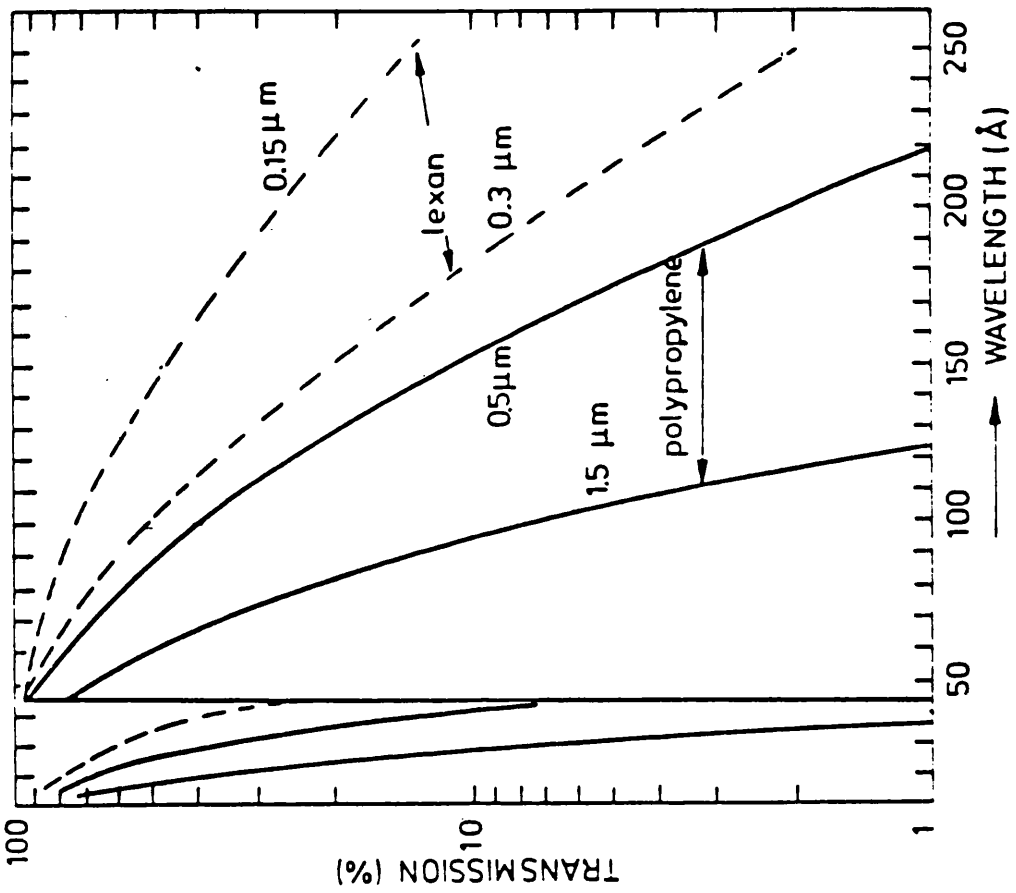

Figure 2.10 *XUV transmission as a function of wavelength for polypropylene and Lexan foils of various thicknes.*

Table 2.1. A comparison of the performance characteristics of imaging detectors in the XUV (50-300Å)

Detector Parameter	Microchannel Plate Detector	Imaging Proportional Counter
Active area	25-75mm diameter	~80mmx80mm
Spatial Resolution (FWHM)	<45µm	230-350µm
Energy Reolution	none	~80-190%
Quantum Efficiency	~2.5-6%	10-90%

2.2.3 The Filters

As the MCP detector has a relatively constant efficiency throughout the EUV, as described in section 2.2.2 above, it is necessary to define a bandpass in the EUV by the use of a filter. If several filters of differing bandpasses are used, crude energy resolution can be obtained. Additionally, the WFSXC is sensitive to background radiation originating in the earth's geocorona, principally the helium II (304Å) and helium I (584Å) resonance lines which yield at least $3x10^3$ and $8x10^4$ counts $cm^{-2}s^{-1}ster^{-1}$ respectively. Filters are needed to suppress the background which otherwise degrades the instrument sensitivity and could saturate the detector.

The WFSXC is fully capable of operating throughout the EUV but intially the sensitivity was restricted to wavelengths below 304Å. Three material combinations were considered that have acceptable transmissions in the 50-300Å band - parylene (Par N), Par N + beryllium and aluminium + carbon. The thicknesses of each filter material were chosen with the aim of achieving the maximum sensitivity for the WFSXC. Figure 2.11 shows the expected transmissions of suggested filter thicknesses - 5000Å Par N, 2500Å Be + 1000Å Par N and 1250Å Al + 1000Å C.

The filter mount is divided into three segments (figure 2.12), the largest sections comprising two of the above filters, and the smallest being covered with thick aluminium foil to enable an independent measurement of cosmic ray and detector dark count events

Figure 2.11 Nominal filter transmissions

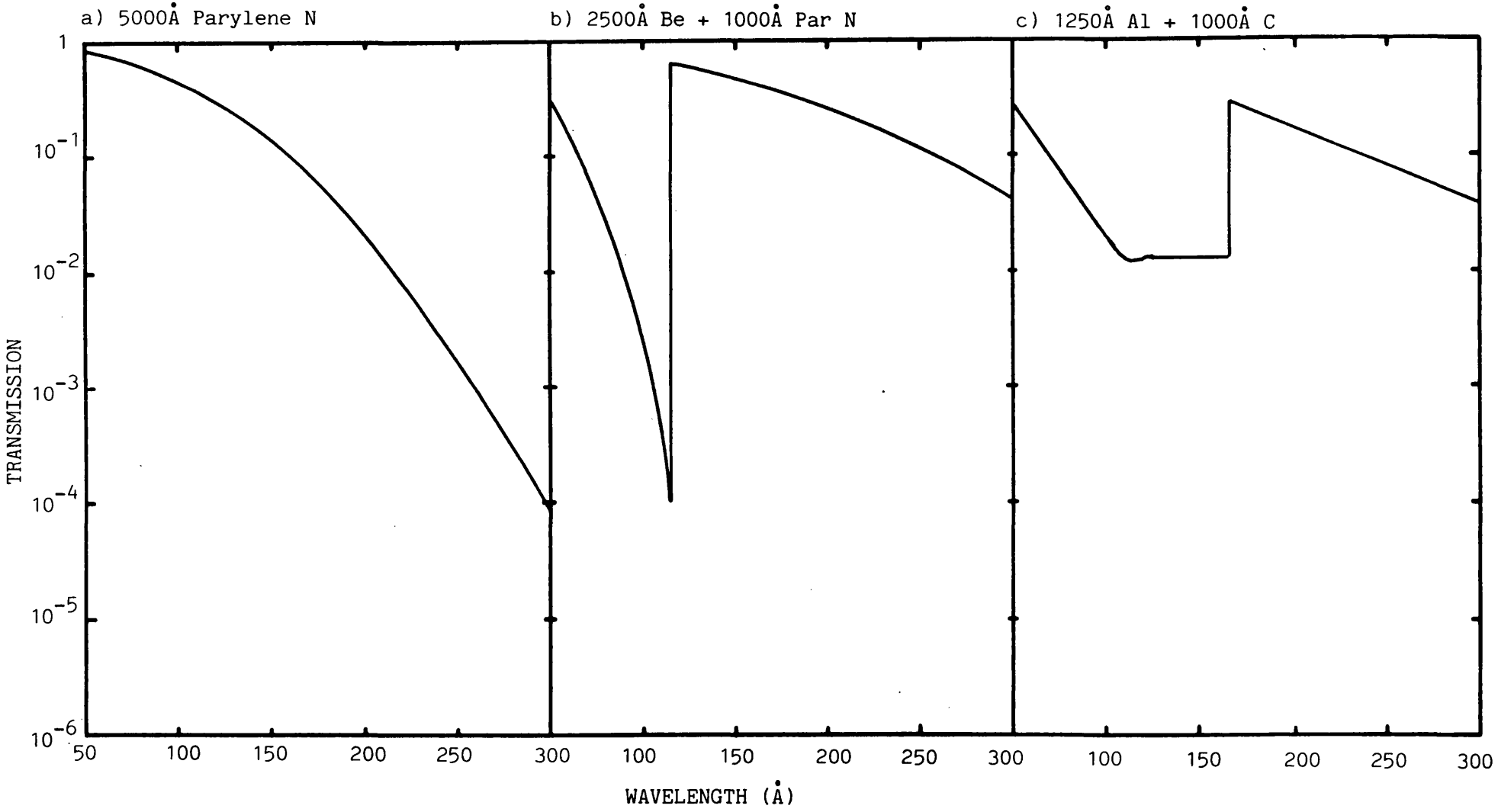

to be made. If the experiment is scanned so that a source passes through both of the bandpass filters, crude two-colour photometry can be undertaken and source temperatures estimated.

2.2.4 Image Readout and Electronics

The image readout system must give a spatial resolution <100μm (RMS, <230μm FWHM). Position encoders can be divided into two broad categories - digital, associating an amplifier and counting circuit with each resolution element (pixel), and analogue, estimating coordinates from the properties of voltage waveforms at a number of output electrodes. However, a digital method would require a large number of counting circuits to obtain the specified spatial resolution over the WFSXC area. For example, the coincidence anode array (Timothy and Bybee, 1975) needs a number of circuits in each axis corresponding to the number of pixels in the axis, L/dX, where dX is the pixel size (FWHM resolution) and L is the image size, a total ~430 for 230μm FWHM resolution. Although the response time of a digital system is ~1.0ns (Oba et al, 1979), telemetry restrictions on the WFSXC limit the maximum count rate to $2500s^{-1}$ and a response time of only ~400μs is needed. Hence, for the WFSXC, an analogue system was chosen to simplify the processing electronics.

Two of the types of analogue readout system used with MCP detectors are the resistive anode (eg. Lampton and Paresce, 1974) and orthogonal wire grids (Smith et al, 1982; Morton and Parkes, 1973, 1-D only; Gott et al, 1970) (figure 2.13). In both methods charge collected by the anode is divided between four preamplifiers, two for

Figure 2.12 The WFSXC filter mount

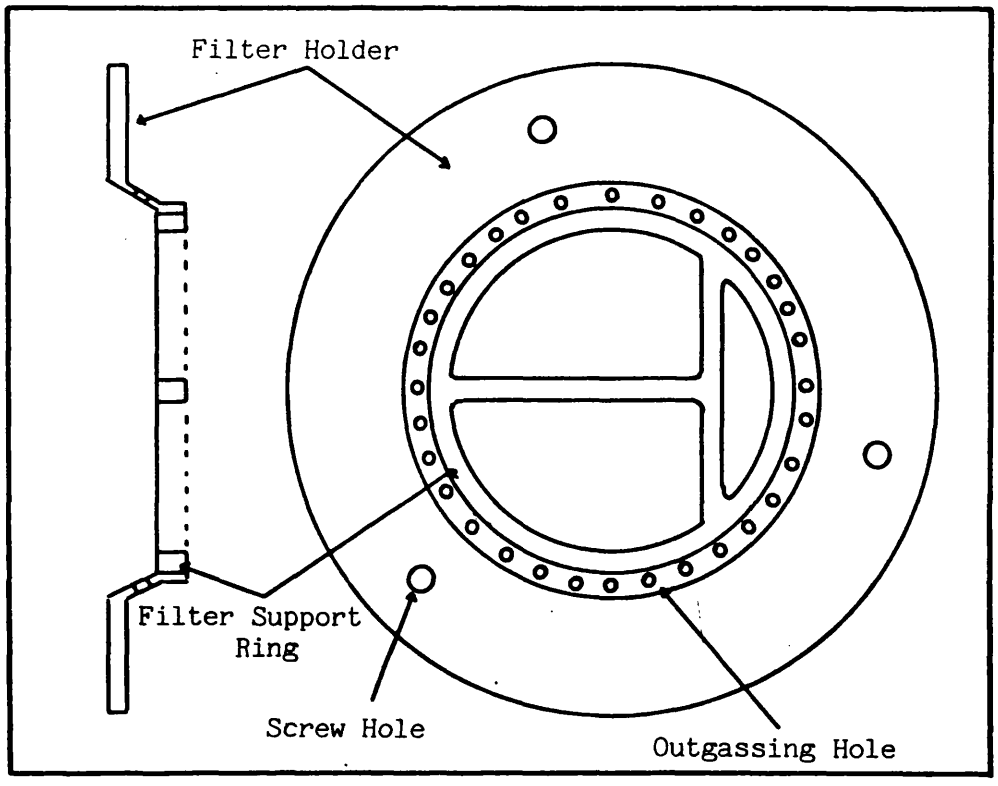

Figure 2.13 Methods of image readout

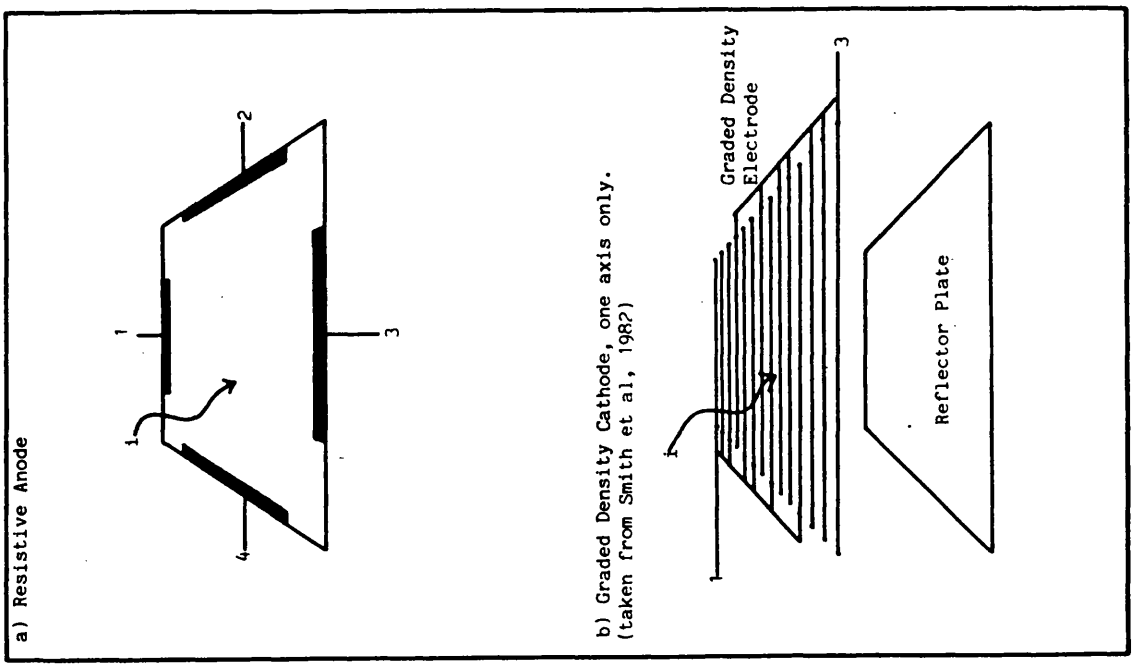

each axis, and the positions calculated from the outputs.

A resistive anode should achieve the resolution required of the WFSXC. Parkes et al (1974) measured an electronic resolution of 18μm (RMS, ≡42μm FWHM) at the centre of a 20mm long 1-D resistive strip. This corresponds to L/dX~500 compared to L/dX~220 required. Theoretical predictions (Fraser and Mathieson, 1981) have suggested that 2-D resistive anodes can achieve comparable resolutions. Unfortunately all resistive anodes suffer from geometric distortion, resulting from the coupling of the charge signal between output electrode pairs. The magnitude and shape of the distortion depends generally upon the shape of the anode, the size and disposition of the electrodes and the resistance and capacitance of the anode. However, the characteristics of resistive anodes have been examined theoretically (Fraser, 1980; Fraser et al, 1981; Fraser and Mathieson, 1981) enabling determination of the optimum anode resolution and resistance. The theory can also be used to predict the distortion characteristics of a given anode, allowing the use of numerical methods to linearise an image.

Of several wire grid imaging systems, the graded density readout (Smith et al, 1982) gives the best performance. The wires of a given grid are electrically interconnected in two groups such that the density of each group changes in an approximately linear manner across the width of the image field. This system has high linearity (non-linearity less than 0.8%) and good resolution (less than 100μm FWHM). However, the linearity of the image from a system of spaced wires does not necessarily vary smoothly over short distances of the order of the

wire spacing. This "differential non-linearity" may degrade the resolution by positional uncertainty and distort the image in an oscillatory manner across the field of view. Although in principle it would be possible to calibrate the readout and remove the distortion during data anaylsis, such measurements are difficult to obtain, whereas the resistive anode behaviour can be predicted.

The resistive anode has the advantage of electronic simplicity and mechanical robustness by comparison with the wire grid system. Both methods achieve similar resolution and have some problems with image distortion. As the resistive anode distortion is potentially predictable it was decided to use this on the WFSXC.

The payload image processing electronics must amplify the anode output and calculate the positions of detected events. Early work with MCP detectors at Leicester suggested that the electronics would be required to handle events ~5-6pC in magnitude. Four preamplifiers are mounted underneath the vacuum housing bulkhead, as close to the anode as possible to minimise electronic pickup. The four preamplified anode signals are then passed to four shaping filter amplifiers in the analogue electronics (figure 2.14). After shaping into a bipolar pulse, the signals are stretched, in the sample and hold, into square pulses of duration proportional to their amplitudes. Pairs of filter amplifier signals, corresponding to opposite electrodes, are summed, fed through a sample and hold unit and then combined with one filter amplifier output in a ratiometric analogue to digital converter (ADC), deriving the position signal and then digitising the output. Each of the single stretched signals are also

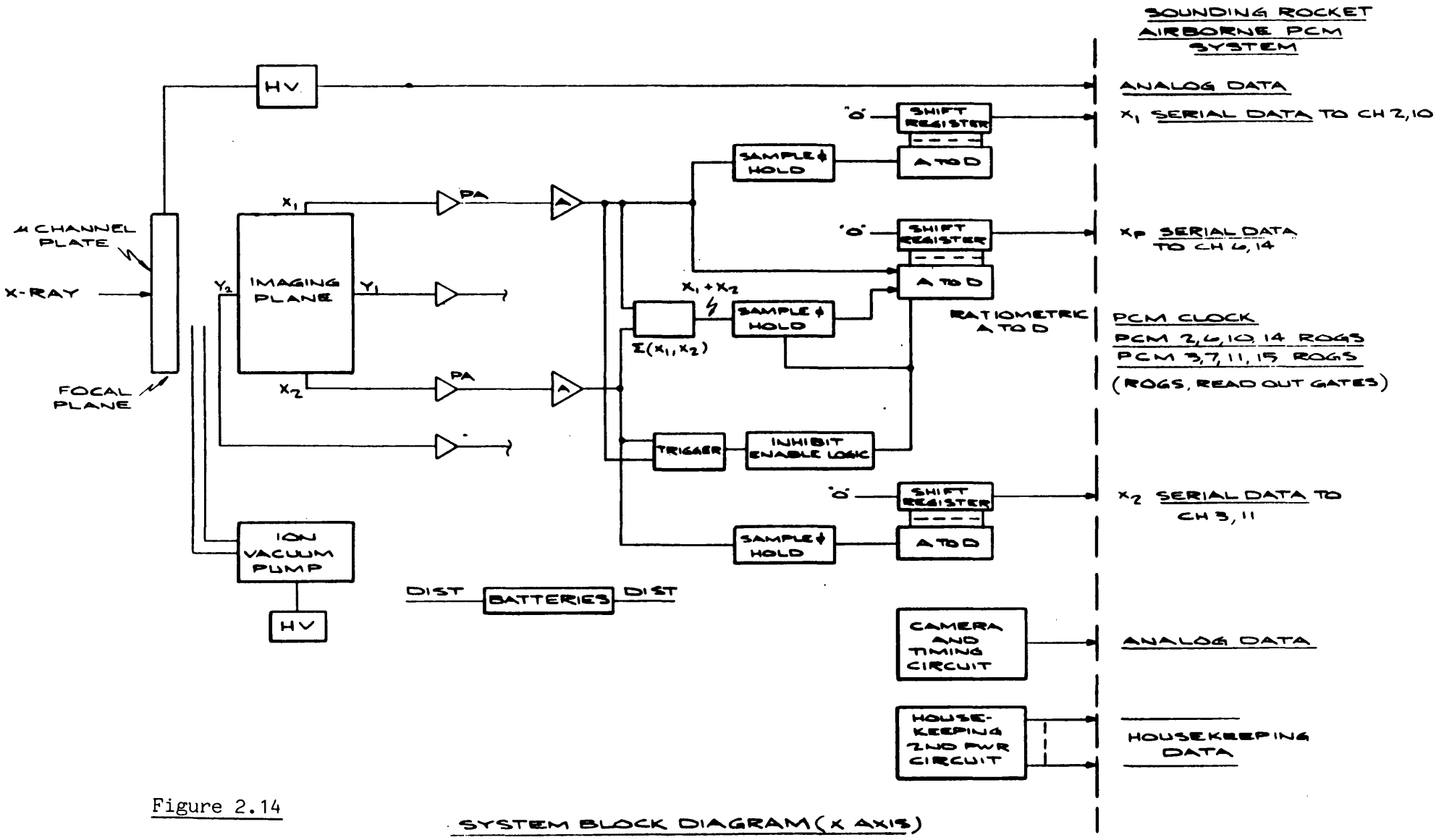

Figure 2.14

SYSTEM BLOCK DIAGRAM (X AXIS)

digitised.

The accuracy of the digitisation must correspond to the required resolution. The WFSXC field comprises 490 pixels, hence digitisation of the position to an accuracy of 9 bits (0-511) is sufficient.

All the digitised signals are held in shift registers until readout sequentially into the TM when stimulated by its clock pulse. When all the data has been shifted into the TM the circuit elements are reset, ready for the next event. The TM can readout 15 channels (1 frame) every 0.8ms, 1250 frames s^{-1}. Each event package of six channels can therefore be transmitted twice in every frame, a net count rate of $2500s^{-1}$. As the count rates expected in the XUV are <500 count s^{-1}, this is an acceptable event rate. Transmitting the four individual anode signals builds in a redundancy as positions can be recovered on the ground, should one or both telemetered positions be lost, and the charge level of an event can be calculated by summing the anode signals, a useful tool for examining the detector performance.

2.3 The WFSXC Sensitivity

2.3.1 The Minimum Detectable Flux from a Point Source

Photon counting follows poissonian statistics (Bevington, 1969). During the observation of a source, a single detection element (pixel) will see a contribution from background effects (b events) and a number of photons from the source (s events). The total number of events is $N=s+b$ and the error (or deviation) in the measurement is $N^{1/2}=(s+b)^{1/2}$. The significance of a source detection (σ) is the

number of deviations represented by the source count, hence

$$\sigma = s/(s+b)^{1/2} \qquad (2.4)$$

so that

$$s = \frac{\sigma^2}{2}\left[1+\sqrt{1+\frac{4b}{\sigma^2}}\right] \qquad (2.5)$$

σ is related to the probability that an observed source is due to statistical fluctuations in the background by the gaussian probability distribution function whose mean is N. A 3σ detection (σ=3) represents a probability of 0.00135 and a 5σ detection a probability of 3×10^{-7}. The required value of σ determines the minimum number of events that must be observed for a positive detection. If the background count rate is B events $s^{-1}ster^{-1}$ then

$$b = BT\theta^2 \qquad (2.6)$$

where: T is the observation time (s)

θ^2 is the area of one pixel (steradians)

The integrated count from a source depends upon the collecting area of the instrumentation and the source spectrum

$$s = A.T. \int F(\lambda).E(\lambda).d\lambda \qquad (2.7)$$

where: $F(\lambda)$ is the source flux at the earth (photons $cm^{-2}s^{-1}\mathring{A}^{-1}$)

$E(\lambda)$ is the efficiency of the instrument

A is the geometric collecting area (cm^2) of the instrument

If a flat source spectrum is assumed then the source is characterised by a flux S (photons $cm^{-2}s^{-1}\mathring{A}^{-1}$), thus

$$s = S.A.G.T \qquad (2.8)$$

where: G is the grasp of the instrument ($\mathring{A}$)

$$G = \int E(\lambda).d\lambda \qquad (2.9)$$

Thus the minimum detectable flux in the instrumental band is

$$S_{min} = \frac{R.\sigma^2}{2A.G.T}\left(1+\sqrt{1+\frac{4B\theta^2T}{\sigma^2}}\right) \qquad (2.10)$$

(photons $cm^{-2}s^{-1}$)

where: R is the interval covered by the bandpass of the instrument (Å)

A more useful quantity is the energy flux, ergs $cm^{-2}s^{-1}$, which can be estimated by a linear energy spectrum (corresponding to the flat photon spectrum).

$$F_{min} = S_{min} \frac{\int_{E_1}^{E_2} E.dE}{E_2-E_1} \qquad (2.11)$$

(ergs $cm^{-2}s^{-1}$) (photons $cm^{-2}s^{-1}$)

where: E_1 and E_2 are the limits of the bandpass

As

$$\int_{E_1}^{E_2} E.dE = (E_2^2-E_1^2)/2 = (E_2-E_1)(E_2+E_1)/2$$

then

$$F_{min} = S_{min}.(E_2+E_1)/2$$

In terms of wavelength instead of energy

$$F_{min} = \frac{\lambda_0 \ (\lambda_2-\lambda_1)\sigma^2}{\lambda_1\lambda_2 \ 2.A.G.T}\left(1+\sqrt{1+\frac{4BT\theta^2}{\sigma^2}}\right)2x10^{-8} \qquad (2.12)$$

where: λ_0 is the centre of the band and

λ_2 and λ_1 its upper and lower limits respectively

If the total background count per pixel in a source observation ($BT\theta^2$) is small by comparison with σ^2, F_{min} is proportional to 1/T, a special case known as the "photon limited" regime. When the above condition does not hold F_{min} is "background limited".

From equation 2.12 the expected sensitivity of the WFSXC can be calculated as a function of time if the grasp of the instrument is known. The grasp (equation 2.9) is simply calculated from the combined efficiencies of the mirrors, detector and filters, which have all been estimated in section 2.2. Figure 2.15 shows the expected instrument response for each filter where the filter transmissions have been calculated for an angle of incidence of 30°. The grasp is calculated for the nominal bandpasses of each filter, defined by the points at which the WFSXC efficiency is 10% of the peak efficiency, which are 50-170Å (Par N), 114-230Å (Be + Par N) and 165-300Å (Al + C).

The instrument background will be dominated by the HeII (304Å) geocoronal line and the detector dark count. If the HeII line is assumed to have its maximum night time value of 1 Rayleigh (1 Rayleigh = 7.96×10^4 photons $cm^{-2}s^{-1}ster^{-1}$), WFSXC fluxes will be ~5, 10^4 and 10^4 counts $s^{-1}ster^{-1}$, given the 250cm^2 collecting area, through Par N, Be + Par N and Al + C filters respectively. Typical detector dark counts are less than 1 count s^{-1} per cm^2 of the detector (Wiza, 1979; Lecomte and Perez-Mendez, 1978) giving an estimated net count rate of 20 counts s^{-1} for the WFSXC detector. As the WFSXC subtends a solid angle of 0.015 steradians (8° diameter circular field), the detector noise represents a rate of 1325 counts $s^{-1}ster^{-1}$.

Figure 2.15 The expected efficiency of the WFSXC instrument
a) with Par N filter b) with Be + Par N filter c) with Al + C filter

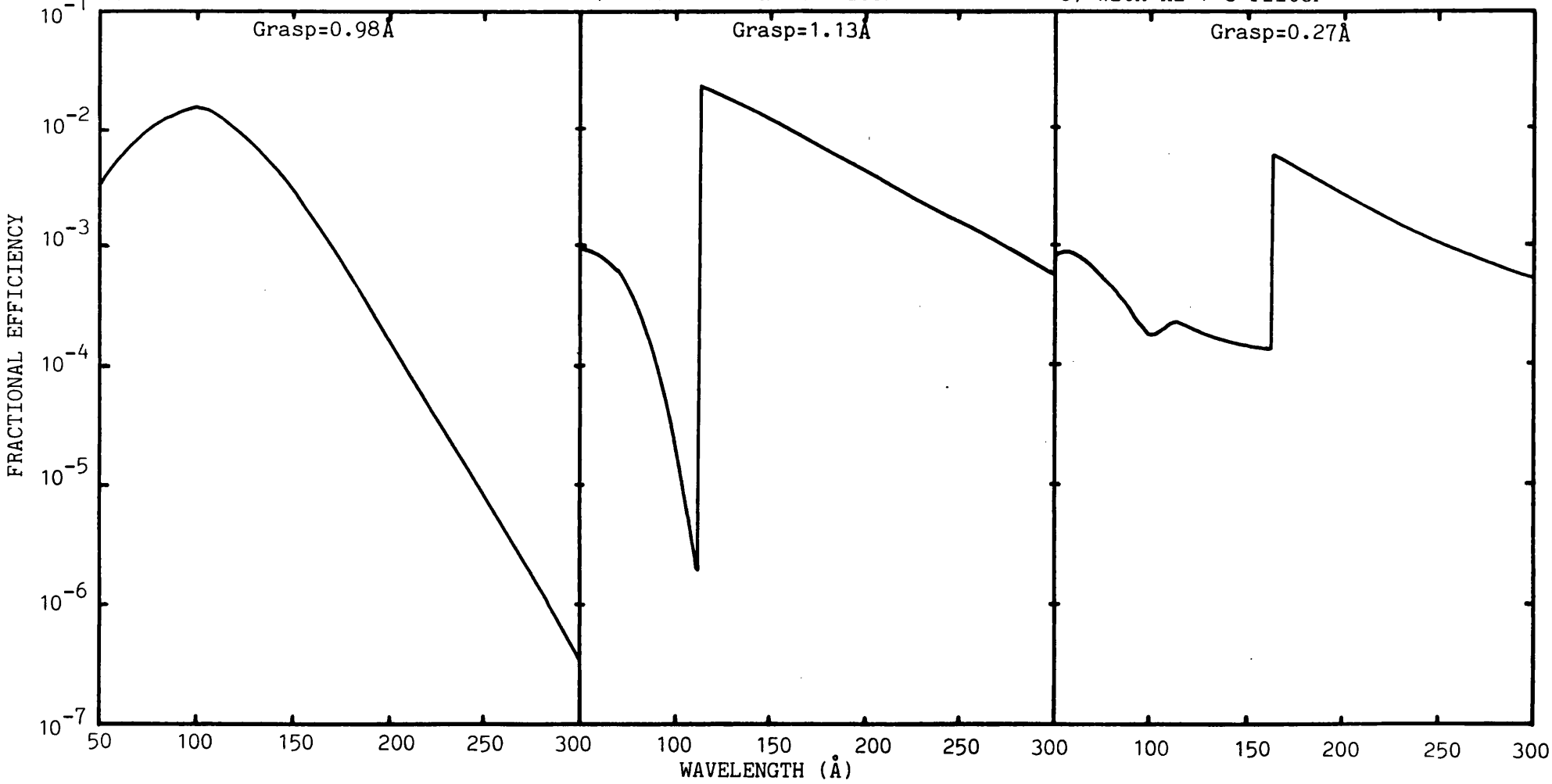

Figure 2.16 shows the WFSXC 3σ sensitivity in each filter band calculated for pixel sizes of a square arcminute (=10^{-7}ster), the expected resolution on-axis, and 50 square degrees (=0.015 ster), as if the WFSXC were a non-imaging instrument. The expected flux in each band from HZ43 is shown in the figure for comparison. With the 10^{-7}ster pixel size the sensitivity is photon limited in all three bands up to the maximum time considered (300s). It is apparent that, besides the advantage of high spatial resolution, the imaging instrument shows an improvement in sensitivity over the non-imaging case, as a result of better signal-to-noise.

Typical sounding rocket observation times are ~300s and will limit the sensitivity that can be achieved. There must be a tradeoff between this and the area of sky that can be covered in a single rocket flight. Choosing a scan rate of $0.25°s^{-1}$ will allow point source detections down to ~1/60 of the brightness of HZ43 in the Par N filter, and much lower in the other bands, over ~600 square degrees of sky. This area represents only 1.5% of the whole sky. Even if this area were increased by a factor 4, accepting a reduction in sensitivity to ~1/15 HZ43, it would take ~17 flights to image the whole sky. Hence, within the constraints of payload size (limiting the collecting area), current technology (photocathode efficiency) and sounding rocket observation times, an all sky survey is not practical with the WFSXC.

Nominal WFSXC sensitivities can be quoted for each filter assuming the above scan rate of $0.25°s^{-1}$ and an observation entirely in a single filter, giving an exposure time of 30s. The sensitivities

Figure 2.16 The sensitivity of the WFSXC in each filter band

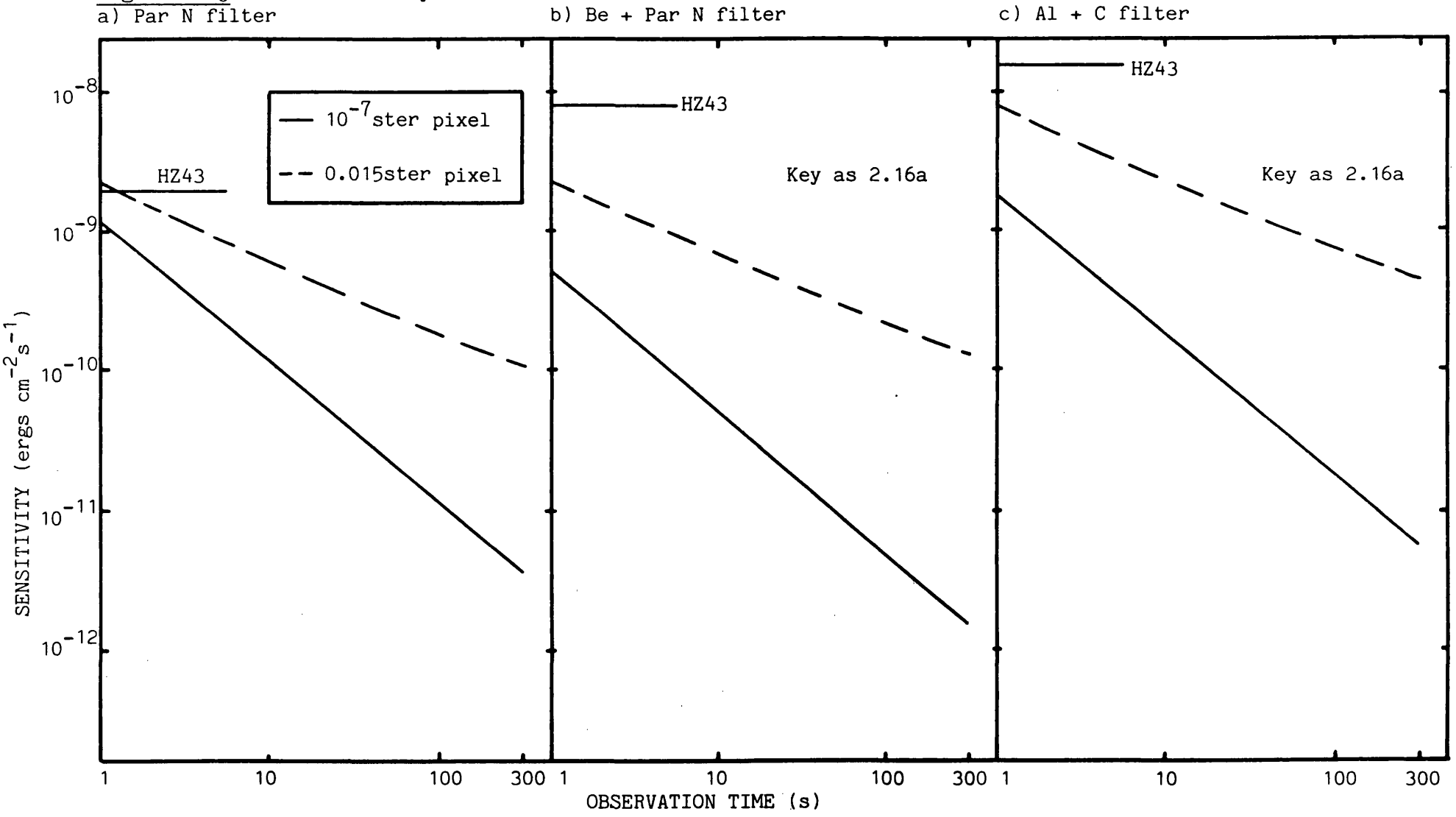

thus calculated - 3.5×10^{-11} (50-170 Å) 1.6×10^{-11} (114-230Å) and 5.5×10^{-11} ergs $cm^{-2} s^{-1}$ (165-300Å) - are compared with those for previous experiments in figure 2.17. The expected sensitivity of the WFSXC is better than ASTP, which had observation times of several minutes.

2.3.2 Detectability of Likely EUV Emitters

The theoretical and experimental arguments for EUV emission from a number of different types of object were discussed in section 1.3. It is possible to estimate the expected fluxes from these objects and determine whether or not they can be detected by the WFSXC.

a) Blackbody Fluxes from Hot white Dwarfs

EUV blackbody fluxes can be calculated directly from the Planck equation

$$F(\lambda) = 1.1 \times 10^{17} \cdot \frac{r'^2}{D'^2} \cdot \frac{2\pi hc^2}{\lambda^5} \cdot \frac{hc \cdot 10^8}{\left(e^{\lambda k T_{bb}} - 1\right)} \qquad (2.13)$$

where: r' is the blackbody radius ($R_\odot$)

D' is the distance of the body (pc)

T_{bb} is the temperature (K)

λ is the wavelength of the radiation (Å)

k is Boltzmann's constant

Figure 2.17 Comparison of the WFSXC with other instruments

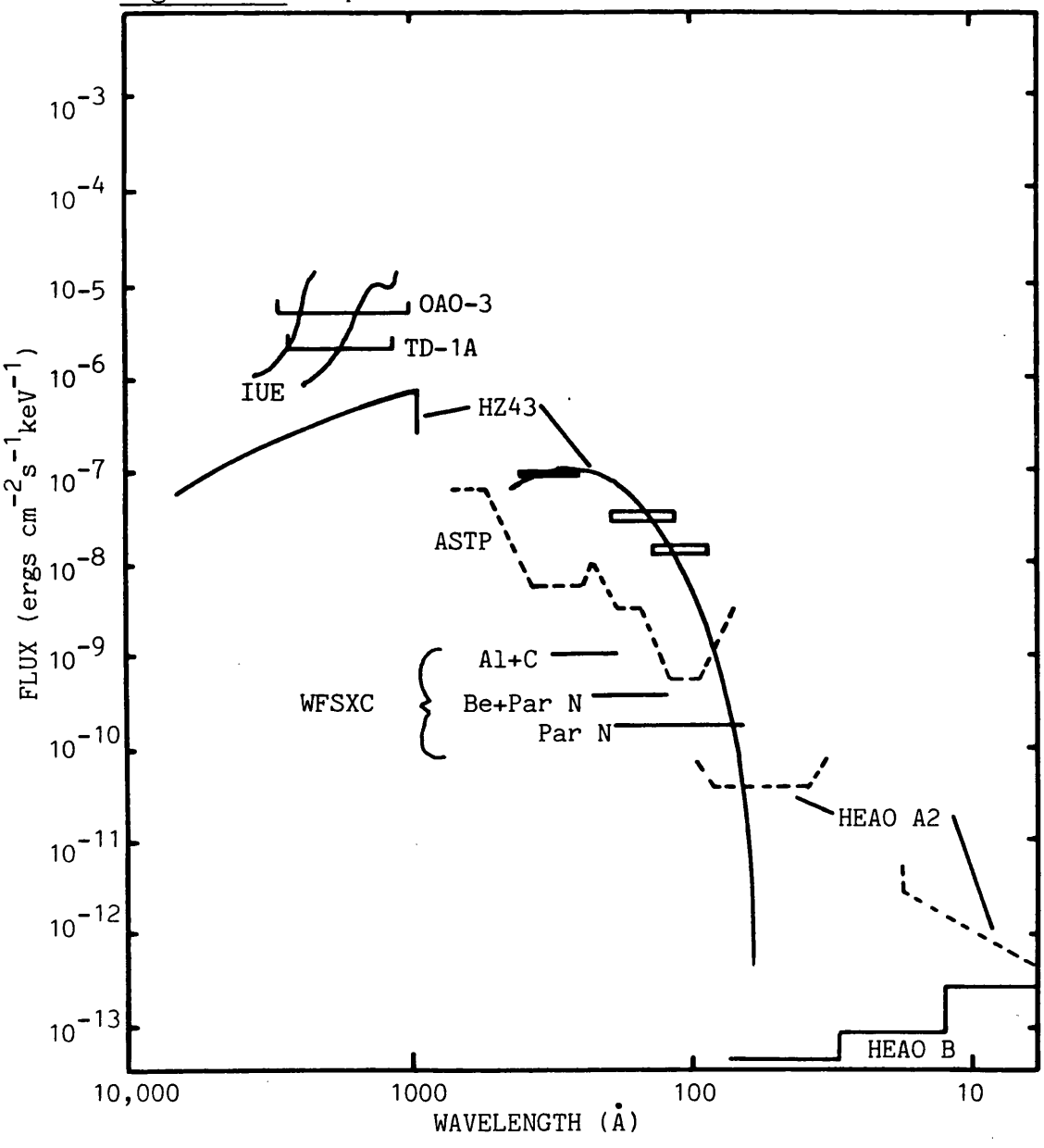

These fluxes are particularly sensitive to changes in temperature and absorption. As an example figure 2.18 shows the fluxes (ergs cm^{-2} s^{-1} $\AA^{-1}$) at the earth from a white dwarf sized blackbody (0.01 $R_\odot$) at a distance of 100pc, with temperatures of 10^5K and $6x10^4$K and hydrogen column densities (N_H) of 10^{17}, 10^{18} and 10^{19} atoms cm^{-2}. The model used to correct the spectrum and fluxes for interstellar absorption is based on that of Cruddace et al (1974). The integrated fluxes in the bands covered by the WFSXC (50 - 170Å, 114 - 230Å, 165 - 300Å) are plotted as a function of N_H for the above temperatures in figure 2.19, showing a cutoff for $N_H > 10^{19} cm^{-2}$. The above calculation necessarily makes assumptions about the temperature, distance and N_H of an object. It is possible to put constraints on the values of some of these by using flux measurements made in adjacent wavebands.

The Einstein telescope surveyed a number of hot white dwarfs in the soft X-ray band, 0.1 - 4.0keV (124 - 3Å). Consider, as an example one particular star, EG233, which was detected at a rate of ~1 count s^{-1} (Petre, private communication) using the high resolution imager (HRI) (Kellogg et al, 1976). Assuming a temperature typical of hot white dwarfs (~10^5K) for the star, 1 HRI count s^{-1} corresponds to ~1 photon cm^{-2} s^{-1} at the earth, most of the flux appearing in the long wavelength end of the band. This flux can be used to estimate fluxes at longer wavelengths without having to make assumptions about the distance of the object or its size. Figures 2.20a and 2.20b show the estimated fluxes in the WFSXC passbands as both a function of temperature (K) and N_H (cm^{-2}). The sensitivities of the WFSXC are shown for comparison, illustrating the practicality of detecting this

Figure 2.18 Blackbody spectra from a white dwarf ($0.01R_\odot$) at a distance of 100pC for two temperatures and a range of N_H

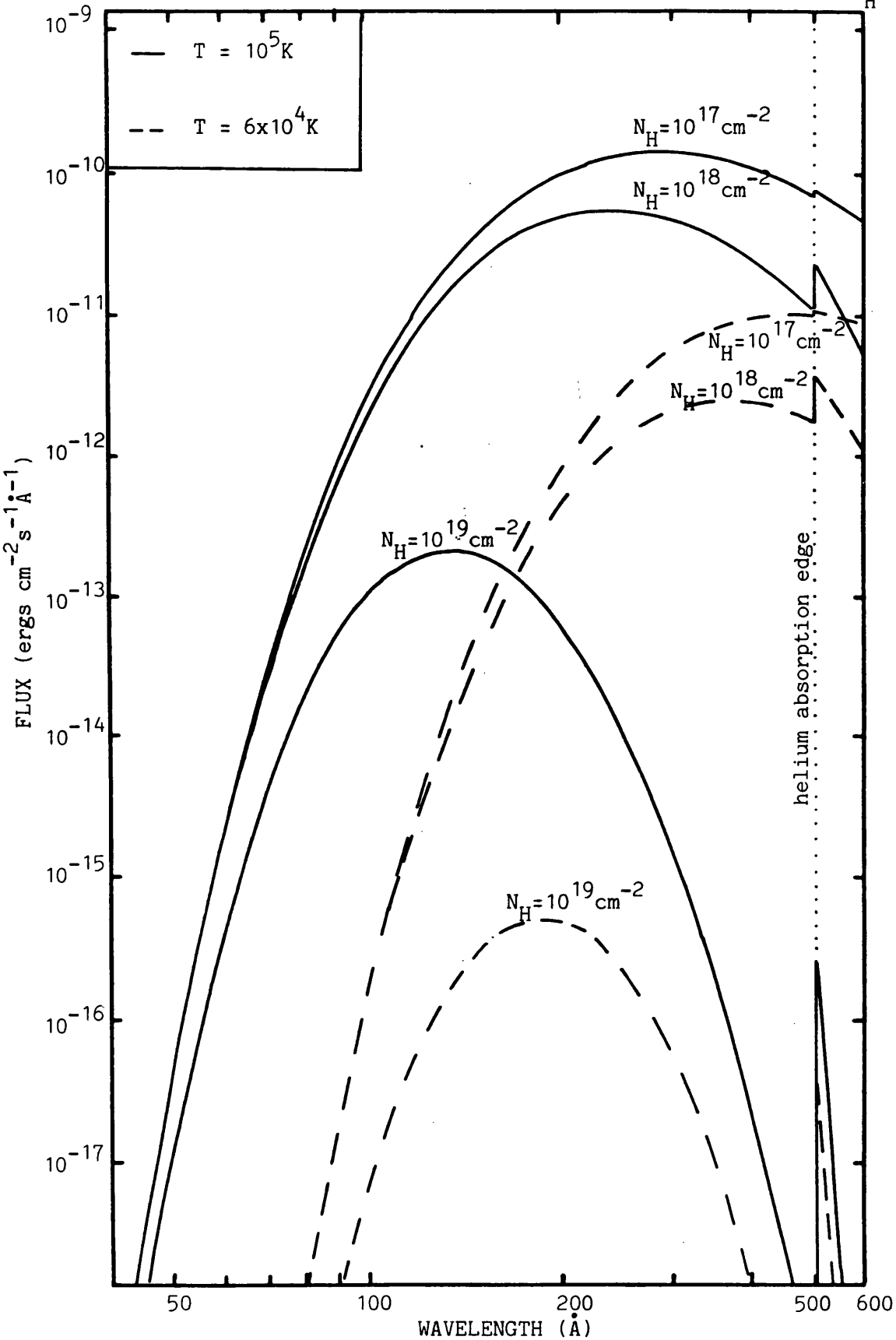

Figure 2.19 Flux in the WFSXC bands as a function of N_H assuming a radius of $0.01R_\odot$ and a distance of 100pC

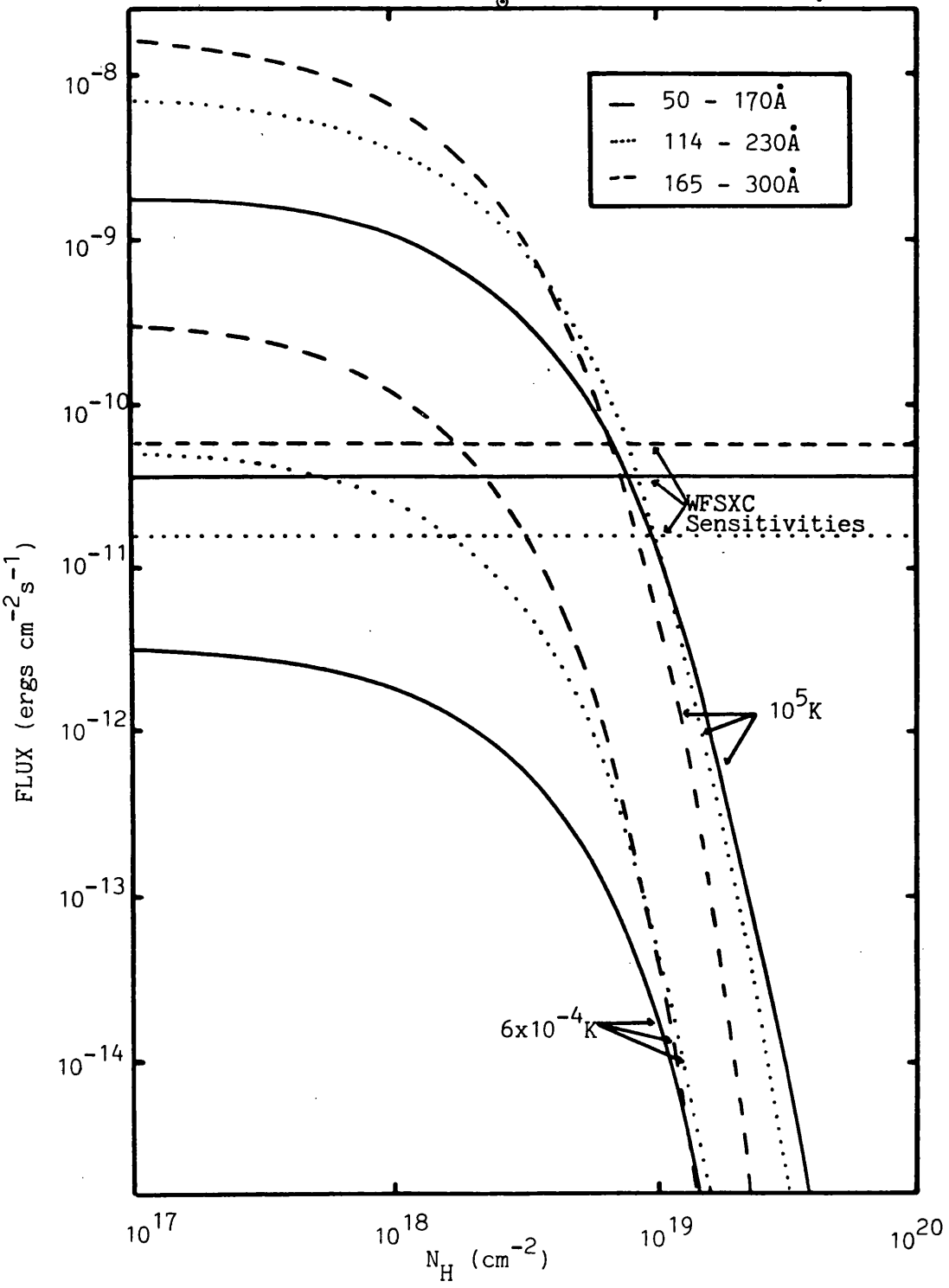

Figure 2.20a Integrated flux in the WFSXC bands of a blackbody spectrum fitted to the Einstein flux from EG233 as a function of temperature (N_H assumed to be 4×10^{17} cm^{-2}).

Figure 2.20b As figure 2.20a but as a function of N_H at a temperature of 10^5K.

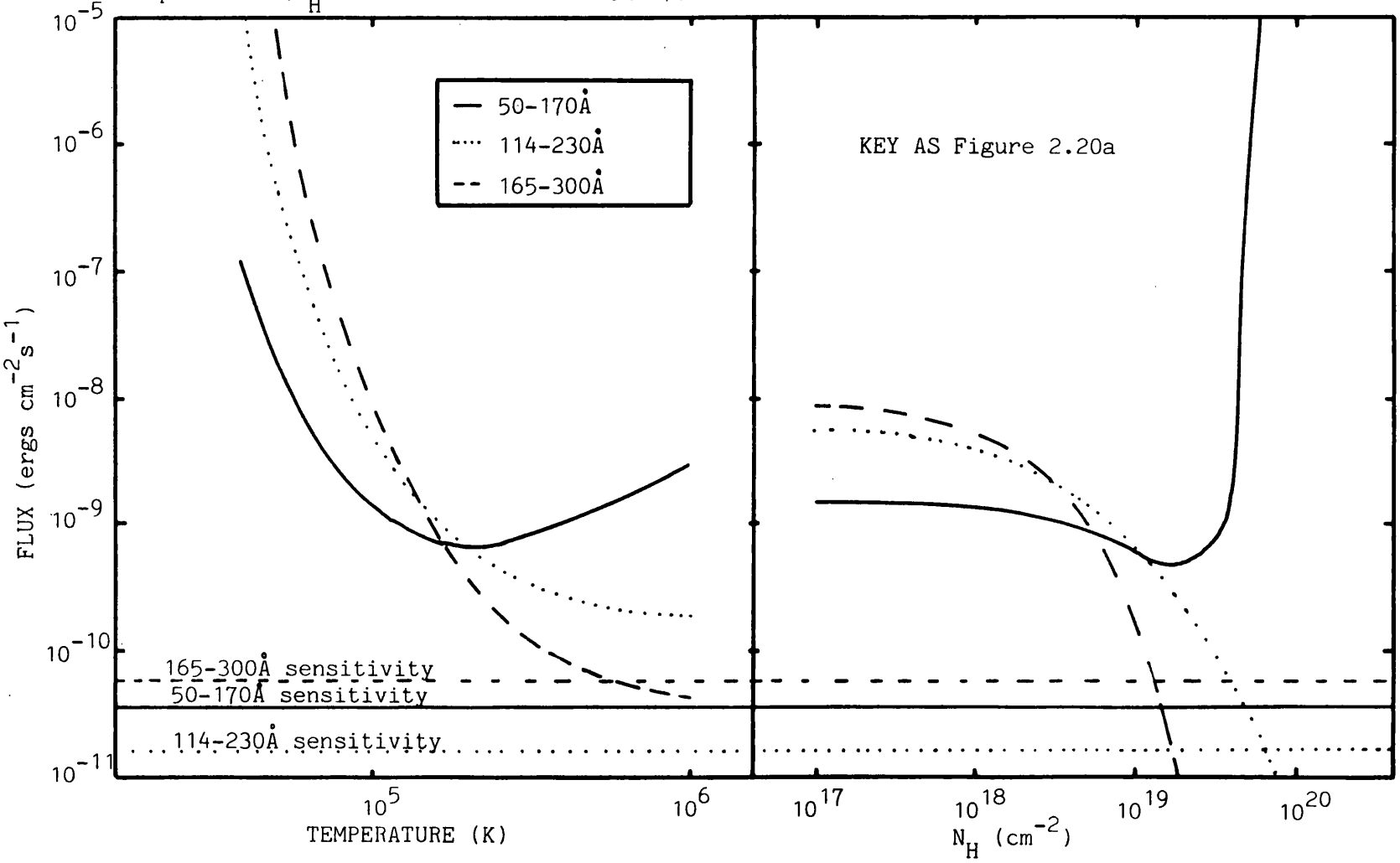

object. Figure 2.20b shows that the object cannot be detected if N_H is greater than $\sim 3 \times 10^{-19}$ cm^{-2}. It should be noted however that the blackbody spectrum has a steep gradient below 124Å (Figure 2.18) which will lead to some uncertainty in the flux estimates, which will become larger at longer wavelengths.

The calculations outlined above may be applied to any blackbody emitter - O-B subdwarfs, planetary nebulae nuclei, UV stars, neutron stars - scaling appropriately for the size of the object ($F(\lambda) \propto r^2$).

b) Planetary Nebulae Nuclei

Calculation of the expected flux from a planetary nebula nucleus is complicated by the presence of absorbing material in the surrounding nebula. Hence, it is necessary to estimate the amount of absorbing material that lies in the nebula along the line of sight. The central stars of these nebulae are mostly population II and composed mainly of hydrogen. Assuming on this basis that the composition of a nebula is similar to that of the interstellar medium then to a first approximation a nebula can be considered as an enhancement in the column density along the line of sight. Typical planetary nebulae radii are $\sim 2 \times 10^4$AU (3×10^{17}cm, 0.1pc) with densities ranging from 10^2 - 10^4 atoms cm^{-3}, resulting in column densities of 3×10^{19} to 3×10^{21} atoms cm^{-2} if the material in the nebula is uniformly distributed in a sphere about the central star. Although this is a relatively crude calculation it does suggest that in general the WFSXC will not be sensitive enough to see planetary nebulae nuclei. As a nucleus is expected to be evolving slowly towards the white dwarf

stage its radius will lie somewhere between $0.01R_\odot$ (typical white dwarf radius) and $1.0R_\odot$. Even by scaling the fluxes of figure 2.19 for $r'=1R_\odot$ (multiplying $F(\lambda)$ by 10^4) it can be seen that any but the most tenuous (most evolved) nebulae, where the nebula has expanded to give a line of sight column density below $\sim 3 \times 10^{19}$ atoms cm^{-2}, are below the sensitivity of the WFSXC. However, the assumption that the matter contained in the nebula is uniformly distributed does not necessarily hold (Capriotti, 1978) and it may exist as a shell rather than as a sphere. The column density will then depend upon the thickness of the shell and its orientation with respect to the line of sight when the material is unevenly distributed. With favourable conditions EUV observations could yield important information about the density of material composing these nebulae.

c) Stellar Coronae and RS CVns

The flux at the earth (F_e) from a stellar corona can be simply estimated, using the observable solar flux as a standard ($\sim$1.0 erg cm^{-2} s^{-1} in each band - 50 - 170Å, 114 - 230Å, 165 - 300Å)

$$F_e = F_s . d^2/D'^2 \qquad (2.14)$$

where: F_s is the solar flux

d is the distance to the sun from the earth

D' is the distance of the source

The results of this calculation indicate that solar type coronae may only be detected by the WFSXC within ~1 parsec of the sun.

However, many stars have coronae that are much more active than that of the sun and have been observed in the soft X-ray band. The soft X-ray spectra fit thermal bremsstrahlung models. It is possible to estimate the EUV flux by scaling the theoretical spectrum F(E), which needs a normalising factor (K), to a measured soft X-ray flux.

$$F(E) = K.\quad 0.242\times10^{-11}.e^{-E/kT_c}.E^{-0.3} \qquad (2.15)$$

$$(\text{ergs cm}^{-2}\text{s}^{-1}\text{keV}^{-1})$$

where: T_c is the characteristic temperature

The RS CVn system HR1099 has a measured luminosity of 1.2×10^{31} ergs s^{-1} (0.15 - 2.8keV), lies at a distance of 33pc and has a column density of 5×10^{17} cm^{-2} (Walter et al, 1980). Assuming a plasma temperature of 10^7K, the expected EUV flux at the earth will be $\sim9\times10^{-11}$ergs $cm^{-2}s^{-1}$ (50 - 170Å) and $\sim5\times10^{-11}$ergs $cm^{-2}s^{-1}$ (114 - 230Å) and $\sim3\times10^{-11}$ergs $cm^{-2}s^{-1}$ (165 - 300Å) after correction for interstellar absorption. This analysis is not strictly correct as above ~170Å line emission (eg. FeIX to FeXIII) will contribute to the total flux, as it does in the solar spectrum. The Einstein stellar survey suggests the presence of plasma temperatures $\sim10^7$K in most types of star, allowing the application of the preceeding analysis to these results.

d) Flare Stars

Flare star plasmas also have temperatures similar to those above. Consequently the emission in the bands of the WFSXC can be calculated from the ASTP flux in a similar manner to the HR1099 fluxes. Taking Proxima Centauri as a model of flare star emission, the fluxes have been calculated as a function of distance for several plasma temperatures. A mean interstellar hydrogen density of 0.03 atoms cm^{-3} was assumed to take account of interstellar absorption (Cruddace et al, 1974). It would appear from these calculations, made by scaling the Proxima Centauri flux like the solar flux in equation 2.14, that the WFSXC will only be able to "see" flare stars within distances of ~5pc from the sun. Proxima Centauri lies at 1.32pc and should be easily detected.

e) Supernova Remnants

The WFSXC has the capability of imaging extended objects such as SNRs. As with any other object visibility will depend upon the amount of absorbing material between the observer and the SNR. An indication of this can be obtained by looking for a low energy cutoff in the soft X-ray spectrum of the remnant. If no cutoff is present an upper limit on N_H can be obtained, $<10^{21}cm^{-2}$ for spectra above ~0.1keV. Such an upper limit lies well above the absorption cutoff in the XUV (Figure 2.19) and is consequently of little use. Alternatively N_H can be estimated from the local volume density which can be determined from observations of the SNR expansion through the local ISM (Smith, 1977).

The SNR IC433 is ~4000-5000 years old and is probably in the adiabatic phase of its evolution (Clark and Culhane, 1976). Its column density, calculated for a distance of 2kpc and a local density of $0.15cm^{-3}$, is $\sim 10^{21}cm^{-2}$, too high for XUV observations. The Vela SNR is a soft X-ray emitter which could be interesting at lower energies. Jenkins et al (1976) have found plasma temperatures of $\sim 10^{4}$-$3x10^{5}K$ from Copernicus UV measurements of the emission lines of stars lying behind the remnant. However the column density is high, at $\sim 2x10^{20}cm^{-2}$ (n_H=$0.15cm^{-3}$, assumed distance 500pc; Clark and Culhane, 1976). The aforementioned value lies within the range estimated from soft X-ray data by Seward et al (1971) at $1\text{-}8x10^{20}cm^{-2}$, the latter depending upon the spectrum fitted to the data. Seward et al also derive N_H values of $3x10^{20}$-$5x10^{21}cm^{-2}$ for the Puppis A SNR.

The above data suggest that XUV observations of SNRs will not be practical if these densities are typical. However the picture is not entirely gloomy. Soft X-ray observations of SN1006 made by Einstein (Pye et al, 1981) show no apparent cutoff in the spectrum down to 0.1keV, into the range of the WFSXC (0.05-0.25keV). An imaging telescope flown in a previous collaboration between Leicester University and MIT observed the SNRs Puppis A, IC433 (Levine et al, 1979) and the Cygnus Loop (Rappaport et al, 1979) in the 0.15-1keV band, again overlapping the WFSXC. Unfortunately no spectra were published for any of the three SNRs and consequently the proportion of the flux overlapping into the XUV cannot be calculated.

Should the column density to an SNR be low enough a secondary problem is the aquisition of sufficient counts over the area of the remnant to produce a detailed image. This may require integration times which are a large fraction of a single rocket flight. If an extended source emits a total flux S, then the flux per pixel is $S.\theta^2/A_s$ where A_s is the area subtended by the source on the detector. Therefore

$$s = S.A.G.T.\theta^2/A_s \qquad (2.16)$$

and the minimum detectable flux is simply

$$S_{min}(\text{extended}) = S_{min}(\text{point source})A_s/\theta^2 \qquad (2.17)$$

This is the condition imposed if we require information from each pixel in the image. A simple source detection can be made if S_{min} is determined for a pixel size of the area of the source.

The above calculations and discussion show clearly that many of the objects discussed in section 1.3 should be detected by the WFSXC. Blackbody temperatures below $\sim 4 \times 10^4$K are not detectable with the current 50 - ~300Å bandpass and no sources can be detected with column densities $\gtrsim 3 \times 10^{19}$cm^{-2}. It should be pointed out that the predictability of sources in new fields of astronomy is notoriously bad. The uncertainty in the parameters and models used to predict fluxes may cause quite large discrepancies between predicted values and those ultimately measured. Of course the most outstanding sources

may not be considered at all as there is always the possibility that new types of object may be discovered in a new branch of astronomy (eg. X-ray binaries in X-ray astronomy).

2.4 Summary: Developments for the WFSXC Project

The concept of the WFSXC has been outlined and the expected performance discussed, as summarised in table 2.2. Briefly, the instrument comprises a nest of three grazing incidence mirrors with anticipated on-axis resolution of $1'$, an $8°$ field of view and collecting area $\sim 250 cm^2$. An MCP detector with resistive anode readout, in the focal plane, gives comparable resolution. Coarse, two band energy resolution will be provided by two filters having different bandpasses, selected from three choices - Par N, Be + Par N and Al + C. Calculations of the WFSXC sensitivity show that, in a single rocket flight, quite large areas of sky (~600 square degrees) can be observed, with sensitivities of 3.5×10^{-11}, 1.6×10^{-11} and 5.5×10^{-11} ergs $cm^{-2} s^{-1}$ in the above filters respectively, corresponding to ~1/60, ~1/500 and ~1/300 of the flux from HZ43 (the brightest EUV source). However, as 600 square degrees is only ~1.5% of the whole sky, an all-sky survey is not practical with current constraints on payload size and sensitivity.

The task of payload development was to achieve the aims outlined in table 2.2 and, if possible, to improve on the specification. Responsibilities were divided between MIT and Leicester as follows;

a) MIT

Table 2.2. Summary of predicted WFSXC performance

Collecting area of mirror nest	$300cm^2$ (on-axis) $250cm^2$ (mean)		
Focal length	35cm		
Field of view	Circular, 8° diameter		
Spatial resolution (RMS)	1″ (on-axis) 20″ (off-axis)		
Count rate capability	$2500s^{-1}$		
FILTERS	5000Å Par N	2500Å Be + 1000Å Par N	1000Å C + 1250Å Al
Bandpass (Å)	50-170	114-230	165-300
Grasp (Å)	0.98	1.13	0.27
Net Background (counts s^{-1} $ster^{-1}$)	1330	$1.1x10^4$	$1.1x10^4$
Sensitivity (ergs $cm^{-2}s^{-1}$, 30s exposure)	$3.5x10^{-11}$	$1.6x10^{-11}$	$5.5x10^{-11}$
Source detectability in 30s (fractions of HZ43 flux)	1/63	1/525	1/291

i) Grazing incidence optics

ii) Payload electronics

iii) Payload structure and vacuum system

iv) Filters

v) Ground support equipment

b) Leicester

i) MCP detector

ii) Resistive anode readout and pre-amplifiers

iii) Filters

The rest of this thesis comprises a review of the advances made on the instrument and its component parts in the course of this research.

- Development, testing an calibration of detectors for two flights of the WFSXC
- Photocathode development to improve detector efficiency
- Development, testing and calibration of a resistive anode readout
- Design optimisation and calibration of thin film filters
- Testing of the grazing incidence mirrors and integrated payload
- Flight planning

As both flights of the WFSXC have so far been beset by technical problems, the final chapters give an account of the analyses and tests

carried out to diagnose and rectify the problems in preparation for future re-flights.

CHAPTER 3

GAIN CHARACTERISTICS OF THE DETECTOR FOR THE WIDE FIELD SOFT X-RAY CAMERA

3.1 The Use of Microchannel Plate Detectors in Astronomy

Microchannel plates (MCPs) have been used as photon detection devices in several sounding rocket and satellite-borne experiments, in soft X-ray, XUV and far ultraviolet wavebands, both in imaging telescopes and spectrometers.

The most successful example of an MCP detector in an imaging telescope has been the "high resolution imager" (HRI) (Kellogg et al, 1976), on board the the Einstein observatory. The HRI operated with good stability throughout the mission (1978-1981) and recorded several hundred image fields, in the energy band ~0.1-4.0keV, accumulating over 10^4 hours of operation. At a more modest level, a sounding rocket borne imaging telescope used an MCP detector, with resistive anode image converter (RANICON) (Lampton and Paresce, 1974), to observe hot white dwarfs in the EUV waveband (250-750Å) (Cash et al, 1978b and 1979).

Examples of imaging MCP detectors used to record the dispersed spectrum from a diffraction grating include Bowyer et al's (1981) use of a RANICON, on board the US Airforce Space Test Program Satellite P78-1, to observe the geocoronal background in the EUV (275-1420Å). Both Voyager spacecraft carry EUV/UV spectrometers (500-1700Å), which have been used to study hot stars during the interplanetary phases of the Voyager mission (eg. Holberg et al, 1982). The MCP detectors have now each seen over 30,000 hours of nearly continuous operation.

Weiser et al (1976) devised an instrument covering a range 1160-1750Å and McClintock et al (1982) one covering a band 1500-1800Å, both for flight on sounding rockets.

An MCP detector was chosen for the WFSXC against the background of flight experience. Nevertheless a number of development tasks had to be undertaken for the WFSXC detectors in respect of their gain optimisation, quantum efficiency and readout linearity which extended the performance of an MCP detector beyond that achieved in these earlier missions. These developments are described in the following three chapters of this thesis.

3.2 A Qualitative Description of MCP Operation

An MCP is an array of 10^6-10^7 parallel, close-packed, equal diameter channel electron multipliers. Channel diameters (D) from 12.5-50μm are available (Mullard, 1976). They are manufactured by repeated drawing and stacking of lead-glass fibres, which have a soluble glass core, until the required channel diameter has been achieved, when the assembled matrix is cut into slices which are polished. The core material is then etched away and the MCP baked in hydrogen to establish the required secondary electron emission characteristics. Finally, nichrome electrodes are vacuum-deposited on each face of the MCP. Figure 3.1 shows the main steps in MCP production which has been described in more detail by Washington et al (1971).

When a potential difference ~1-2kV is applied across the electrodes the MCP acts as an electron multiplier. A photon entering the low potential end of the channel and colliding with the channel wall produces one or more electrons by photoionization and by secondary emission. These primary electrons are accelerated by the applied field and collide with the wall further along the channel and liberate more electrons by secondary emission. This process is repeated along the channel producing a large number of electrons at the output (figure 3.2).

As the secondary electron yield is a function of the primary electron energy, varying between 1-2 electrons (Hill, 1976), the number of secondary electrons at each multiplication stage is not well defined. The result of this, after successive multiplications, is a large uncertainty in the overall gain of the MCP. The histogram of the number of events at a given gain is a characteristic of the MCP channel dimensions and the applied potential and is commonly called the pulse height distribution (PHD). At low gains the gain is proportional to the applied potential, the linear mode of operation, and the PHD follows a negative exponential function (figure 3.3a).

At higher gains a saturation effect occurs due to net positive charge residing in the channel wall following electron multiplication. As the event propagates along the channel, the electron collision energy decreases and the secondary electron yield eventually falls to unity. The magnitude of the output charge cloud stabilises or "saturates" and has a peaked, quasi-gaussian PHD (figure 3.3b). The width of the distribution decreases as, with increasing gain, the

Figure 3.1 (from Mullard, 1976)

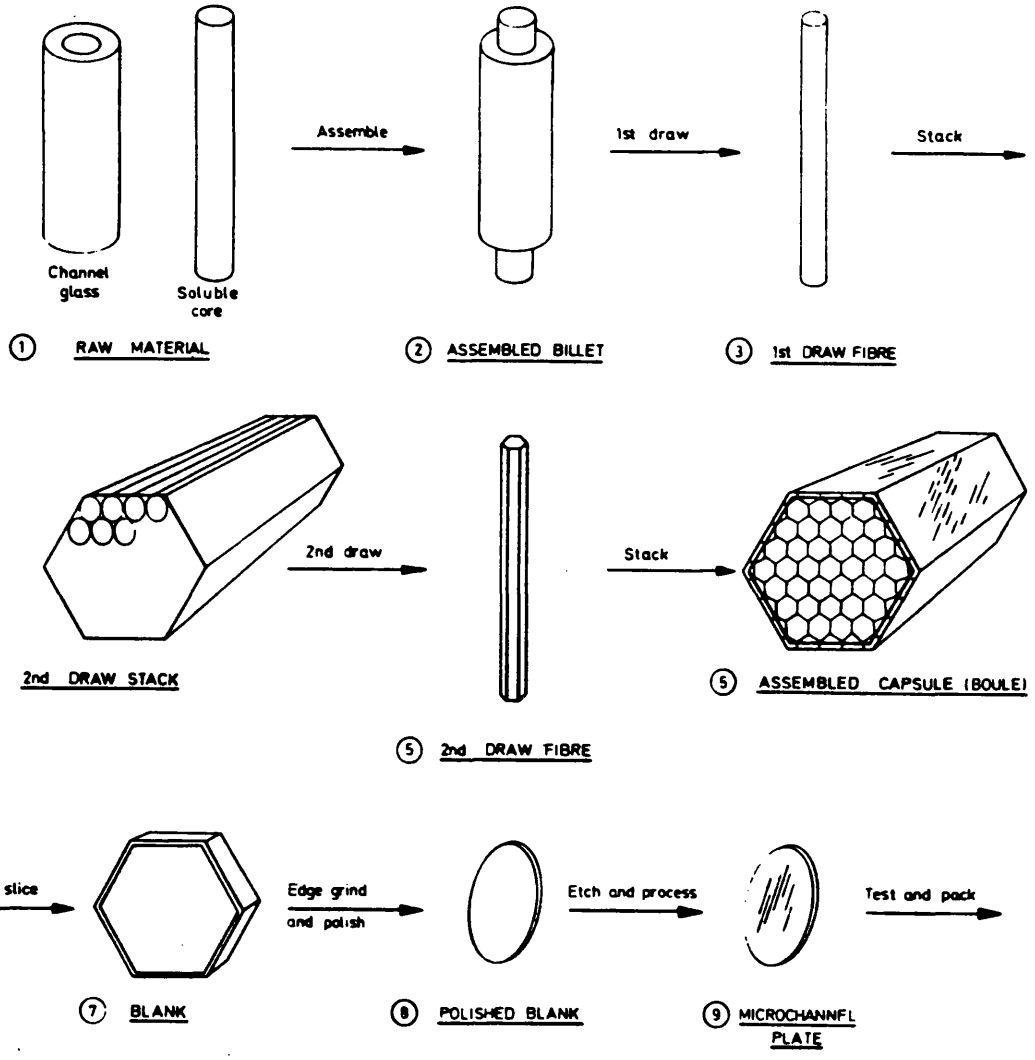

Steps in the manufacture of microchannel plates

Figure 3.2 Diagram of electron multiplication in a straight channel.

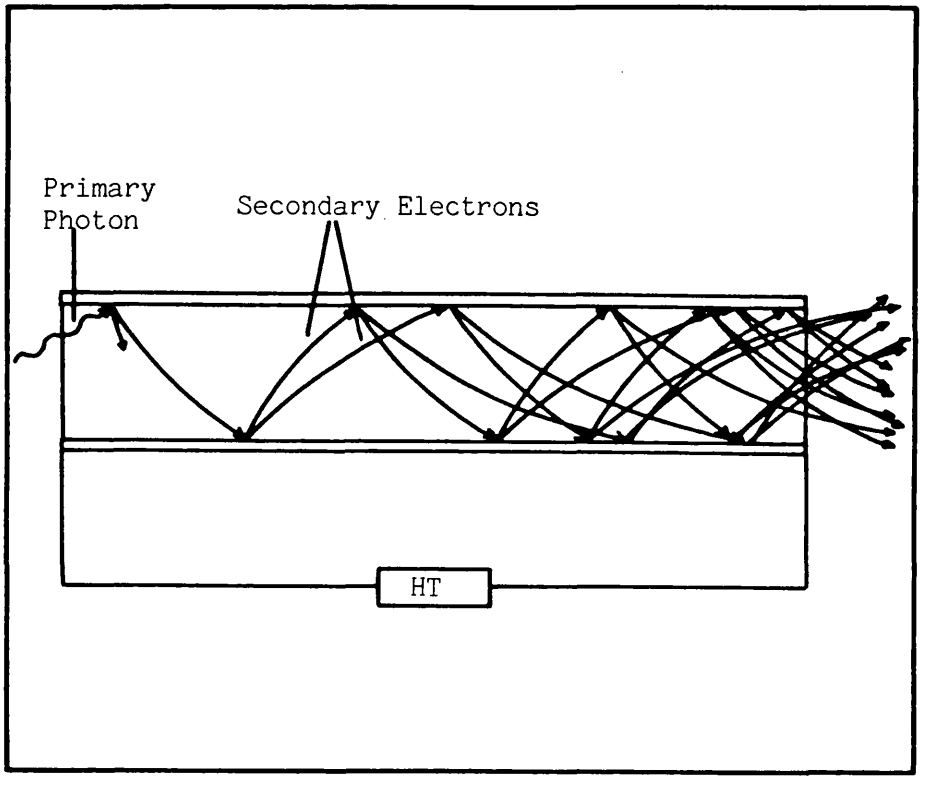

Figure 3.3a Example of an exponential pulse height distribution.

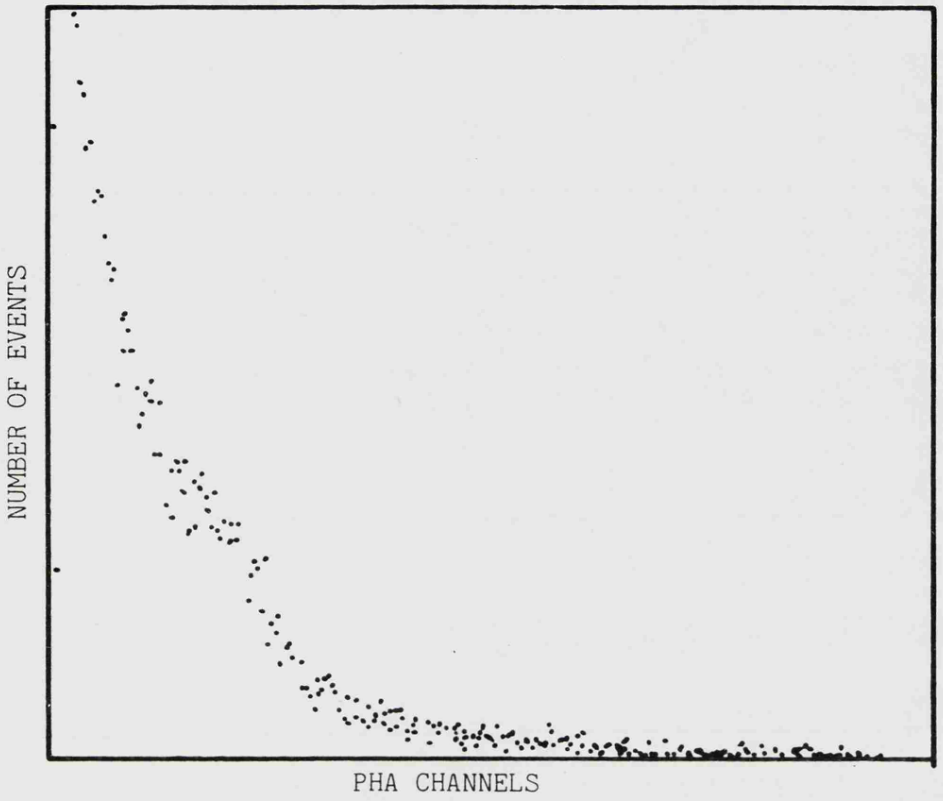

Figure 3.3b Example of a peaked pulse height distribution.

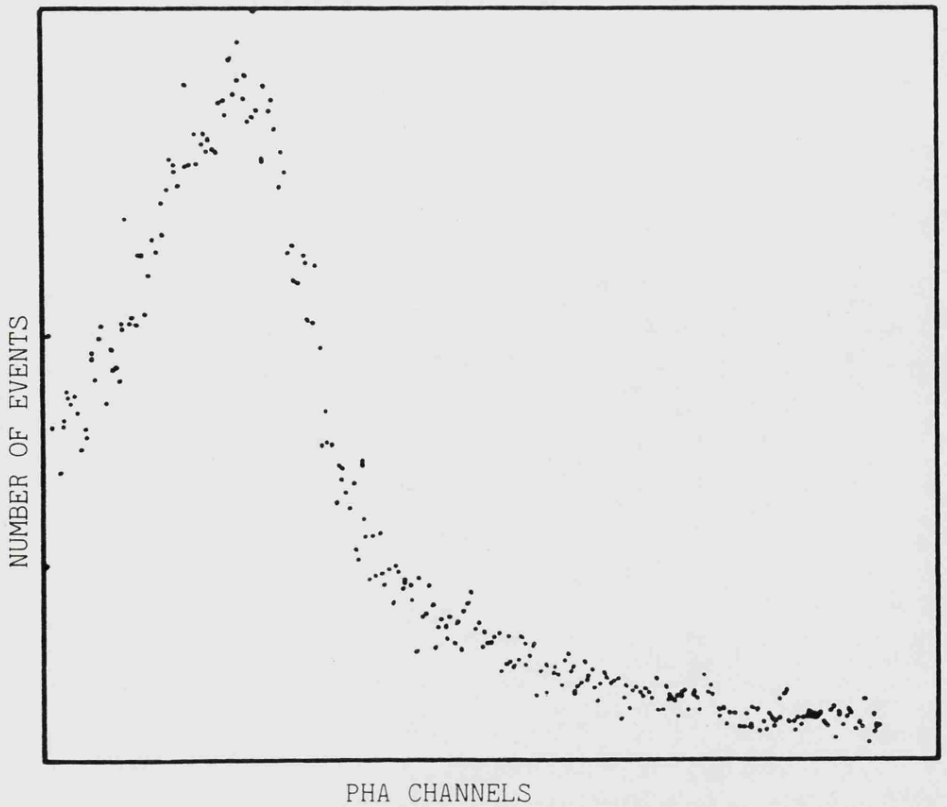

saturation becomes "harder".

Wall charging occurs because the transit time of a pulse is much shorter, at ~1-1.3ns (Oba et al, 1979; Mullard, 1976), than the time needed to replace the charge abstracted from the channel. This recovery time depends upon the channel resistance and capacitance and may be of order 10^{-2}s (Wiza, 1979). The recovery time will also limit the count rate capability of a channel since no further photon detection may take place until the depleted charge has been replaced. For a given input count rate (C_R) the apparent count rate (C_A) is a function of the recovery time, or dead time, DT.

$$C_A = C_R(1-\exp(-1/DT.C_R)) \qquad (3.1)$$

With DT~10^{-2}s up to 20 counts s^{-1} can be detected by a single channel without significant loss (<1%) of events. If n channels are illuminated by the photon beam then the maximum count rate is simply ~20n counts s^{-1}channel^{-1}.

The electron yield per photon of MCP glass is a function of the photon energy. As it is low and not well defined the total number of initiating electrons cannot be determined from the MCP gain and conventionally MCP detectors have been regarded as having no intrinsic energy resolution. However, recent work using a CsI photocathode on the front MCP of a chevron has shown that energy resolution is possible, on account of the higher photoelectric yield of the CsI (Fraser and Pearson, 1983).

The useful gain of a single MCP is limited to a maximum of 10^4-10^5 by the problem of ion feedback (Wiza, 1979). As the gain increases so does the probability of producing a positive ion, in the high charge density region at the output of the MCP, by electron collisions with residual gas molecules within the vacuum chamber and with gas molecules desorbed from the channel walls. These ions accelerate back up the channel exciting further secondary electrons at the channel input which then produce secondary avalanches appearing as after-pulses. The incidence of ion feedback depends upon the residual gas pressure and the electron density.

Ion feedback can be suppressed in MCPs by two alternative methods, either by curving the channels of the MCP or by operating two MCPs in cascade in a chevron arrangement (Parkes and Gott, 1971). The chevron combines two MCPs of differing bias angle (the angle between the channel axes and the normal to the MCP surface) or two MCPs of the same bias angle, oriented so that the two sets of channels are inclined to each other (figure 3.4). The directional change at the interface of the two MCPs, typically 10-20°, prevents ions produced at the output of the rear plate from reaching the input of the front MCP.

Chevron peak gains of 10^7-10^8 (Parkes and Gott, 1971; Kellogg et al, 1976) can be obtained providing a much improved signal-to-noise for signal processing electronics. As the distribution is peaked, the gains of most of the photon events fall above those of the background noise pulses. Hence, a discriminator can be used to reject the noise without losing many events. Electrons from the front MCP of a chevron pair will spread over a number of channels of the second MCP in the

gap between the plates. Activating more channels in the rear MCP increases the area of the output charge cloud and may cause a degradation of the resolution. This problem can be avoided if an electronic readout which determines the centroid of the charge cloud is used.

Experimentalists have observed that the gain of a straight channel MCP changes as a function of the total accumulated count (Parkes et al, 1970; Parkes, 1974). The results of Parkes et al show three phases in the lifetime of a single Mullard G40 (D=40μm, p=50μm) MCP (figure 3.5)

1) A clean up period, the gain decreasing towards a plateau ($\sim 10^8$ events).

2) A plateau region of stable gain up to $\sim 6 \times 10^9$ events.

3) A fatigue region above $\sim 10^{10}$ events where the gain decreases and the width of the distribution increases. To some extent this can be recovered by operating at a higher voltage.

The initial decrease in gain is caused by the progressive removal of gas molecules, which have an enhanced secondary electron yield and are absorbed on the channel walls, by the electron avalanches associated with each event. When the absorbed gas is removed by vacuum baking the MCPs (Parkes, 1974) the initial clean-up period is

Figure 3.4 The chevron detector.

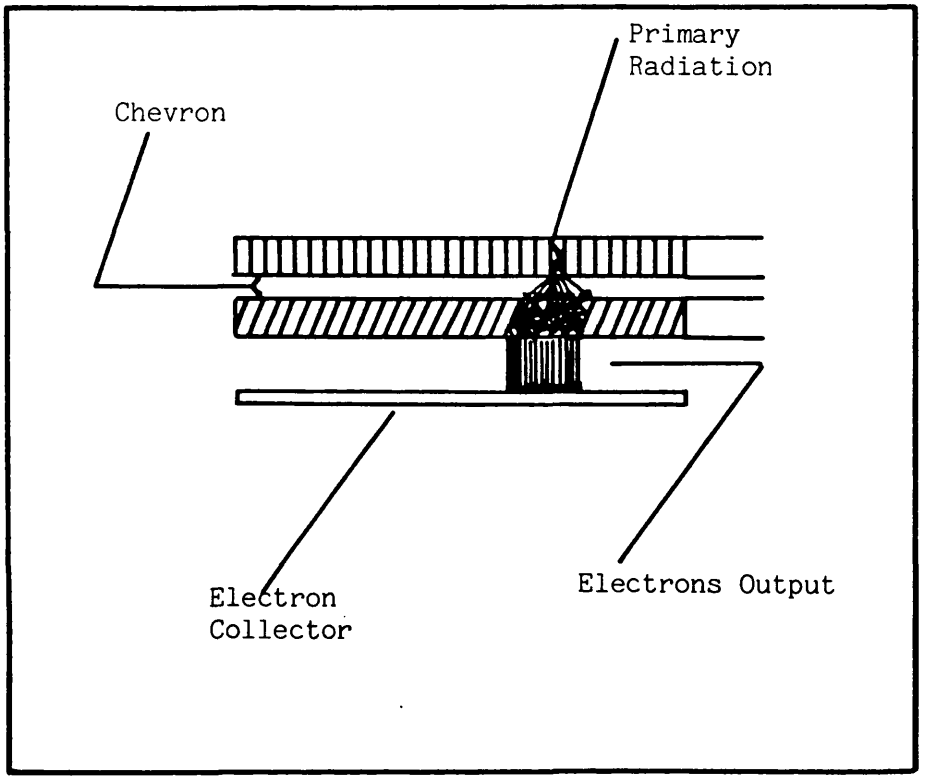

Figure 3.5 Mean MCP gain as a function of the total number of events observed showing the characteristic lifetime curve (from Parkes et al, 1970).

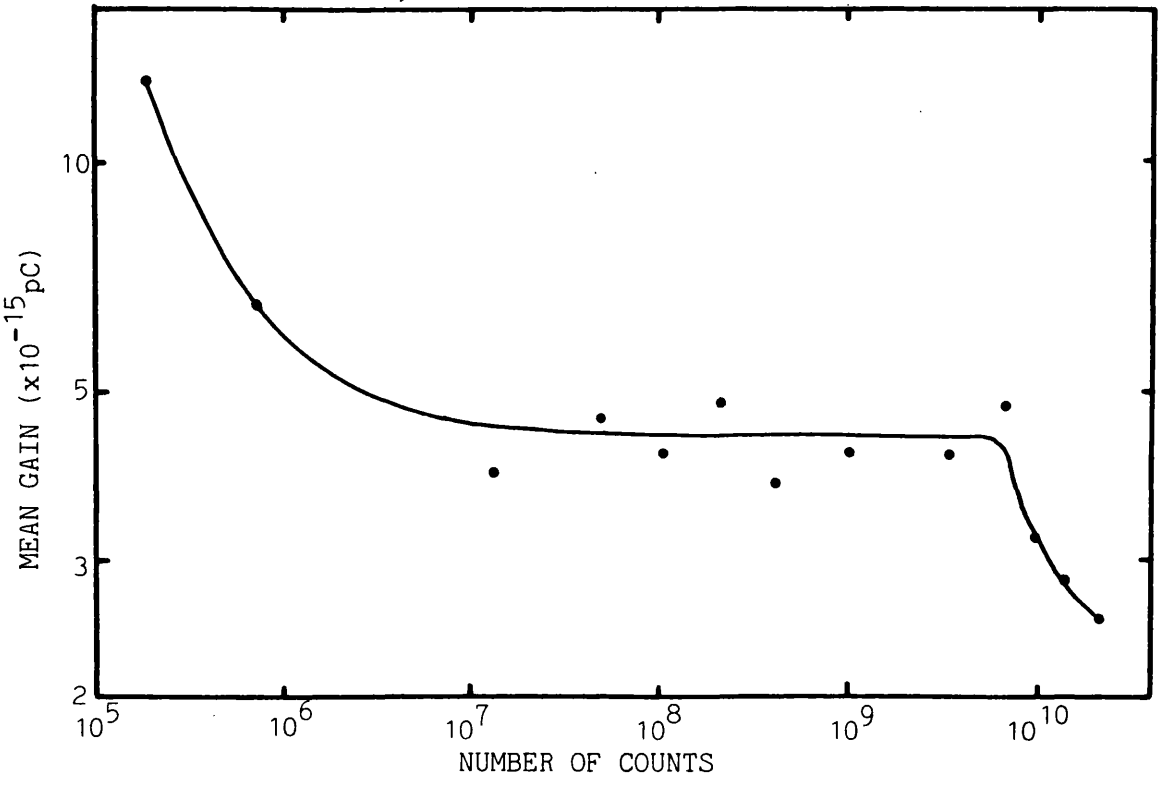

eliminated.

The fatigue region is not as well understood. Hill (1976) and Authinarayanan and Dudding (1976) found that the secondary electron yield from MCP glass decreased with desorption of hydrogen and reduction of potassium surface concentrations by electron bombardment. Either of these two processes could cause a reduction in gain. However, Rager and Renaud (1974) attributed gain degradation in their experiment to pump oil contamination.

MCP detectors are expected to have a background dark count, explained by Henry et al (1977) as the field emission of electrons from defects within the channels. The electrons, which are then multiplied in the channel, may be emitted at any point along a channel and most of them will have lower gain than a photon, which excites an electron at the channel input. Hence, the resultant distribution of noise events is quasi-exponential and they occur randomly over the MCP area resulting in an integrated image which is uniform. The count rates are highly dependent upon the operational voltages of the MCPs, the length of time for which the detector has been pumped and the pressure and cleanliness of the vacuum system in which the detector is operated, but are generally < 1 count $cm^{-2}s^{-1}$ (Wiza, 1979).

3.3 Design of the WFSXC Detector

The specification for the WFSXC imposed certain restrictions on the configuration of the MCPs. A circular detector area of ~50mm diameter and a spatial resolution of ~100μm were required. Additionally there was a mechanical requirement that the detector be

capable of surviving the vibrations experienced during launch.

A plate diameter of 53mm was chosen as being the standard size closest to the specified diameter. A limit to the resolution is imposed by the distance between individual channel centres, the channel pitch (p), which is determined by the channel diameter D and the wall thickness which is usually ~2-10μm. Standard channel diameters of 12.5μm, 25μm and 40μm are available from manufacturers, all well below the 100μm resolution required.

The resolution is not simply a function of the MCP pitch but is also determined by the signal-to-noise in the image readout system and high detector gains are necessary. The chevron configuration was chosen for the WFSXC to allow the possibility of achieving a gain ~$3\text{-}4\times10^{7}$ (5-6pC), for which the payload electronics were designed (see section 2.2.4), whilst avoiding noise contributions from ion feedback. The front MCP has a 0° bias so that the angle of incidence of the photon beam, and therefore the quantum efficiency, is the same from any point on the mirror. The rear MCP has a 13° bias angle to provide the necessary directional change to eliminate ion feedback. As the electronic noise generated by the resistive anode and associated electronics is generally ~10^{3}-10^{4} electrons, the signal to noise is ~10^{4}, compared to ~10 with a single MCP (gain ~10^{4}-10^{5}).

The width of the pulse height distribution also influences the attainable resolution, as the lower gain events have a worse signal-to-noise. If this width is minimised the potential problem will be reduced. Kellogg et al (1976) noted that MCP pairs with a channel length-to-diameter ratio (L/D) of 80:1 have a narrower width than

those with an L/D of 40:1. An L/D of 120:1 was chosen for the WFSXC in an attempt to obtain still narrower distributions and hence better signal-to-noise. In order for the WFSXC MCPs to have sufficient mechanical strength, 25μm diameter channels were chosen, resulting in an MCP thickness of 3mm for L/D=120:1.

Figure 3.6 shows the engineering construction of the MCP detector for the WFSXC. PTFE rings support the two MCPs, stacked in a fibreglass holder, with electrical connections to the front and back of each MCP provided by gold plated annular electrodes. The MCP/electrode assembly was mounted inside an aluminium holder which also holds the resistive anode. Each output terminal of the anode is connected to one of four plugs in the base of the detector body which allow the detector to be plugged directly into a baseplate to which the preamplifiers are mounted. This assembly is either installed in the payload, for flight, or in a vacuum test facility, for calibration. Since the detector must be operated in a vacuum, holes were drilled in the detector body to provide outgassing paths from all closed volumes. The assembled detector is shown in figure 3.7.

To operate a detector the MCPs must be negatively biased (front to back). This can be done by either having the front electrode at ~0V and the rear electrode at high positive potential, or by having the front electrode at high negative potential and the rear electrode at ~0V. The latter is the preferred arrangement, since it allows the anode to be close to earth potential and prevents the problem of decoupling the preamplifiers if the anode were at high voltage. Additionally, the negative front surface potential repels stray

Figure 3.6 Engineering diagram of the WFSXC detector.

1) Aluminium body
2) Fibreglass holder for MCP assembly
3) Front MCP
4) Rear MCP
5) PTFE ring holding MCP
6) Fibreglass spacer between front electrode and outer case

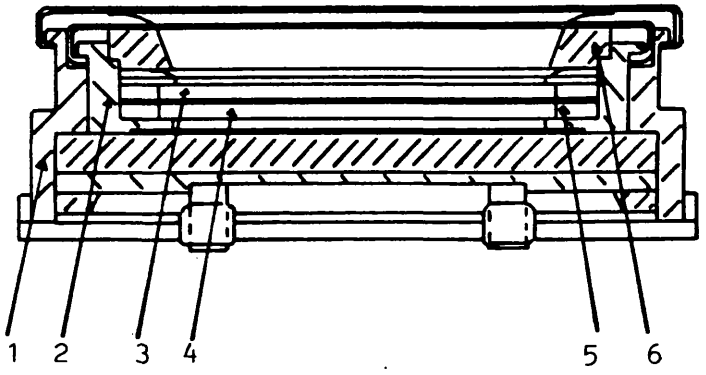

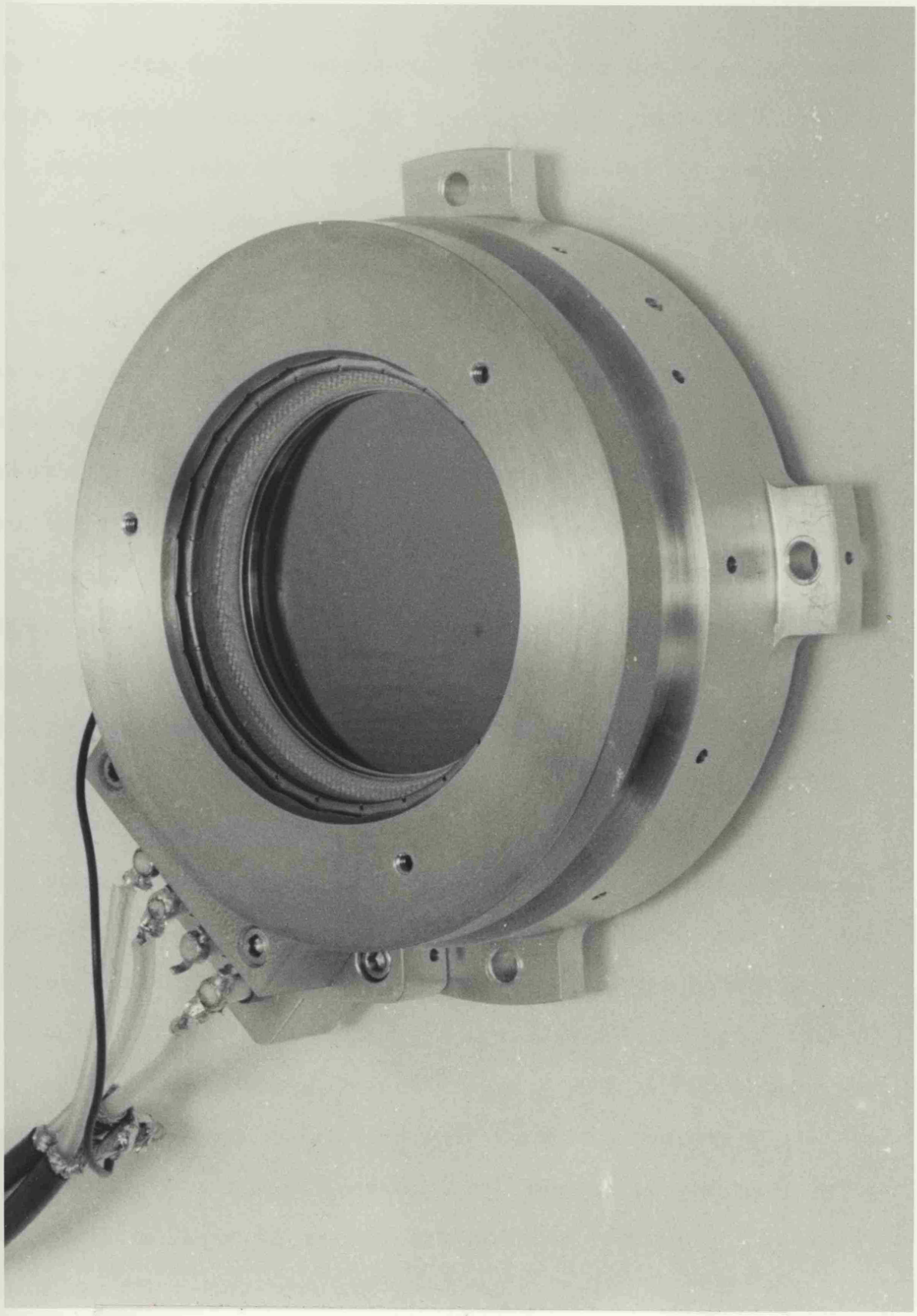

Figure 3.7 The assembled WFSXC detector

electrons with energies below ~4keV, which could otherwise contribute to the detector background. The total potential required to obtain the necessary gain should be as low as possible to minimise the electrical stress on insulators and reduce the risk of electrical breakdown.

The active detector area is ~2000mm^2 and the channel packing density ~1300 mm^{-2} for D=25μm MCPs. It is expected that the background countrate in the detector will be ~200 counts s^{-1} corresponding to ~8x10^{-5} counts s^{-1}channel^{-1}. The expected count rate from the brightest EUV source, HZ43, is 20-50 counts s^{-1} or 2-5 count s^{-1}channel^{-1} for a 100μm resolution element. The channel dead time places an upper limit on the count rate of 20 counts s^{-1}channel^{-1}, estimated in section 3.2. Consequently, no channel dead time problems will be experienced with either EUV sources or instrument background.

3.4 Experimental Techniques

All laboratory tests were performed in the vacuum system at Leicester, except during integration of the detectors into the payload. The system (figure 3.8) comprised a large aluminium tank pumped by an oil diffusion pump with liquid nitrogen cold trap to prevent oil backstreaming from the pump. The diffusion pump was backed by a trapped rotary pump which was also used to rough out the tank. MCP detectors should generally be operated at pressures below 5x10^{-5}Torr in order to prevent spurious ion feedback. The vacuum system described above attained pressures of 8x10^{-6} to 2x10^{-5}Torr.

X-rays were generated in the vacuum system from a Coolidge type X-ray source, in which electrons emitted from a hot tungsten filament were accelerated onto a copper anode. The required X-ray wavelength was produced by painting the anode with an appropriate material and applying a suitable accelerating potential between cathode and anode. A twelve position filter wheel was placed directly in front of the source and behind a simple two hole collimator. A monitor proportional counter, mounted on a moveable arm, could be swung between the collimated X-ray beam and the MCP detector to calibrate the beam intensity (figure 3.9). The MCP detector was mounted on a turntable which allowed rotation of the detector about an axis bisecting the front MCP surface in order to vary the angle of incidence of the X-ray beam to the surface.

Voltages were applied to each electrode with individual power supplies so that the potentials across each MCP, the interplate gap and the rear MCP-anode gap could be varied separately (figure3.10). The gain performance of the detector, monitored as the applied potentials were altered, was characterised by its pulse height distribution, in terms of the peak of the distribution (G_C) and its full width half maximum (dG_C/G_C). Pulse height distributions were obtained by summing the charge from each of the four resistive anode electrodes using the circuitry in figure 3.10 and were displayed by feeding the output from the summing circuit filter amplifier into a Canberra pulse height analyser (PHA). The distribution was calibrated by feeding a pulse of known charge through the test inputs of all four preamplifiers. During all laboratory tests the total count

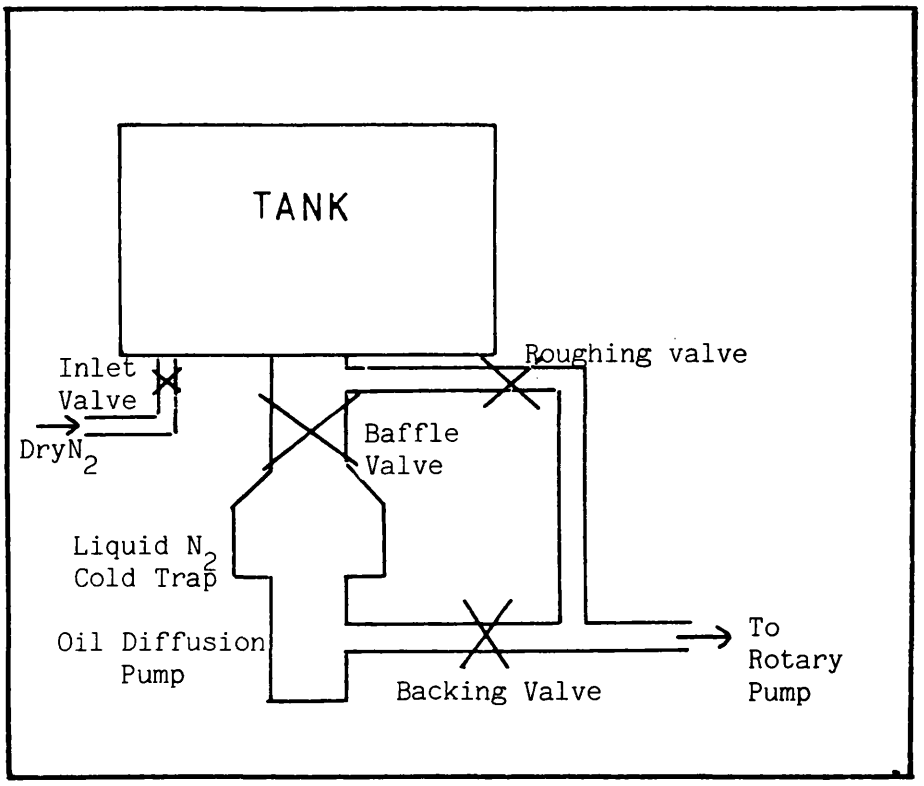

Figure 3.8 The vacuum system used for detector testing.

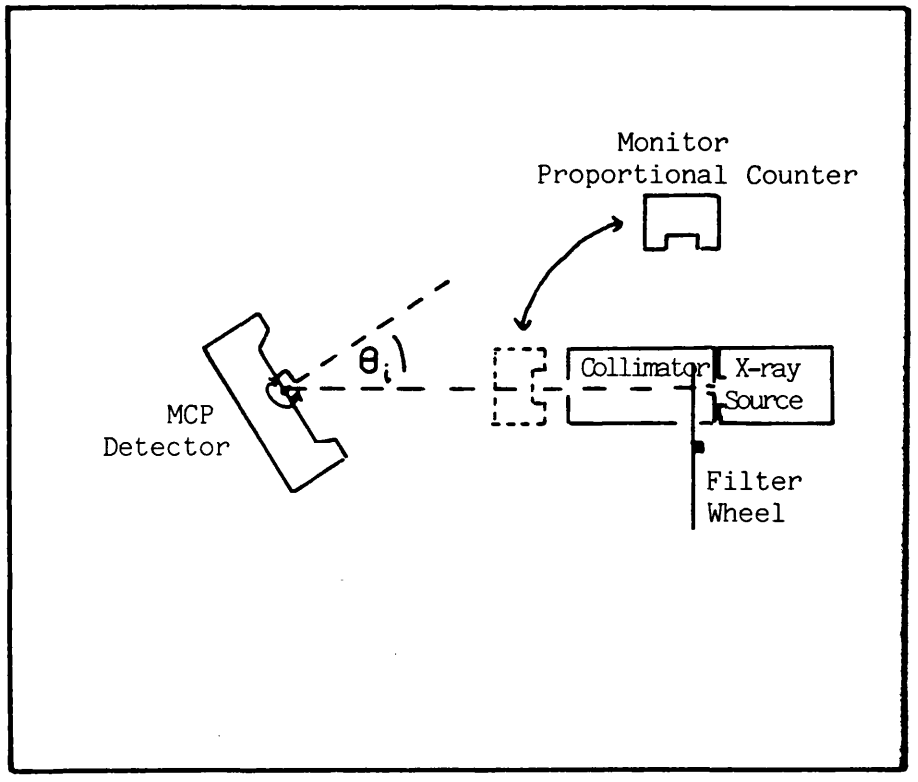

Figure 3.9 Diagram of the soft X-ray source, filter wheel and monitor counter inside the detector test system.

Figure 3.10 Circuit for measuring detector pulse height distributions.

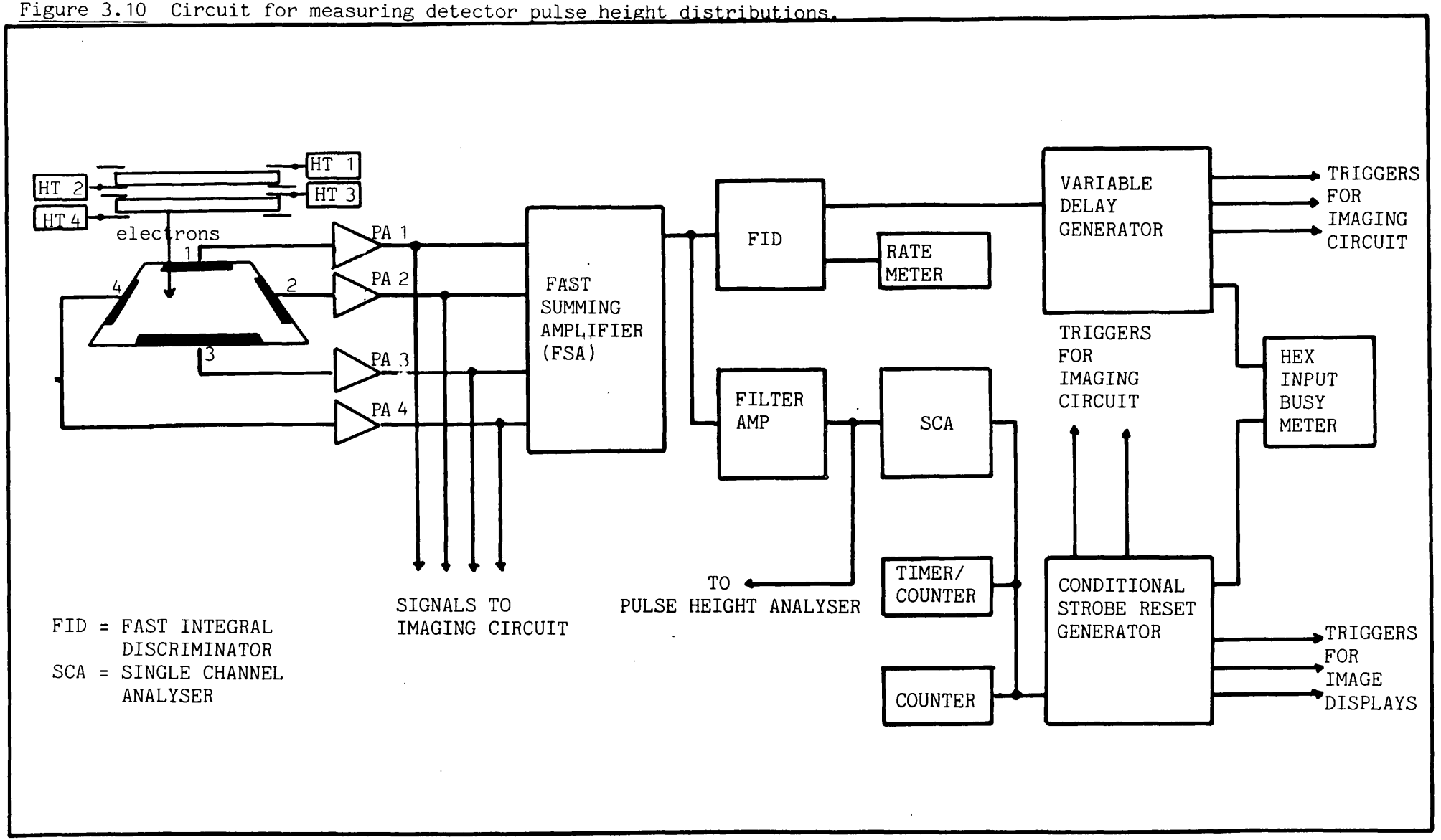

accumulated by each detector was monitored, from the detector background noise and from X-rays.

3.5 Detector Development

Three detectors were constructed to the design outlined in section 3.3. For the first of the two rocket flights, a flight model (detector 1) and a flight spare model (detector 2), in case of a detector failure during payload integration, were built. For the second flight the MCPs used in detector 2 were replaced by a third pair and this model, which will be referred to as detector 3, was used as the flight instrument with detector 1 as a backup. All three pairs of MCPs were cut from the same boule of glass and were processed together.

Detector 1 was initially assembled inside a laminar flow cabinet and was transferred to the vacuum system in a sealed polythene bag to protect it from dust. During the first tests considerable problems were experienced with concentrated patches of noise, "hotspots", in areas of the detector (figure 3.11), with count rates up to ~10 counts $cm^{-2}s^{-1}$ (~100 counts s^{-1} over the $10cm^2$ detector area) compared with the expected <1 count $cm^{-2}s^{-1}$. A number of hotspot positions could be associated with trapped dust particles discovered on inspection of the detector. Dust probably generates noise by electrostatic charging of the particles by the potential applied to the front MCP surface, the resulting local distortion of the electric field causing emission of electrons. To eradicate this problem detector handling was transferred to a clean room and all detector surfaces were carefully

inspected with a microscope during assembly and all dust particles seen were removed.

Even with improved handling, hotspots remained. However, all lay at the edge of the detector field of view. One single hotspot was much more intense than the others and was found to be associated with several damaged channels in the front MCP. These channels were drilled out but no active area was lost as they lay under the front electrode. In order to remove the dust generated by the drilling, the plates were "washed" by ultrasonic cleaning in isopropyl alcohol for ~10 minutes and then rapidly immersing them in water at ~100°C. When all gas was expelled from the channels the MCPs were removed from the water and air-baked at 70°C to dry them. It was thought that the damaged channels were caused by a hotspot becoming very bright and drawing too much current. In order to prevent this problem in the future, protection circuitry was added to the HT supplies to limit the current that could be drawn.

The hotspots at the edge of the field of view (figure 3.12) were intermittent, appearing in random positions. Suggestions that the problem may be due to electrical breakdown because of the high potential applied to the front electrode (~3.7kV) were disproved by a series of breakdown tests carried out on each of the detector components. These tests established a breakdown potential >4kV in dry nitrogen for each non-conducting detector component.

All hotspots seen at the edge of the detector occurred when the internal diameters of the electrodes were identical (figure 3.13a). Similar problems experienced by Mullard Ltd during MCP operation (R.

Figure 3.11 Detector image recorded by a storage oscilloscope showing hotspots.

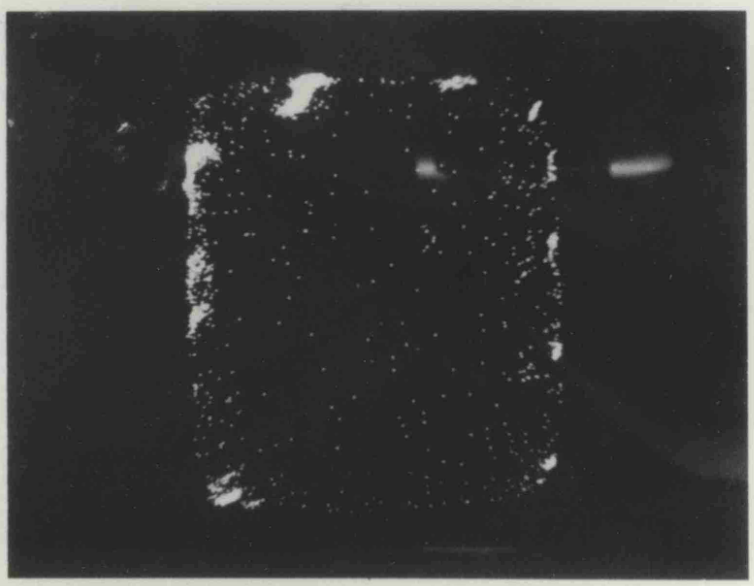

Figure 3.12 Detector image recorded by a storage oscilloscope showing hotspot at the edge of the detector field of view (note the square shape of the field is a result of the anode distortion).

Field, private communication) were remedied by stepping in the internal diameters of the electrodes towards the rear of the detector (figure 3.13b). Following this procedure with the WFSXC detectors completely eliminated the noise problem. Unfortunately this resulted is an effective loss of field of view, with the current MCP diameter, as the active area was reduced to 36mm diameter, equivalent to 6°.

It is possible that the cause of the noise problem is some interaction of the electrodes with the MCPs. The step of an electrode onto the nichrome front MCP surface must produce a local distortion of the electric field at the inner edge of the electrode. If the field distortion generates electrons a hotspot will be observed. Stepping in the electrode diameters does not eliminate the cause but merely masks the effect from the resistive anode.

Having eliminated the noise problems, residual count rates between 0.1 and 1 counts $cm^{-2}s^{-1}$, a total of 1-10 counts s^{-1} over the detector area, were obtained over the voltage range from V_F=1.60kV to 2.0kV as figure 3.14 shows. Approximately 90% of the noise events fall below 1pC at these operating potentials.

The noise problems limited the potentials that could be applied to the MCPs and only a few gain measurements could be made. Once the noise problems had been eliminated comprehensive calibrations of gain and quantum efficiency were performed, using CKα (44.7Å) X-rays, with the washed MCPs. All the calibrations of detector 1 were carried out without using an interplate gap potential as a single 125μm thick interplate electrode was installed in this model.

Figure 3.14 Detector dark count as a function of the front MCP potential (V_F) (V_G=0, V_R=1.6kV, V_B=100V).

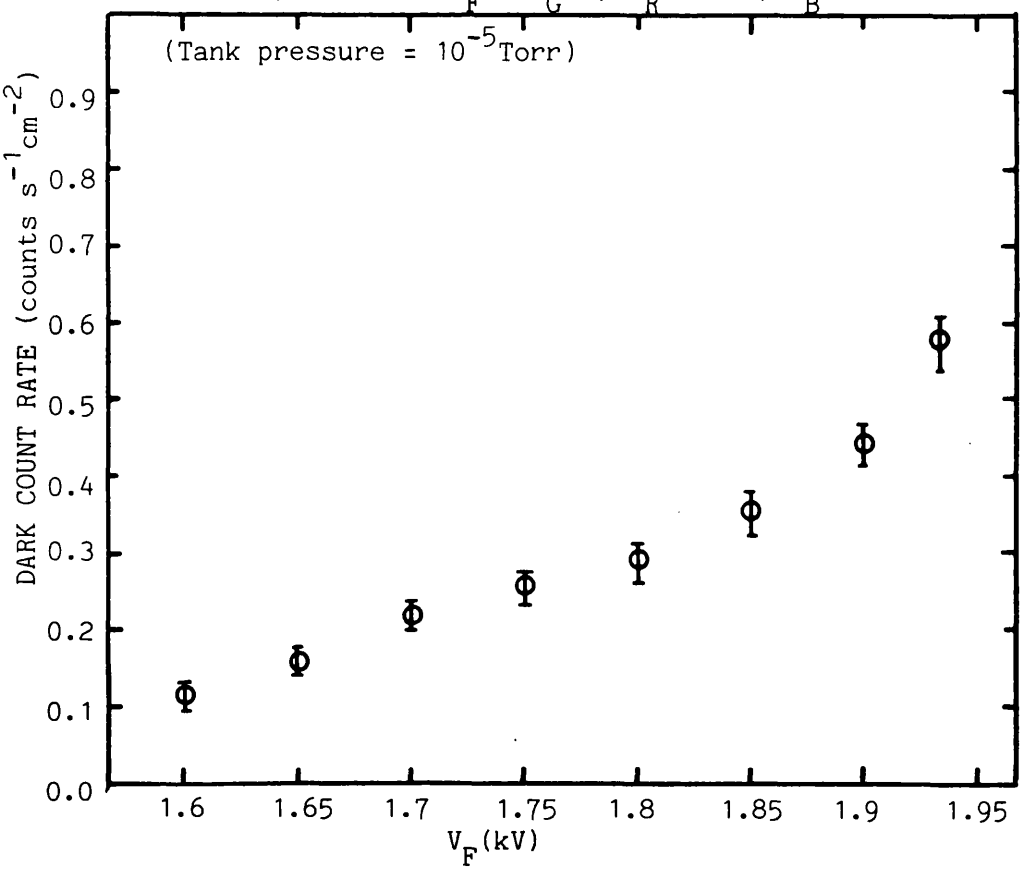

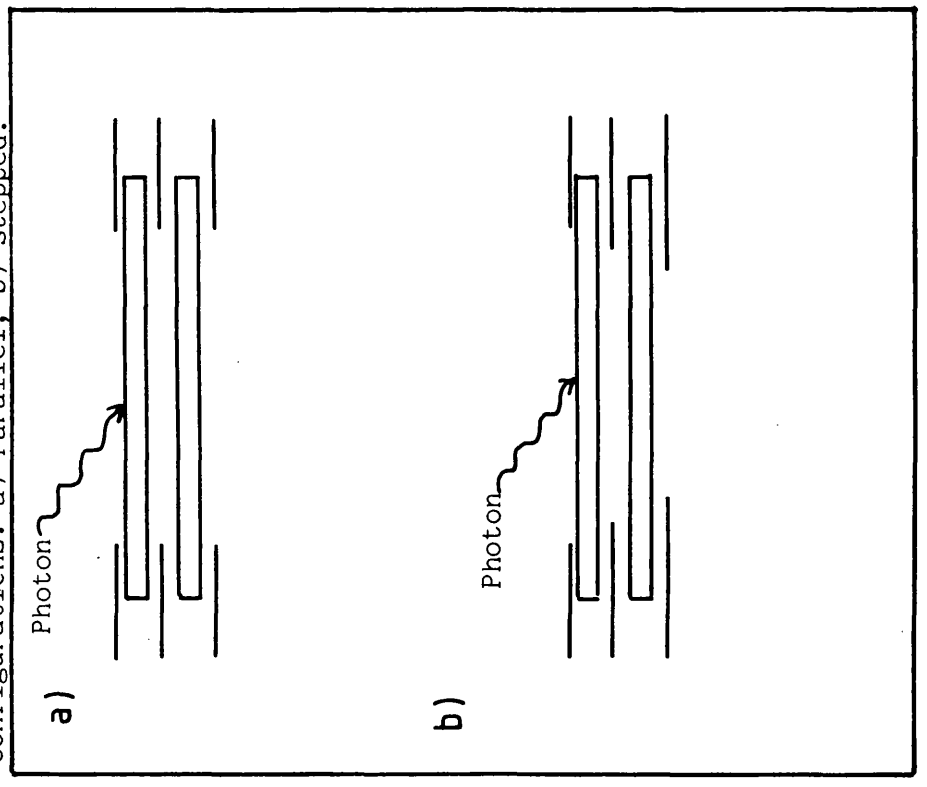

Figure 3.13 WFSXC detector electrode configuraticns. a) Parallel, b) stepped.

Following initial calibration the front MCP was coated with an MgF_2 photocathode to enhance the quantum efficiency (further details of coating techniques will be discussed in the next chapter). The effiency was recalibrated using carbon Kα, boron Kα (67.6Å) and beryllium Kα (114Å) wavelengths before transportation to the USA for integration into the rocket payload.

Having benefited from the experience obtained with detector 1 no similar noise problems were experienced with detector 2. Unfortunately during initial calibration a power failure caused the vacuum system to backfill with oil from the diffusion pump contaminating the MCPs. The MCPs were cleaned as described earlier, to try to remove the oil from the channels. In order to avoid a recurrence of the contamination problem, the vacuum system baffle valve was automated to close in the event of a power failure. As with detector 1, detector 2 was calibrated before and after coating with an MgF_2 photocathode. Two other X-ray wavelengths were included in this calibration, Cu Lα (13.34Å) and Al Kα (8.34Å). After calibration the detector was stored in dry nitrogen and transported to MIT as a flight spare in case of failure of detector 1 during integration.

Two further developments were incorporated into detector 3. A CsI photocathode was used in order to further improve the quantum efficiency of the detector. As CsI is a hygroscopic material the MCPs were baked out before use to expel water vapour. This also had the advantage of bringing the detector quickly onto the stable gain plateau described in section 3.2. The use of CsI required that all detector assembly and storage should be in a dry N_2 atmosphere,

whereas previously the detectors were only stored in dry N_2 and the vacuum system backfilled with it. Secondly, an interplate potential was used, applied by a 170μm thick double sided interplate electrode. This technique was expected to reduce the width of the pulse height distribution below that achieved with the earlier detectors (Wiza et al, 1977).

Detector 3 was calibrated before and after deposition of the photocathode at 8.34Å, 44.7Å and 67.6Å. The CsI quantum efficiency was monitored at regular intervals to ensure that no degradation had occurred. Before transport to MIT the detector was also calibrated with Fe^{55} X-rays (5.9 and 6.5keV) so that the gain and efficiency could be monitored in the payload, when the detector could only be illuminated through a beryllium window.

All three detectors were mechanically qualified before shipment to the USA for integration. Each was vibrated with a sine wave acceleration, through a range of frequencies from 20-2500Hz three times, with amplitudes of 1, 3 and 10g. The detectors were given a final calibration after vibration and no problems were observed.

3.6 The Measured Gain Performance of the WFSXC Detectors

3.6.1 Detector 1

Pulse height distributions were obtained using CKα X-rays at an angle of incidence of ~15°. The detector was illuminated by a beam covering the whole field of view with a shadow mask of Cu/Be alloy producing an image on the detector ~$50mm^2$ in area (figure 3.15). This method of collimation gives a range of angles of incidence ~10-20°.

Figure 3.15 Detector image recorded by a storage oscilloscope of the EUV shadow mask used for gain calibration of detector 1.

Figures 3.16a and 3.16b show G_C (pC) and dG_C/G_C (%) as functions of the front plate potential, V_F (V_R=1.8kV, V_B=50V), before the MCPs were washed (open circles). The maximum gain achieved is only ~3pC and dG_C/G_C ~200%, at V_F=1.8kV. Compared with these results are measurements made after the MCPs were washed (filled circles). A marked increase in gain is seen (9pC at V_F=1.8kV) but dG_C/G_C is still ~200%. Increasing the front MCP voltage further reduces the value of dG_C/G_C dramatically to less than 100% at V_F=2.0kV, with the gain increased to 29pC. 2.0kV is the maximum useful potential that can be applied to the front MCP. Above this level ion feedback effects appear and the detector noise becomes too high (> 1 count $s^{-1}cm^{-2}$).

G_C and dG_C/G_C were also measured as functions of the rear MCP potential (figure 3.17; V_F=2.0kV, V_B=100V)). There appears to be a linear relationship between G_C and V_R, varying between 10pC (V_R=1.6kV) and 37pC (V_R=1.8kV). However, dG_C/G_C remains relatively constant.

The variation of G_C as a function of V_B is shown in figure 3.18 (V_F=2.0kV, V_R=1.6kV). An increase ~50% is seen between 50V and 100V from 7pC to 10pC. The gain then remains constant up to V_B=250V, when it begins to increase further. The width of the pulse height distribution does not appear to change as V_B is altered.

The resistive anode material comprises a mixture of glass and resistive ink. After deposition the anode is fired and the glass migrates toward the surface of the anode. It is therefore conceivable that there may be a thin surface layer of glass that the electrons must penetrate. The change in gain at V_B=100V can then be explained by an increase in the fraction of electrons with sufficient energy to

Figure 3.16a Peak gain G_C as a function of V_F.
V_R=1.8kV, V_G=0, V_B=50V, λ=44.7Å, angle of incidence=15°

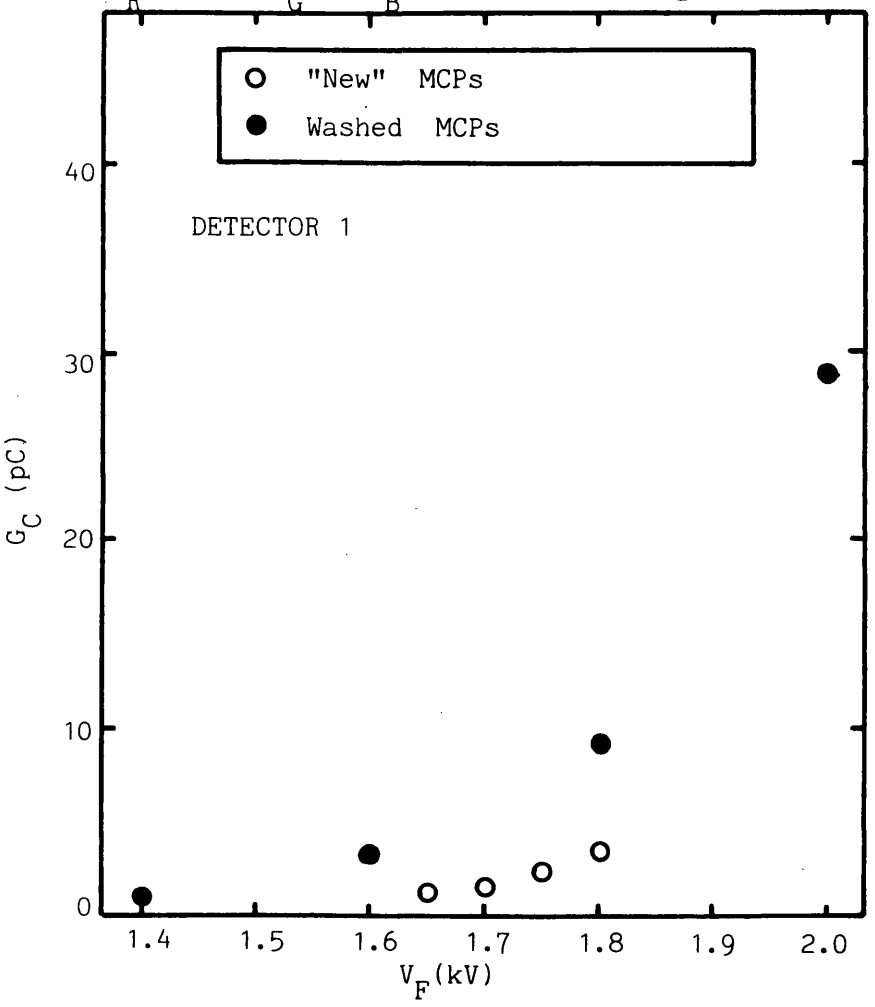

Figure 3.16b FWHM of the PHD (dG_C/G_C) as a function of V_F. All parameters as figure 3.16a.

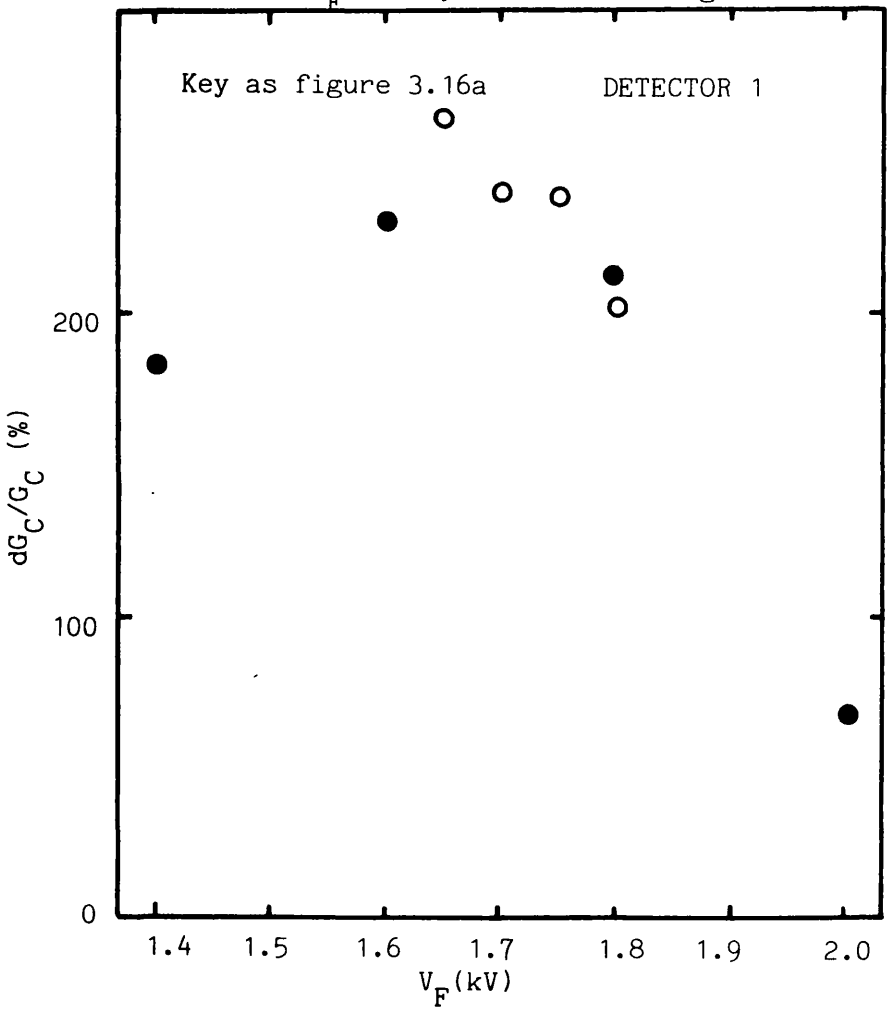

Figure 3.17 G_C and dG_C/G_C as functions of V_R. V_F=2.0kV, V_G=0, V_B=100V, λ=44.7Å and the angle of incidence = 15°

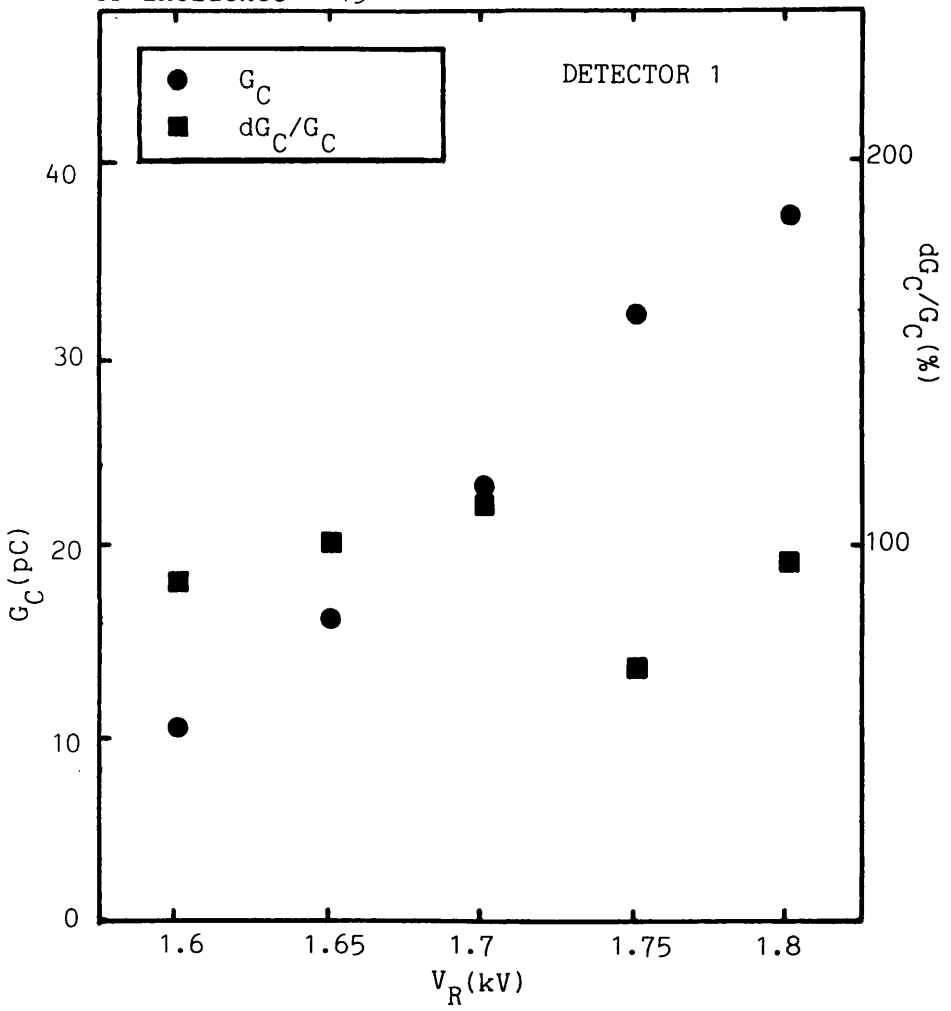

Figure 3.18 G_C and dG_C/G_C as functions of V_B. V_F=2.0kV, V_R=1.6kV, V_G=0, λ=44.7Å and the angle of incidence = 15°.

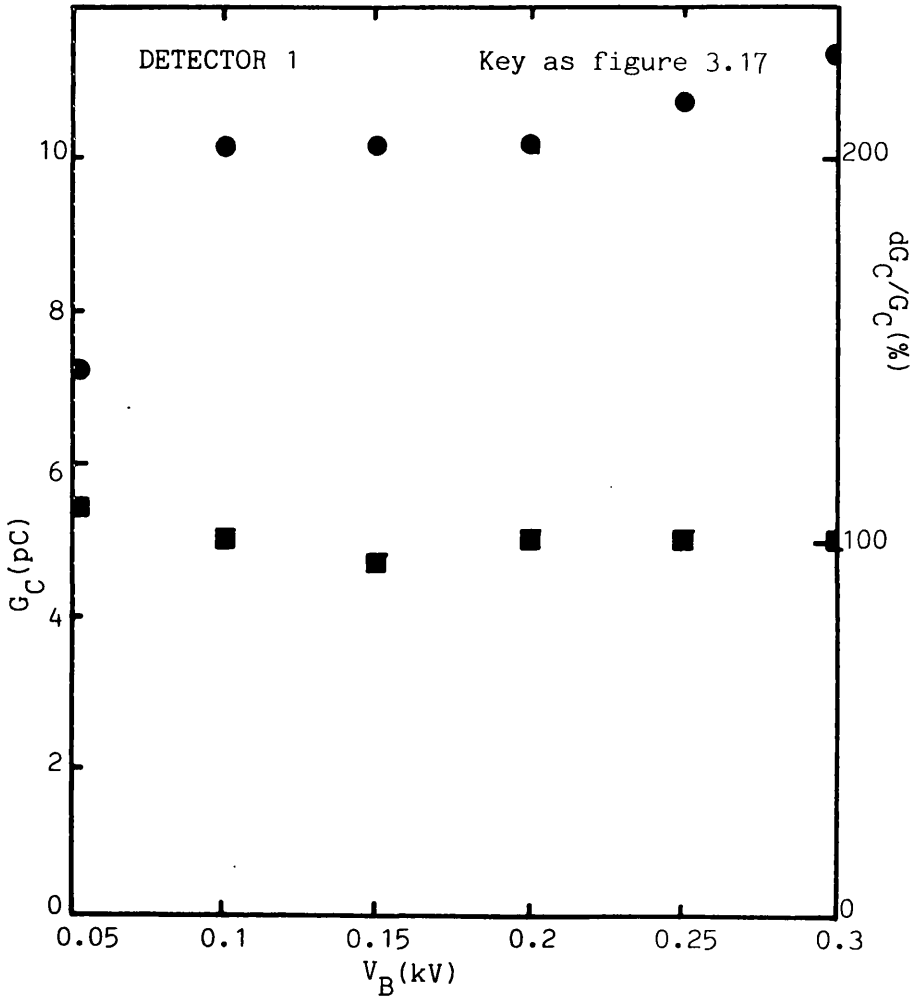

penetrate the surface layer. The second increase in gain may be due to the onset of appreciable secondary electron emission from the anode at higher energies.

All the above calibrations were made at a nominal angle of incidence of 15° with a range of angles of 10-20°, determined by the collimation. Observations of the performance of the chevron pulse height distribution (V_F=2.0kV, V_R=1.6kV and V_B=100V) as a function of angle of incidence were also made and the results verified that the distribution remained constant over the range of angles that apply to the WSFXC telescope (20° to 30°). Figure 3.19a shows the appearance of a typical distribution, at 12°. Below 10° the distribution begins to broaden (figure 3.19b) but the peak remains at the same position. At an angle of 6° the distribution becomes flat at the height of the peak, below the peak charge level (figure 3.19c). As the angle is decreased further the pulse height of the "peak" charge drops below the heights of the lower charge levels (figure 3.19d). At 0° the distribution is quasi-exponential (figure 3.19e).

3.6.2 Detector 2

Detector 2 was calibrated by a more tightly collimated beam than that used to illuminate detector 1, through a carbon coated polypropylene window rather than a shadow mask, with a half angle of ~2°. The illuminated area was ~133mm^2, the total area of the beam at the detector, compared with 50mm^2 for detector 1.

Figure 3.19 The chevron pulse height distribution at a range of angles of incidence. V_F=2.0kV, V_R=1.6kV, V_B=0.1kV.

Figure 3.19a Angle=12°.

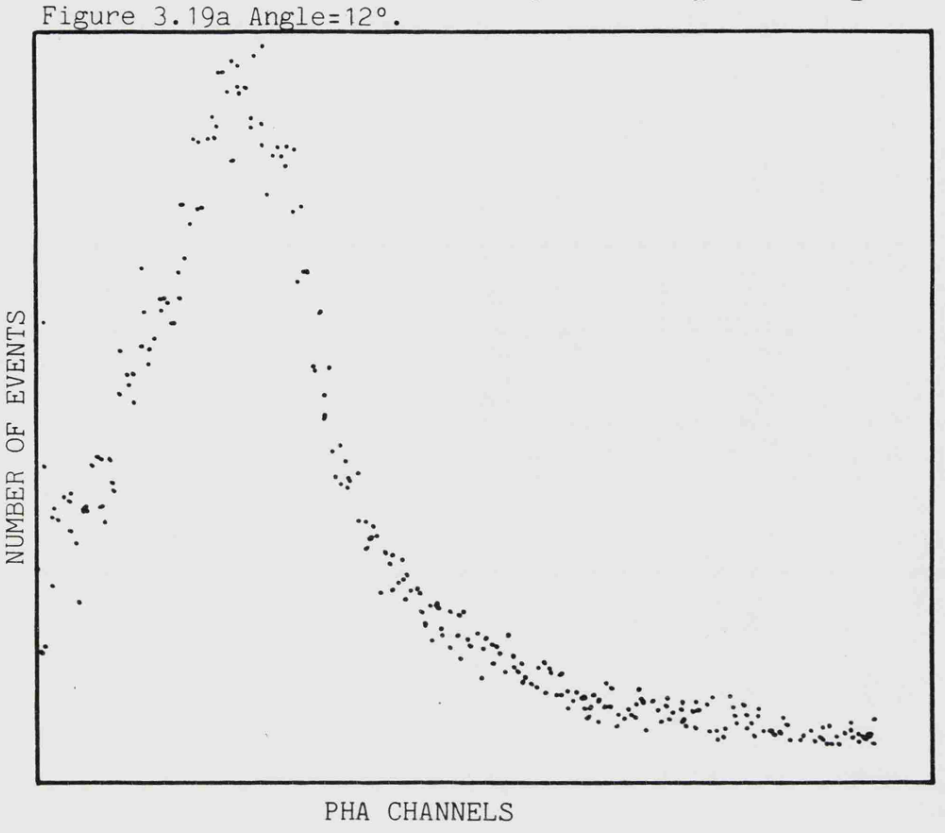

Figure 3.19b Angle=8°

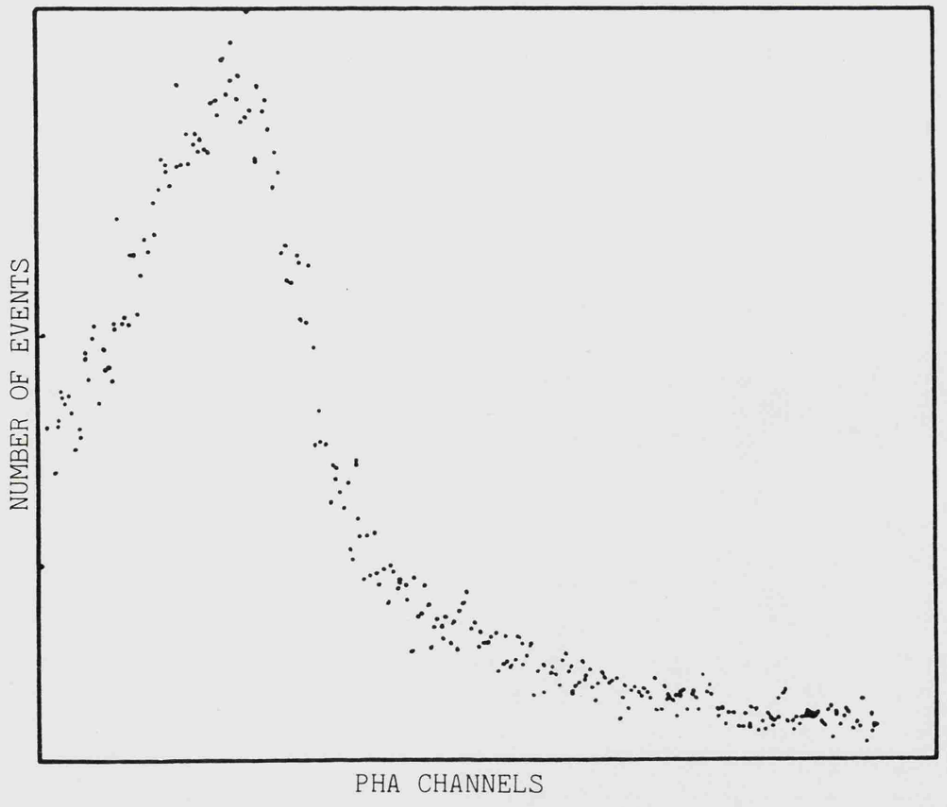

Figure 3.19c Angle=6°

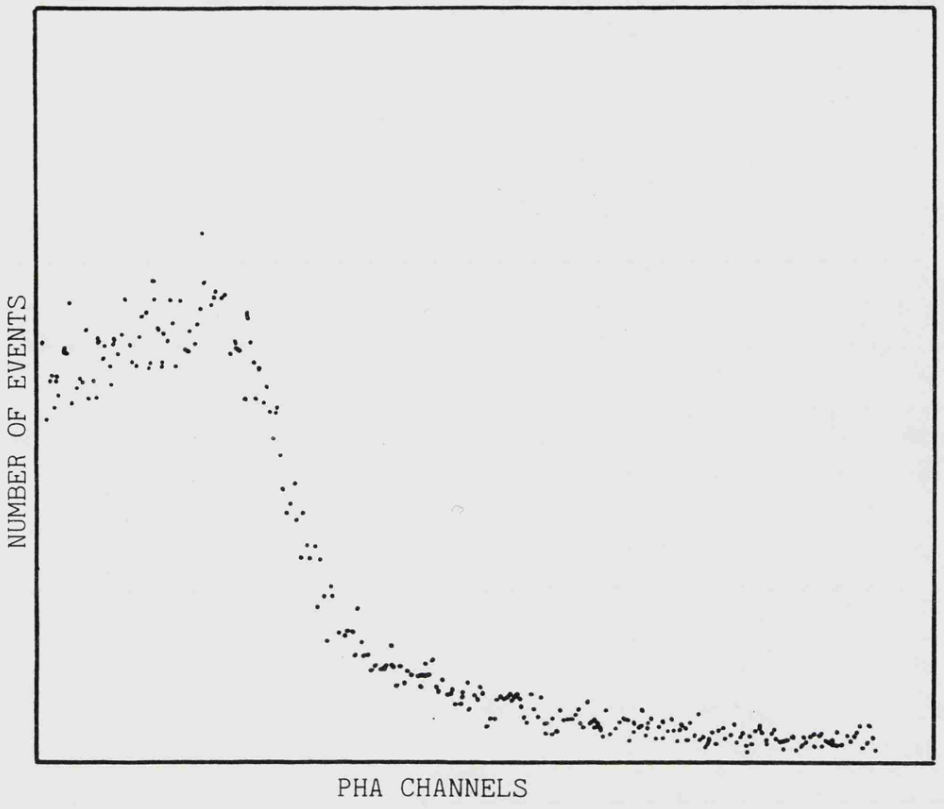

Figure 3.19d Angle=3°

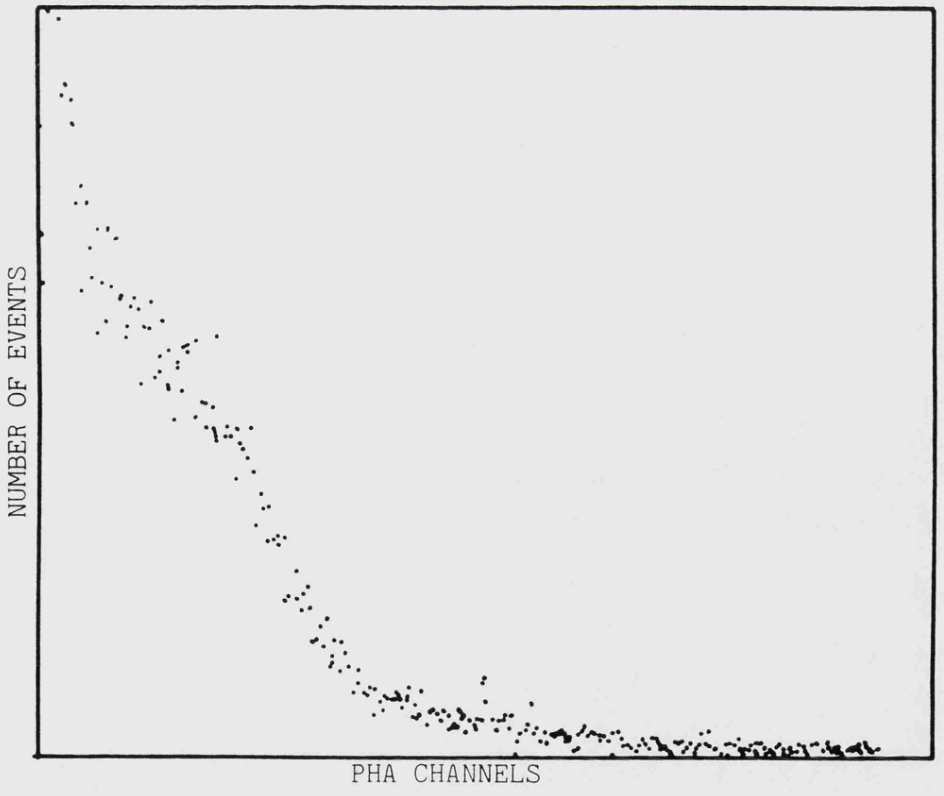

Figure 3.19e Angle=0°

With the new MCPs minimum dG_C/G_C was obtained (at 100%) when V_F=1.8kV (V_R=1.6kV, V_B=100V) (figure 3.20a). After the contamination accident and subsequent wash V_F=1.95kV was required to minimise dG_C/G_C. Additionally, G_C was ~1/2 its original value at the same potentials (figure 3.20b) falling from 1.8pC to 1.0pC at V_F=1.8kV.

3.6.3 Detector 3

When detector 3 was calibrated the X-ray collimation had been improved further, illuminating an area ~20mm^2 at the detector.

As before, G_C and dG_C/G_C were measured as functions of V_F and V_R (figures 3.21 and 3.22). Hard saturation of the detector occurs at a front plate potential of ~2.0kV (V_R=1.6kV, V_G=0 and V_B=100V), as seen in the other detectors, with a peak gain of 5.6pC and a minimum width of 100%. The rear MCP acts as a linear amplifier up to V_R=2.1kV when the gain curve flattens reaching a maximum of 38pC (V_F=2.0kV, V_G=0 and V_B=100V). It is interesting to note that the width has a minimum at 1.8kV of 60% and increases to ~90% at 2.2kV.

The potential across the interplate gap (V_G) was varied between +100V and -100V relative to the front plate. In both cases, as V_G was increased the gain of the chevron decreased (figure 3.23a). At V_G=+100V (electron accelerating) the gain is 6.8pC, < half its value at 0V. At V_G=-100V (electron retarding) the gain was ~0.07 of the value at V_G=0. An improvement in dG_C/G_C is seen with an accelerating potential, from 80% at V_G=0 to a minimum of 60% at 25V (figure 3.23b). The retarding potential generally gives a worse width but is comparable with that measured with an accelerating potential at >25V.

Figure 3.20a Comparison of dG_C/G_C, as a function of V_F, before and after MCP contamination. V_R=1.6kV, V_B=0.1kV, V_G=0, λ=44.7A, angle of incidence=15°.

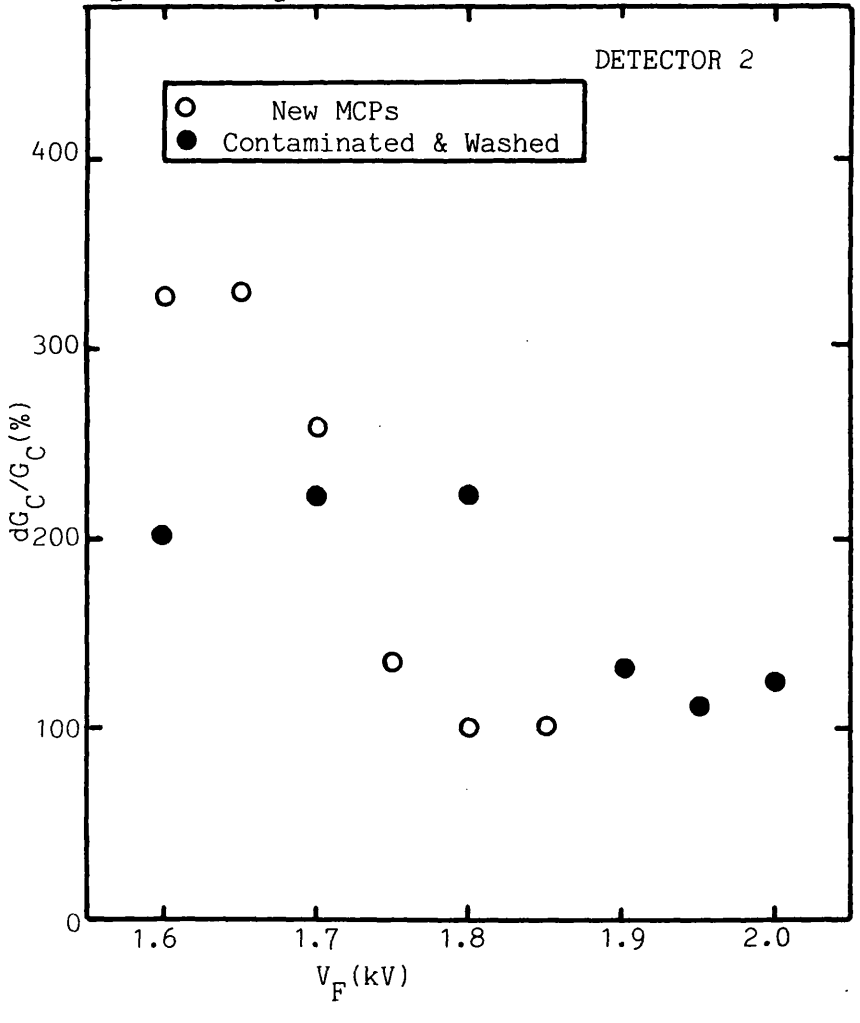

Figure 3.20b Comparison of G_C, as a function of V_F, before and after MCP contamination. V_R=1.6kV, V_B=0.1kV, V_G=0, λ=44.7A, angle of incidence=15°.

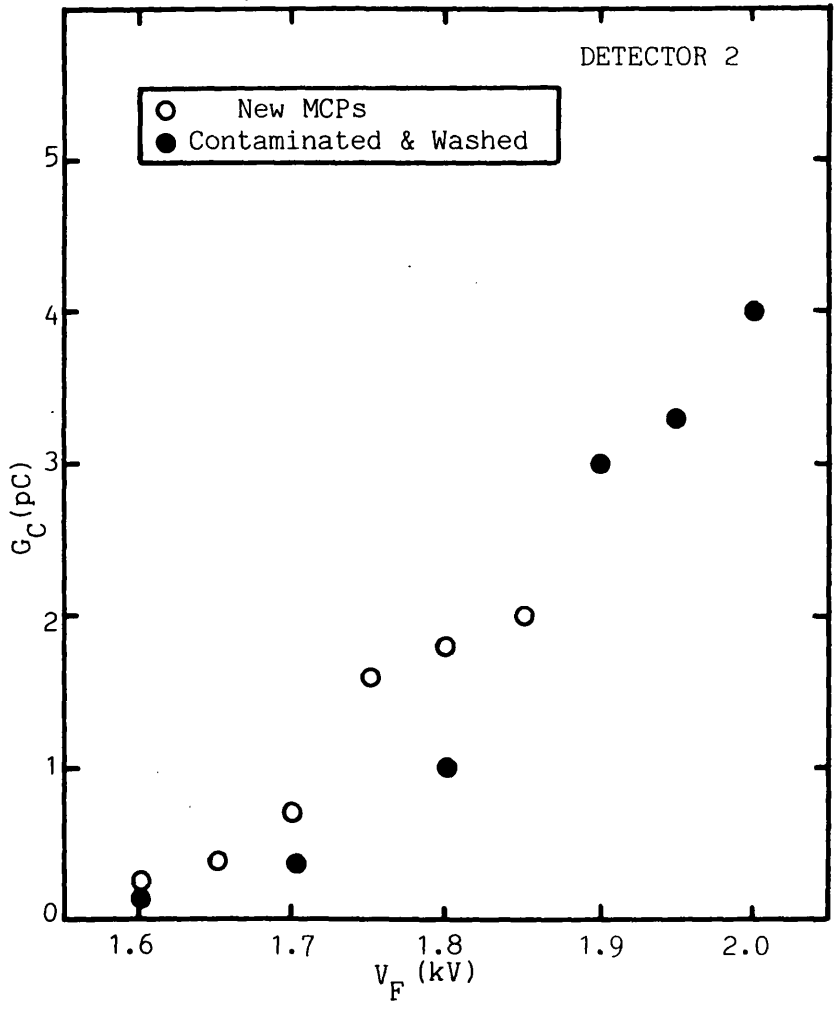

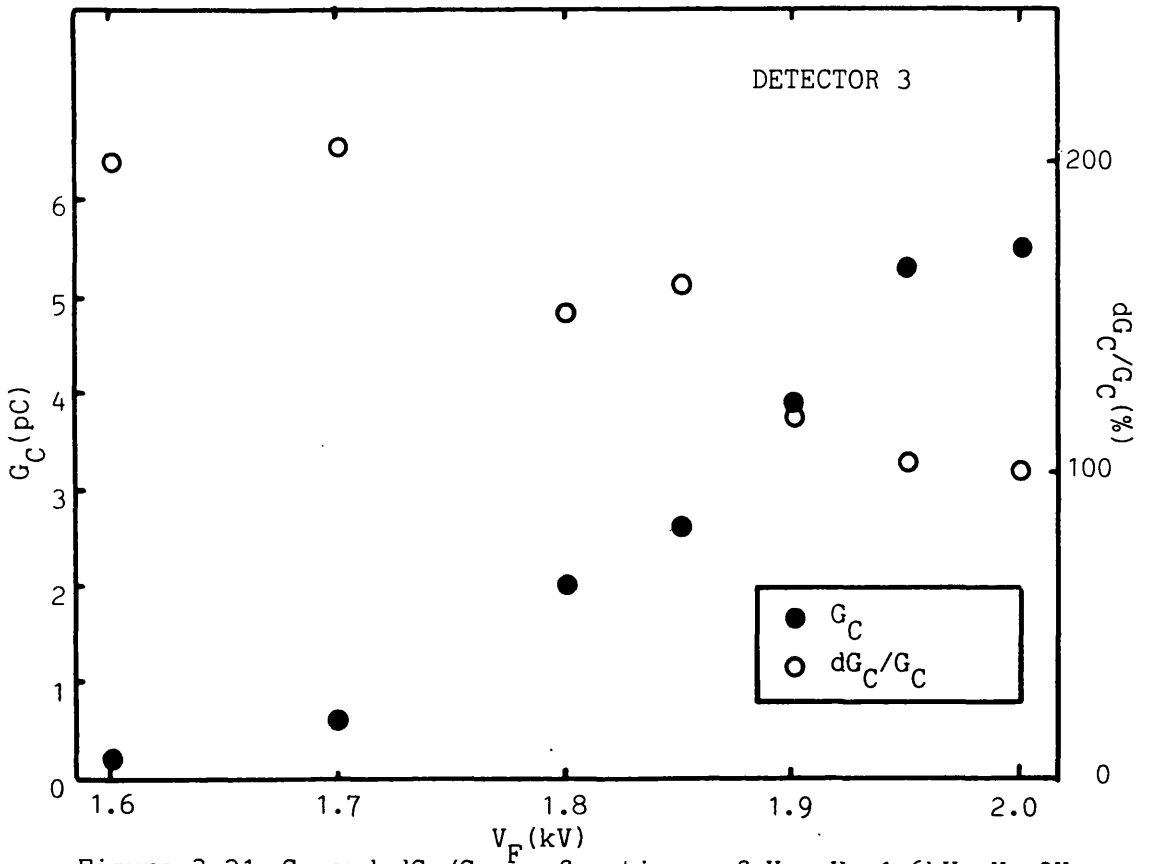

Figure 3.21 G_C and dG_C/G_C as functions of V_F. V_R=1.6kV, V_G=0V, V_B=0.1kV, Angle of incidence=15°, λ=44.7A.

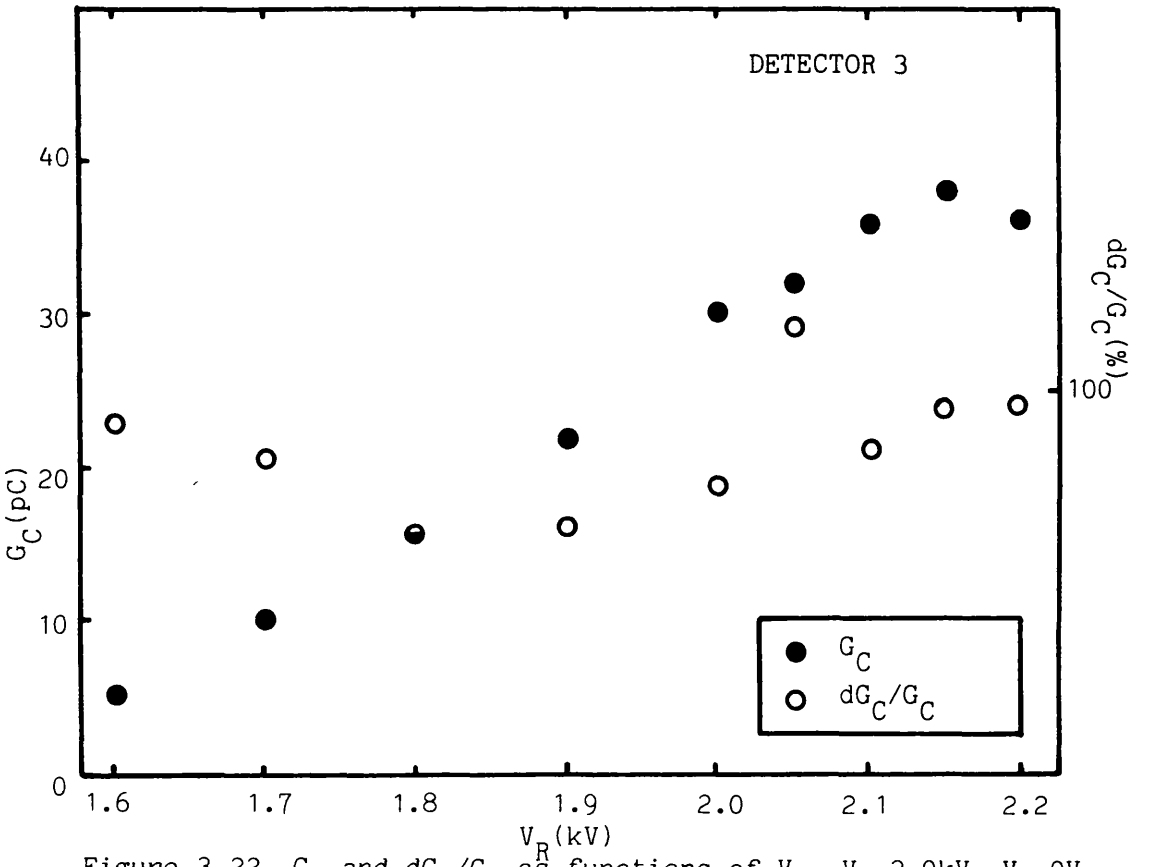

Figure 3.22 G_C and dG_C/G_C as functions of V_R. V_F=2.0kV, V_G=0V, V_B=0.1kV, Angle of incidence=15°, λ=44.7A

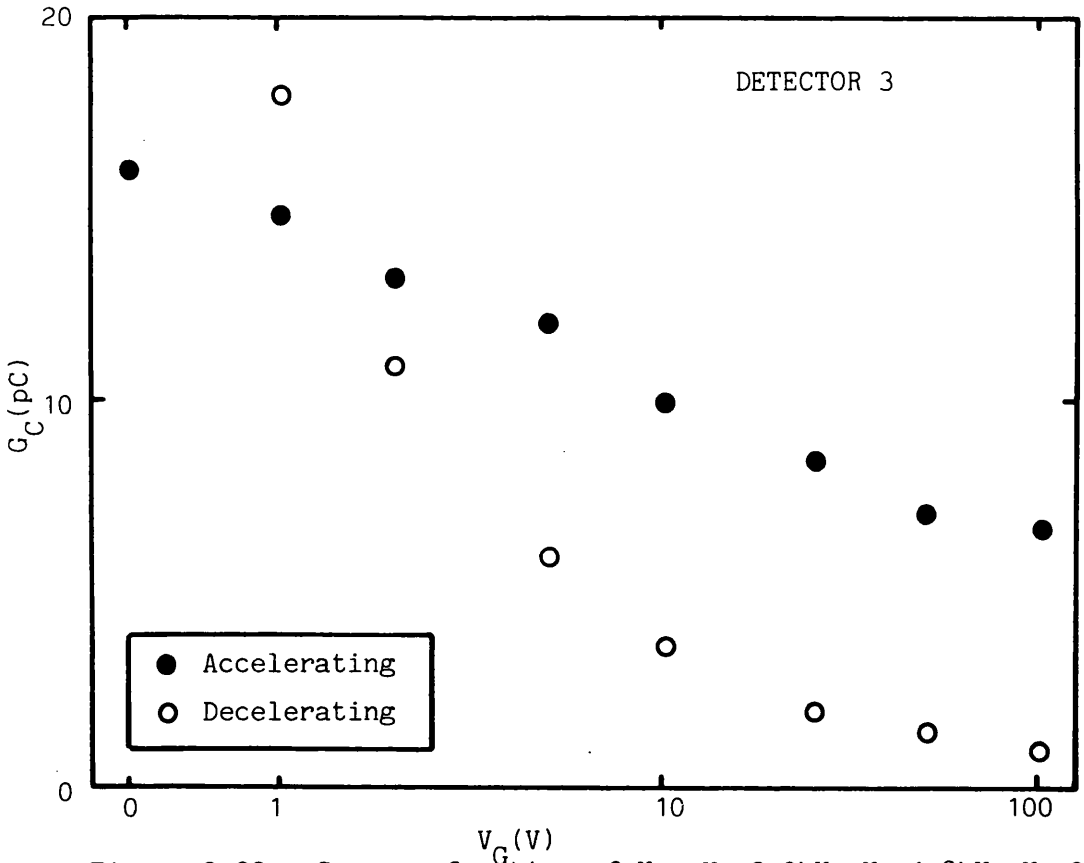

Figure 3.23a G_C as a function of V_G. V_F=2.0kV, V_R=1.8kV, V_B=0.1kV, Angle of incidence=15°, λ=44.7A

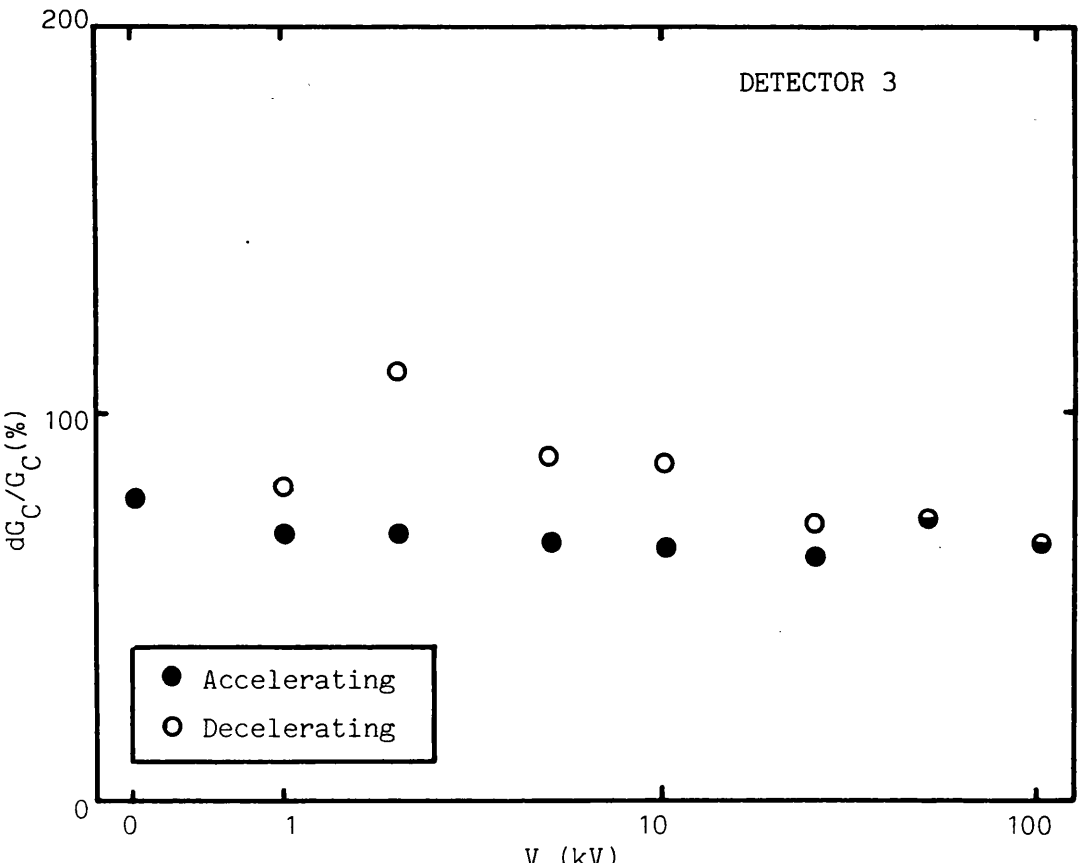

Figure 3.23b dG_C/G_C as a function of V_G. V_F=2.0kV, V_R=1.8kV, V_B=0.1kV, Angle of incidence=15°, λ=44.7A

After the front MCP had been coated with CsI the detector gain increased by more than a factor 2 (figure 3.24), from 5.4pC to 13pC at V_F=1.95kV (V_G=0; V_R=1.6kV), an effect that was not observed when detectors were coated with MgF_2. However, this increase may not have been caused by the CsI as the rear MCP was accidentally exposed to air of normal humidity when in storage, by the failure of a dry N_2 supply, which could have increased the gain of the rear MCP. Hard saturation occurred at the lower potential of V_F~1.9kV, the gain being 6.5pC and the width 72% when V_R=1.6kV and V_G=25V.

The gain however, did not remain stable after this calibration but decreased progressively as the total abtracted charge (pC mm^{-1}) increased (figure 3.25). As the MCPs were baked out before use the detector should have been on the gain plateau observed by Parkes (1974). During calibration of detectors 1 and 2 only a few tens of pC were abstracted which, from figure 3.25, was insufficient to observe any change in gain.

Shortly before the detector was vibration tested and given a final calibration, it was found necessary to replace the interplate electrode because the internal diameter was identical with that of the rear electrode leading to noise at the edge of the field of view. The only available replacement with the correct internal diameter was twice as thick (340μm). As a result the gain was increased by ~50% to 5pC (figure 3.25). A small decrease in dG_C/G_C from 87% to 82% was noted.

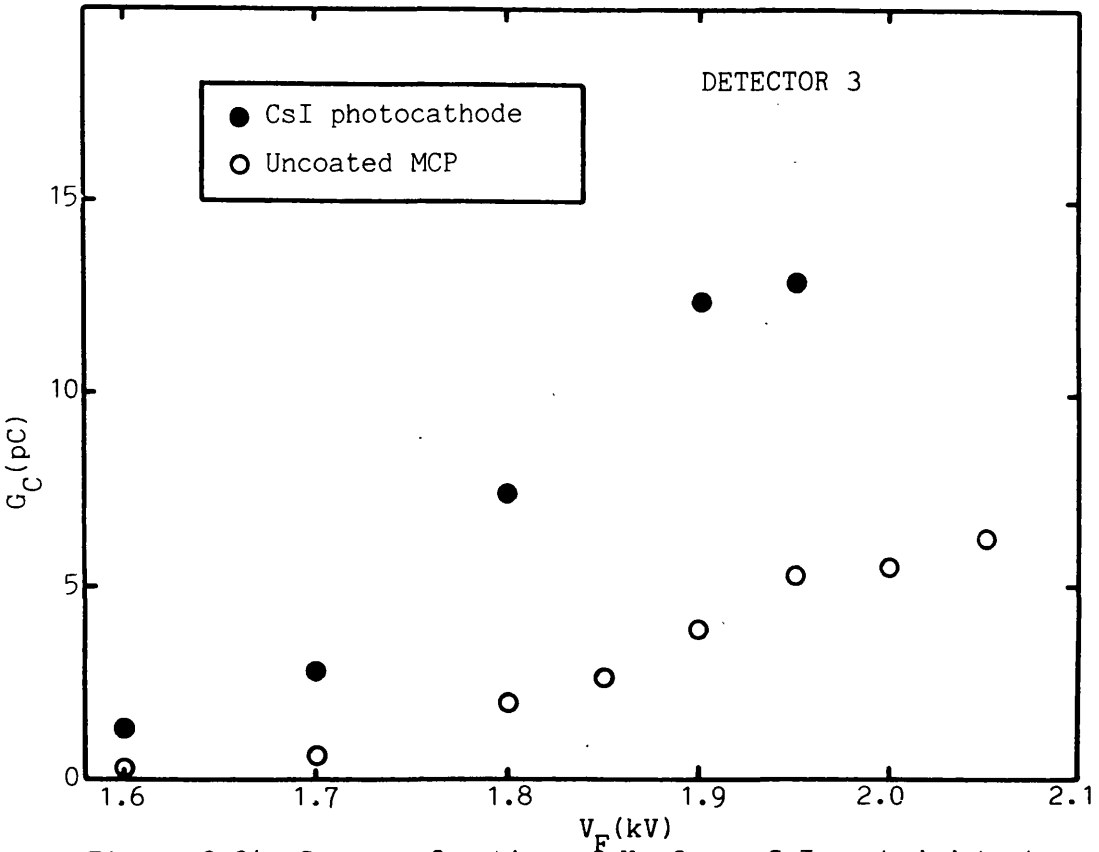

Figure 3.24 G_C as a function of V_F for a CsI coated detector and an uncoated detector. V_R=1.6kV, V_G=0, V_B=0.1kV, l=44.7A, angle of incidence=15°.

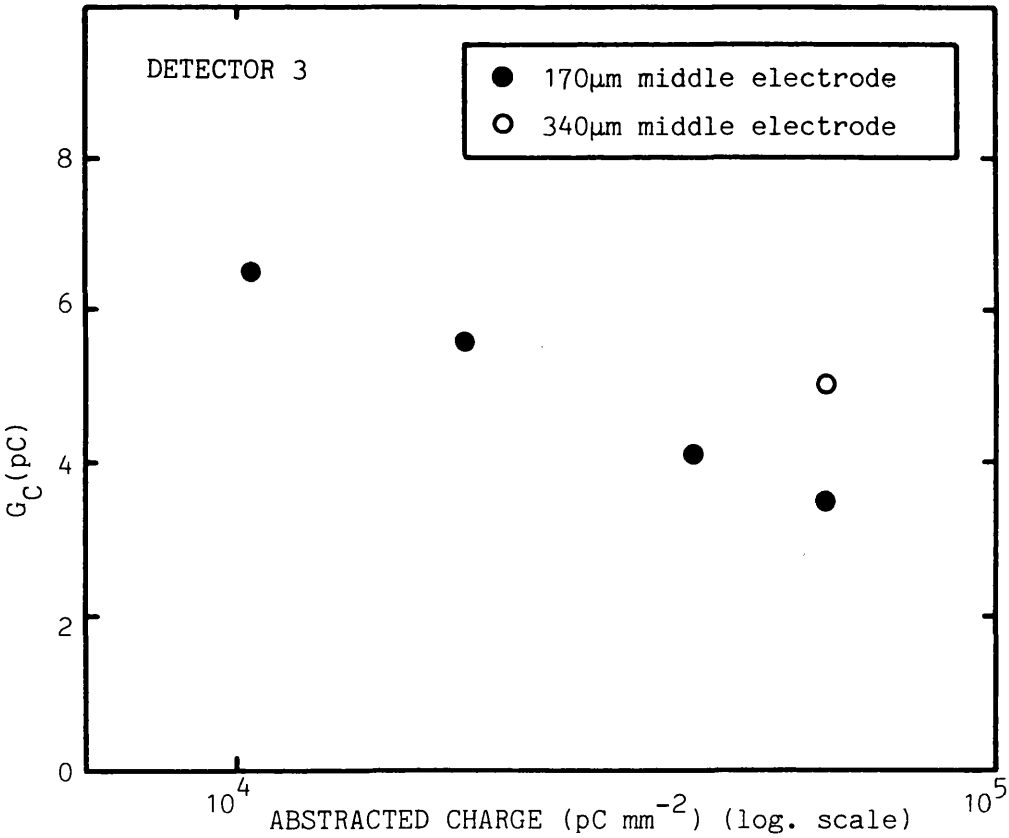

Figure 3.25 G_C as a function of the charge abstracted from the detector. V_F=1.9kV, V_G=25V, V_R=1.6kV, V_B=0.1kV, λ=44.7Å, Angle of incidence=15°.

The gain was also calibrated using an Fe^{55} source, on two occasions during the above tests. The detector was nominally illuminated at 0° angle of incidence but the source collimation had a cone angle of ~10°. A gain of 5pC was measured on the first test (before replacement of the interplate electrode) with dG_C/G_C being 67%. The second measurement was the final calibration before the detector was transported to MIT, yielding a peak gain of 4.3pC and width of 85%.

3.7 Selection of Operating Potentials

The operating potentials selected for the WFSXC detectors were decided by the design requirements already defined.

a) A gain of the order 5-6pC ($3\text{-}4\times10^7$)

b) The narrowest possible pulse height distribution

c) Minimum overall voltage possible

The calibration data show that the narrowest distribution is obtained when the front MCP is run at its highest useful potential, V_F=2.0kV for detectors 1 and 2 and V_F=1.9kV for detector 3. Above these potentials the detectors become excessively noisy (>1 count $cm^{-2}s^{-1}$) and ion feedback occurs. In the case of detector 3 the width can be reduced further by adjusting V_G. dG_C/G_C reaches a minimum plateau at V_G~10V but a value of 25V was chosen to allow for

fluctuations in the voltage from the payload's power supply.

dG_C/G_C is relatively insensitive to V_R. Therefore, once dG_C/G_C has been minimised, the required gain can be set by independently varying V_R. The lowest value that gives a gain of the order that required is 1.6kV for each detector.

V_B was chosen to be 100V for each detector as all the charge is collected from the chevron and the behaviour of the detector is not complicated by secondary emission from the anode.

3.8 Conclusion

Table 3.1 summarises the final pre-integration performances of each WFSXC detector at the potentials determined above. Detector 1 had a peak gain of 10pC and a distribution width of 90%. Although the gain was higher than originally specified the gains of the payload amplifiers could be adjusted to accommodate this.

Detector 2 should have been identical to detector 1. It is clear from table 3.1 that the oil contamination degraded the performance, the gain being reduced to 4pC. The best width that could be achieved was 120%. This detector was not flown and was only kept as a backup for the first rocket flight.

Detector 3 had an improved distribution width (82%), ~10% better than for detector 1, at the expense of lower gain (5pC). However, the gain was not stable but decreased as the total charge abstracted increased (figure 3.25). During a single rocket flight an expected flux of ~500 counts s^{-1} (for a CsI photocathode) will result in an abstracted charge of ~10^3pC mm^{-2} (assuming G_C=5pC) compared to a total

Table 3.1. Final pre-integration performance of the detectors

Detector	V_F (kV)	V_G (kV)	V_R (kV)	V_B (kV)	G_C (pC)	dG_C/G_C (%)	
1	2.0	0.0	1.6	0.1	10.0	90	
2	2.0	0.0	1.6	0.1	4.0	120	
3	1.9	0.025	1.6	0.1	5.0	82	(CKα)
					4.3	85	(Fe^{55})

All detector 1 and 2 data was measured with CKα X-rays.

already abstracted of $\sim 6 \times 10^4$ pC mm^{-2}. Therefore, the gain should not change appreciably during flight.

CHAPTER 4

QUANTUM DETECTION EFFICIENCY OF THE WFSXC DETECTORS

4.1 Introduction

The quantum detection efficiency of the MCP detector is an important factor in determining the sensitivity of the WFSXC. "Bare" MCPs (ie. those where the glass and electrode surfaces prepared by the manufacturers act as photocathodes) have efficiencies of only a few percent (Fraser, 1982), at the angles of incidence that apply to the telescope mirrors (20-30°), in the XUV waveband. It is possible to increase the quantum efficiency by coating an MCP with a photocathode material with a higher photoelectric yield than that of the MCP glass. Selection of a photocathode is constrained by the need to optimise the MCP efficiency in the WFSXC waveband, its ease of deposition, stability at typical operating pressures ($\sim 10^{-5}$ Torr) and an ability to survive, photoelectrically unaltered, the vacuum breaks that must occur during detector development and payload integration. Additionally the photocathode should be stable under photon and electron bombardment to a degree commensurate with the desired detector lifetime.

In the soft X-ray and EUV bands MgF_2 has been widely used as a photocathode on MCPs (Henry et al, 1977; Eng and Landecker, 1981) and single channel multipliers (Smith and Pounds, 1968; Lapson and Timothy, 1973; Lapson and Timothy, 1976). The photocathode survey of Smith and Pounds observed that the MgF_2 efficiency degraded in air with a long decay time of $\sim$100 days. LiF has also been used in these wavebands (Smith and Pounds, 1968; Lapson and Timothy, 1973) and was

found to rank second in stability to MgF_2 by Smith and Pounds.

CsI is known to have a high photoelectric yield (eg. Saloman et al 1980). However, it is a hygroscopic material and therefore there is a problem of stability. Several authors have obtained improved quantum efficiencies in the far-UV with CsI (eg. Timothy et al, 1979, far-UV; Martin and Bowyer, 1982, EUV and far-UV) but reports on the stability of CsI are conflicting. Carruthers (1981) reports that CsI photocathodes, used on electrographic detectors, lose sensitivity over a period of several weeks or months in a low-humidity air or dry N_2 environment but he notes that the response is stable in continuously pumped devices. Alternatively, Saloman et al (1980) give evidence of long term stability of plane CsI photocathodes when stored under dry N_2 with minimal exposure to air.

A range of other candidate materials exist - the alkali chlorides (NaCl, KCl, CsCl, RbCl), NaF, CaF_2 and KI - of which only CaF_2 has been tested on a single channel multiplier (Smith and Pounds 1968). The photocathode chosen for the first flight was MgF_2 because of its proven stability. By the time of the second flight, enough research had been done on CsI to indicate that a high, stable quantum efficiency would be achieved and therefore this material was used.

4.2 A Model of Soft X-ray MCP Quantum Detection Efficiencies

Fraser (1982, 1983a, 1983b) has made a detailed theoretical investigation of photocathode quantum efficiencies at soft X-ray energies, considering planar photocathode and MCP geometries. The aim of the investigation was to see if the poor quantum efficiency of

MCPs could be improved by choosing suitable materials for use as photocathodes.

The net quantum detection efficiency of an MCP (Q) can be regarded as the sum of two components, Q_C, the open area contribution, and Q_S, the contribution of the front surface. When the MCP front surface is operated at high negative potential, as in the WFSXC, Q_S is negligible. An earthed filter is always present in front of the detector in the WFSXC configuration. Hence, a parallel field between filter and front MCP exists which sweeps photoelectrons emitted on the front surface towards the filter. The X-ray interaction with MCP glass and front surface electrode material is essentially a surface effect for the range of energies considered (0.02-20keV = 620Å-0.6Å). Therefore, only the response of a single channel need be considered in evaluating the open area contribution (Q_C) of the MCP. The open area of an MCP (A_{open}) is given by

$$A_{open} = \frac{2}{3} (r/p)^2 \qquad (4.1)$$

where: r is the channel radius (figure 4.1a)

p is the channel pitch (figure 4.1a)

and is ~63% for the WFSXC MCPs (r=25μm and p=30μm). The grazing angle of the X-rays on the channel wall (α) is a function of the photon angle of incidence (θ_i, figure 4.1b) and the polar angle in the cylindrical channel (ψ, figure 4.1a).

Figure 4.1a Plan view of a cell of a hexagonally-packed microchannel plate. Channel radius r, channel pitch p, minimum septal thickness s_{min} (from Fraser, 1982).

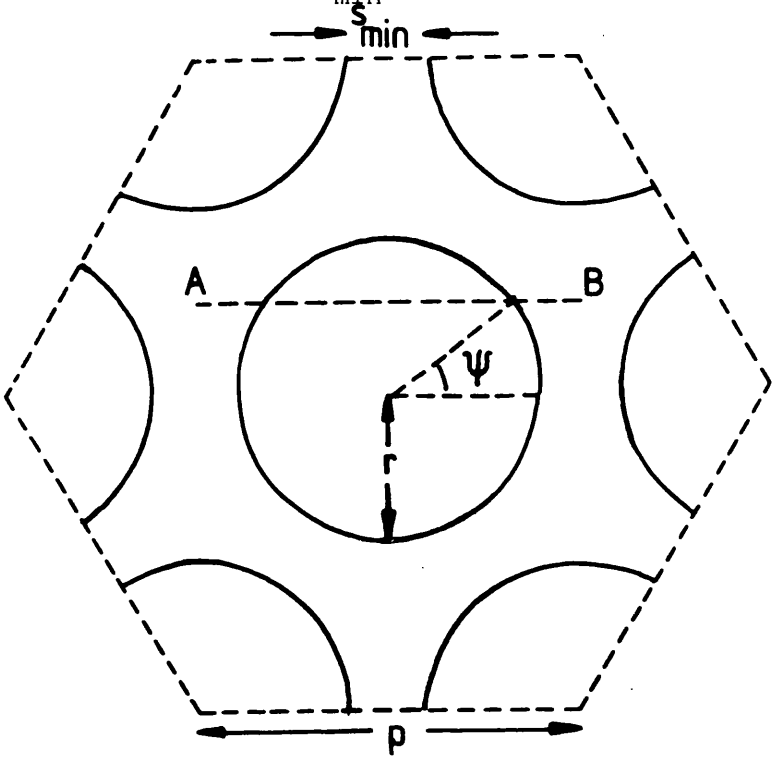

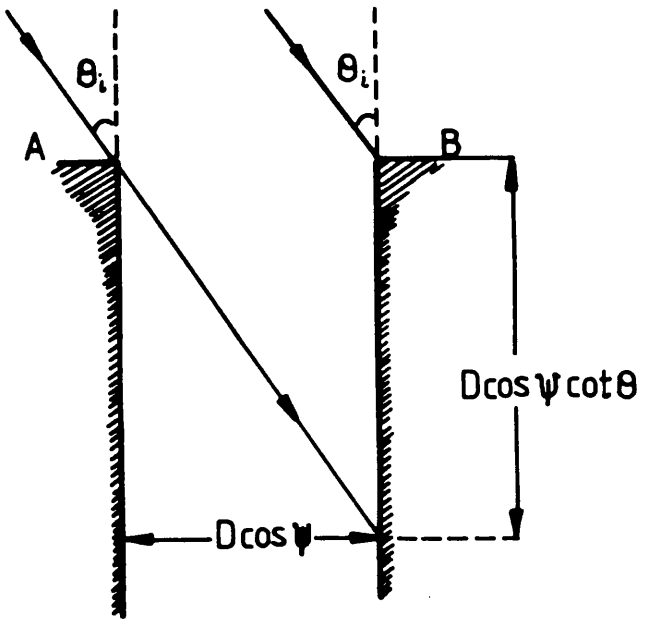

Figure 4.1b Vertical section through a channel along the line AB, at polar angle ψ . X-rays incident at an angle θ_i illuminate the channel to a depth $D.\cos\psi.\cot\theta_i$. This figure illustrates an MCP with a bias angle of 0°. (from Fraser, 1982).

$$\mathrm{Sin}\alpha = \mathrm{Cos}\Psi.\mathrm{Sin}\theta_i \qquad (4.2)$$

The quantum detection efficiency depends upon the probability that one or more electrons enter the evacuated channel when an X-ray is absorbed in the channel wall. A number of photoelectrons result from X-ray absorption and may be accompanied by the release of one or more Auger electrons. The probability that a primary electron escapes into the vacuum depends upon the depth at which the X-ray is absorbed (Z), determined by the X-ray grazing angle (equation 4.2) and the absorption cross-section of the glass, and the electron range which can be estimated from a suitable electron energy-range formula (such as Tabata et al, 1972 or Burke, 1977).

The energy of the photo/Auger electrons that do not escape is given up to the creation of low energy secondary electrons in the bulk of the material. The secondary electron characteristics can be described by three parameters - ϵ is the energy required to excite one internal secondary electron and can be regarded as a material constant that is independent of the X-ray energy, $P_S(0)$ is the probability that an electron escapes from the channel surface and L_S is the secondary electron escape length. The secondary electron escape probability from a depth Z below the photocathode surface ($P_S(Z)$) is

$$P_S(Z) = P_S(0).\exp(-Z/L_S) \qquad (4.3)$$

$P_S(0)$ and L_S can be determined from measured secondary electron yields

for plane samples of MCP glass or deposition photocathodes.

The total quantum yield (Q_T, counts photon^{-1}) is a combination of the yield from the primary electrons (Q_P) and secondary electrons (Q_S)

$$Q_T = Q_P+Q_S-Q_P.Q_S \qquad (4.4)$$

Finally, the probability of this electron "batch" yielding a valid output pulse will have a complicated dependence on the energy of the initiating electrons, the secondary electron yield of the glass and experimental factors such as the MCP gain and pulse height discriminator settings.

The basic principles discussed above can equally well be applied to deposition photocathode materials or MCP glass. Fraser (1983a, 1983b) describes in detail a semi-empirical model that may be used to predict absolute photoelectric yields in the wavelength range $1<\lambda<300$Å. Combining the predicted yields with an analysis of MCP channel geometry (equation 4.2) the quantum detection efficiency of coated and uncoated MCPs can be predicted. Manufacturers use a nichrome ($\sim Ni_7Cr_2Fe_3$) electrode coating of density 8.4gm cm^{-3} and a front surface thickness ~300Å, commonly extending one channel diameter into the channels at each face of the MCP. At large angles of incidence the photoelectric yield of the electrode material must be considered in order to determine the quantum efficiency, by computing a composite electrode/channel glass response. Similarly a composite photocathode/channel glass response must be computed for coated MCPs.

Figure 4.2 presents a comparison of photocathode materials between λ=1-10Å using the secondary electron photocurrent (electrons photon^{-1}) as a criterion. This comparison translates into the XUV although the exact order of materials depends on the disposition of the absorption edges in this band. It can be seen, with hindsight, that MgF_2 (used for the first flight) is in fact the worst choice of material. CsI would appear to be the best choice of photocathode and this was the basis on which it was proposed for the second flight.

4.3 The Development of Photocathodes for the WSFXC

4.3.1 Vacuum Deposition Techniques

The WFSXC photocathodes were deposited using standard vacuum evaporation techniques with an NGN 12S-2 system, which had a domed bell jar of height 530mm and diameter 290mm. After the evaporation rig had been pumped down to operational pressure ($\sim 10^{-5}$Torr) the system was allowed up to corona pressure with dry N_2 ($\sim 10^{-2}$ to 5×10^{-4}Torr depending on voltages and the electrode configuration) by a small leak. A high tension voltage ($\sim$100V) applied to the gas produced a glow discharge to "scrub" the substrate with electrons and ions. The photocathode material was then heated in a molybdenum boat by passing a current of ~50-100A through the boat at a pressure low enough ($<2 \times 10^{-5}$Torr) to allow the material to evaporate as soon as it melted. The MCP substrate was held in a position above the source of material at as large a distance as possible so that the flux of material approximated a parallel beam. Clearly, from the size of the open MCP area (42mm) compared to the height of the vessel, the

approximation was poor, the half angle spread being ~2°. A calibrated Edwards quartz crystal monitor, mounted in the same plane as the MCP directly above the source, was used to determine the coating thickness on the MCP's front surface, by monitoring the change in the oscillator frequency caused by the deposition of material onto the crystal. If the source of material were directly below the MCP, material would pass straight down the channels and would only form a very thin layer on the channel wall. The photocathode source was therefore offset from the MCP (figure 4.3), to increase the channel wall thickness for a given front surface thickness. In order to obtain an even coating around the whole circumference of a channel, the MCP was rotated slowly during deposition.

4.3.2 Stability of Thick MgF_2 Coatings

The photocathode must be mechanically stable. An unstable layer may break up under vibration and cause particles of photocathode to lodge in the MCP channels which would then act as sources of noise. Ultimately the stability can only be tested by coating an MCP. However, such experiments are time consuming and, at a cost of several thousand pounds per plate, are expensive.

An attempt was made to test the stability of various thicknesses of MgF_2 by coating a series of glass blanks, of the same dimensions as the detector MCPs, with thicknesses between 4,000Å and 20,000Å. All the glass blanks were initially cleaned with alcohol to remove grease and then glow discharge cleaned before coating at room temperature. The coatings were compared qualitatively in terms of their visual

Figure 4.2 The ranking of insulating photocathodes at 1.94, 5.4 and 8.3A X-ray wavelengths in terms of the secondary photocurrents $(\chi_c)_s$ at grazing angle=20°. The vertical line is the Mg K absorption edge. (from Fraser, 1983b)

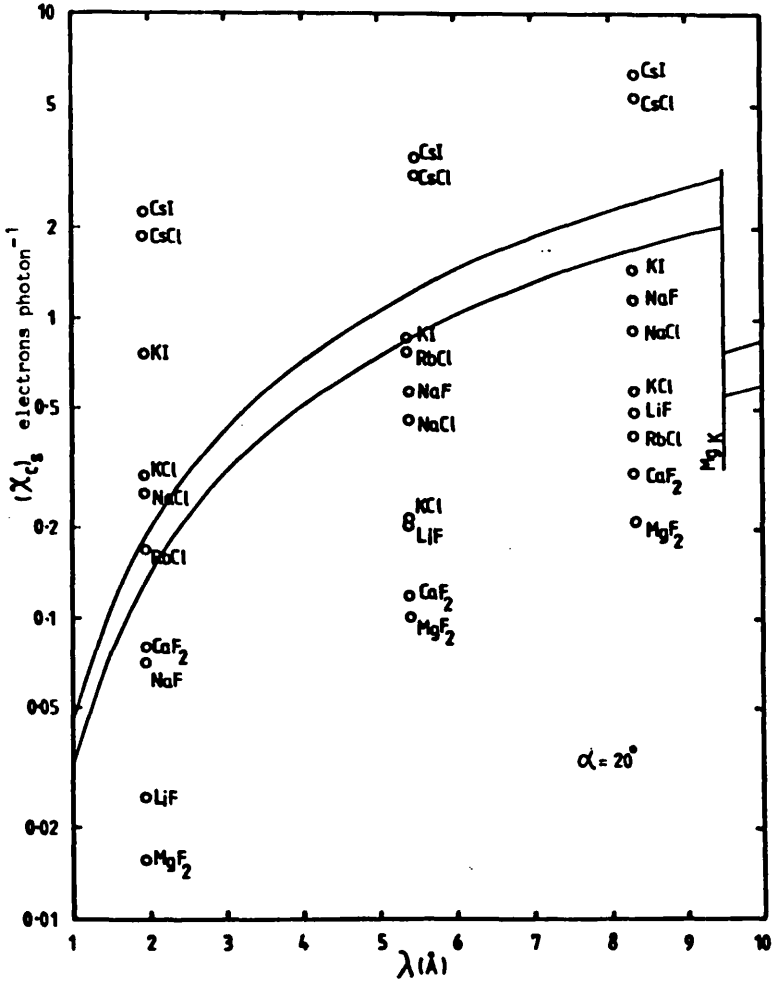

Figure 4.3 Diagram of photocathode evaporation geometry.

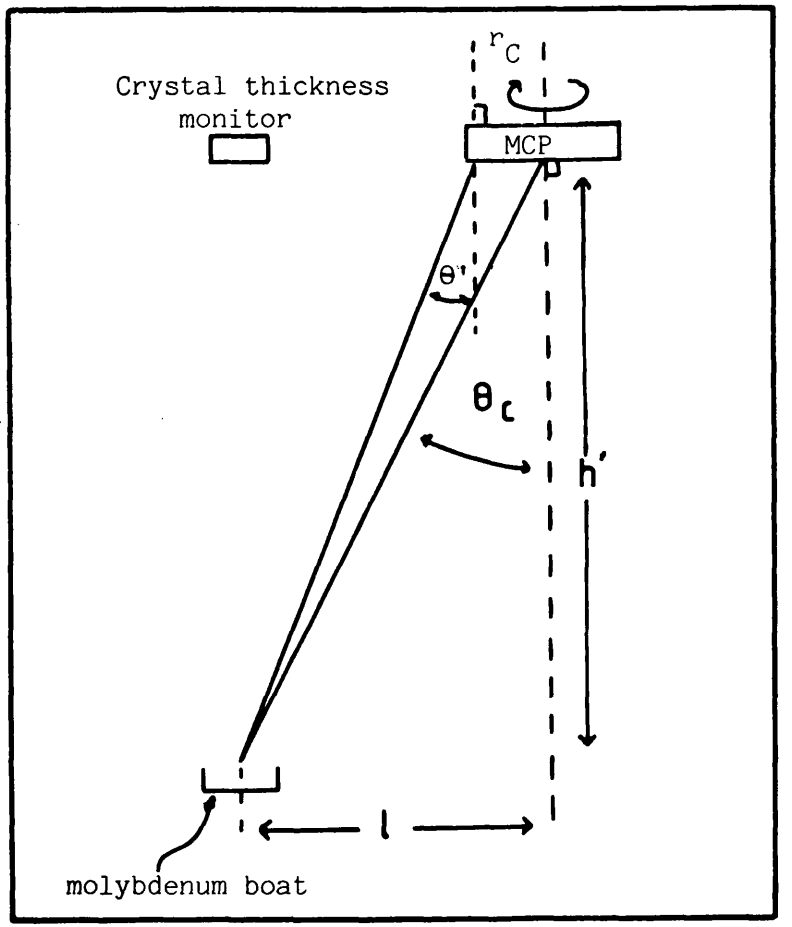

appearance and stability when rubbed with a finger, with sodium hydroxide and iso-propyl alcohol to see how they adhered to the glass. All coatings were stored in air for periods of several days and were tested again after this time.

A coating of 4,000Å appears uniformly transparent. The coating cannot be removed, even with vigorous rubbing as described above. After storage in air for five days no degradation of the quality of the coating was noted. Thicknesses of 6,000Å and 7,000Å exhibited the same behaviour.

An 8,000Å coating exhibited a slightly powdery, but even, appearance although it proved to be quite stable after attempts to remove the coating and after storage. At 12,000Å the powdery appearance was much more marked and was also patchy. The more powdery areas were easily removed but other parts were quite stable. Similarly a 20,000Å coating, although uniform, was extremely powdery in appearance and easily removed. After the powder was removed a thin uniform coating remained.

All the above observations were repeated for each coating thickness as a test of the reproducability of the coating technique. From these tests, a criterion for an acceptable coating was decided as one that was transparent, without any powdery appearance, as these appear to be mechanically stable. The 6,000Å coating fulfilled the requirements. As the above experiments were carried out on glass blanks the 6,000Å coating was tested on an old MCP. The behaviour was found to be the same. Holland (1956) notes that MgF_2 is friable when the substrate is coated at normal temperatures but not when the

substrate is heated. Thicker coatings might therefore be obtained if the substrate could be heated.

4.3.3 The Photocathode Geometry for the WFSXC

The thickness of material inside a microchannel and its distribution along the channel influence the efficiency of a given photocathode deposit. It is important that the efficiency should be uniform across the MCP and should appear so from any direction of illumination. Uniform efficiency requires a photocathode thickness which is uniform within a channel and is the same for all channels of the MCP. In order to optimise the photocathode deposition so that this condition was met as far as possible, a detailed analysis of the geometry involved in coating an MCP was performed (Appendix A).

In the treatment of Appendix A it is assumed that -

i) Evaporation is from a point source

ii) The molecules travel in straight lines

iii) Deposition occurs with no reflection from the channel walls

iv) The flux of molecules is uniform and constant

v) The MCP rotates at a constant rate

The model considers evaporation onto an MCP, mounted in relation to the source of material and crystal thickness monitor as shown in figure 4.3, where the nominal coating angle is θ_C ($\theta_C = \mathrm{Tan}^{-1} l/h'$). As the MCP is rotated, the coating is the same for any channel at a given radius (r_C) from the MCP centre. A point in a channel is defined by the distance along the channel from the entrance (Y) and the polar angle (γ) relative to the point in the channel closest to the MCP

centre (figure 4.4). ϕ is the angle defining the rotation of the MCP and is a periodic function of time.

The depth of the coating along the channel at a given value of ϕ (Y_C) can be expressed in terms of the geometrical parameters outlined above.

$$Y_C = \frac{D.h'}{x}.\mathrm{Cos}\left[\mathrm{Sin}^{-1}\left(\frac{l.\mathrm{Sin}\phi}{x}\right)-\gamma\right] \qquad (4.5)$$

where: $x^2=r_C^2+l^2-2r_C.l.\mathrm{Cos}\phi$ ($\mathrm{Tan}\theta'=x/h'$)

D is the channel diameter

For each value of γ, Y_C has as maximum value (Y_0) when $(l/x).\mathrm{Sin}\phi=\gamma$. The locus of Y_0 represents the maximum extent of the photocathode along the channel.

The thickness of photocathode at a given point ($T'(Y,\gamma,r_C)$) can be related to that measured by the crystal thickness monitor (T'_0) by a geometric parameter ($G'(Y,\gamma,r_C)$)

$$T'(Y,\gamma,r_C) = T'_0.G' \qquad (4.6)$$

where:

$$G' = \frac{1}{2\pi}\int_{\phi_1}^{\phi_2} \frac{h'^2.x}{(h'^2+x^2)^{3/2}}\,\mathrm{Cos}\left[\mathrm{Sin}^{-1}\left(\frac{l.\mathrm{Sin}\phi}{x}\right)-\gamma\right]d\phi \qquad (4.7)$$

G' must be integrated numerically between the limits ϕ_1 and ϕ_2, which are determined by Y and γ, defining the period when that position on the channel wall is illuminated by the coating source (ie. $Y<Y_C(\phi)$).

Ideally, G' should be constant for any value of γ in any channel (any value of r_C). This occurs if the MCP is sufficiently distant from the source, ie. r_C/l and r_C/h' are both ~ 0, making θ' a constant equal to θ_C. G' then simplifies to the "ideal" parameter ($G_P(Y)$)

$$G_P(0) = \frac{1}{\pi}.\mathrm{Cos}^2\theta_C.\mathrm{Sin}\theta_C \qquad (4.8)$$

When $r_C=0$, $r_C/l=0$ and $r_C/h'=0$, thus the geometry at the centre of the MCP is in fact the ideal geometry.

The maximum X-ray depth along the channel is given by the minimum expected angle of incidence (20°). This represents a maximum interaction depth of 2.75D therefore the maximum penetration depth (Y_0) of the photocathode should never be less than this value at the edge of the MCP. Within the confines of the vacuum coating apparatus θ' varies across the MCP. Therefore, in order to satisfy the above condition for Y_0 θ' must be 20° at the edge of the photocathode farthest from the coating source. If the photocathode extends to a radius r_m from the centre of the MCP then $\mathrm{Tan}20°=(l+r_m)/h'$. The WFSXC detector has an open front diameter of 42mm. In order that the photocathode does not lie under the front electrode, which might prevent the electrode making electrical contact with the nichrome

Figure 4.4 Definition of the geometrical variables involved in the analysis of the coating geometry.

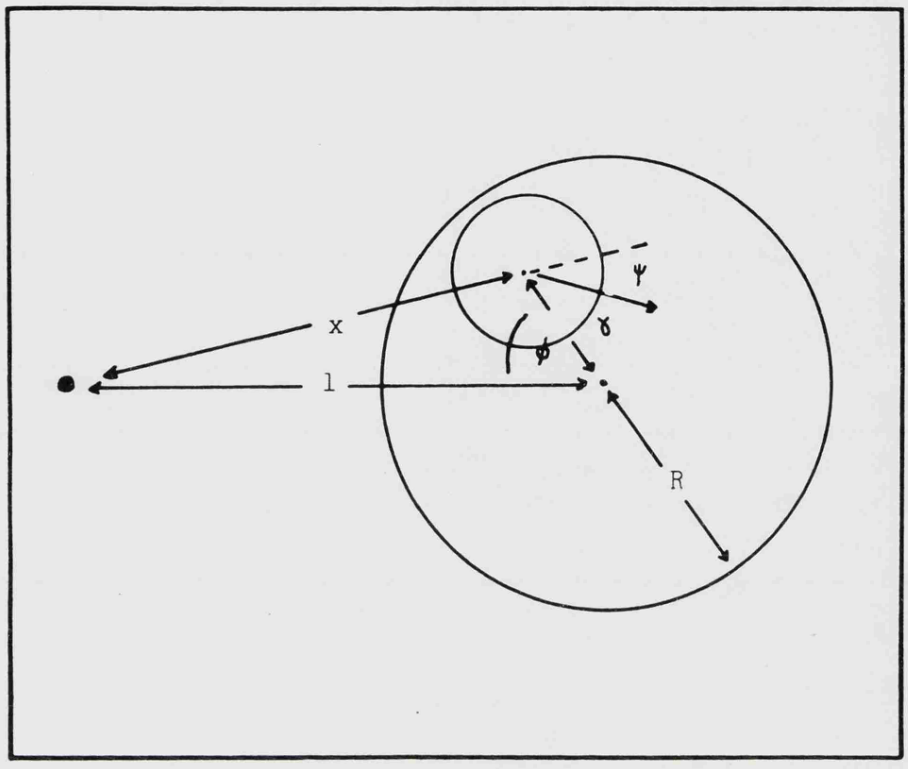

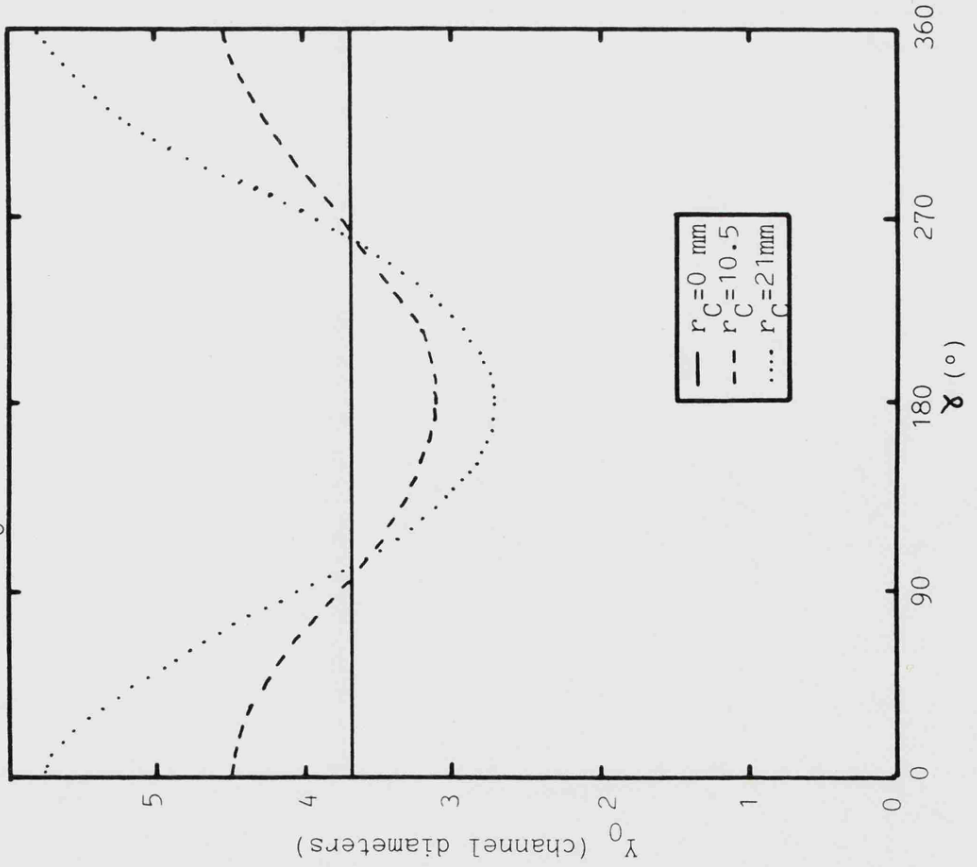

Figure 4.5 Maximum penetration depth of the photocathode (Y_0) as a function of γ.

(MgF_2 and CsI are both insulators), its diameter is 40mm, hence r_m is 20mm. h' is a maximum of 219mm therefore l must be 59mm and h'/l=3.7, a nominal coating angle of 15°. Figure 4.5 shows how Y_0, calculated for h'/l=3.7 varies with γ at different distances from the centre of the MCP, always being greater than 2.75D.

Using G_p (figure 4.6) allows a simplified analysis of X-ray penetration and absorption given the coating material and the telescope angles of incidence. The fraction of X-rays of wavelength λ and grazing angle α absorbed in a photocathode is defined by

$$N_A = 1-\left[\exp -\left(\frac{\mu_1(\lambda)}{\sin\alpha} \cdot T'(Y,\gamma,r_c)\right)\right] \qquad (4.9)$$

where: $\mu_1(\lambda)$ is the linear absorption coefficient of the photocathode material

Figure 4.7 shows the fraction of X-rays absorbed by an MgF_2 photocathode as a function of Y, calculated from G_p and μ_1 (figure 4.8) for the nominal coating thickness of 6,000Å and an X-ray grazing angle of 30°, at λ=50Å and λ=200Å. At λ=200Å it can be seen that 6,000Å absorbs nearly all the X-rays, but at λ=50Å, where μ_1 is lower, only ~50% of the X-rays are absorbed in the photocathode.

In reality G_p cannot be attained in the current coating system. The coating profile thus varies around a channel and across the MCP. Figures 4.9 and 4.10 show G', calculated by numerical integration at various positions across the MCP for γ=0 and γ=180. From these values

Figure 4.6 The perfect geometrical coating parameter G_P as a function of Y (h'/l=3.7).

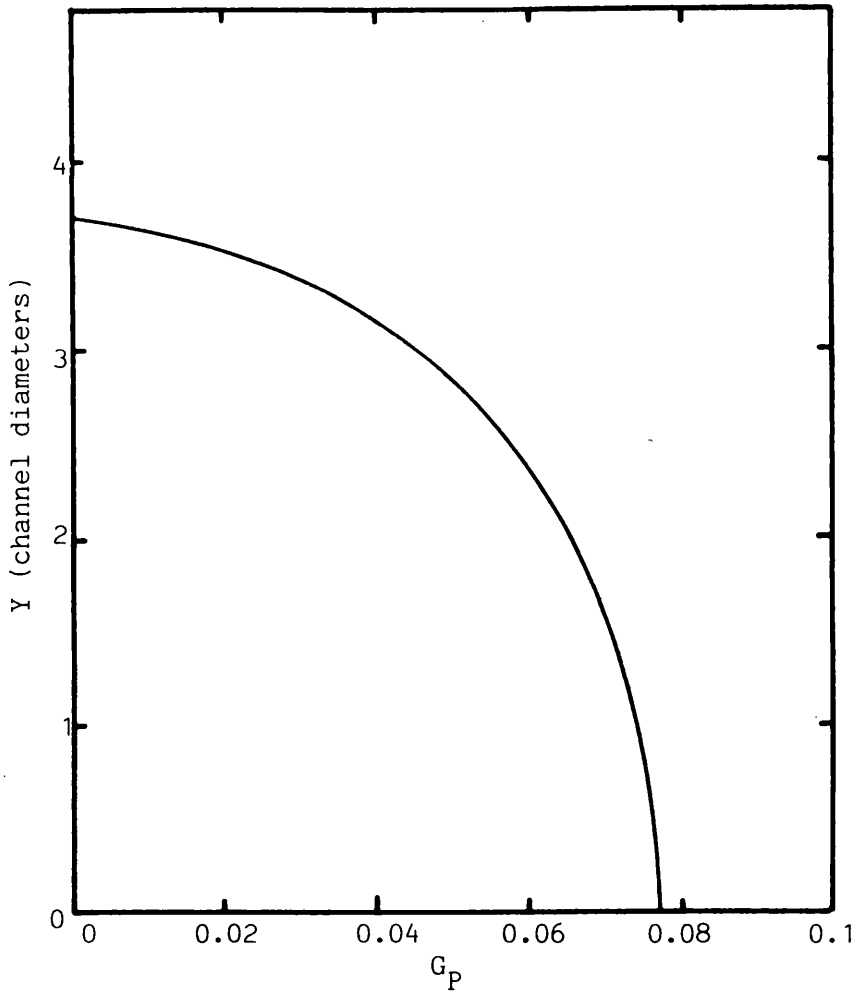

Figure 4.7 Fraction of X-rays absorbed by MgF_2 (N) as a function of Y (T_0'=6000A, α=30°,)

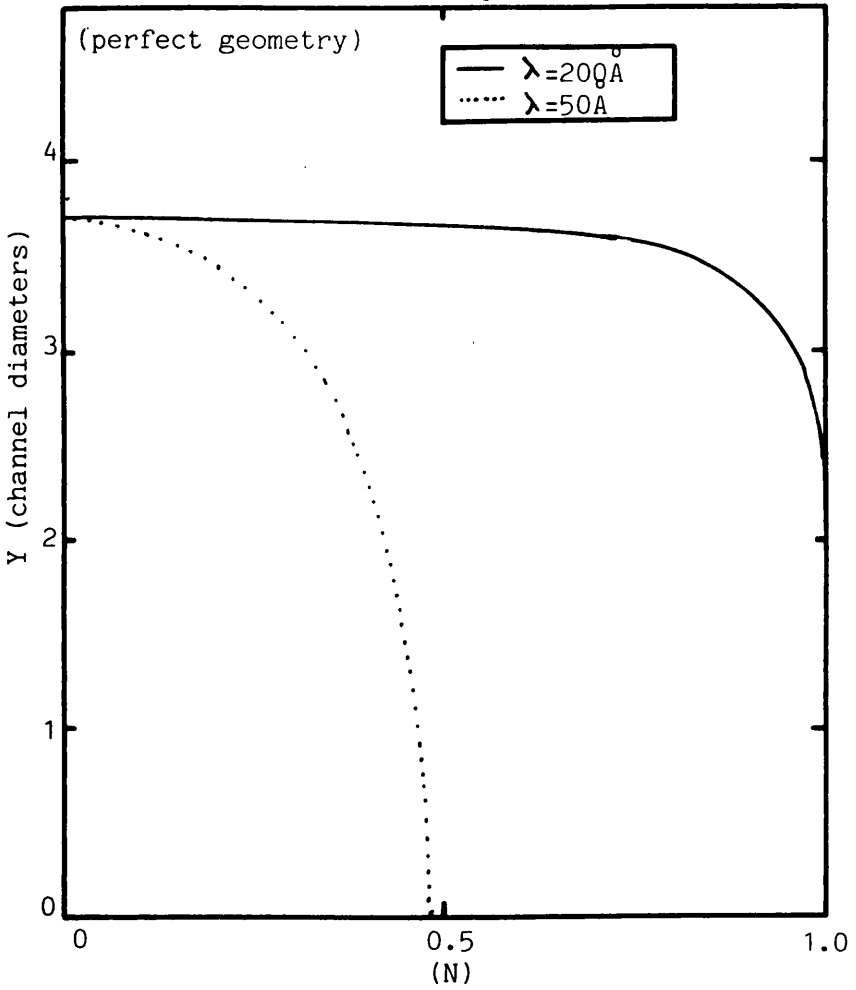

Figure 4.8 The linear absorption coefficient of MgF_2 (from Cromer and Liberman, 1970).

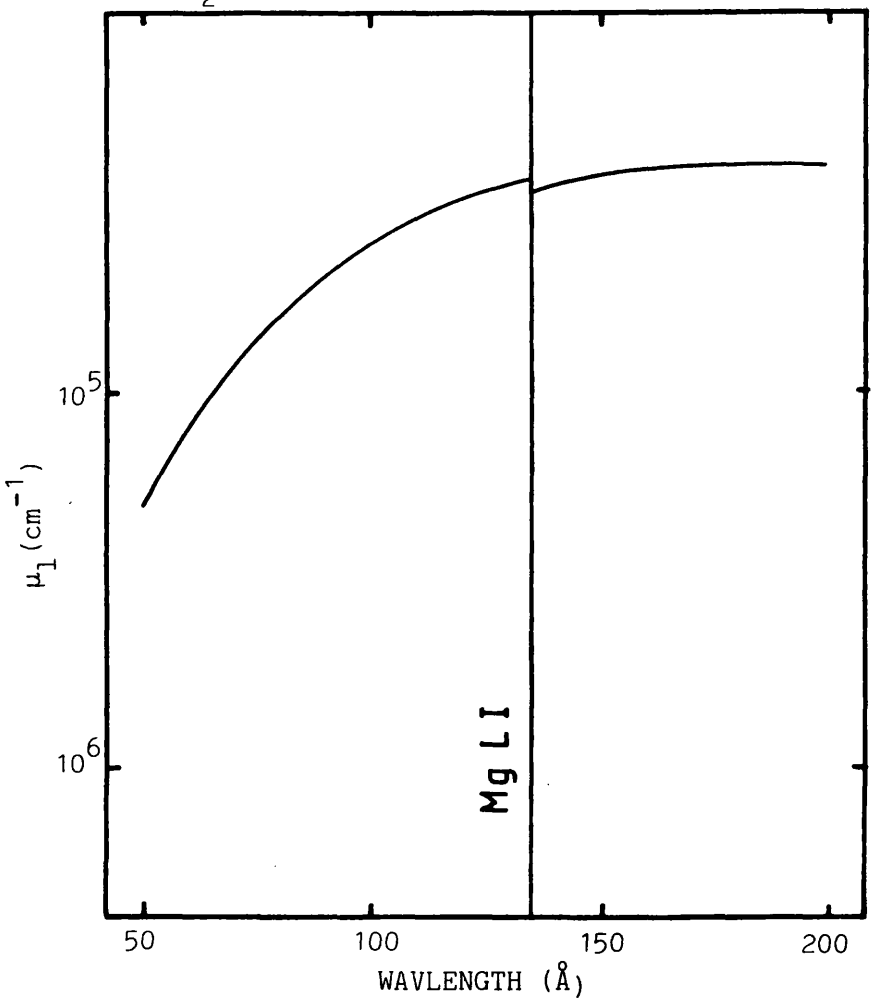

Figure 4.9 Variation of the real coating parameter (G') as a function of Y at three values of r_c (γ=0, h=219mm, l=59mm). The horizontal line is the maximum X-ray penetration.

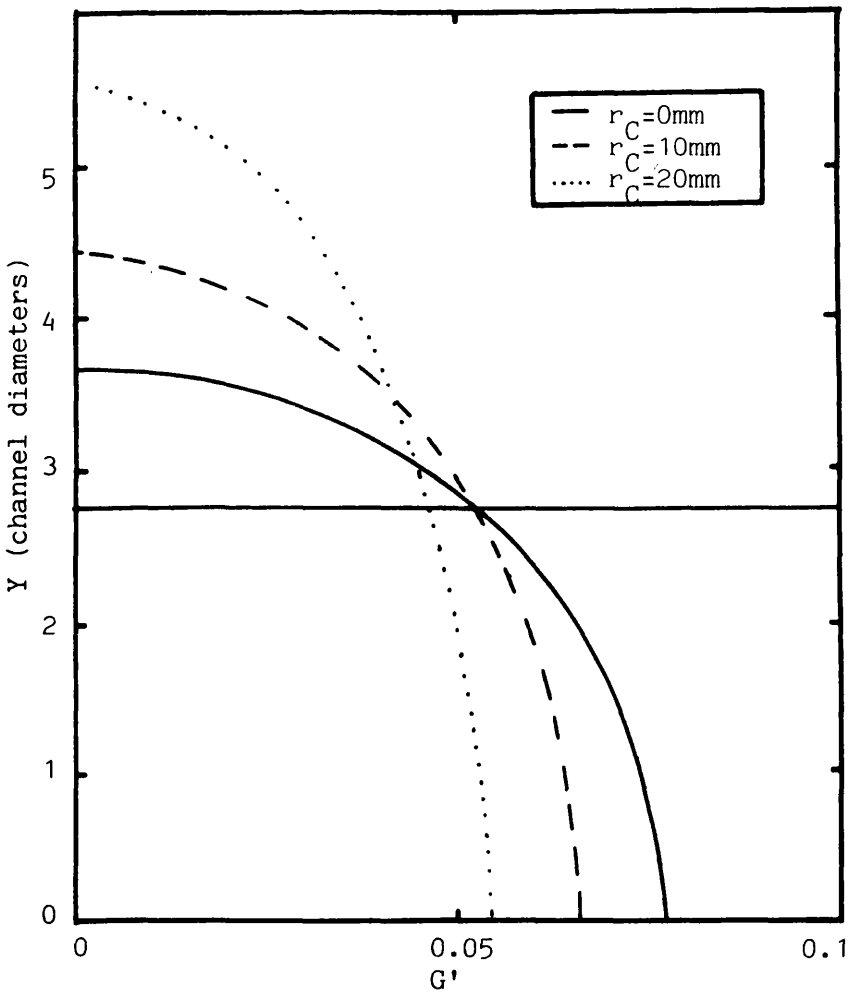

of G' the variation of X-ray absorption across the MCP can be derived, plotted in figure 4.11 for Y=0, which shows the uniformity of the coating viewed from a single direction. At λ=200Å the net percentage change in absorption across the MCP (from r_c=20mm, γ=0 to r_c=20mm, γ=180) is 2% and at λ=50Å it is 33%.

Finally, it is necessary to ensure that the coating does not significantly reduce the open area of channels, otherwise the advantage of the photocathode may be lost. With D=25μm a 10% reduction in the open area requires a nominal front surface thickness of ~180,000Å with the WFSXC geometry. A 6,000Å coating only reduces the area by 0.8%.

4.3.4 Development of Special Coating and Handling Techniques for CsI

The geometrical analysis of the above section applies equally to CsI using the linear absorption for this material. Tests similar to those in section 4.3.2 above were performed on CsI coated glass blanks (M.J. Whiteley, private communication). The effects of heating the substrate were observed which appeared to allow a thicker (up to ~20,000Å), mechanically more stable, photocathode deposit to be applied. However, a detailed theoretical analysis of the photocathode (G.W. Fraser, private communication) suggested that a thickness of 6,000Å was sufficient to obtain maximum efficiency in the XUV band.

A development programme was undertaken independantly of the WFSXC to establish the practicality of using CsI as a photocathode in the XUV. As CsI is hygroscopic the MCPs were baked out to 275°C for ~48 hours to expel water vapour prior to coating. During evaporation the

Figure 4.10 As figure 4.9 but with γ=180°.

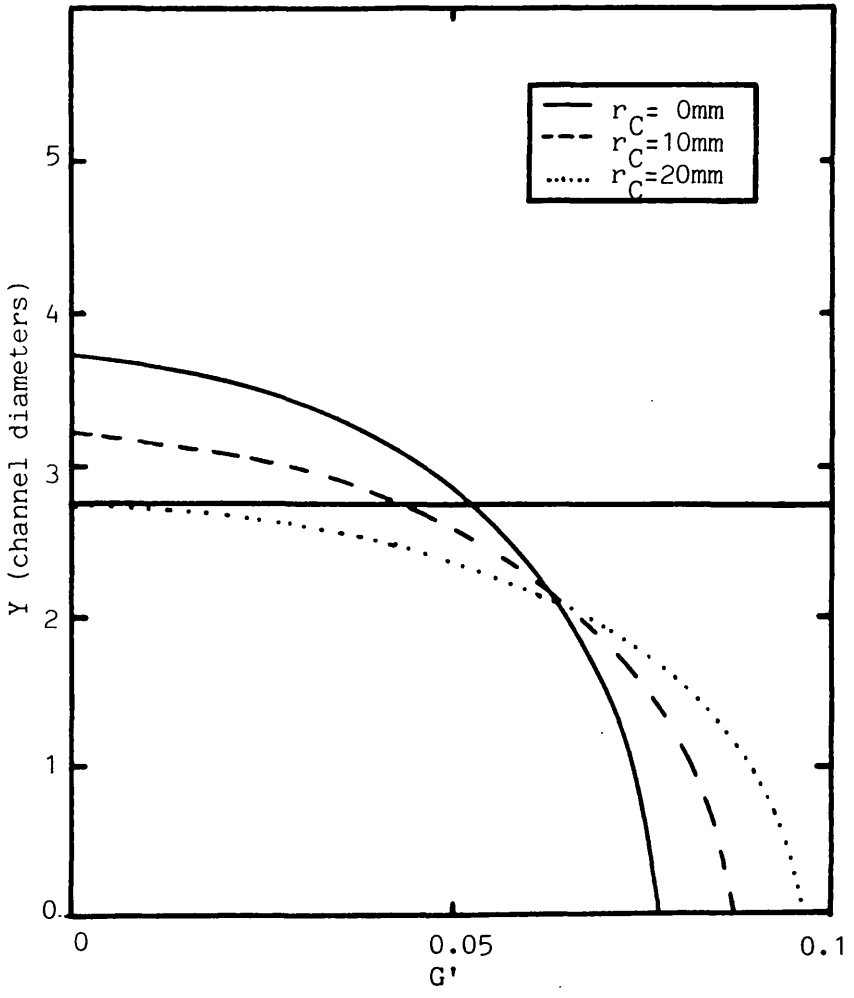

Figure 4.11 Fraction of X-rays absorbed in MgF_2 as a function of r_C at γ=0° and 180° for the real coating geometry (h=219mm, l=59mm, h'/l=3.7, T'_0=6000A, Y=0, α=30°, λ=50A and 200A).

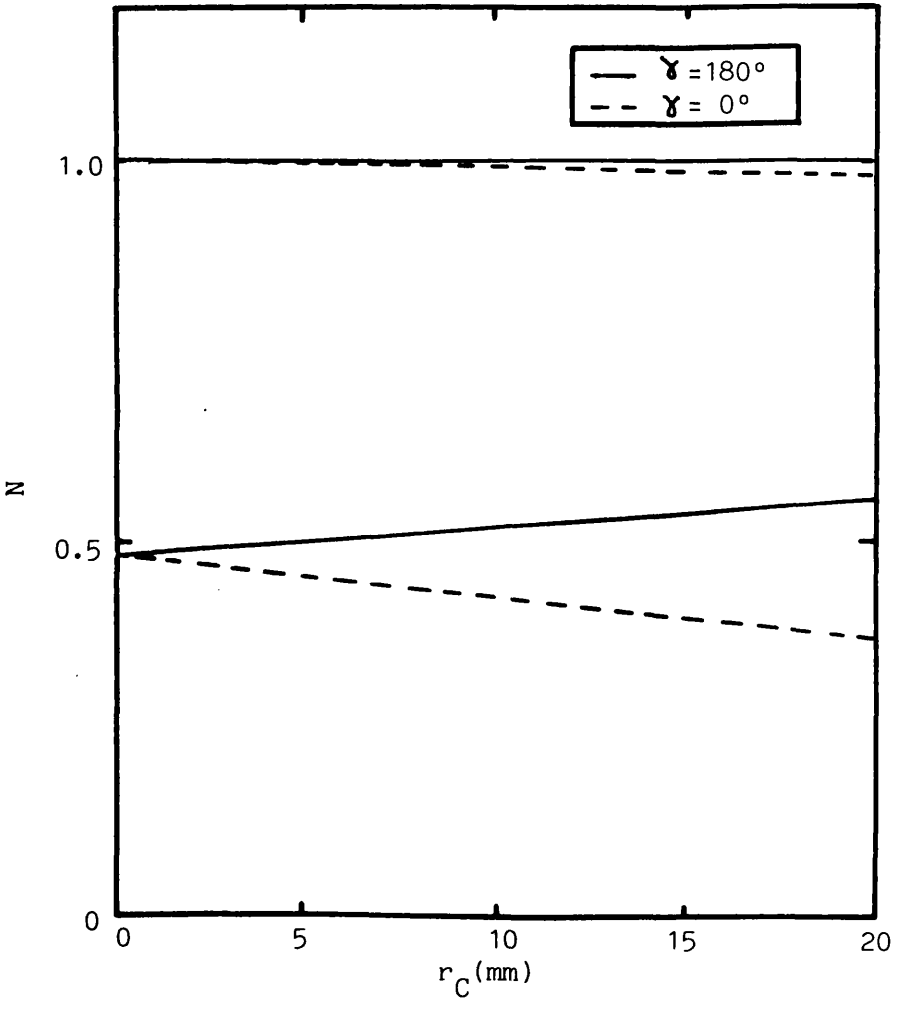

substrate was heated to 100°C to improve the mechanical stability of the photocathode. Efficiency measurements made on two detectors showed large improvements with adequate stability provided the CsI was maintained in a dry N_2 environment when not under vacuum (Fraser et al, 1982). Exposure to air for a total period of 8 hours with relative humidities of 42%-53% (temperature ~ 22-25°C) did not lead to any degradation of the photocathode. Subsequent measurements after storage in dry air showed that the efficiency was stable up to a period of ~300 days.

In order to maintain a dry environment during handling of the detector, during testing at Leicester and payload integration, some simple techniques were developed. All detector assembly was carried out in a dry bag which was inflated with dry N_2. To transfer the assembled detector from the bag to the vacuum system, a snug-fitting cover was attached to the detector body through which dry N_2 was flowed continually. The cover was removed immediately before pumping down the system. These techniques were easily adapted for use on the WFSXC payload, allowing work to be carried out on the vacuum box and pumping system while maintaining the detector under dry conditions.

4.4 Measured Quantum Detection Efficiencies

All the efficiency measurements were made using the operational potentials determined by the gain calibration. The photon flux onto the MCP detector was measured using a monitor proportional counter having a carbon coated polypropylene window of known transmission. An earthed window from the same piece of polypropylene was placed in

front of the MCP detector to simulate the electric field of the WFSXC (which has filters in front of the detector) and to prevent detection of charged particles, present in the vacuum system, as background noise. The proportional counter window was always normal to the X-ray beam but the MCP detector window was at a variable angle of incidence (θ_i). Consequently when calculating the value of the quantum efficiency, $Q(\theta_i,\lambda)$, a correction had to be made for the increased absorption of the MCP window at angle θ_i compared to the proportional counter window at normal incidence. Hence, the quantum efficiency is given by (G.W. Fraser, private communication).

$$Q(\theta_i,\lambda) = t_m.t_w^{(1-\mathrm{Sec}\theta_i)}.(T_{MCP}-N_{MCP})/T_{PC} \qquad (4.10)$$

where: t_m is the transmission of the mesh supporting the proportional counter window

t_w is the transmission of the window

T_{MCP} is the measured MCP count rate

N_{MCP} is the MCP background noise count rate

T_{PC} is the proportional counter rate

The proportional counter noise was negligible by comparison with the signal and was ignored.

4.4.1 Quantum Efficiency of Uncoated MCPs

The uncoated quantum efficiency of each WFSXC detector was measured as a function of angle of incidence at CKα (44.7Å) (figure 4.12), representing MCP glass in three different states - washed (detector 1), "new" (detector 2) and baked out (detector 3). $Q(\theta_i,44.7)$ showed characteristic behaviour having a minimum at $\theta_i=0$ and a peak at $\theta_i\sim4°$ decaying from this peak at larger angles. $Q(\theta_i,44.7)$ for the washed MCPs was lower than either of the other two data sets at all angles. At the WFSXC angles of incidence (20-30°) efficiencies lay between 2 and 6% for detectors 2 and 3, twice those of detector 1 (1-3%). Detector 2 and detector 3 showed close agreement at angles greater than ~10° but there was a difference of ~30% between the peak efficiencies, that of detector 2 being the greater. The peak efficiency of detector 1 was ~60% that of detector 2.

Uncoated plate efficiencies were also measured at two other several wavelengths (AlKα, CuLα). The results are summarised in table 4.1, for 30° angle of incidence and for the peak efficiency with CKα data. The data show that at $\theta_i=30°$ Q decreased with decreasing wavelength from 2.5% at 44.7Å, for both baked and new MCPs, to 1.75% at 13.34Å (new) and 1.25% at 8.34Å (baked). Lower peak efficiencies of 21% (8.34Å) and 33% (13.34Å) were measured compared to 35% (baked) and 48% (new) at 44.7Å. The angle of the peak efficiency decreased from 4° at 44.7Å to 2.5° and 1.5° at 13.34Å and 8.34Å respectively. Some predictions of the efficiency model of Fraser (private communication) are shown for comparison in table 4.1, calculated for

Figure 4.12 Quantum efficiency ($Q(\theta_i,\lambda)$) of the three WFSXC detectors with uncoated front MCPs at λ=44.7Å.

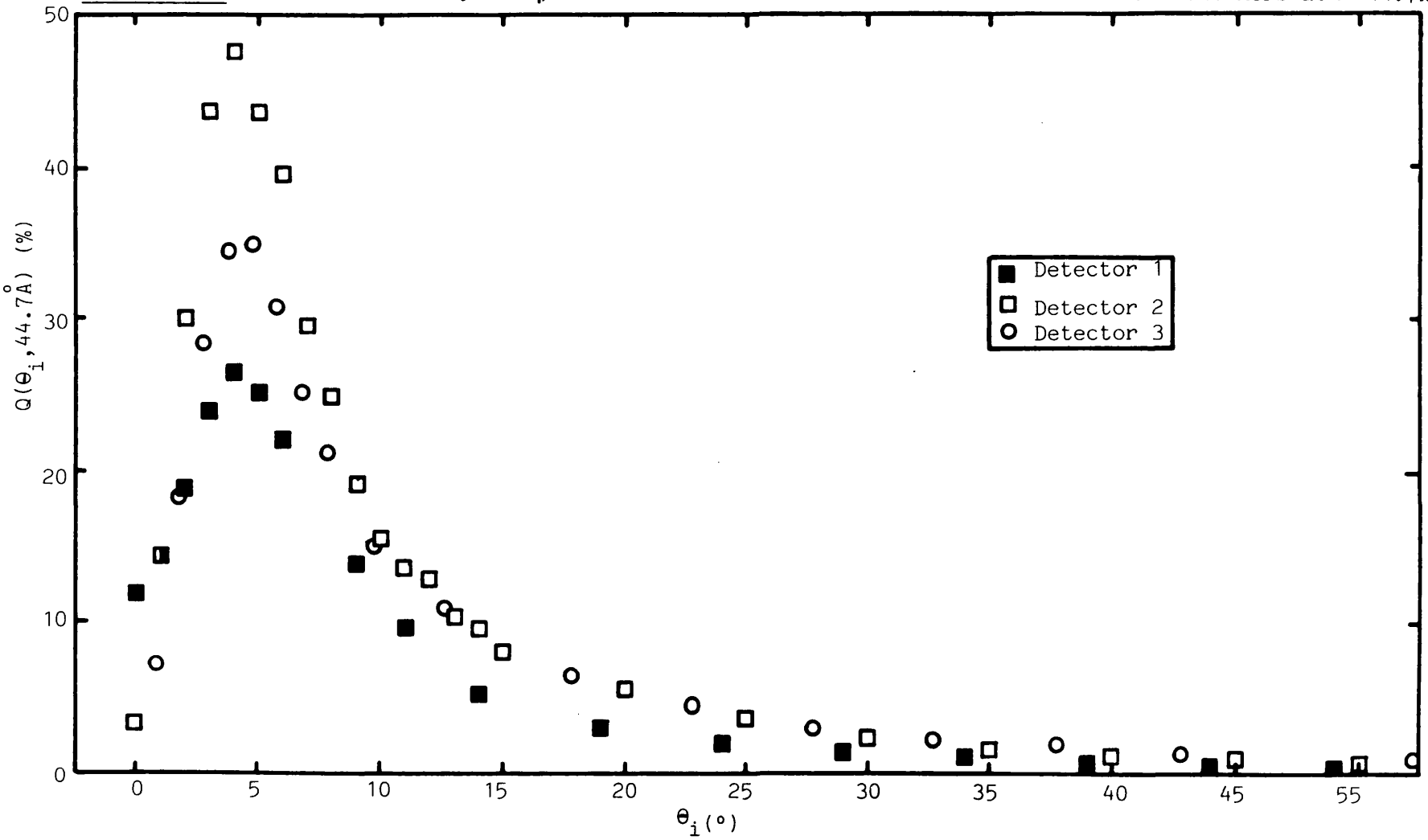

Table 4.1. A comparison of experimental and theoretical quantum efficiencies of uncoated MCPs

λ(Å)	*Q(Predicted) (%) Q(peak)	Q(30°)	Q(Measured) (%) Q(peak)	Q(30°)	Detector/ glass state
8.34	31.1	1.57	21 (1.5°)	1.25	3 baked
13.34	-	-	33 (2.5°)	1.75	2 new
44.7	38.3	2.46	26 (4.0°)	1.4	1 washed
"	"	"	35 (4.0°)	2.5	3 baked
"	"	"	48 (4.0°)	2.5	2 new

* All predictions made for a baked glass model

baked MCP glass and incorporating the effect of the nichrome electrode. There appears to be good agreement at large angles, for both detector 2 (new) and detector 3 (baked) at CKα, and detector 3 at AlKα.

4.4.2 Quantum Efficiencies of Coated MCPs

Both detectors 1 and 2 were coated with 6,000Å of MgF_2 at a nominal coating angle of 15°, optimised as described in section 4.3.3. Figure 4.13 shows $Q(\theta_i)$ measured at 44.7Å, 67.6Å (BKα) and 114Å (BeKα) using detector 1, compared with the uncoated efficiency at 44.7Å for this detector. It can be seen that the efficiencies were improved. At 25° Q was 3.5%, 4.5% and 9% at 44.7Å, 67.6Å and 114Å respectively, compared to an uncoated efficiency of 2% at 44.7Å.

The detector 2 photocathode was deposited after the contamination and washing of the MCPs. The coating appeared to be mechanically stable. Efficiencies similar to those obtained with detector 1 were measured (figure 4.14) except at angles of incidence below ~20°. Detector 2 was also calibrated at 8.34Å (AlKα) and 13.34Å (CuLα) giving efficiencies of 1.6% and 1.9% respectively at 25°.

Detector 3 was coated with CsI for the second flight of the WFSXC. During evaporation, after deposition of only a few hundred Å of CsI, the quartz crystal monitor failed. This was replaced, necessitating the cycling of the vacuum system which was vented to dry N_2 to prevent the MCP from readsorbing water vapour. After pump down the MCP was subjected to a second glow discharge before, at the second attempt, depositing a nominal thickness of 6,000Å CsI at a coating

Figure 4.13 $Q(\theta_i, \lambda)$ of Detector 1 with an MgF_2 photocathode at 44.7, 67.6 and 114Å, compared with the uncoated efficiency at 44.7A.

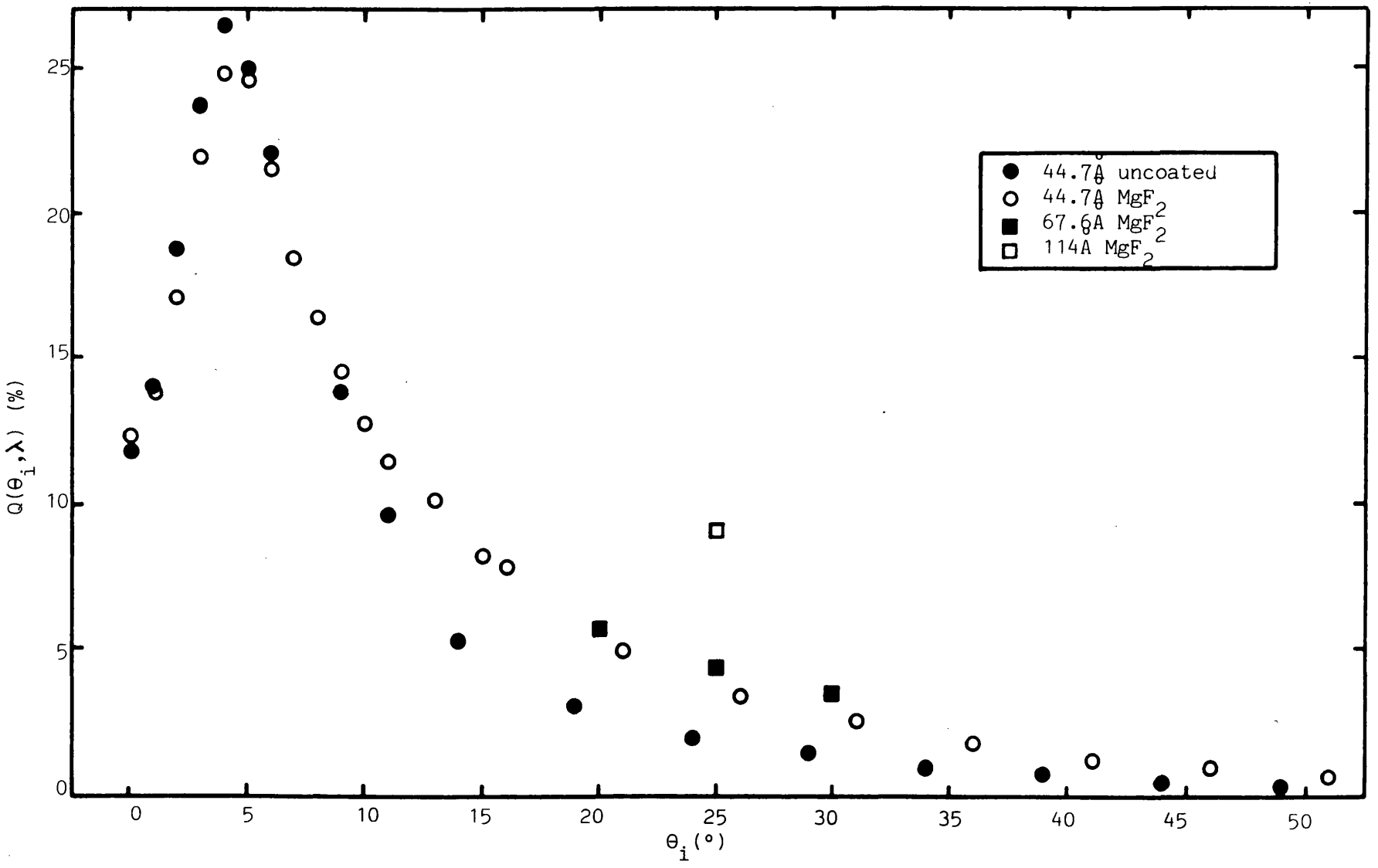

angle of 15°.

The coated instrument was calibrated at several wavelengths - 8.34Å, 44.7Å and 67.6Å. Figure 4.15 shows the results of these calibrations. The efficiencies at large angles (>15°) were very similar at each of the wavelengths and much higher than either the uncoated or MgF_2 efficiencies, ~20% at θ_i=30°, increasing to ~27% at θ_i=20°.

The quantum efficiency was also measured using the Fe^{55} source (5.9keV and 6.5keV) and collimator described in section 3.6.3. At Fe^{55} X-ray energies the proportional counter was not 100% efficient. However, its effiency was estimated to be ~38% from the absorption cross-section of the gas mixture (90% Ar + 10% CH_4, μ=230 cm^2gm^{-1} for Fe^{55}). The quantum efficiency of the CsI coated detector was 6.4% at 30°.

4.5 Discussion and Interpretation of the WFSXC Data

The typical response of the quantum efficiency as a function of incident angle can be simply explained. The decrease from the peak efficiency is due to the increasing absorption depth of photons in the channel wall, which must reduce the probability of a photoelectron escaping into a channel. Increasing absorption depth also accounts for a decrease in efficiency with decreasing wavelength. It is the onset of X-ray reflection at shallow angles that determines the fall-off below the peak. As the reflection coefficient increases so does the number of photons that are reflected one or more times along the channel and therefore have a reduced probability of producing a valid

Figure 4.15 Efficiency of CsI coated Detector 3 at 8.34A, 44.7A and 67.6A.

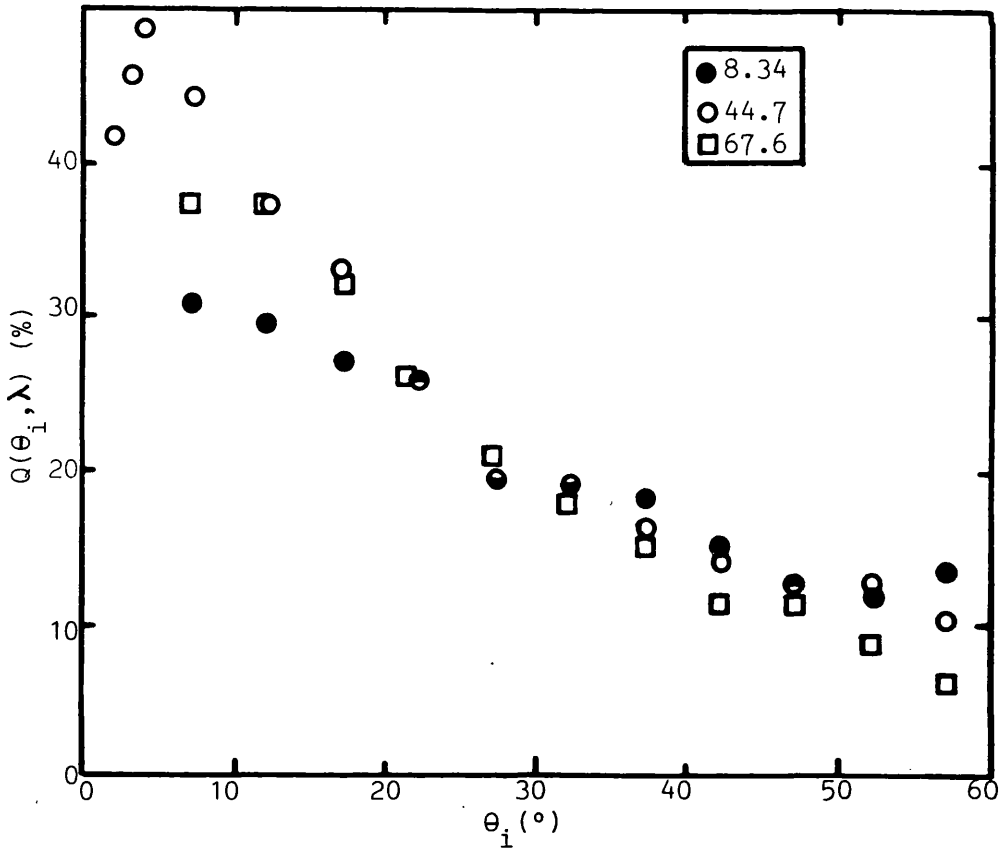

Figure 4.14 Comparison of MgF_2 efficiencies for Detectors 1 & 2 at 44.7A.

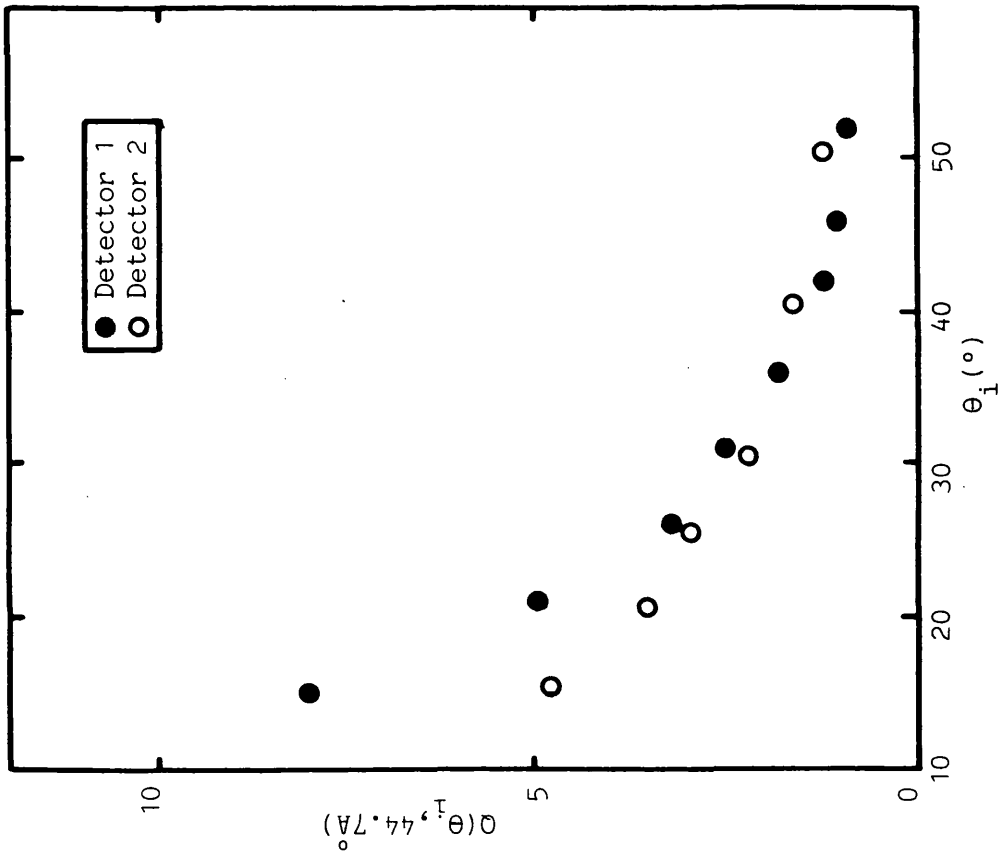

output pulse. The angle of the peak decreases with decreasing wavelength as observed (4° at CKα, 2.5° at CuKα and 1.5° at AlKα).

The magnitudes of $Q(\theta_i)$ were seen to differ between uncoated MCPs that had been treated differently (figure 4.12). The efficiency of an MCP is a weighted combination of the yield from the nichrome electrode material (~300Å thick, 1 channel diameter in extent) and from the MCP glass according to angle. If $\theta_i > 45°$ all the contribution is from the nichrome, while at small angles the major contribution is from the MCP glass. Baking out the MCP appears to have changed the efficiency of the glass as $Q(\theta_i)$ only differed from that of "new" glass at angles around the peak. It has been suggested (R. Field, private communication) that lead and bismuth migrate from the glass bulk into the surface layers at bake out temperatures (~275°C) which could explain the reduction in efficiency. This conclusion is supported by the agreement between the theoretical predictions, which incorporated the above suggestion for baked glass into the efficiency model, and experimental data (table 4.1).

Washing the MCP reduced both glass and nichrome contributions to the efficiency. The temperatures involved in this process (~70°C) are unlikely to have physically changed either the glass or the nichrome hence the reduction in efficiency must have been caused by the adsorbed water vapour preventing the escape of photoelectrons.

Coating the front MCP with MgF_2 improved the quantum efficiency of detector 1. A useful means of expressing this improvement in efficiency is by taking the ratio $Q(MgF_2)/Q(\text{uncoated})$ for all values of θ_i at λ=44.7Å (figure 4.16). The vertical line represents the

minimum WFSXC angle of incidence. At small angles (θ_i<10°) the ratio is of order unity. This similarity between coated and uncoated efficiencies is because most of the photons interact with the glass beyond the photocathode layer, given the coating angle of 15°. At angles above the coating angle a substantial improvement in efficiency can be observed (~ a factor 2). The change in the ratio between 10° and 20° shows the effectiveness of the optimisation of the coating geometry.

Following the same exercise for detector 2 at 44.7Å and 13.34Å, comparing coated with "new" glass efficiencies shows a reduction in efficiency (the ratio is <1) below θ_i~40° (figure 4.17). The similarity between the MgF_2 44.7Å efficiencies of detectors 1 and 2 shows that this effect is a result of the relatively high "new" glass efficiency, rather than a reduction in that of MgF_2 caused by the MCP contamination. Fraser (1983a) predicts this, noting that the value of the parameters that determine the efficiency (ϵ, $P_S(0)$ and L_S) are similar for MgF_2 and new MCP glass.

All the MgF_2 calibration data at θ_i=25° is compared with the efficiencies predicted by Fraser from the model of section 4.2 (private communication) (figure 4.18). It can be seen that there is excellent agreement between the experimental and theoretical data. The discrepancy at 67.6Å is most likely to be due to contamination of the X-ray source. Lines at wavelengths longer than 44.7Å are difficult to obtain without contamination. BKα is particularly susceptible as, with a generating potential of 0.3kV, a small amount of CKα (0.28keV) may be excited, the source of carbon being in the

Figure 4.16 Ratio of coated and uncoated efficiencies for Detector 1 at 44.7A.

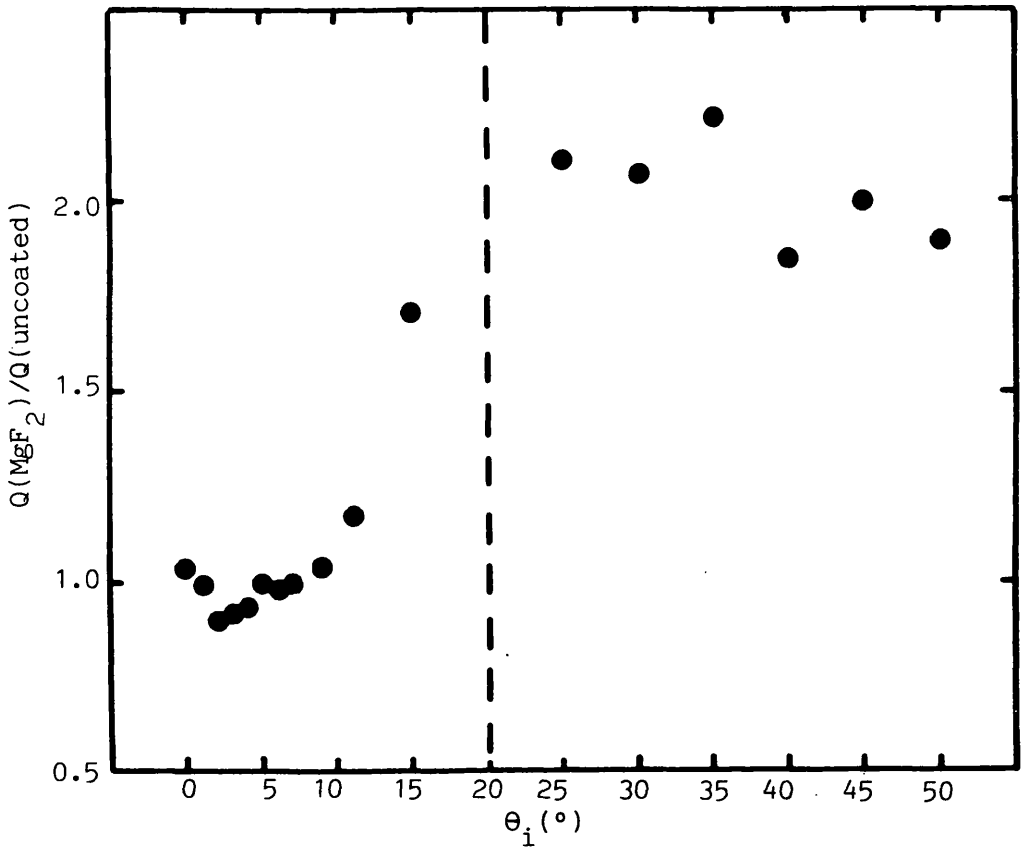

Figure 4.17 Ratio of coated and new glass efficiencies for Detector 2 at 44.7A.and 13.34A.

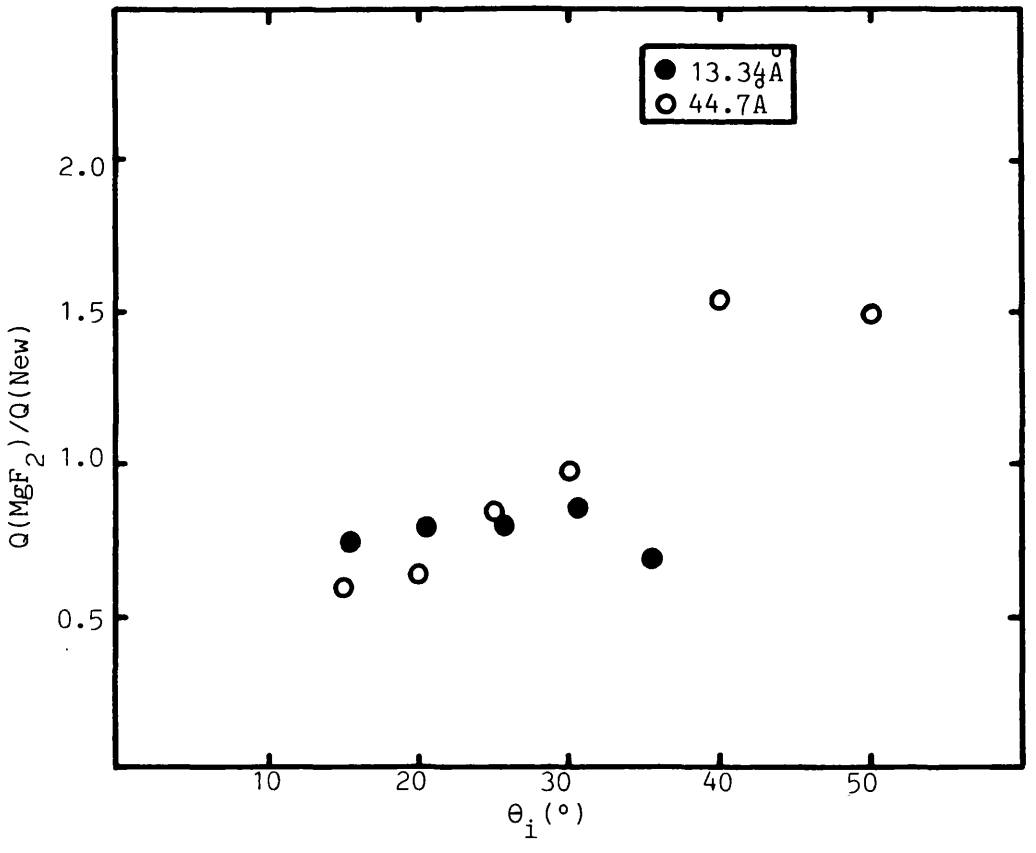

diffusion pump oil and vacuum greases. As the MgF_2 efficiency at CKα is expected to be lower than that at BKα the measured efficiency at BKα will be lower than the expected value, the difference depending upon what proportion of the total flux is CKα radiation.

The improvements obtained using the CsI photocathode can be seen by plotting the ratio Q(CsI)/Q(uncoated) as for MgF_2 (figure 4.19). Increases of a factor 5-10 and 14-20 can be seen at CKα and AlKα respectively. The cutoff in the improvement below the nominal coating angle (15°) is not so evident as for the MgF_2 photocathode (figure 4.16) which has a ratio ~1 for θ_i<10°. This must be due to the large contribution that CsI makes to the efficiency even when much more of the illuminated area of the channel is uncoated.

The experimental CsI quantum efficiencies are compared with theoretical curves plotted for several characteristic photocathode thicknesses, G'(Y=0), (550Å, 450Å 370Å; Fraser, private communication; figure 4.20a-c). The comparison suggests that a characteristic thickness of ~550Å is appropriate compared to 462Å predicted from G_p for the WFSXC geometry. As the "perfect" geometry could not be obtained in the limited dimensions of the coating apparatus the photocathode thickness must have changed across the MCP, becoming thinner on the part of the channel wall facing out from the MCP (γ=0) and thicker facing inward (γ=180). The X-ray beam illuminated the inward facing part of the channel hence the coating would appear to be thicker. The approximate position of the X-ray beam was r_c=10mm. At this position the predicted characteristic thickness is 570Å, calculated from G'(Y=0, r_c=10mm, γ=180) in figure

Figure 4.18 Comparison of $Q(25°,\lambda)$ with the theory of Fraser for a detector coated with MgF_2. The theory is calculated for L/D=120.

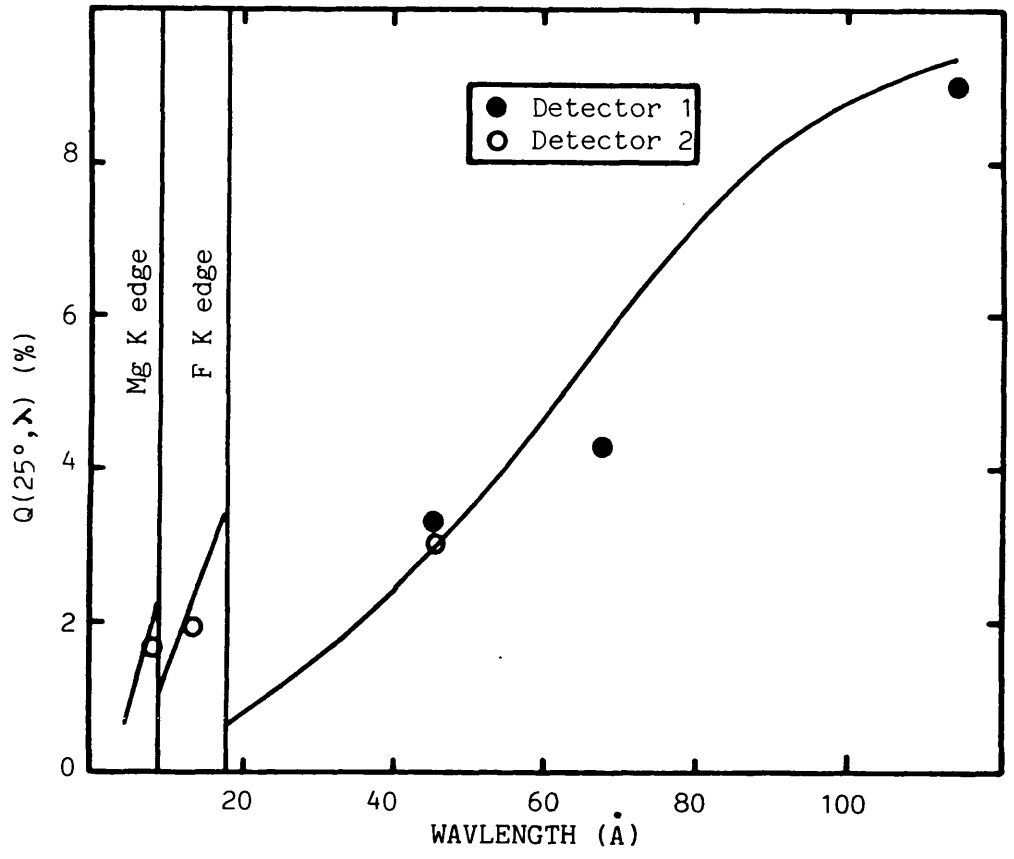

Figure 4.19 Ratio of CsI and uncoated efficiencies for Detector 3 at 44.7A and 8.34A.

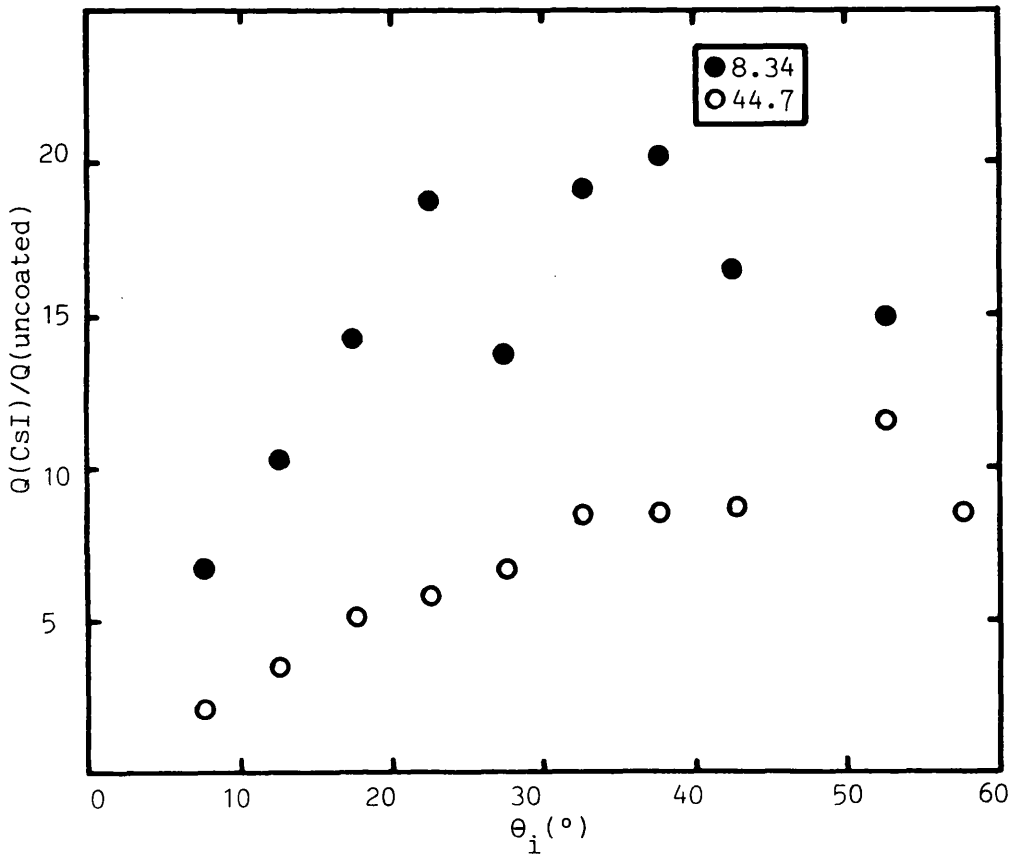

Figure 4.20 Comparison of CsI efficiencies measured by Detector 3 with theoretical prediction for several characteristic wall thicknesses of photocathode.

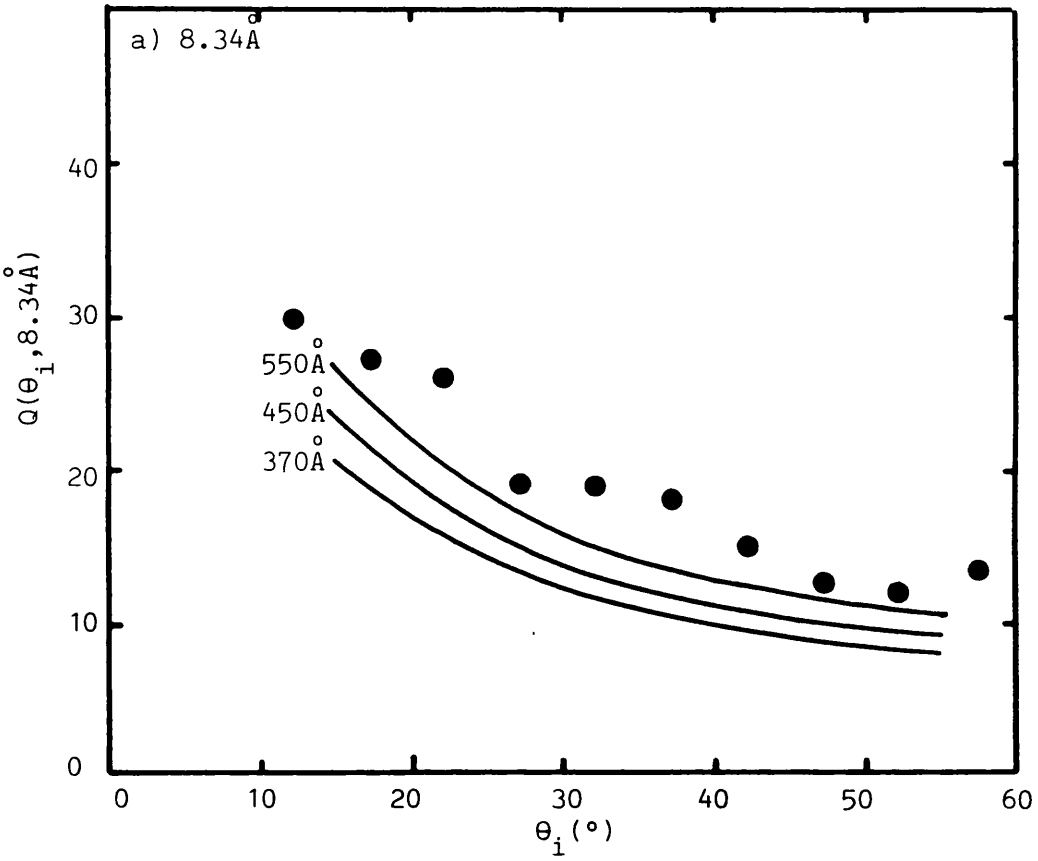

Figure 4.20b

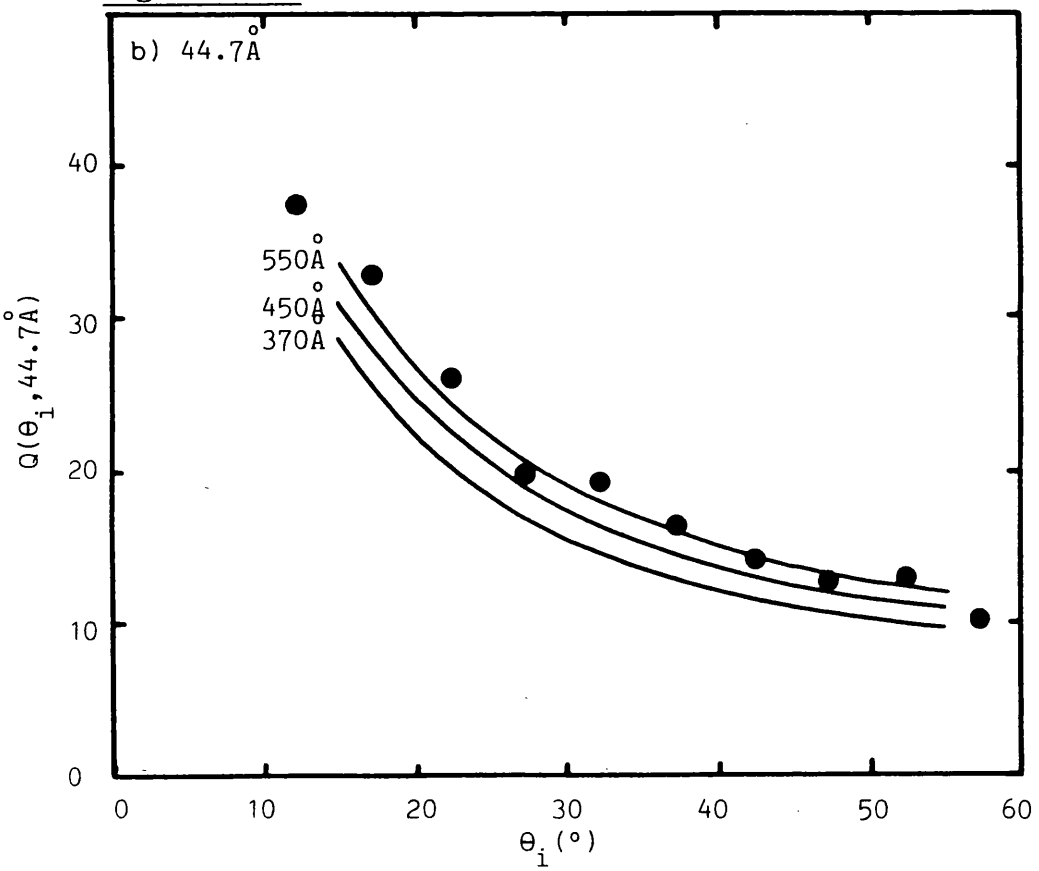

4.11. This lends further support to the accuracy of the coating analysis and theoretical model.

4.6 Conclusion

The measured efficiencies of uncoated WFSXC MCPs were poor (<5% "new" and < 2.5% washed at 44.7Å) as expected. An MgF_2 photocathode improved the efficiency of washed MCPs by a factor ~2 to 5% at 20°. Where the bare MCP efficiency had not been degraded by washing nothing was gained by using MgF_2 as a photocathode. Therefore, with hindsight, it appears that MgF_2 was a poor choice. By comparison CsI gave dramatic improvements, between 5 and 10 times the uncoated efficiency at 44.7Å. Also earlier experimental work had suggested that a CsI photocathode should be stable over the timescales required in a rocket programme (several months). Special handling techniques were devised to cope with the hygroscopic nature of CsI to ensure that the quantum efficiency would not degrade during payload integration. However, in view of the potential instability the CsI efficiency should be frequently monitored.

For the present it is not possible to obtain calibration data at wavelengths longer than 114Å at Leicester. The demonstrated agreement between experimental data and the theoretical model allows the use of the model to predict the detector response out to 300Å, for both MgF_2 (figure 2.9) and CsI (figure 4.21). These predicted curves can then be used to estimate the net response of the WFSXC, as described earlier in chapter 2.

Figure 4.20c

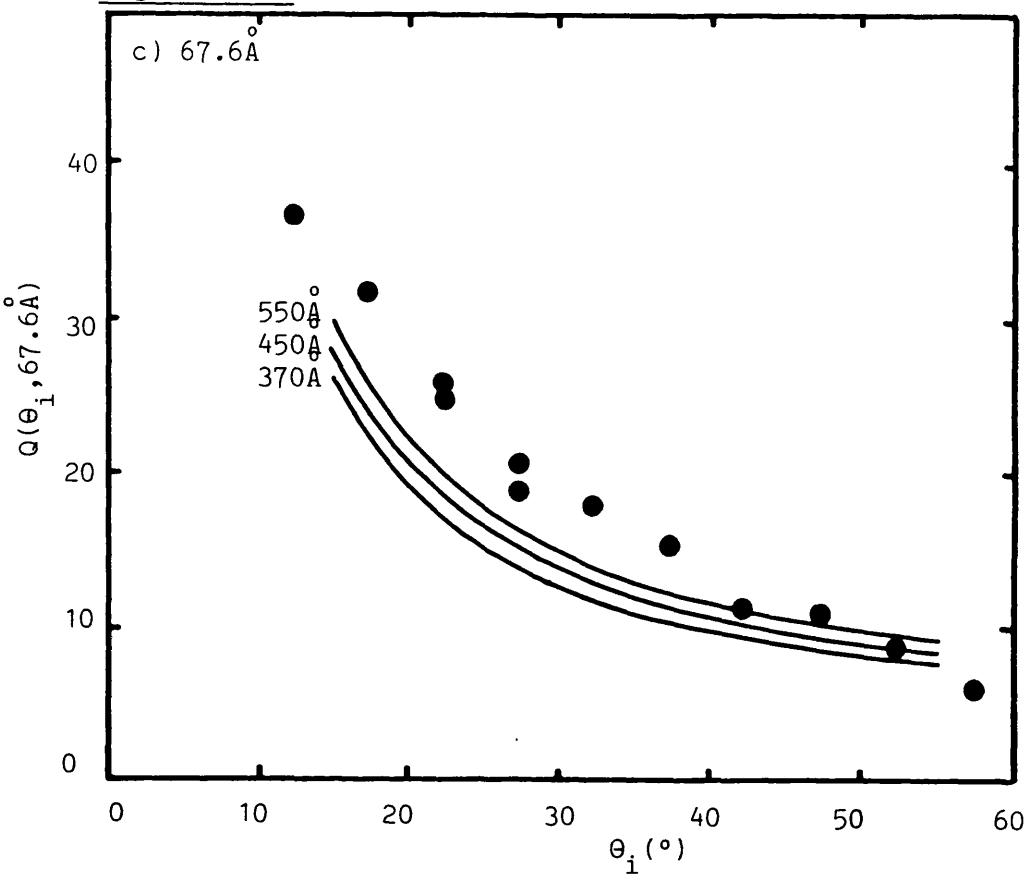

Figure 4.21 Theoretical efficiency of a CsI coated MCP at 30° angle of incidence (from G.W. Fraser)

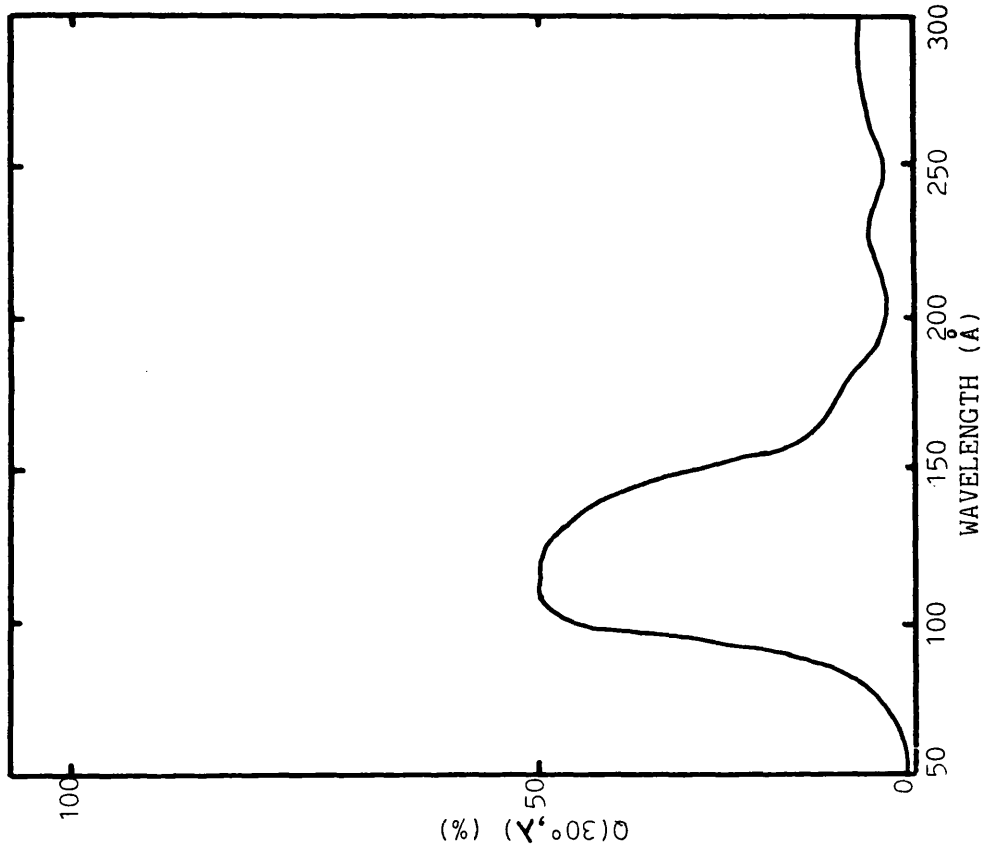

CHAPTER 5

THE IMAGING PERFORMANCE OF THE WFSXC DETECTOR

5.1 Introduction

The MCP part of the detector acts as an X-ray converter and electron amplifier, providing an output charge cloud from which the position of a photon can be determined using the resistive anode. The position signals (Q_X,Q_Y) in each axis are derived from the amplitude ratio algorithm

$$Q_X = i_1/(i_1+i_3)$$

$$Q_Y = i_2/(i_2+i_4) \qquad (5.1)$$

where: $i_j (j=1,2,3,4)$ are the peak currents of the output pulses from the electrodes (figure 5.1)

The resistive anode and associated image processing electronics must be capable of achieving a resolution <100μm (RMS), which is equivalent to ~230μm full width half maximum. It is known that resistive anodes suffer from an inherent distortion, ie. the relationship between the position of the injected charge (X_i,Y_i) and the output position signals (Q_X,Q_Y) is not linear, which degrades the resolution if not accounted for in the data analysis. It was hoped that theoretical analysis of the anode behaviour would allow prediction and linearisation of distorted images, a technique that would be easier than calibrating the anode over the whole area.

Figure 5.1 Diagram of a square resistive anode having the disposition of the electrodes used in the WFSXC anode.

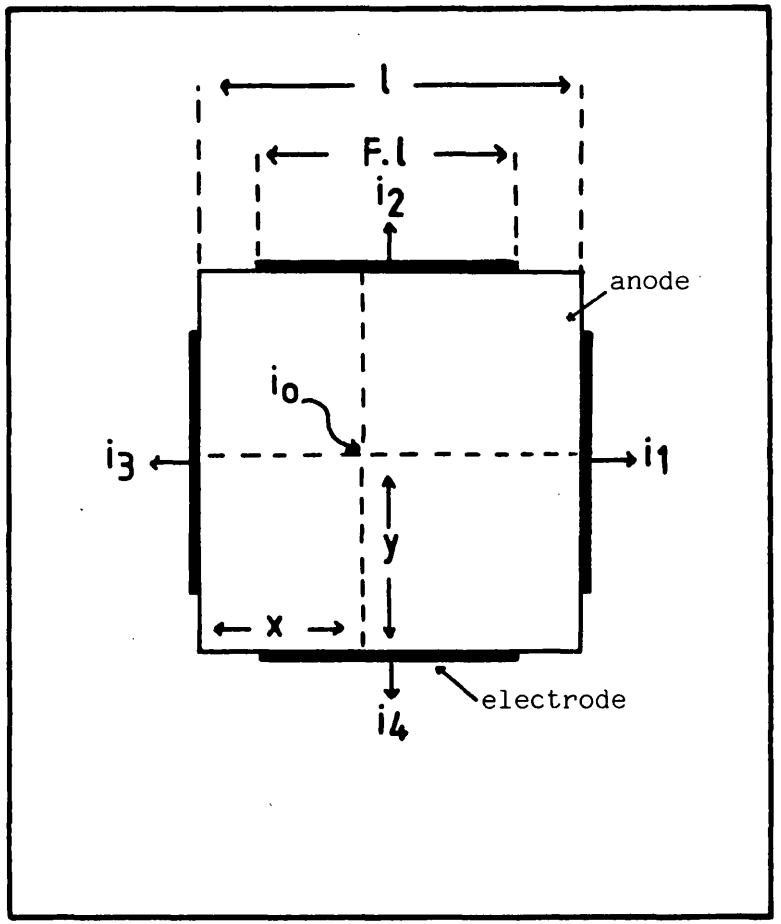

This chapter describes the performance of a resistive anode calibrated for the WFSXC and tests image restoration techniques.

5.2 The Imaging System

5.2.1 The Characteristics of the Anode/Filter-Amplifier Combination

The resistive anodes used in the WFSXC were supplied by EMI (microelectronics) Ltd., Hayes, Middlesex, England. They were produced by coating a ceramic base with a 54mmx54mm homogeneous mixture of resistive ink and glass using a screen printing technique. After coating, the anodes were fired to produce a hard and durable film of thickness between 6.0μm and 8.0μm for the blend of ink used. The electrodes, central to each side and of length 36mm, were deposited using the same technique but with a conducting ink and coating thicknesses of 9μm to 11μm.

The anode can be characterised by the fraction of the anode side (length L) occupied by the electrode (the electrode fraction, F), its resistance per square $R_{\square}$ and its total capacitance to ground C. $R_{\square}$ is the resistance that would be measured between two electrodes of F=1 on opposite sides of the anode with no electrodes on the remaining sides. The value of $R_{\square}$ cannot be measured directly for an individual anode of the type in figure 5.1, but can be determined from a test anode with F=1 electrodes produced from the same batch of resistive material. $R_{\square}$, measured by EMI for two such test anodes, from the WFSXC batch of material, was 696kΩ/□.

However, other resistive parameters can be measured directly. R_1 is the resistance measured between one electrode and the remaining three electrodes (these at ground) and R_2 is the resistance measured between two adjacent electrodes connected together and the other two

electrodes. R_1 was measured at each terminal of the flight anode (note: the same anode was used in each flight detector) giving values of 330, 326, 318 and 317 kΩ (all ±2kΩ), having a mean of 323kΩ. As R_1 would be identical at each electrode if the anode was perfectly uniform, the similarity between the results is an indication of the uniformity of the WFSXC anode. R_2 was found to be 300kΩ (the average of two measurements).

C is determined by the dielectric constant (8.2-9.6) of the ceramic mounting block (fired alumina) by that of other surrounding material in the detector and by the parallel-plate arrangment of the MCPs and anode. C was obtained for two experimental configurations of the anode, with and without the MCP assembly, at each electrode with the remaining electrodes held open circuit. Averaged over all four electrodes C was 74.63pF without the MCP assembly and 10.5pF with the MCP assembly.

The resistive anode electrodes are connected to charge sensitive pre-amplifiers, and are therefore at virtual ground potential. Signals from the pre-amplifiers are fed into matched (ie. all stages of the filter have the same time constant) doubly differentiating, singly integrating ($[CR]^2[RC]$) pulse shaping filter amplifiers. The anode/filter system can be described by a normalised time constant (T_n; Fraser, 1980)

$$T_n = \pi^2 . T_a / R_{\square} C \qquad (5.2)$$

where: T_a is the filter time constant (seconds)

$R_{\square}C/\pi^2$ is the anode time constant (seconds)

If T_a is large compared to the $R_{\square}C$ product the anode operates in the d.c. limit, where the output pulse from the anode has zero rise time by comparison with the filter time constant (T_n>3).

Prediction of the anode behaviour requires determination of how an input current (i_o) is divided between each electrode for a given input position. In the d.c. limit exact numerical solutions can be found but in non-d.c. cases approximations must be made. Typically T_a is ~2μs for the filter amplifier used, which gives T_n=0.38 (without MCPs) and T_n=0.27 (with MCPs) for $R_{\square}$ and C as described earlier. Hence the WFSXC anode operates under non-d.c. conditions.

5.2.2 Image Processing Electronics

The payload electronics were outlined in chapter 2 with the payload description. In order to test the imaging properties of the WFSXC detector without the payload, a similar circuit was needed. The circuit in figure 5.2 is designed to determine positions using the amplitude ratio algorithm (equation 5.1). The system can be separated into two basic parts, one that handles the individual signals from the filter amplifiers and determines Q_X and Q_Y and one that handles the sum of the output signals (this part has been discussed already in chapter 3) and from which the pulse height distribution is obtained. The summing circuit operates photon counters and strobes the ratio circuitry appropriately for each event allowing selection or rejection of events by pulse height discrimination.

Each filter amplifier (FA) has an output peak voltage (V_j), proportional to i_j, which is converted into a square pulse of amplitude proportional to the peak height of the amplifier output by

Figure 5.2 Block diagram of the electronic circuit that derived the position signals from the pre-amplifier outputs.

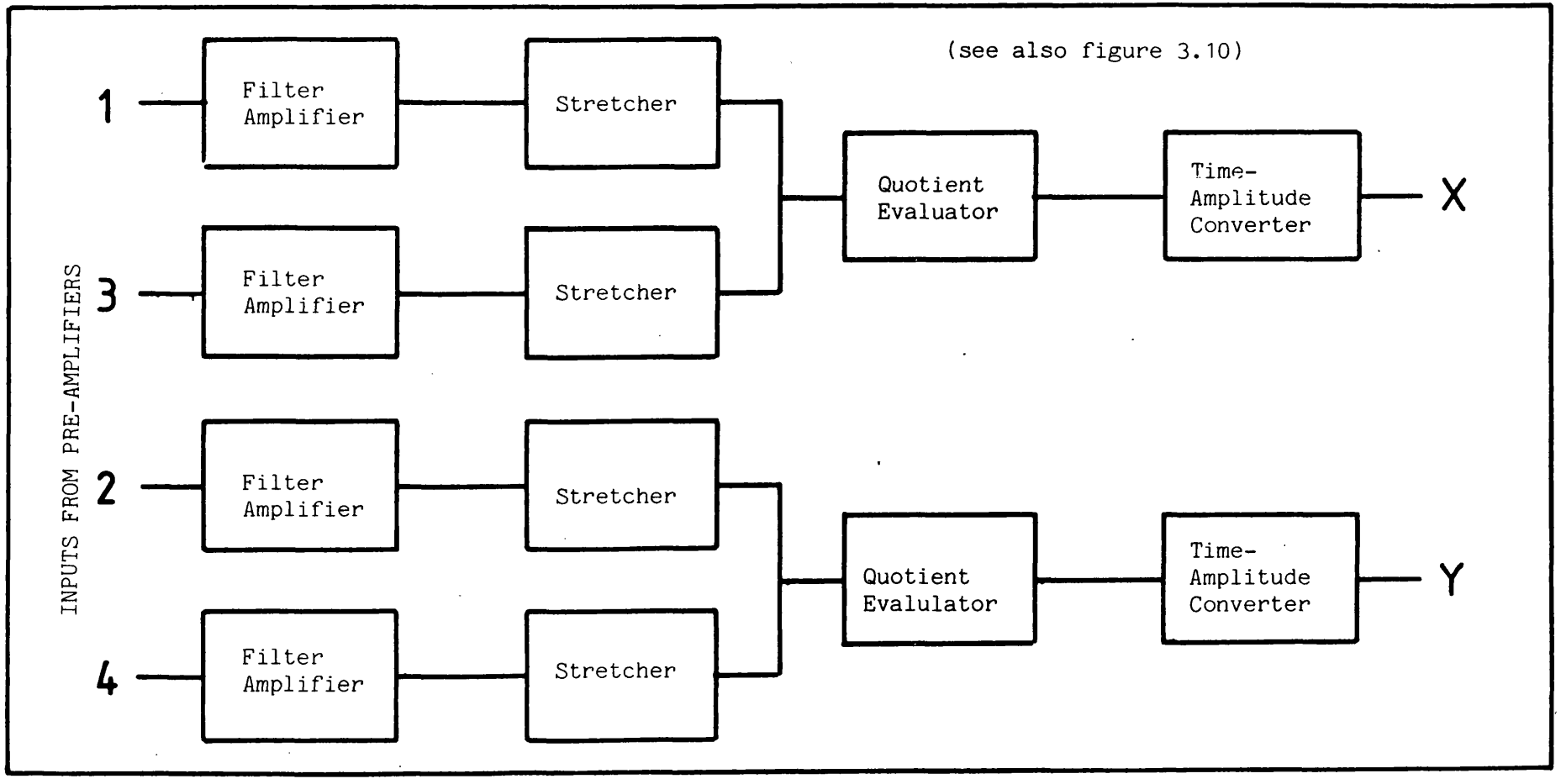

the stretcher. Two square pulses (amplitudes A_1 and A_2) from appropriate FAs are combined in the quotient evaluator (QE) whose output is a square pulse of duration proportional to $A_1/(A_1+A_2)$. A time-amplitude converter (TAC) is driven by the QE output. When biased by the onset of the QE square wave the TAC generates a ramp voltage until the QE square pulse ends. The voltage reached by the TAC output is therefore proportional to the duration of the QE pulse, thus the time signal is converted back into an amplitude, Q_X or Q_Y. Hence, the test electronics have analogue output signals, unlike the payload positions which are digitised. These output signals can be used to drive a storage oscilloscope or TV display giving a two dimensional image or a pulse height analyser which can only display information from one axis at a time.

The timing of individual elements of the circuit is crucial to the efficiency of the system. As only one photon event at a time may be processed there is an electronic limit to the rate at which events can be analysed. This could have an effect on the quantum efficiency of the instrument, reducing it artificially if the incident photon flux is too high. After an event has been processed all elements of the circuit are reset to their initial states. An approximate timing diagram is shown in figure 5.3. The system is ready to process the next event when the TACs have been reset to zero hence the duration of one event is $\sim 50\mu s$ allowing count rates up to $\sim 2 \times 10^4$ s^{-1} before encountering any "pulse pile-up" problems.

5.3 Resistive Anode Theory

The theory of the resistive anode has been definitively described by Fraser (1980) and it is not proposed to discuss it here in great detail. It was intended, however, to use this theoretical model to predict the anode distortion and develop a procedure to remove it from the WFSXC images during data analysis. Therefore, some discussion is necessary in the context of the WFSXC anode/filter-amplifier system.

The equivalent noise charge (q_n) is defined as that charge which when placed at the pre-amplifier input gives an output voltage equivalent to the RMS noise. In the d.c. limit the impedance represented by the anode at the pre-amplifier input can be considered as purely resistive. Hence, ignoring the preamplifier noise contribution Fraser (1980: Chapter 4) gives

$$q_n^2 = (2kT_e/\pi).\gamma'^2.(T_a/R_1) \qquad (5.3)$$

where: k is Boltzmann's constant

T_e is the absolute temperature

γ' is a dimensionless factor determined by the shaping properties of the filter amplifier

The effects of the electronic noise on the positional resolution can be described by a dimensionless resolution parameter D(X,Y). If the RMS position uncertainty is dX and q_o the injected charge then

$$dX = D(X,Y).q_n/q_o \qquad (5.4)$$

where: q_n is the equivalent noise charge

q_o is the injected charge

It can be seen that the resolution is inversely proportional to the input charge and therefore a function of detector gain.

When the positions are determined by the amplitude ratio method

$$D(X,Y) = \frac{a}{dQ_X/dX}\left[\frac{(V_1^2+V_3^2)}{(V_1+V_3)^4}\left\{1-2.\frac{V_1.V_3.r_{op}}{(V_1^2+V_3^2)}\right\}\right]^{1/2} \quad (5.5)$$

where: V_1 and V_3 are the peak voltages of the pre-amplifier pulses corresponding to i_1 and i_3

a is the peak amplitude of the filter response to a unit step

r_{op} is a coefficient ($r_{op}=1-R_1/R_2$) which expresses the correlation between noise signals at electrodes on opposite sides of the anode. For the WFSXC anode R_1 and R_2 are 323kΩ and 300kΩ respectively, hence r_{op} is -0.076. Resolution degrades from the centre of the anode but slowest towards the electrodes from which the position signal is derived (1 and 3 for Q_X, 2 and 4 for Q_Y).

The WFSXC anode does not operate in the d.c. limit hence the dimensionless resolution parameter is also a function of the normalised time constant, increasing as T_n decreases away from the d.c. limit. In addition equation 5.3, defining q_n, no longer holds. In the d.c. limit the admittance of the anode is simply the reciprocal of R_1 (hence the $1/R_1$ factor in q_n^2). With finite capacitance the admittance of the anode can be approximated numerically. Introducing a dimensionless noise parameter $\mu(T_n)$, which increases with increasing

T_n.

$$q_n = (kT_eC)^{1/2}\mu(T_n) \qquad (5.6)$$

The departure of the anode from a linear performance can be described by a distortion parameter (δ), which is the RMS displacement of the image points from the true positions expressed as a percentage of L, the side length. The value of δ depends upon the fractional central area of the anode that is being used and in the non-d.c.limit is a function of T_n. A perfectly linear anode will have δ=0. δ=1.0% can be considered as a good restoration, whereas δ=10% would be poor.

5.4 The Linearity of the WSFXC Anode

5.4.1 Experimental Measurements of Anode Distortion

Measurements of anode linearity were made using two configurations, with a test probe and using X-rays with the MCPs assembled.

The test probe comprised a metal probe with a hemispherical tip which was capacitively coupled to the anode, representing a point source of charge when driven by a pulse generator. Pulses were injected at constant frequency into the anode at a given position by the probe. The apparent positions were then calculated manually from the measured FA output peaks, using the difference ratio algorithm

$$\frac{V_3-V_1}{V_1+V_3} = 2Q_X-1$$

$$\frac{V_4-V_2}{V_2+V_4} = 2Q_Y-1 \qquad (5.7)$$

Equation 5.7 merely gives the photon positions in a different coordinate system, with the image centre at (0,0), to the ratios of equation 5.1, where (0,0) is at one corner of the image. Manual calculation eliminated the extra noise that would be introduced by the stretchers and quotient evaluators of the position encoding electronics. This technique could not be used for X-rays as sophisticated data handling facilities, able to store the individual output pulses for each event, were not available.

Accurate measurements of the linearity required knowledge of the precise position of the input pulse. A mask was constructed comprising a square 9x9 array of 2mm diameter holes, with a spacing between hole centres of 6mm, the central hole of the array being located at the centre of the anode. Inserting the probe through a hole in the mask allowed accurate location of the probe on the anode thus the relationship between (Q_X,Q_Y) and (X_i,Y_i) could be determined.

An image was recorded using the test probe, inserting it into each mask hole in turn and measuring the four filter amplifier outputs. The pulser rise time was set to be lower than the anode time constant so that the distortion was determined entirely by the anode/filter amplifier characteristics. Figure 5.4 compares the test probe image plotted in normalised coordinates* with the theoretical grid, predicted for the anode time constant of 5.2μs and filter amplifier time constant of 2.1μs (T_n=0.4), showing good agreement between the two. However, the predicted grid is slightly overscaled compared to that measured. With a glazed thick film resistor of the WFSXC anode type there may be a mismatch of source and anode impedance. The effect of this is to increase the rise times of the

* Anode edges are -1 to +1 for eqn 5.7 and 0 to +1 for eqn 5.5.

Figure 5.3 Approximate timing diagram for the imaging circuit.

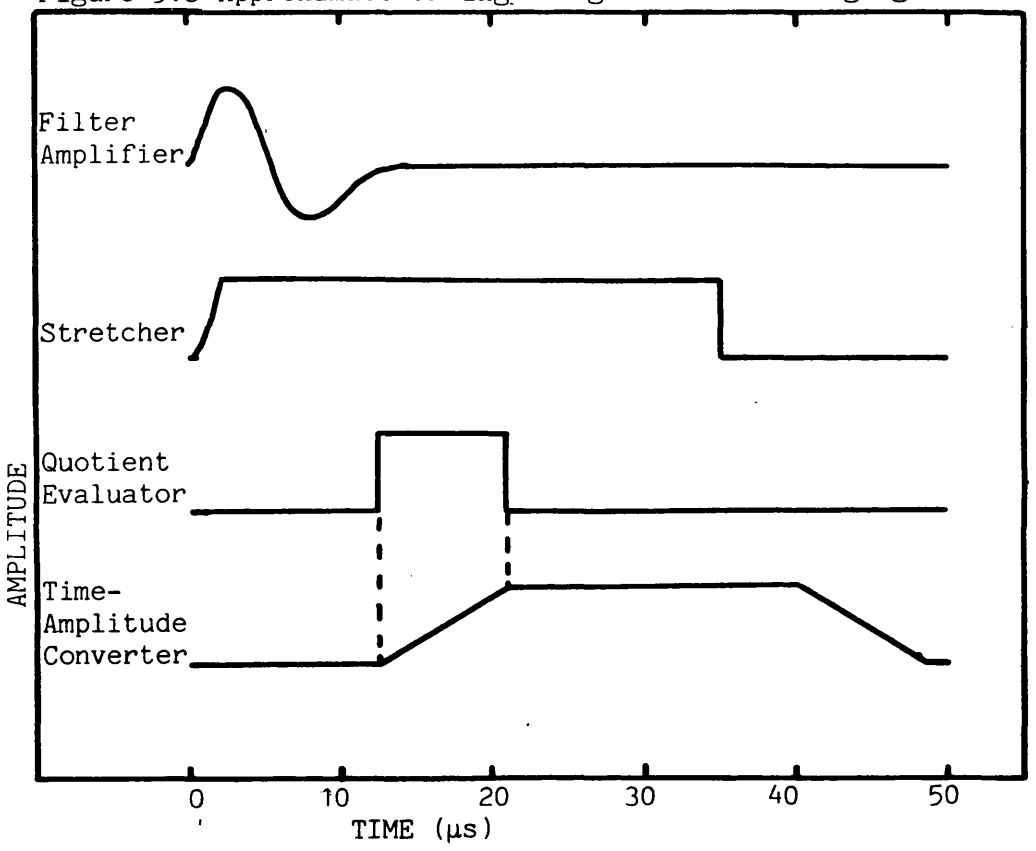

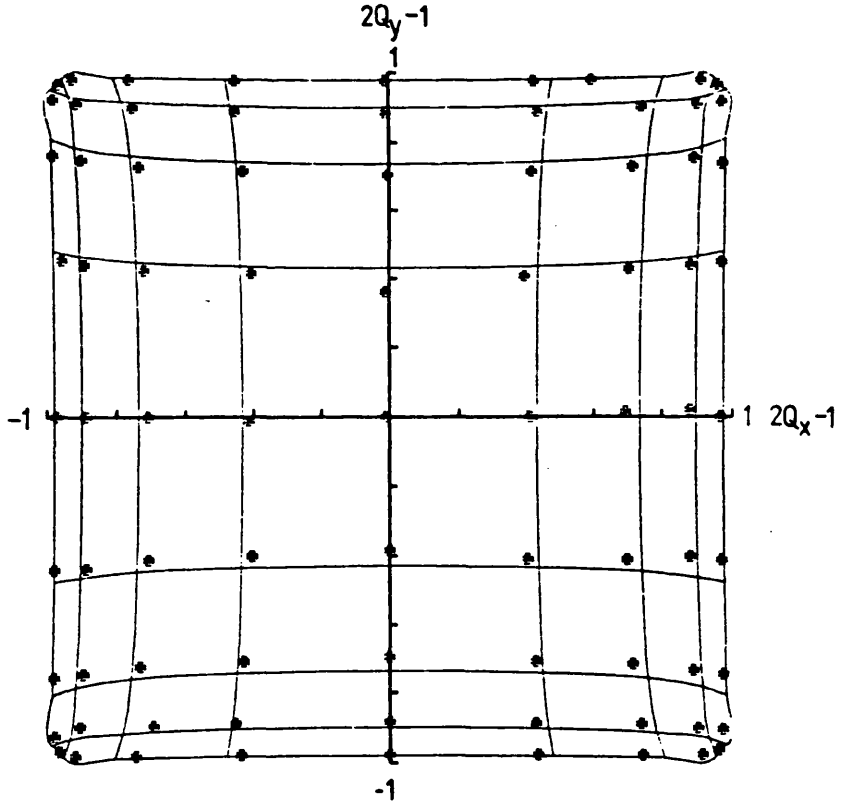

Figure 5.4 : **Comparison of measured (individual crosses) and theoretically predicted (the intersections of the full grid) difference ratios corresponding to charge injection via a test probe to a square anode with S electrodes, electrode fraction F = 0.67.** (figure by courtesy G.W. Fraser, 1980)

output voltages, an effective increase in the normalised time constant. The theoretical prediction assumed impulse current into the anode. The zero cross time was measured on the electrode and was found to be 4μs (=2.T_a) increasing discontinuously by ~3μs going onto the anode. Hence, T_n was underestimated accounting for the overscaling of the distortion figure.

The similarity of the measured distortion in all four quadrants of the anode showed that the anode was uniform, as suggested earlier by the similarity between measured values of R_1.

The test probe technique did not represent the "real" operating conditions of a detector. The pulser could not simulate the output pulse height distribution of X-rays expected from the MCP chevron, the short arrival time envelope of the charge cloud (~1ns compared with 100ns for the pulser rise time) or the spreading of charge across the anode in the rear MCP-anode gap. X-ray measurements were made by illuminating a mask of 50μm diameter holes with an X-ray beam covering the whole detector field of view. The holes were arranged in a similar manner to the test probe grid. Although they did not form a perfectly regular array the positions of all points on the grid were well known (figure 5.5). The circle in figure 5.5 is the detector field of view (36mm diameter) and the square the total anode area (54mmx54mm).

X-ray positions of the mask holes were recovered by recording the output of each TAC on a pulse height analyser generating first the X coordinate for each hole and then the Y coordinate. Recording the output of a single TAC gave a plot of the number of events in each channel position along the axis of the TAC integrated over all positions in the other axis. As the mask comprised several rows of

Figure 5.5 Diagram of the mask used for the X-ray imaging tests with the WFSXC detector. The outer square represents the anode area.

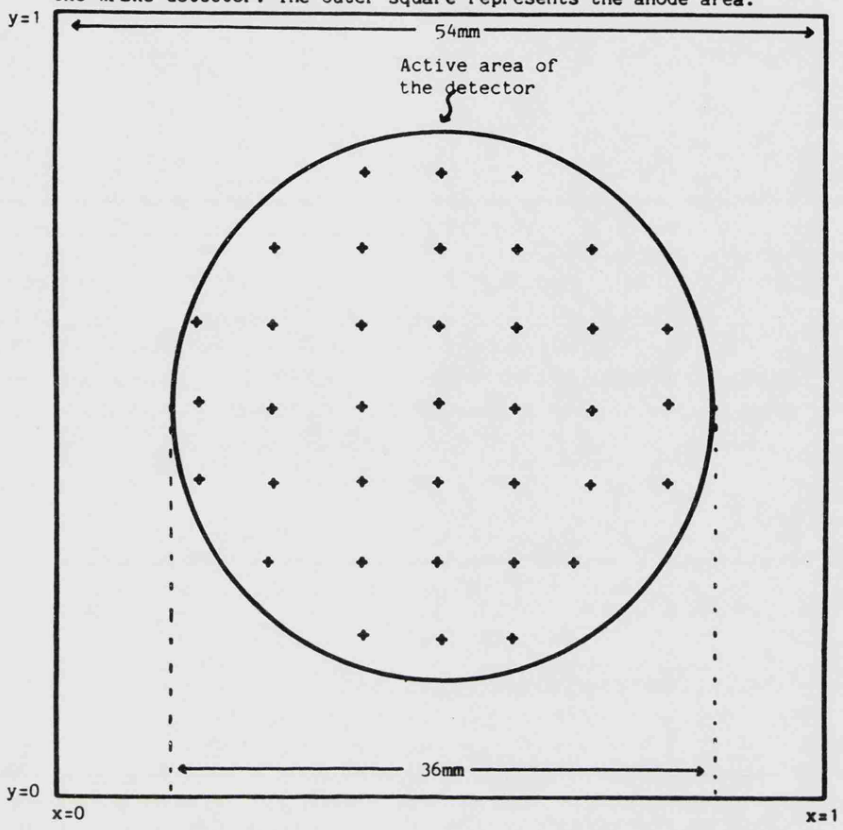

Figure 5.6 TAC output discriminated to show a single row of holes.

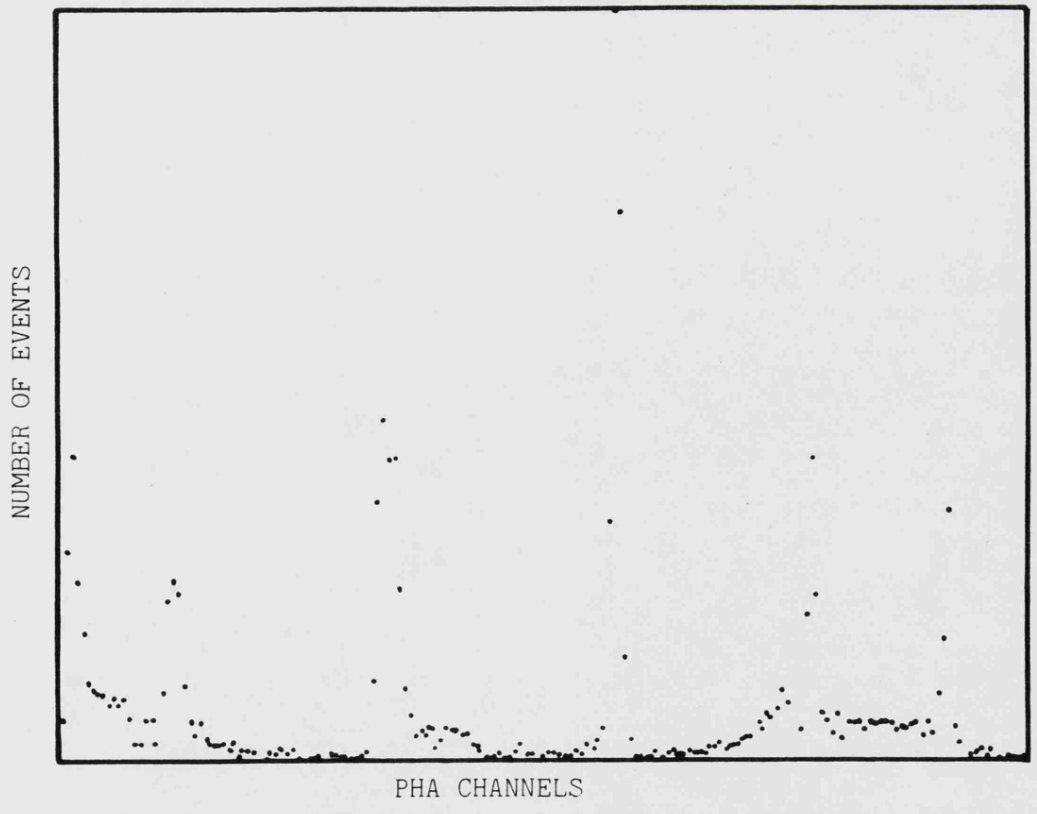

holes the 1-D plot of the TAC superimposed the rows onto each other. To recover accurate positions it was necessary to be able to select a single row of holes running parallel to the axis whose coordinates were required (figure 5.6). This was achieved by using appropriate discriminators on the other axis to reject all events outside two points denoting a band of coordinates within which the required row, but no other was found.

Figure 5.7 shows the measured X-ray image derived as described. The crosses shown are the peaks of the spatial X-ray distribution from each hole. The fractional area of anode used with the X-ray image was $A_E=(\sim 67\%)^2$ hence the distortion at the edge of the image was less severe compared to the test probe image (figure 5.4, $A_E=(89\%)^2$).

5.4.2 Linearisation of Anode Images

Fraser (1980, chapter 5) outlined two techniques of differing degrees of sophistication for linearising the distorted image obtained with a resistive anode.

A polynomial fitting technique was used to calculate the charge injection positions (X_i,Y_i) from the ratio estimate (Q_X,Q_Y), illustrated by the linearisation of the test pattern of figure 5.4. The restoration was carried out for $T_n=0.4$ (figure 5.8a) and also for an empirically assumed value of $T_n=0.55$ (figure 5.8b) taking into account the finite rise time of the input pulse.

Some residual distortion remains with the polynomial fitting technique, particularly at the anode edges. A more sophisticated technique, the "look-up" table in principle allows vanishingly small distortion levels over the whole anode area. A "look-up" table requires a knowledge of (X_i,Y_i) as a function of the estimates

Figure 5.7 The X-ray image from the test mask unlinearised.

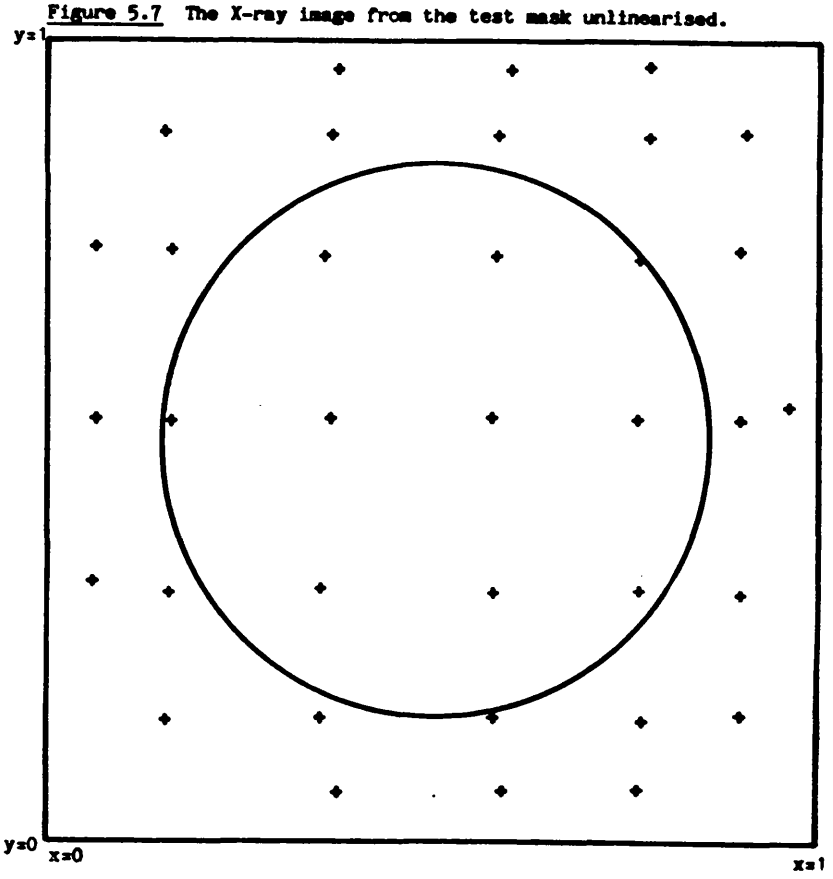

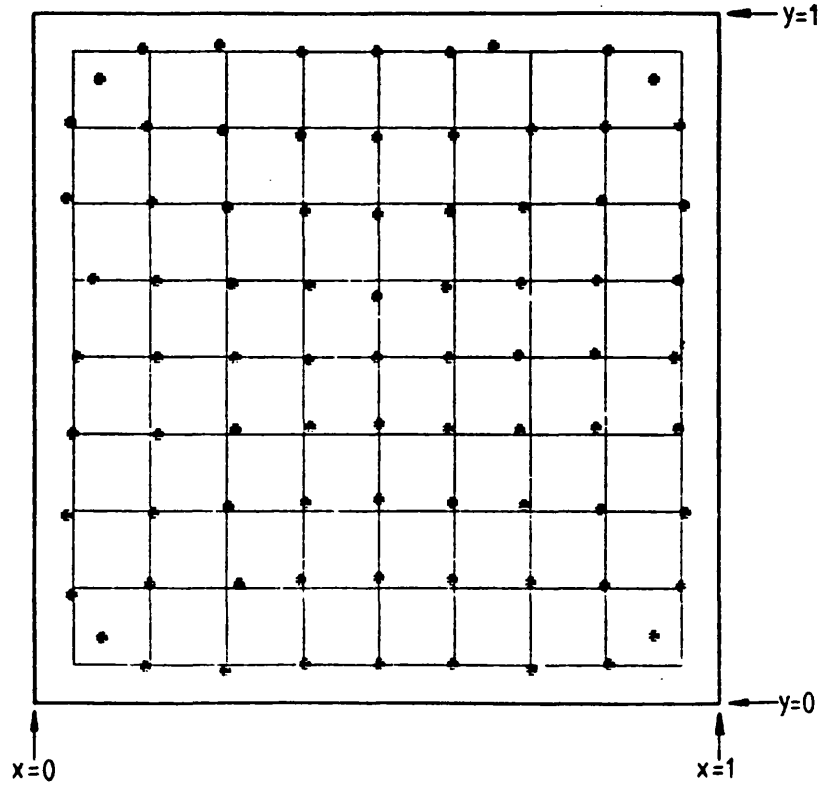

Figure 5.8a : Recovered positions (individual crosses) resulting from test probe charge injection to a square anode at the intersections of the solid grid. The outer border represents the edge of the grid. $T_n = 0.4$ assumed. (From Fraser, 1980)

(Q_X,Q_Y). A matrix of X_i is generated at regular intervals of Q_X and Q_Y using the predicted values of $Q_X(X_i,Y_i)$ and $Q_Y(X_i,Y_i)$ with an interpolation routine. The symmetry of the distortion makes the X_i and Y_i matrices identical. An estimate of the value of X_i from a value of Q_X is derived from a 20x20 matrix of $X(2Q_X-1,2Q_Y-1)$ by bivariate interpolation. Fraser (1980) expects that interpolation over six points of the 20x20 array will reduce δ to a level of less than 1% over the detector active area.

Figure 5.9 shows the restoration of the X-ray data of figure 5.7 by a matrix calculated for the WFSXC anode with T_n=0.27, the value for the anode+MCP configuration. The restoration is compared with original grid positions, which were corrected for the displacement of the image caused by the 15° angle of incidence of the X-ray beam and the distance of the mask from the detector. Good agreement can be seen over most of the detector area. However there is a discrepancy at the edge of the field of view.

The distortion parameter δ can be calculated for the linearised images to test the efficiency of the routines. A value of 0.7% is found for the "look-up" table linearisation (figure 5.9), calculated over all points in the array, covering a circle of diameter 64% of the anode side. By comparison δ is 1.76% and 1.57% for the test probe data, for T_n assumed to be 0.4 and 0.55 respectively (figures 5.8a and 5.8b). However, δ was measured over a larger anode fraction ($89\%^2$) than the X-ray data. Thus, the results confirm the usefulness of both methods of image restoration, giving confidence that they can be used on the flight data.

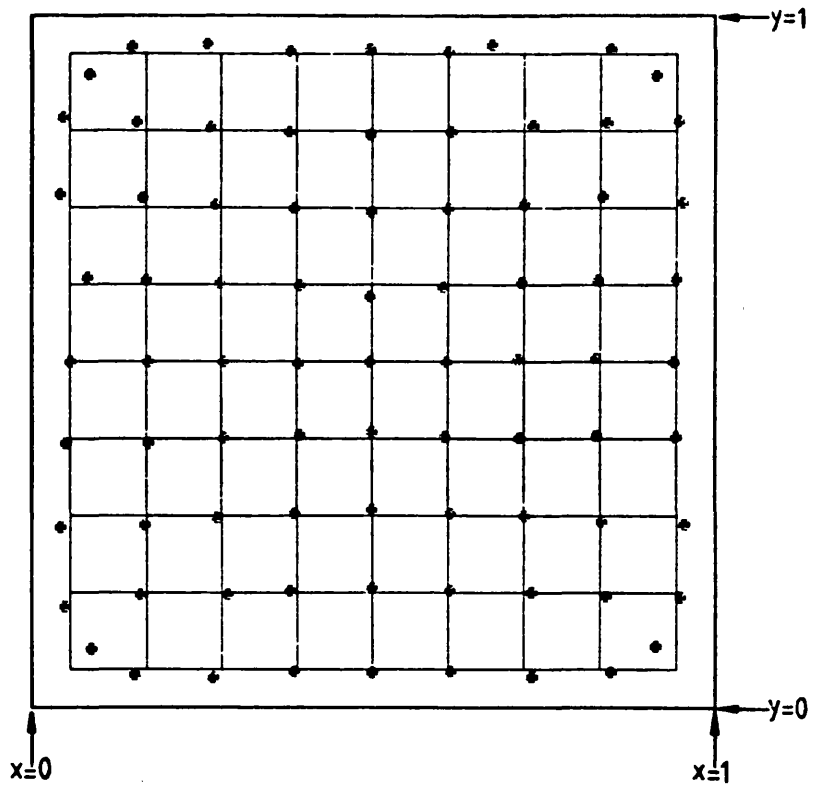

Figure 5.8b: **The experimental data of Fig.5.4 subject to linearisation under the empirical assumption that the normalised time constant, T_n, has the value 0.55.** (from Fraser, 1980).

Figure 5.9 Linearised X-ray image compared with the test mask.

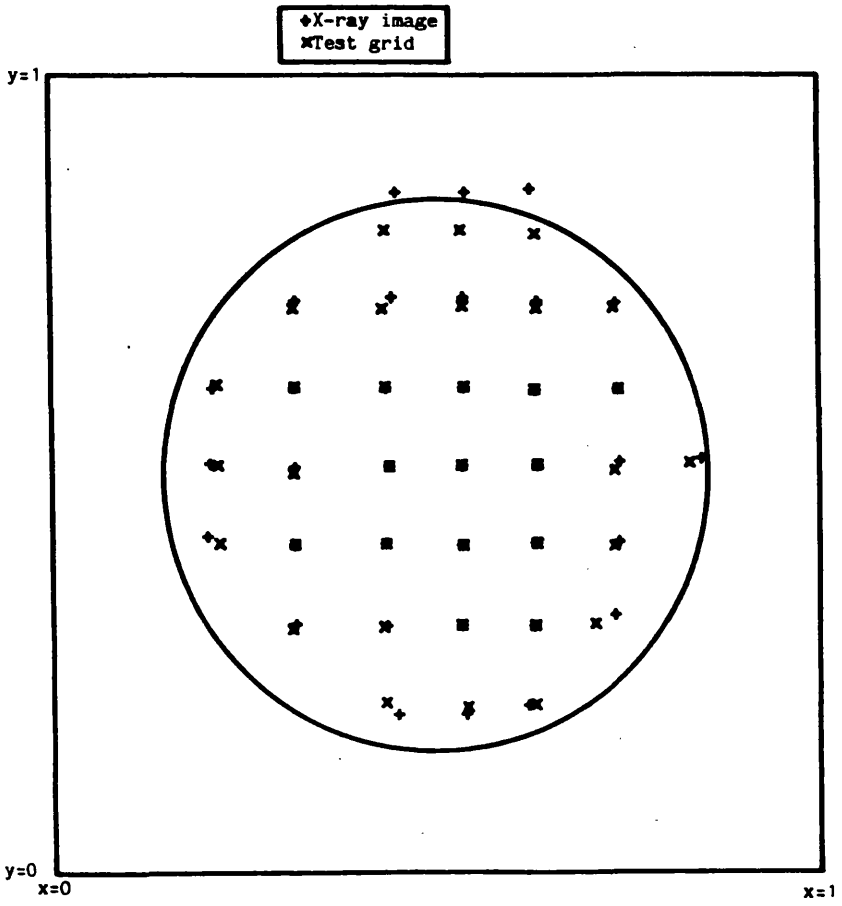

5.5 Anode Noise and Resolution

5.5.1 Electronic Noise

The equivalent noise charge (q_n) can be measured experimentally, by injecting charge (q_o) onto the centre of the anode using the test probe. In a perfect, noiseless system the output charge distribution from each pre-amplifier would be a delta function. The effect of noise in the system is to produce a population of output pulses distributed symmetrically about the delta function. The peak of the distribution from each electrode corresponds to one quarter of q_o, when q_o is injected at the centre, hence the RMS noise can be defined as

$$q_n = \frac{FWHM}{2.36} \cdot \frac{q_o}{4} \qquad (5.8)$$

where: FWHM is the full width half maximum of the signal from the electrode

In order to measure the noise, the output charge from the electrode is amplified, introducing an extra noise component. To determine q_n the pre-amplifier/filter-amplifier noise, measured by injecting charge directly into the pre-amplifier input, is subtracted quadratically from the total noise.

Figure 5.10 shows experimental values of q_n, averaged over measurements at each of the four output terminals, as a function of filter time constant and compares the data with the predictions of Fraser et al (1981). The experimental error bars represent the scatter on the anode noise at the four output terminals. Curve (1),

Figure 5.10 Comparison of measured an predicted RMS anode noise charge, q_n, as a function of the filter time constant (T_a). Curve 1 represents the prediction for an anode time constant of 5.3μs and curve 2 is the d.c. limit.

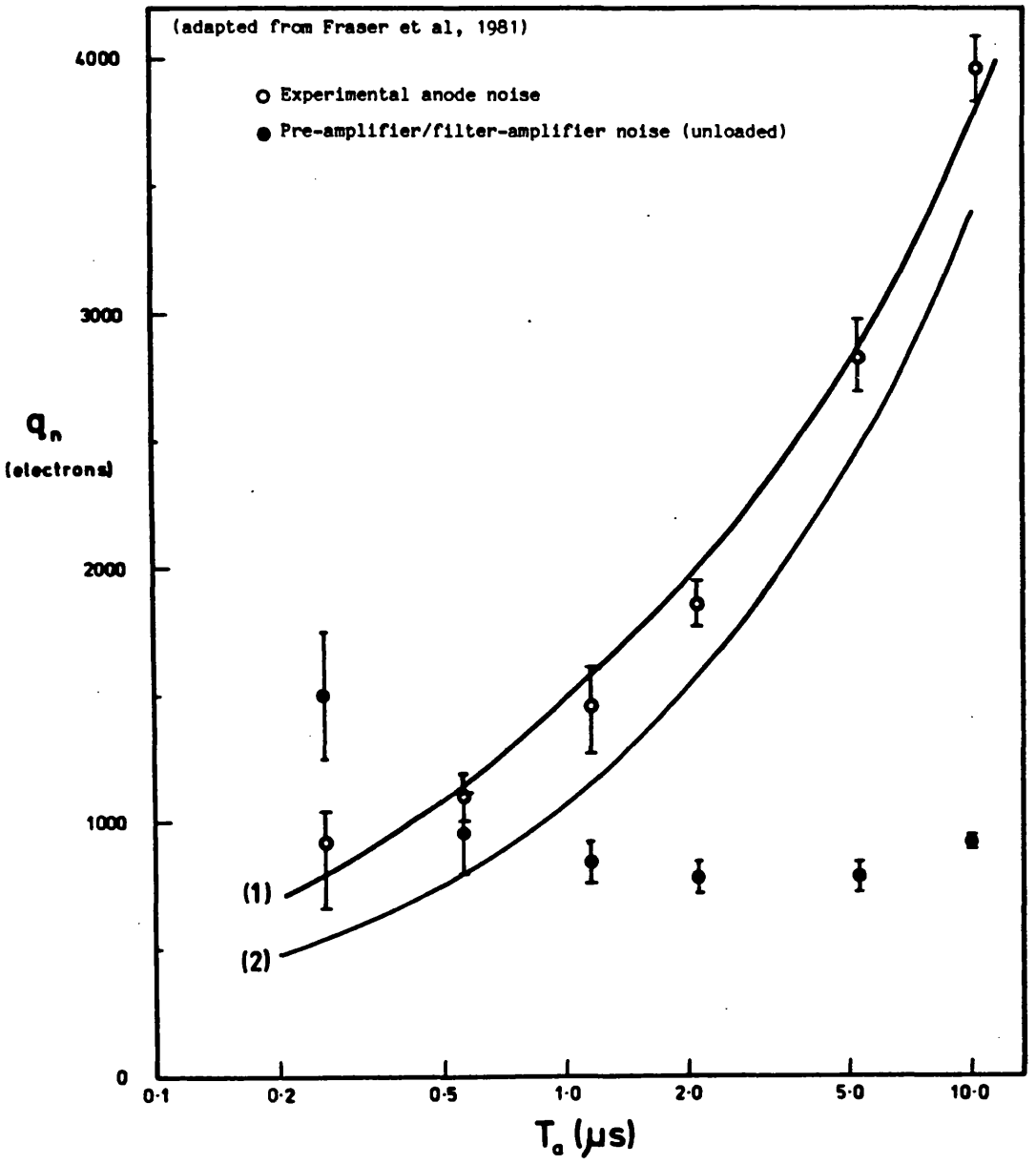

calculated for an experimental anode time constant $R_{\square}C/\pi^2$ of 5.3μs, shows good agreement with the experimental data. Curve (2), the prediction in the d.c. limit (the approximation of equation 5.3), gives a substantial underestimate of the anode noise.

5.5.2 Position Resolution

Test probe measurements of the anode/filter amplifier resolution were made in both anode axes by measuring the widths of the position peaks generated by the test probe, using the imaging electronics, at each point of the test grid. The full width half maximum resolution (in μm) at estimated coordinates (Q_X,Q_Y) in the X-axis was

$$dX(Q_X,Q_Y) = 6x10^{-3}.FWHM.2/\ (X_{n+1}-X_{n-1}) \qquad (5.9)$$

where: FWHM is the full width half maximum of peak n (analyser channels)

$(X_{n+1}-X_{n-1})$ is the distance between the adjacent peaks (analyser channels)

the linear spacing between peaks was 6mm

A minimum resolution of 80μm was found at the centre of the anode, increasing to ~600μm at the edge (figure 5.11). The theoretical FWHM resolution (solid curve, 2.36xRMS resolution), derived from equation 5.4 with D(X,Y) calculated for the WFSXC anode (T_a=2.1μs, q_n~2000 electrons, pre-amplifier/filter-amplifier noise ~900 electrons), only showed reasonable agreement with the experimental data at the anode centre.

As can be seen in equation 5.4 dX is proportional to $1/q_o$. The resolution at the anode centre, as a function of input charge, is compared in figure 5.12 with the theoretical predictions calculated from equation 5.4. As expected the resolution decreases as q_o increases. However, the theoretically predicted curve falls below the experimental points.

The theoretical prediction of the resolution does not take into account the effects of noise from the processing electronics. As q_o increases the contribution of the anode to the net resolution of the system becomes smaller than the contribution from the rest of the electronics. If q_o is sufficiently high, the measured resolution will be entirely electronic. Assuming that this limit occurs at q_o=4pC gives an electronic contribution of ~40μm, from figure 5.12. Adding this noise contribution quadratically to the theoretical prediction (broken line in figure 5.12) gives good agreement with the experimental resolution. Towards the edge of the anode the dynamic range between signals from opposite electrodes is ~25:1, hence the signal-to-noise of one component of the ratio becomes small. A resulting increase in electronic noise is probably responsible for the difference between theory and experiment in figure 5.11.

X-ray resolutions were measured with a mask of 50μm diameter holes arranged in the shape of a cross with 3mm spacing. The resolution was determined from the FWHM of each hole image (figure 5.13), as for the test probe, and 50μm was subtracted quadratically to account for the finite beam size. This data was of poorer resolution than the test probe data, being ~100-120μm at the anode centre. At 0.25 (normalised coordinate) from the centre the X-ray resolution is ~300μm at one side and 150μm at the other.

Figure 5.11 Resolution along a line bisecting the anode along the X-axis, with the test probe. q_o=1pC, T_a=2.1μs, y=0.5.

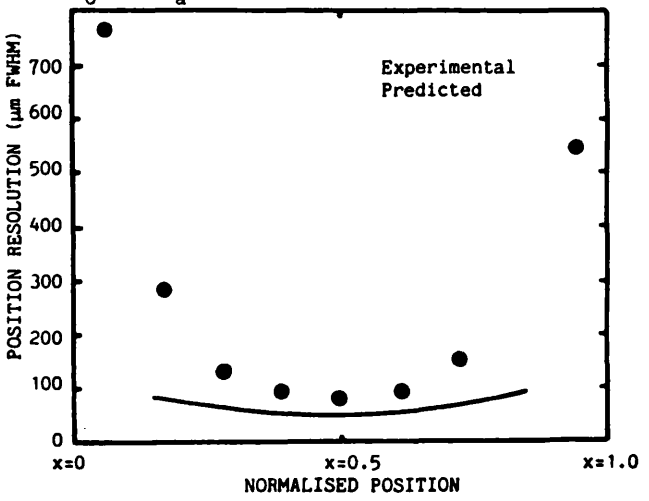

Figure 5.12 Position resolution as a function of the input charge at the centre of the anode. T_a=2.1μs

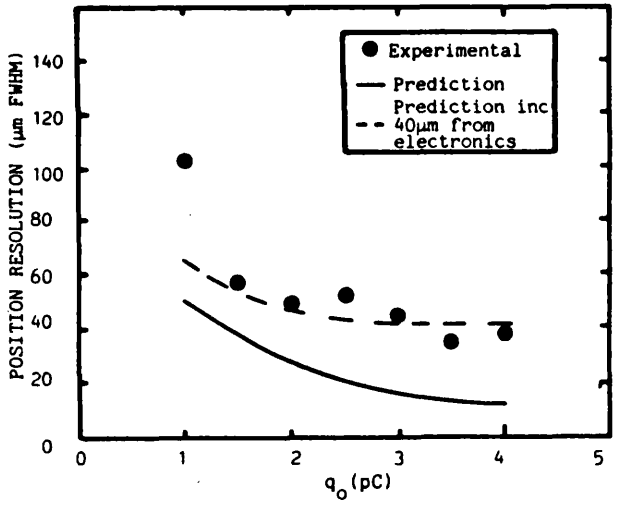

Figure 5.13 Position resolution measured using X-rays. Detector peak gain =3pC. 50μm subtracted quadratically for the source width.

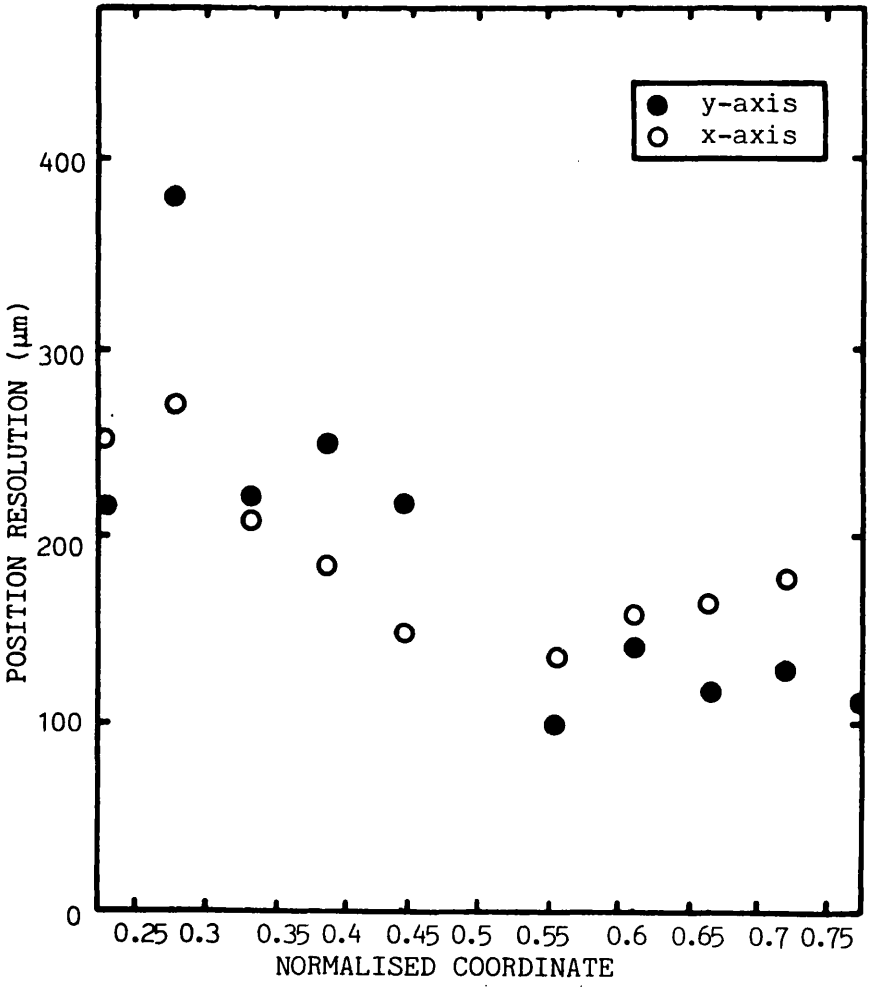

As the detector gain was ~3pC a resolution of 46μm (including the 40μm electronic contribution) was expected from the theoretical model. However, the output charge from the detector had a range of charge levels. All the events below 3pC will have had a poorer resolution leading to a worse average resolution than expected. The asymmetry either side of the anode centre is most likely to have been caused by the noise contribution from the quotient evaluator, which derived the positions according to equation 5.1. For an event of given input charge, when the numerator of the ratio is small (at 0.25 in figure 5.13) the QE signal to noise is lower, and hence the resolution poorer, than when the numerator is larger (at 0.75 in figure 5.13).

5.6 Conclusion

This chapter has demonstrated how the resistive anode operates. Experimental distortion measurements agreed with the theoretical predictions of Fraser (1980). Fraser's restoration techniques have been applied to the distorted X-ray and test probe images and were shown to work with low residual distortion, $\delta = 0.7\text{-}1.8\%$. It was reasonable, therefore, to apply either of these techniques to the WFSXC flight data. The "look-up" table was chosen as it was tested with X-rays ("real" conditions) and also had the lowest residual distortion.

Both test probe and X-ray resolution measurements demonstrated that, at the centre of the field of view, the detector was capable of achieving the required 230μm (FWHM) resolution, ~100μm being measured. At the edge of the field (a normalised position of 0.33 from the detector centre) the mirror resolution, for the displaced detector, was predicted to be ~23'=2300μm (FWHM) compared to a detector

resolution of 150-300μm with X-rays. Consequently the performance of the detector was well within the specification.

Although it has been demonstrated that the WFSXC detector performs with the specified resolution, the Leicester test electronics were used for the measurements. The flight filter amplifiers were designed to have the same shaping characteristic as the test amplifiers. Hence the distortion characteristics and resolution of the anode/filter-amplifier combination should be the same, but the contribution to the resolution from the payload ratio calculation may be different.

CHAPTER 6

FILTERS FOR THE WFSXC

6.1 Introduction

As discussed in chapter 2, the WFSXC requires filters to determine the bandpass of the instrument and to reject background radiation from geocoronal lines. Filter materials that can be used in the EUV fall into two general categories: organic plastic films where the bandpass is in the range 50-200Å, and thin metal films for the range ~100-1000Å. To obtain adequate transmission in the required bandpasses it is necessary to construct the filters using very thin films (<0.5μm) as a result of the high absorption cross section of most materials in the EUV. Therefore the films must be supported by highly transparent metal grids to provide mechanical strength. Pinholes may be a problem in thin films leading to unacceptable transmission of geocoronal background. This problem can be avoided by, where possible, building the filters out of several separate layers of material.

The possible choices of filter materials able to provide band passes between 50 and 800Å had been reviewed, before the start of the WFSXC project, for the ASTP and EXUV missions (table 6.1). Three combinations of materials give bandpasses in the WFSXC band (50-~300Å) - parylene N (a plastic, C_8H_8), parylene N + beryllium and aluminium + carbon. These three filter combinations were suitable for the MgF_2 coated detector of the first rocket flight. However, the introduction of a CsI photocathode, enhancing the far-UV and UV sensitivity of the detector, for the second flight lead to poor background rejection with the parylene filter. Consequently another plastic material, lexan ($C_6H_{14}O_3$), was chosen and used in a composite filter with carbon. The

design, optimisation and testing of the filters, for both flights of the WFSXC are described in this chapter.

6.2 Filter Requirements

The WFSXC filters have a two fold purpose, to define the bandpass of the instrument and to reject sources of background events.

There are three sources of background - geocoronal radiation (section 1.6), the diffuse XUV radiation (section 1.6) and the detector background (section 3.2)- which cover the whole WFSXC field of view. The total background (B, counts $s^{-1}ster^{-1}$) can be estimated by equation 6.1.

$$B = \left(B_D + \frac{B_X . G}{\lambda_2 - \lambda_1} + \sum_i B_i . E_i \right) A \qquad (6.1)$$

where: B_D (counts $cm^{-2}s^{-1}ster^{-1}$) is the detector background

B_X (counts $cm^{-2}s^{-1}ster^{-1}$) is the XUV background

B_i (counts $cm^{-2}s^{-1}ster^{-1}$) are the fluxes from geocoronal lines

E_i are the instrument efficiencies at the line wavelengths

The other parameters are as defined in section 2.3

A further possible source of background events is that from hot O or B stars which may be bright enough in the far-UV to be detected by the instrument. Unlike the other sources of background the flux from a stellar source will only cover an area of the size of the point response function of the WFSXC. The observed flux from a star could be a problem in two ways, either by saturating the electronics if the

count rate is very high or by causing an apparent detection of an EUV source.

The thicknesses of the filters must be chosen with the aim of achieving the maximum sensitivity for the WFSXC (minimum F_{min}, equation 2.12), taking into account the mirror response, the detector quantum efficiency and the non-stellar background (B). The optimised filters must then be sufficiently thick to reject the flux from hot stars in the far-UV and UV bands.

6.3 Filter Absorption

6.3.1 The Process of X-ray Absorption

It is necessary to understand the absorption behaviour of the materials which comprise the filters in order to predict filter transmissions and optimise their thicknesses. The absorption of a material can be quantified by its linear absorption coefficient (μ_l, cm^{-1}) from which the fractional transmission (T_F) can be calculated by the relation

$$T_F = e^{-\mu_l \cdot t_F} \qquad (6.2)$$

where: t_F is the filter thickness (cm)

The fractional absorption is $1-T_F$. μ_l is proportional to the mass absorption coefficient (μ, $cm^2 gm^{-1}$) and the density of the absorbing medium (ρ, $gm\ cm^{-3}$); $\mu_l = \mu . \rho$.

At X-ray energies below 50keV the principal absorption process is the photoelectric effect. The probability of a photoelectric absorption on a particular atomic electron is an increasing function

of decreasing X-ray energy. However, when the energy becomes smaller than the binding energy of the electron the probability of absorption drops to zero because there is no longer sufficient energy to eject the electron. Absorption then takes place in the next "shell" of electrons which have lower binding energies. The discontinuous decrease in absorption probability at this point is known as the absorption edge.

The mass absorption coefficient (μ) is an expression of the absorption probability and can be calculated from the theory of quantum electrodynamics for each element. Cromer and Liberman (1970) (hereafter C&L) have produced theoretical listings of the absorption profiles of most elements. These listings have been used in conjunction with computer programmes to calculate μ for any material from the weighted sum of the absorption profiles of its component atoms. The calculations have been shown to agree very well with experimental data to within a few eV of the absorption edge energy at soft X-ray wavelengths (Willingale, 1979).

The accuracy of the model depends upon the accuracy of the wave functions used and the extent to which the shielding from the nucleus of the outer electrons, by the inner electrons, is taken into account. In addition the model assumes that the absorbing medium is composed of free atoms. Hence, at energies below the soft X-ray band, where the outer electrons of the atom are involved in the absorption, the model might be expected to break down as electron shielding, the band structure in metals and the delocalisation of electrons (in material having covalent bonds) influence the electron energy levels, which therefore differ from those predicted by the wave functions of the model.

6.3.2 A Summary of Linear Absorption Coefficients for the WFSXC Materials in the Range 10-4000Å

Mass absorption coefficients of parylene N (Par N) have been measured throughout the EUV and far-UV by Stern and Paresce (1975). Values of the linear absorption coefficient (derived assuming ρ=1.11gm cm^{-3}), are summarised in figure 6.1. Predictions of μ_1 (10-1000Å) based on the C&L model are shown for comparison, agreeing with Stern and Paresce up to ~100Å.

There are several sources of beryllium absorption data in the XUV - Johnston and Tomboulian (1954, 60-200Å), Henke and Elgin (1970, 50-200Å), Mulder and Vrakking (1978, 304 and 584Å) and Rustgi (1965, 304Å). The imaginary component of the refractive index (k) of Be has been measured in the EUV (480Å-1200Å) by Toots et al (1968), from which the linear absorption can be calculated

$$\mu_1 = 4\pi k/\lambda \qquad (6.3)$$

However, beyond 1200Å no further data exists, as far as can be ascertained from the literature. All the above data are summarised in figure 6.2. It can be seen in figure 6.2 that the data of Johnston and Tomboulian differs substantially with that of Henke and Elgin but the latter agrees with the C&L prediction.

Hagemann et al (1974) have measured the optical constants of several materials between far infra-red and X-ray wavelengths. The data suggests that metals of low Z (eg. Mg, Al) are strong absorbers in the far-UV. The densities of Be and Mg are very similar (1.85 and 1.74 gm cm^{-3} respectively) and they lie in the same group of the

TABLE 6.1 Extreme-Ultraviolet Filter Designs

Filter	Bandpass (Å)	
0.5μm parylene	55 - 150	
parylene + 0.3μm Be	114 - 150	ASTP Mission
1500Å Al	170 - 620	(Paresce, 1977)
1500Å Sn	500 - 780	
900Å parylene + 900Å Al	140 - 280	
500Å C + 2500Å Al	170 - 490	EXUV Phase A Study
2100Å Sb	400 - 570	(ESA, 1979)
900Å Sn + 1000Å Al	475 - 715	

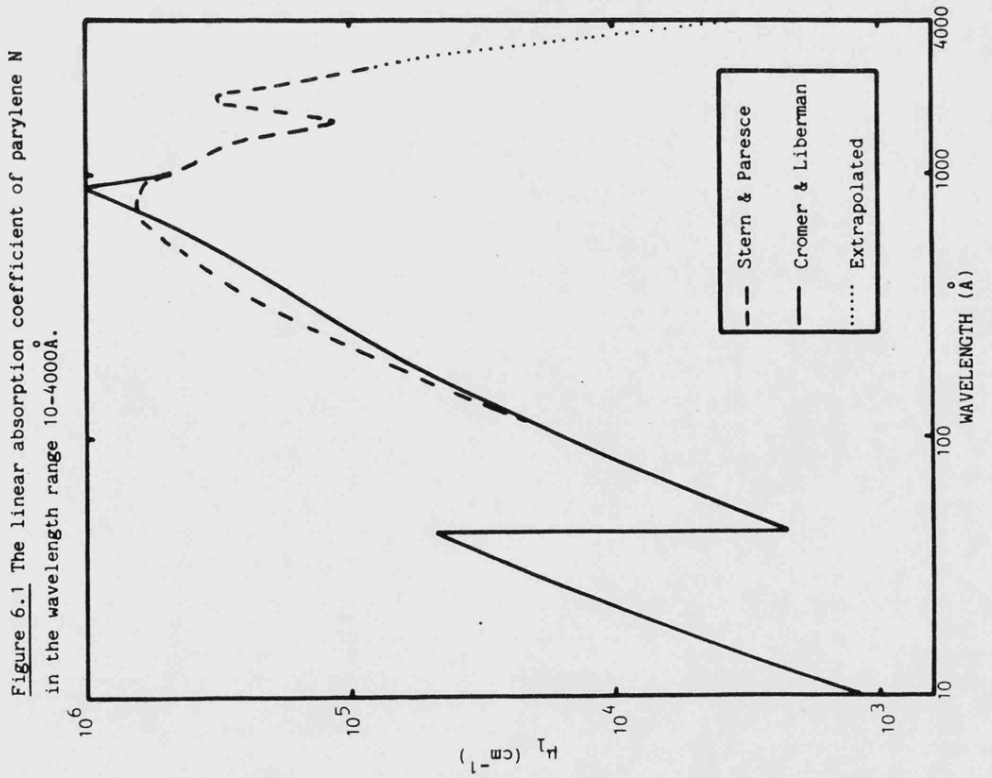

Figure 6.1 The linear absorption coefficient of parylene N in the wavelength range 10-4000Å.

periodic table. Therefore, their absorption properties would be expected to be similar. For the purposes of the background analysis the linear absorption of Be was assumed to approximate to that of Mg in the far-UV (included in figure 6.2). The assumed values of μ_1 are below those inferred from the data of Toots et al, where the ranges overlap, and give lower limits to the absorption coefficient.

Very little experimental data exists for lexan (figure 6.3). Huizenga et al (1979) have measured the XUV absorption (237Å, 256Å and 304Å) and in the far-UV Fabricant et al (1979) obtained lower limits between ~1600 and 2000Å. At wavelengths above 2400Å lexan becomes transparent (Williamson and Maxson, 1975). Consequently heavy reliance must be placed upon the C&L model to predict lexan transmissions.

Figure 6.4 shows the absorption data of Hagemann et al (1974) and Samson and Cairns (1964) for carbon and includes, once more, the C&L prediction. The two experimental data sets obviously differ. Samson and Cairns prepared thin carbon films by evaporation of carbon onto microscope slides, floating off the carbon in a water bath and then picking up the filter on a transparent screen, while Hagemann et al dealt with "glassy" carbon. As the WFSXC filter was manufactured by the method of Samson and Cairns their data is most appropriate for prediction of the filter response. Towards the UV the two data sets converge, hence the data of Hagemann et al can be used to model the carbon absorption longward of 2000Å.

Finally, absorption data for aluminium, taken from Hagemann et al (1974), is shown in figure 6.5 with the C&L prediction from 10 to 1000Å.

Figure 6.2 The linear absorption coefficient of beryllium in the wavelength range 10-4000Å.

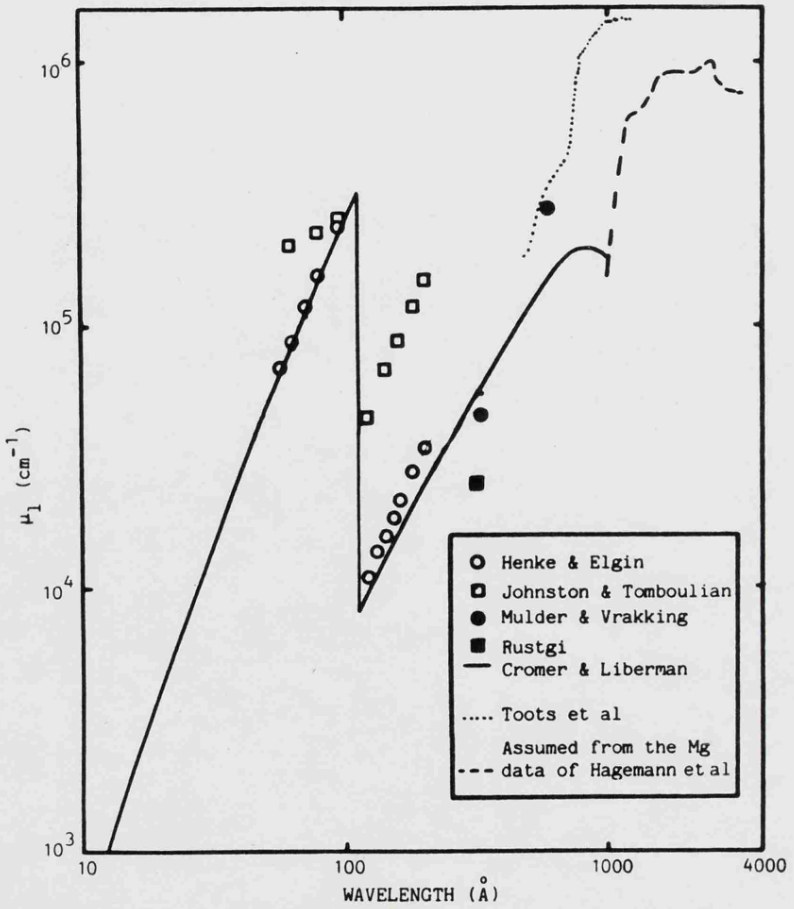

Figure 6.3 The linear absorption coefficient of lexan in the wavelength range 10-4000Å.

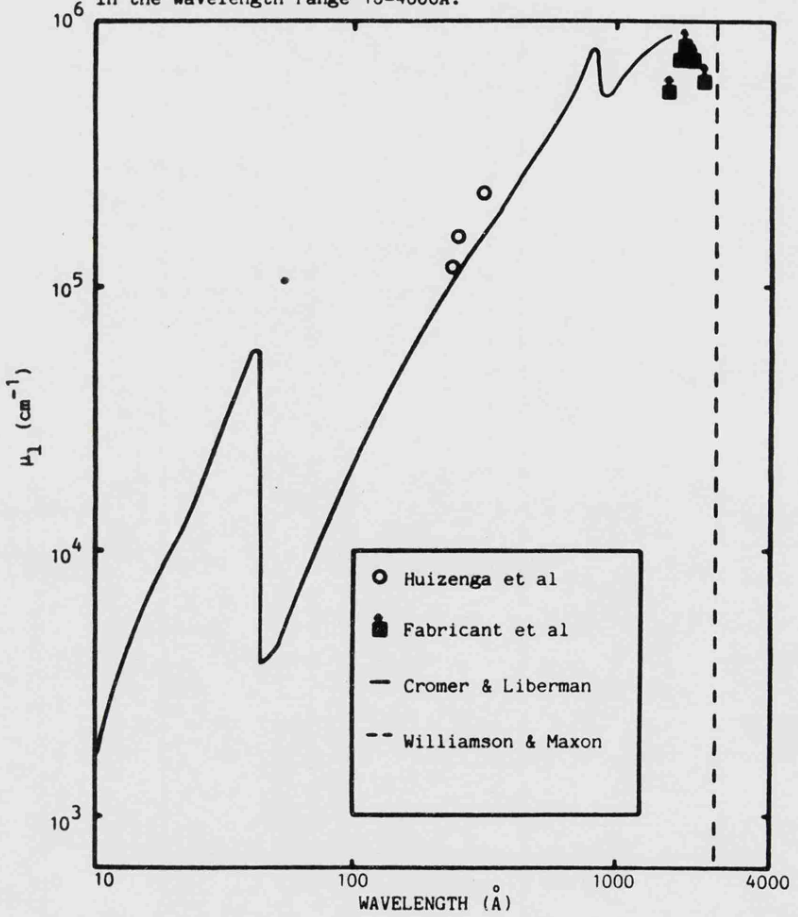

Figure 6.4 The linear absorption coefficient of carbon in the wavelength range 10-4000Å.

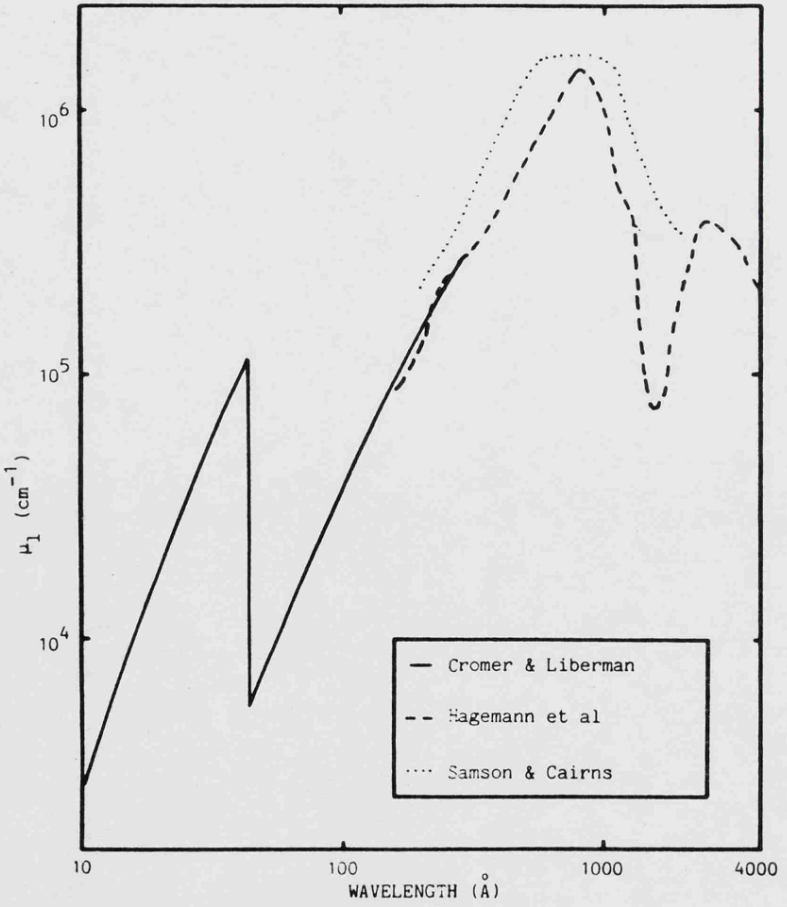

Figure 6.5 The linear absorption coefficient of aluminium in the wavelength range 10-4000Å.

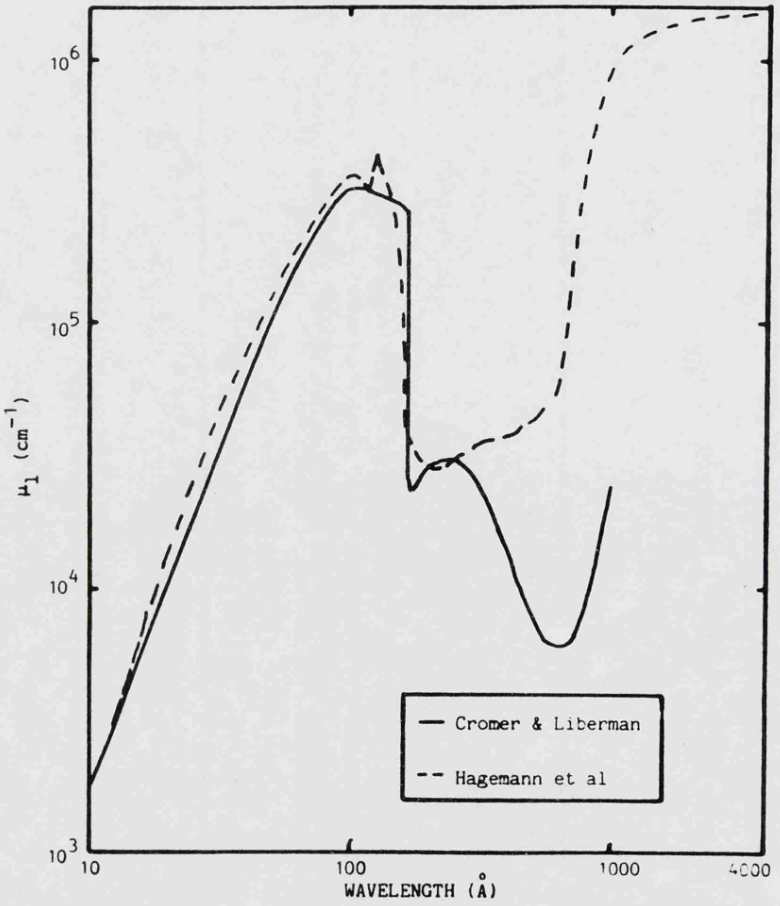

6.3.3 Experimental Measurements of Par N and Beryllium Linear Absorption Coefficients in the XUV

It was thought necessary to resolve the discrepancy between the Be data of Johnston & Tomboulian and Henke & Elgin by calibrating the filters manufactured for the first flight, 5000Å Par N and 2500Å Be + 1000Å Par N.

Transmission measurements were carried out on both beryllium/Par N and Par N filters at 237Å, 256Å and 304Å using an EUV calibration facility at the Space Science Laboratory, University of California, Berkeley, California. The Berkeley facility comprises a hollow cathode discharge tube and an EUV monochromator. A channel electron multiplier with a collecting area of $\sim 1 cm^2$ was used to determine the count rate from the 1mm diameter pencil beam. Using the 304Å line, transmission measurements were performed at a number of locations on each of the two filters to confirm their uniformity. A single location on each was then selected for further measurements. At each wavelength, a series of 10-second integrations were taken with the two filters in the beam in turn. An incident flux of $10^4 s^{-1}$ (stable over the entire run) ensured that a filtered signal was detected at all wavelengths. In addition, readings were taken at a wavelength removed from the line, with and without the filters in place, in order to determine the flux of ultraviolet light scattered in the monochromator and, with the beam off, to measure the detector background. The transmissions determined for the two filters at each of the three wavelengths, corrected for background and detector dead time ($\sim$10% at $10^4 s^{-1}$), are listed in table 6.2.

Table 6.2 Measured filter transmissions.

Wavelength Å	Parylene N (5000Å) UNIT I	Beryllium & Parylene N (2500Å) + (1000Å) UNIT I	Beryllium & Parylene N (2500Å) + (3000Å) UNIT I *
2.75	0.89 ± 0.01		
13.34			0.78 ± 0.01
14.56	0.79 ± 0.01		
17.59	0.72 ± 0.01		0.67 ± 0.01
44.7	0.76 ± 0.01		0.28 ± 0.01
67.6	0.57 ± 0.01		0.048 ± 0.001
237	0.0017 ± 0.0001	0.102 ± 0.001	
256	$7.0\times10^{-4} \pm 2.0\times10^{-4}$	0.084 ± 0.002	
304	$3.7\times10^{-5} \pm 9\times10^{-6}$	0.028 ± 0.005	

* Before the soft X-ray measurements, 2000Å of extra parylene N were added to the beryllium filter.

Wavelength Å	Beryllium & Parylene N (2500Å) + (1000Å) UNIT II	Beryllium & Parylene N (2500Å) + (1000Å) UNIT III
2.75	0.93 ± 0.02	
13.34	0.82 ± 0.01	0.79 ± 0.01
14.56		
17.59	0.73 ± 0.03	0.75 ± 0.02
44.7	0.32 ± 0.02	0.33 ± 0.02
67.6	0.09 ± 0.01	0.099 ± 0.008
237		
256		
304		

All transmissions quoted are uncorrected for the effects of the nickel mesh.

The soft X-ray calibration was carried out using the Two-Crystal Bragg Spectrometer at Leicester University (Hall, 1982) for wavelengths between 2.75Å and 67.6Å. In the Leicester facility soft X-rays are generated by a conventional fluorescent X-ray source and the required wavelengths selected using a crystal monochromator. The detector is a gas-filled proportional counter with a thin polypropylene window. Transmission measurements were performed on three filter units, one of which was the unit calibrated at Berkeley (Unit I). Since the beam intensity changed with wavelength it was necessary to vary integration times between 40 and 200 seconds in order to maintain measurement uncertainties at similar levels. The flux into the proportional counter was monitored with and without the two filters and with test filters of known transmission (1μm polypropylene, 5μm aluminium) for wavelength calibration. Background corrected transmissions of three Be/Par N filters and the Par N filter calibrated at Berkeley are presented in table 6.2.

In order to infer the values of μ_1 for Be from the transmission measurements, it is necessary to take account of the absorption of the Par N and that due to a nickel supporting mesh. The transmission of the mesh is provided by the measurements at 2.75Å, where absorption by either filter is negligible. The average mesh transmission is 0.91 ± 0.03. It thus becomes possible to compute μ_1 for Par N from the corrected values of the transmission through the Par N filter. The uncertainties in μ_1 reflect a combination of the measurement errors and the tolerance on the filter thickness (~5%) as quoted by the manufacturer (Lebow Company, Goleta, California). In figure 6.6 the values of μ_1 are plotted as a function of wavelength along with measurements made by Stern and Paresce (1975). The strong agreement

between the two sets of values suggests that the above transmission measurements are reliable, and serves as an indirect consistency check for the two measurement techniques, for which no wavelength overlap exists. In addition, it provides confidence that the effect of the Par N layer on the transmission of the Be/Par N film can be properly considered and μ_1 be obtained for Be. The values of μ_1 inferred in this manner for Be are plotted in figure 6.7 along with the data of other authors.

6.3.4 Discussion of the Absorption Data

The values of μ_1 measured for Be in section 6.3.3 above (figure 6.7) agree with Henke and Elgin, within measurement errors, either side of the K edge. This indicates that the data of Johnston and Tomboulian is incorrect.

A Be surface forms an oxide layer of typical thickness ~100Å when exposed to air, which protects the metal from further oxidation up to temperatures of ~500°C in air (Mulder and Vrakking, 1978). Some previous determinations of μ_1 may have been affected by the presence of the oxide. If a 1000Å Be film is used, then the oxide layer comprises ~20% of its thickness and would increase the inferred linear absorption coefficient by a factor ~2 at 304Å. In contrast, the values of μ_1 measured in section 6.3.3 are relatively insensitive to the presence of an oxide layer. Since only one surface of the Be is exposed to air (the other is covered by Par N) and a 2500Å thick foil is being used, the oxide layer will comprise only ~4% of the foil thickness. This would raise the calculated linear absorption coefficient at 304Å by only ~25%: in comparison, the measurement error at this wavelength is 18%. Johnston and Tomboulian (1954) used a

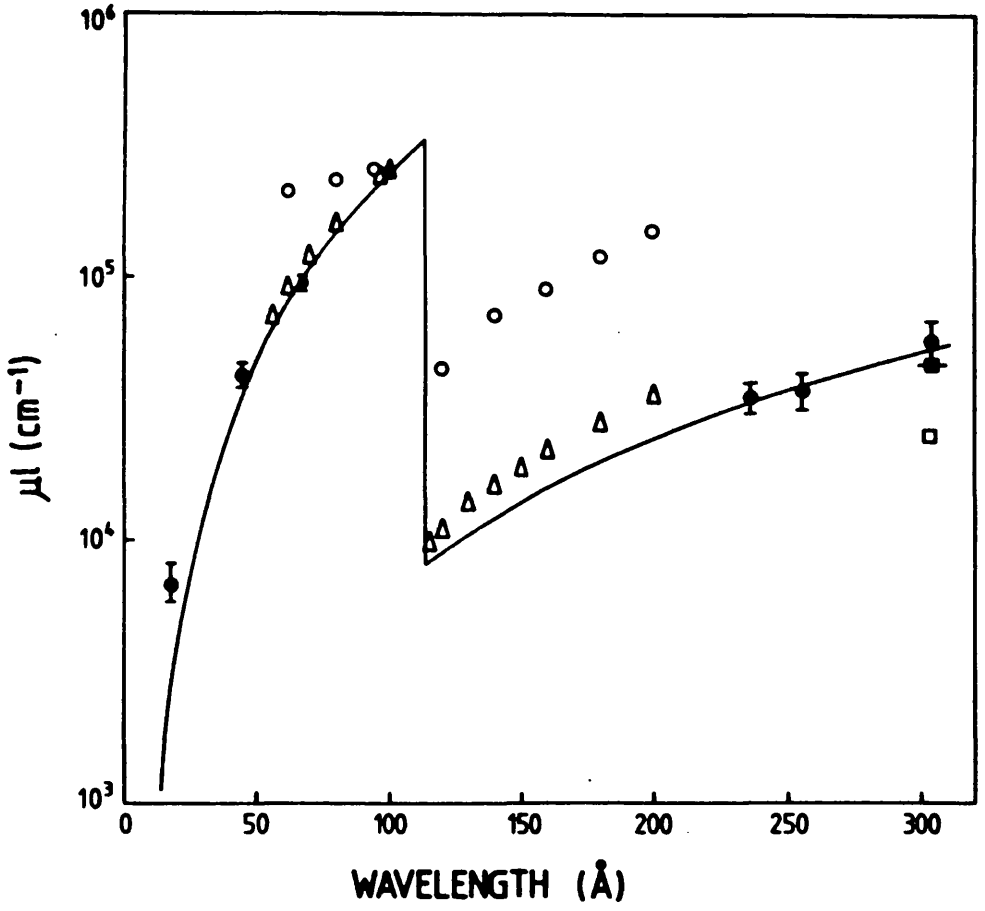

Figure 6.7 Linear absorption coefficient of beryllium as a function of wavelength in the XUV. The measurements of this thesis (filled circles) are compared with those of Johnston & Tomboulian (open circles), Henke & Elgin (open triangles), Mulder & Vrakking (filled square) and Rustgi (open square). The solid curve represents the rpediction of Cromer & Liberman.

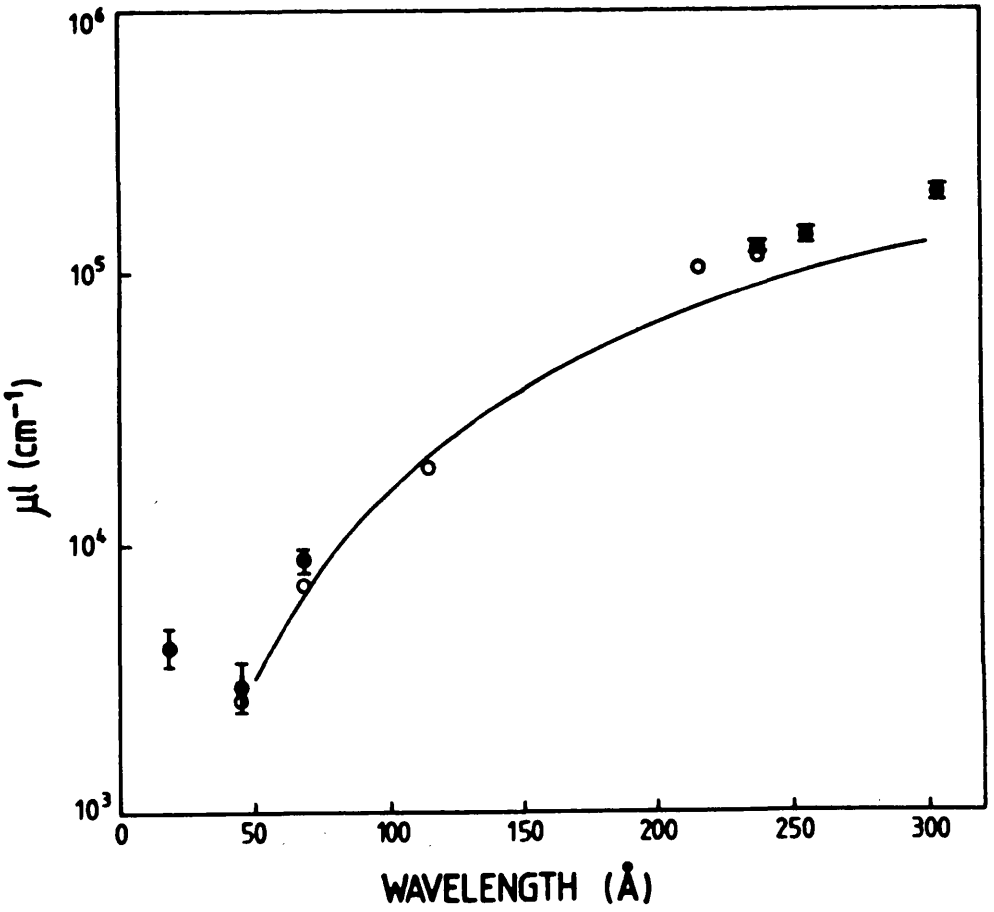

Figure 6.6 Linear absorption coefficient of Par N as a function of wavelength in the XUV. The measurements of this thesis (filled circles) are compared with those of Stern & Paresce (open circles). The solid curve is the prediction of Cromer & Liberman. The half filled circles represent near identical results.

sample of 1000Å thickness, hence the discrepancy in the results does not appear to be entirely explained by the presence of an oxide layer.

The Be and Par N absorption data can also be used to test the C&L model (the solid curves in figures 6.6 and 6.7) in the XUV. The Be curve agrees very well with the experimental data at all points (up to 300Å), whereas above ~100Å the predicted curve for Par N is lower than the measured values of μ_1. Comparisons of the model with the data of other authors at longer wavelengths (>300Å), Stern and Paresce (1975) (figure 6.1) and Toots et al (1968) (figure 6.2) for Par N and Be respectively, confirm these results. Similar behaviour is observed for lexan (figure 6.3), carbon (figure 6.4) and aluminium (figure 6.5).

Consequently, it can be concluded that up to wavelengths ~100-300Å, depending on the material, absorption is well described by the model of C&L. Above these wavelengths band structure and covalent bonding influence the electron binding energies and a longer wavelength model must take these effects into account. Therefore, it is reasonable to use C&L to predict transmissions in the XUV band but not at longer wavelengths. However, it is the only data available for lexan between 304Å and 1600Å.

6.4 Design of Filters for use with an MgF_2 Photocathode

MgF_2 transmits in the far-UV band, hence most of the photoabsorption will take place in the MCP glass or nichrome. An uncoated MCP has very low efficiency at these wavelengths, $<10^{-2}$ counts photon^{-1} at 1216Å decreasing to $\sim10^{-7}$ counts photon^{-1} at 2000Å (Paresce, 1975), added to which the photoelectrons must also escape through the photocathode. Of the far-UV lines Lyman α is the

brightest at $\sim 10^8$ counts s^{-1} (in the earth shadow) entering the telescope. The filter transmissions in the far-UV are less than $\sim 10^{-6}$, and hence the far-UV lines make an insignificant contribution to the background. As the filter transmissions decrease by $\sim 10^4$ between 304Å and 584Å, and the HeI line flux is only an order of magnitude larger than that of HeII, the latter dominates the background.

Optimum filter thicknesses were derived by MIT using the Par N data of Stern and Paresce, the Be data of Johnston and Tomboulian, and carbon and aluminium data from unknown original sources. It was assumed that

i) the HeII line had its maximum night-time value (1R)

ii) the detector background was ~20 counts s^{-1}

iii) the exposure time was ~30s.

giving optimum filter thicknesses of 5000Å Par N, 1000Å Par N + 2500Å beryllium and 1250Å aluminium + 1000Å carbon (figures 6.8a, 6.8b and 6.8c).

The carbon/aluminium filter design did not have a very well defined bandpass by comparison with the other filters and was extremely transparent to 304Å background. Consequently, the Par N and beryllium/Par N filters were chosen for flight.

The measurements of section 6.3.3 showed that the μ_1 values of Johnston and Tomboulian were incorrect, the latter being higher, invalidating the optimisation of the Be/Par N filter. A higher transmission than MIT predicted was actually measured leading to a potential problem with the HeII background. Therefore, for safety, although a loss of sensitivity resulted, MIT added a further 2000Å of Par N to the filter.

Figure 6.8a Transmission of 5000Å Par N in the 50-300Å wavelength range.

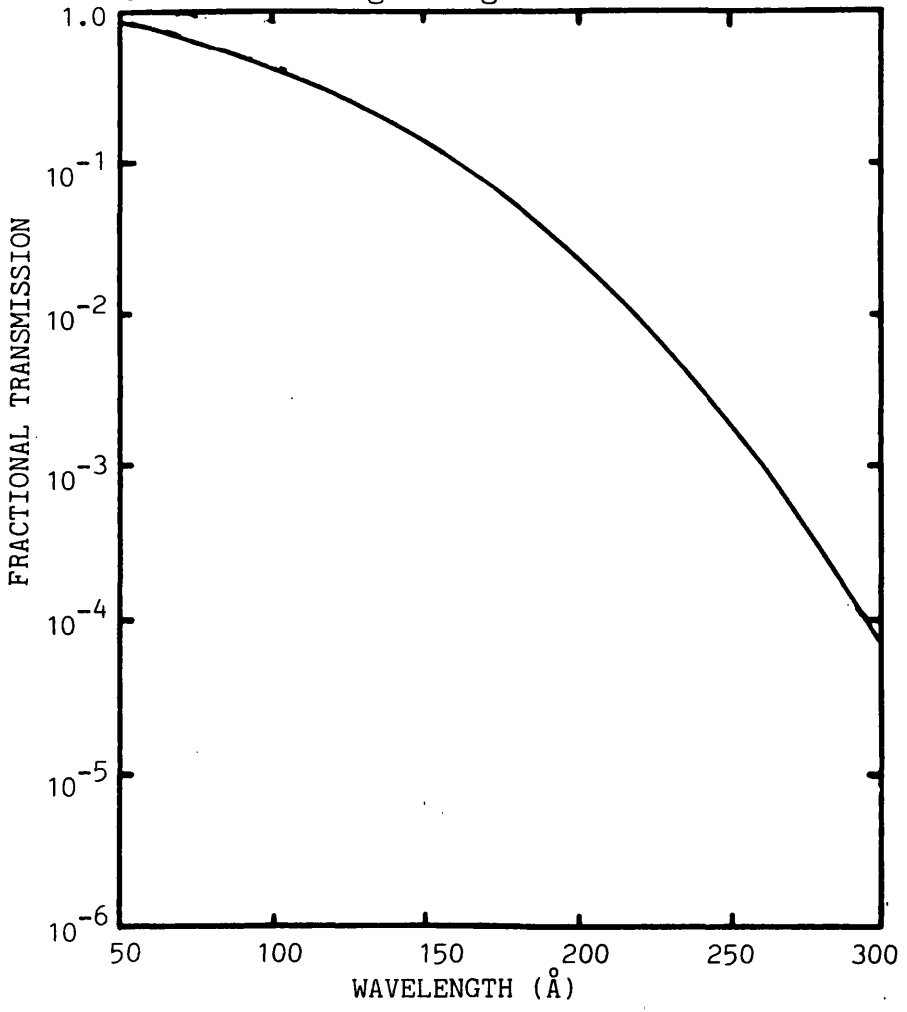

Figure 6.8b Transmission of 2500Å Be + 1000Å Par N in the 50-300Å wavelength range.

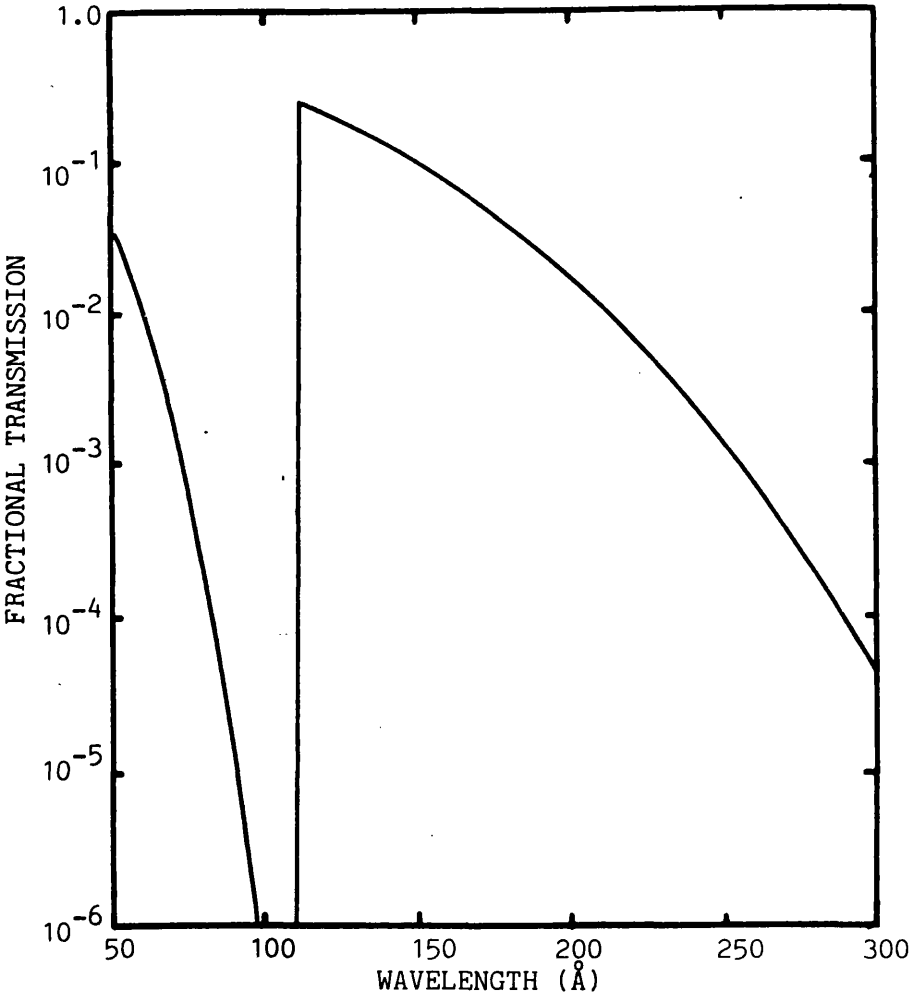

Subsequent re-analysis of the filter design, based on the data of section 6.3.3, showed that the sensitivity was in fact optimised for the original filter design. A filter of 2500Å beryllium + 2000Å Par N yields a similar sensitivity and would be a better choice, as it can be constructed as a 1000Å/2500Å/1000Å sandwich, minimising the dangers of pinholes and improving the mechanical strength of the filter. The transmissions of all three beryllium/Par N combinations are summarised in figure 6.8d.

5000Å Par N and 2500Å Be + 3000Å Par N were the filters flown on the first flight of the WFSXC. Table 6.3 summarises the background contributions and bandpasses of the WFSXC with these two filters. BO stars will not be seen in the Be/Par N filter and only the brightest ($m_v \sim 0$) will be seen in the Par N. Therefore, they will be easily identified if detected and should not constitute a problem.

6.5 Redesign of Filters for Use with a CsI Photocathode

6.5.1 Geocoronal Background Analysis with Flight 1 Filters

Large improvements in the detector quantum efficiency were measured with a CsI photocathode at soft X-ray wavelengths (Chapter 4). This observed enhancement extends out to far-UV and UV wavelengths. Measurements by Timothy (1981) and Martin and Bowyer (1982) are summarised in table 6.4 with the soft X-ray data from chapter 4 (8.34Å, 44.7Å, and 67.6Å) and from CsI development work (Fraser et al, 1982). The soft X-ray data supported the theoretical model of Fraser (1983b) which allowed prediction of the detector response out to ~300Å (figure 4.21).

Figure 6.8c Transmission of 1250Å Al + 1000Å C in the wavelength range 50-300Å.

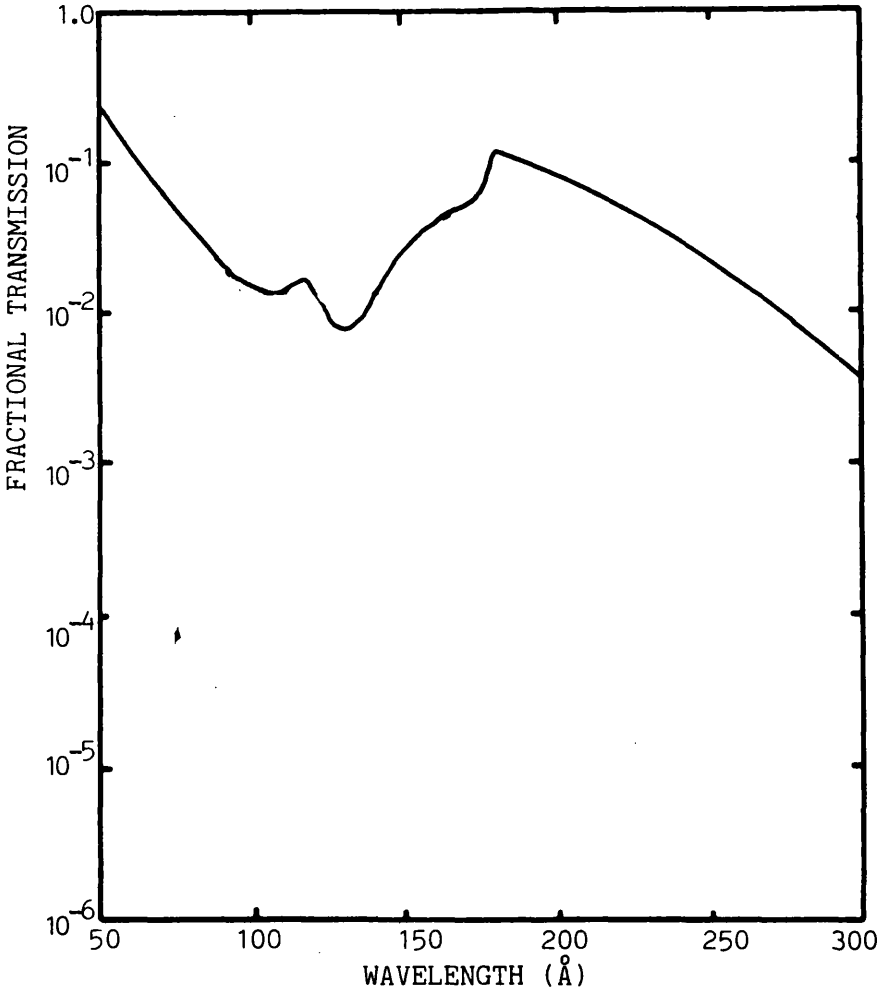

Figure 6.8d Transmission of Be/Par N filter combinations based on Cromer &Liberman data. in the wavelength range 50-300A.

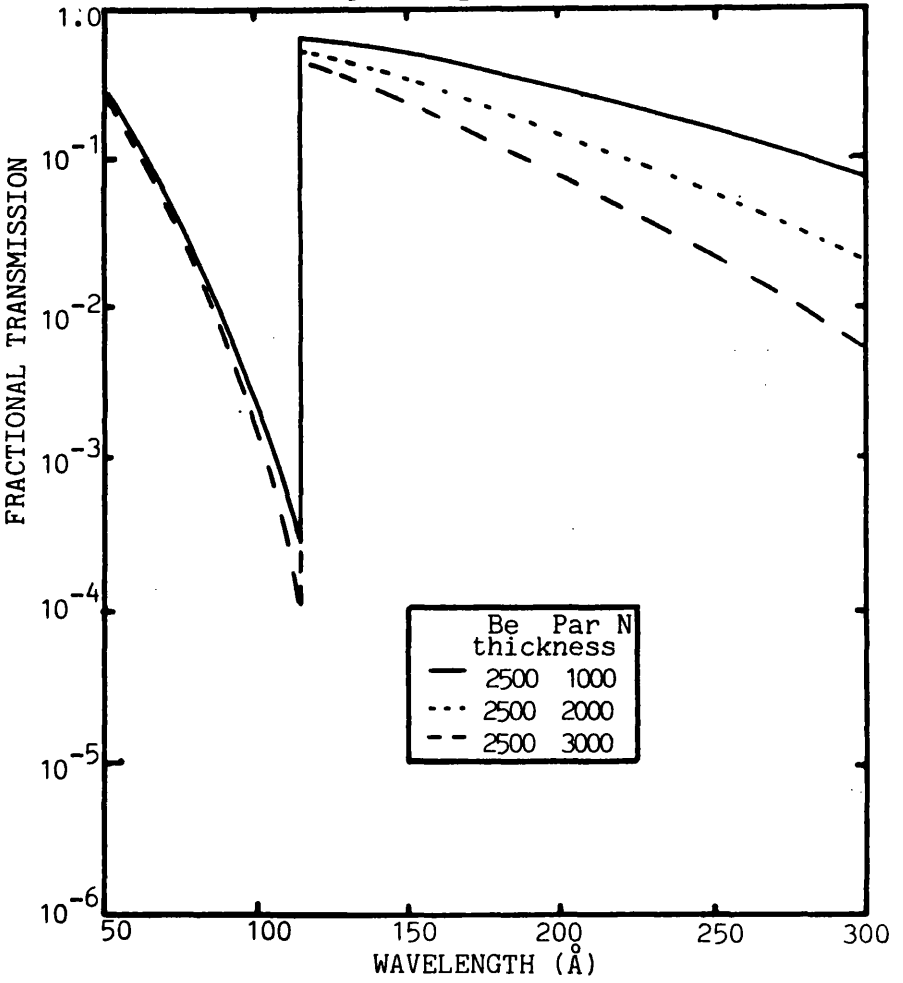

TABLE 6.3 Estimates of the Contributions to the Background Count-rate

	5000Å Par N	3000Å Par N + 2500Å Be
Grasp (Å)	0.98	0.47
E(304Å)	1×10^{-6}	8×10^{-6}
Bandpass (Å)	50, 170	114, 200
B_D (counts $cm^{-2}s^{-1}ster^{-1}$)	1	1
B_X (counts $cm^{-2}s^{-1}ster^{-1}$)	12	5
$B_{304Å}$ (" " " ")	7.96×10^{4}	7.96×10^{4}
B (calculated from eqn 6.2) (counts $s^{-1}ster^{-1}$)	280	400
Total counts in field of view (8.63×10^{-3} ster)	2.5	3.5
Counts from a B0 star (m_v=0) in a single pixel	12	0

Table 6.4. Response of a CsI coated MCP in the XUV, EUV and far-UV

λ(Å)	Efficiency at ~30° angle of incidence	
	CsI Test Detector	Flight Detector
8.34	0.16	0.2
9.89	0.21	
44.7	0.16	0.2
67.6	0.2	0.2
114.0	0.26	
	Timothy (1981)	Martin & Bowyer (1982)*
304		0.2
584		0.23
834		0.24
1025		0.24
1216	0.2	0.2
1400	0.15	0.2
1500	0.15	0.22
1600	0.10	0.20
1700	0.06	0.10
1800	0.025	0.06
1900	0.004	0.04
2000	0.0003	0.01

* This data was used in the estimates of geocoronal background

As a result of the improved efficiency, it is necessary to recalculate the expected background from geocoronal and cosmic sources, which must inevitably increase, in case it is no longer adequately rejected by the WSFXC filters.

Table 6.5 summarises the geocoronal background contributions through 5000Å Par N and 2500Å Be + 2000Å Par N, with transmissions calculated from the data of figures 6.1 and 6.2 for 30° angle of incidence, and geocoronal data of P. Henry (S. Murray, private communication). Henry's data, used to calculate the background contribution in the Einstein HRI, gives larger fluxes than those quoted in chapter 1 and can be considered to give upper limits to the count rates in the detector. The flux in the Par N/Be filter is acceptable, being due almost entirely to HeII. However, the Par N filter no longer rejects the background adequately and the transmitted flux of 2.8×10^5 counts s^{-1} will saturate the telemetry. The cause of the problem is the Par N tranmission band occurring between ~1400Å and 1800Å.

6.5.2 The Effect of Stars in the Field of View

Besides the transmission band in the far-UV, Par N is also transparent longward of ~2000Å. An additional problem may be experienced with the breakthrough of far-UV and UV flux from hot stars. Since the Par N/Be filter is opaque throughout the far-UV and UV, a false detection can only occur in the Par N. However, the observation of far-UV/UV flux in the Par N could be coupled with the detection of XUV flux in one or both filters. The result would be an incorrect determination of the ratio of the XUV fluxes in each filter (the two colour photometry) leading to the wrong estimate of the

temperature of an object.

The potential problem can be usefully characterised by comparing the predicted ratios of the far-UV+UV flux (S_{FUV}) and the XUV flux (S_{XUV}) expected in the Par N filter with that in the Be/Par N filter (S_{BE}) from a blackbody emitter, as a function temperature. The ratios are independent of the source size and, provided negligible absorption is assumed in each band, its distance. The ratios S_{XUV}/S_{BE}, S_{FUV}/S_{BE} and $(S_{FUV}+S_{XUV})/S_{BE}$ are plotted in figure 6.9, where S_{FUV} is integrated between 1000Å and 4000Å. A minimum occurs in the $(S_{FUV}+S_{XUV})/S_{BE}$ curve at 8×10^4K and for T>3×10^4K any ratio is satisfied by two temperatures. Hence, objects with temperatures in the range 3×10^4-8×10^4K are indistinguishable from sources at temperatures above 8×10^4K. As all the blackbody emitters of interest in the WFSXC band have temperatures above $\sim3\times10^4$K this is a serious problem.

The class of O-B0 stars are not of interest to the WFSXC experiment but their temperatures fall in the range 3×10^4K-4×10^4K. They have typical radii $\sim10R_\odot$, 1-3 orders of magnitude greater than other hot blackbodies and consequently will be much brighter in the WFSXC than other objects of similar temperature, a large proportion of the photon flux being in the far-UV.

The spectral photon irradiance ($f(\lambda)$, photons $cm^{-2}s^{-1}Å^{-1}$) from a star of bolometric magnitude m_b is

$$f(\lambda) = \frac{6.73\times10^{10}}{T_e}.10^{-0.4m_b}.P(\lambda,T_e) \qquad (6.4)$$

where: T_e is the effective temperature of the star

Table 6.5. Geocoronal background with CsI photocathode*

λ(Å)	Line	Flux** in field of view	Total flux (counts s^{-1}) in filter 5000Å Par N	2500Å Be + 2000Å Par N
304	HeII	1.6×10^6	4.48	440
584	HeI	1.6×10^6	<0.1	<0.1
834	OII	4.0×10^6	<0.1	<0.1
1025	HI	3.2×10^8	0.21	1.9
1216	HI	1.6×10^9	320	<0.1
1304-1356	OI	1.6×10^9	3200	<0.1
1356-1600	N_2	4.8×10^7	2.8×10^5	<0.1
TOTAL			2.8×10^5	440

* Using the CsI data of Martin and Bowyer (1982).

** Calculated for the WFSXC from the data of Henry.

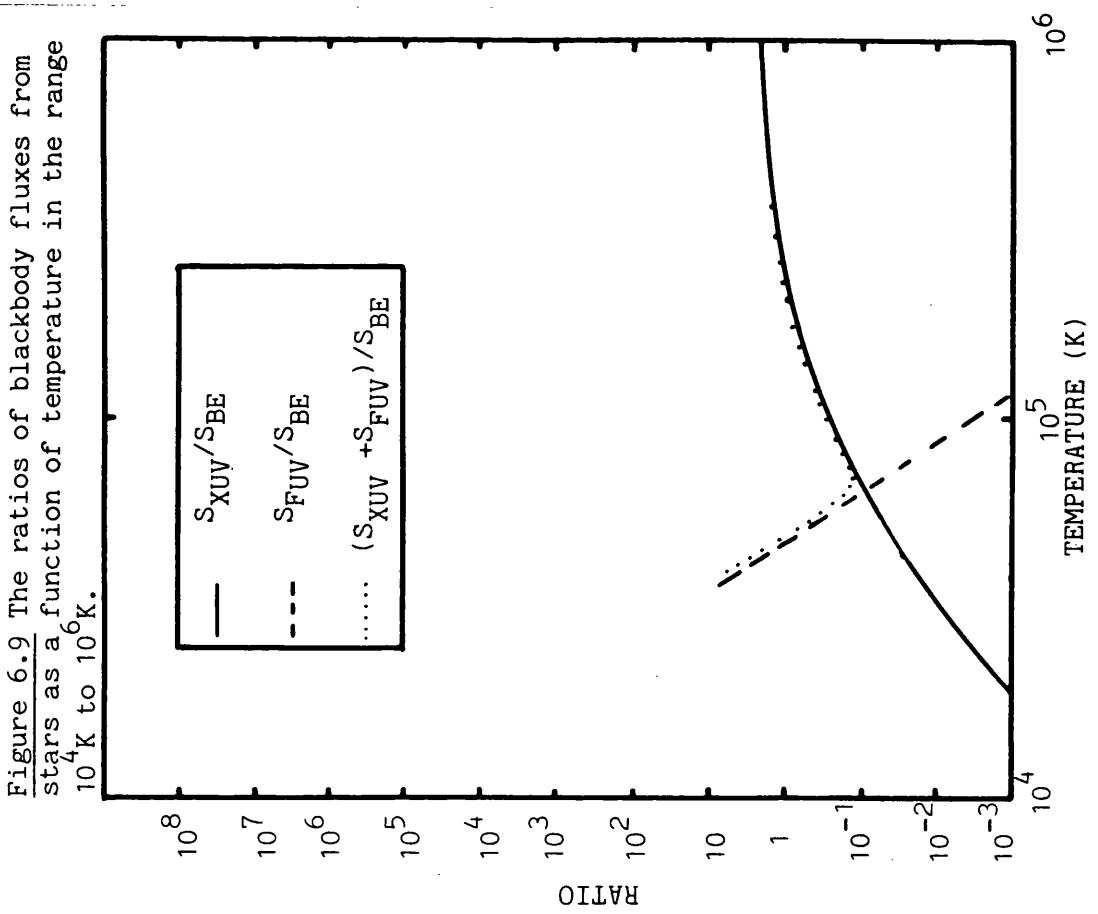

Figure 6.9 The ratios of blackbody fluxes from stars as a function of temperature in the range 10^4K to 10^6K.

$P(\lambda,T_e)$ is the relative Planck function

Folding this through the WFSXC response ($E(\lambda)$) gives the net flux (f_N, counts $cm^{-2}s^{-1}$) in the instrument

$$f_N = \frac{6.73\times10^{10}}{T_e}.10^{-0.4m_b}\int_{band} E(\lambda).P(\lambda, T_e).d\lambda \qquad (6.5)$$

The apparent magnitude of a star (m_v) is related to the bolometric magnitude by the bolometric correction BC ($m_v=m_b-BC$). The count rate from a star in the WFSXC (Par N filter), integrated between 1000Å and 4000Å, is summarised as a function of spectral class (ie. T_e) and m_v in table 6.6. It can be seen that O-B0 stars of $m_v>3$ will saturate the electronics (count rate > 2500 s^{-1}).

In an integration time ~25s a 5σ point source detection requires a count rate ~1 count s^{-1}, assuming the sensitivity is photon limited. From this, an approximate limiting magnitude can be derived for each spectral class of star (figure 6.10). O and B0 stars brighter than 11th magnitude can be detected. Stars in other spectral classes may also be seen in the Par N filter but are too cool to be detected in the Par N/Be filter.

It is possible to quantify the number of O-B0 stars that may be detected by the WFSXC. Allen (1973) gives the number of stars per square degree of sky in the range of $m_v\pm1/2$ (table 6.7). O and B0 stars comprise ~1% of the stellar population. Assuming that they are uniformly distributed in space (a gross assumption) ~1000 of $m_v<12$ will be observed in a single rocket flight (~1/400 of the celestial

Table 6.6. The count rate from a star in the Par N filter as a function of magnitude (m_v) and spectral class

	count rate (s^{-1})						
m_v	O	B	A	F	G	K	M
0	29000	37000	1100	110	53	33	18
1	11000	15000	440	43	21	13	7.1
2	4500	5900	180	17	8.4	5.2	2.8
3	1800	2400	70	6.8	3.3	2.1	1.1
4	720	940	28	2.7	1.3	0.83	0.45
5	290	370	11	1.1	0.53		
6	110	150	4.4	0.42			
7	45	59	1.8				
8	18	24	0.7				
9	7.2	9.3					
10	2.9	3.7					
11	1.1	1.5					
12	0.45	0.59					

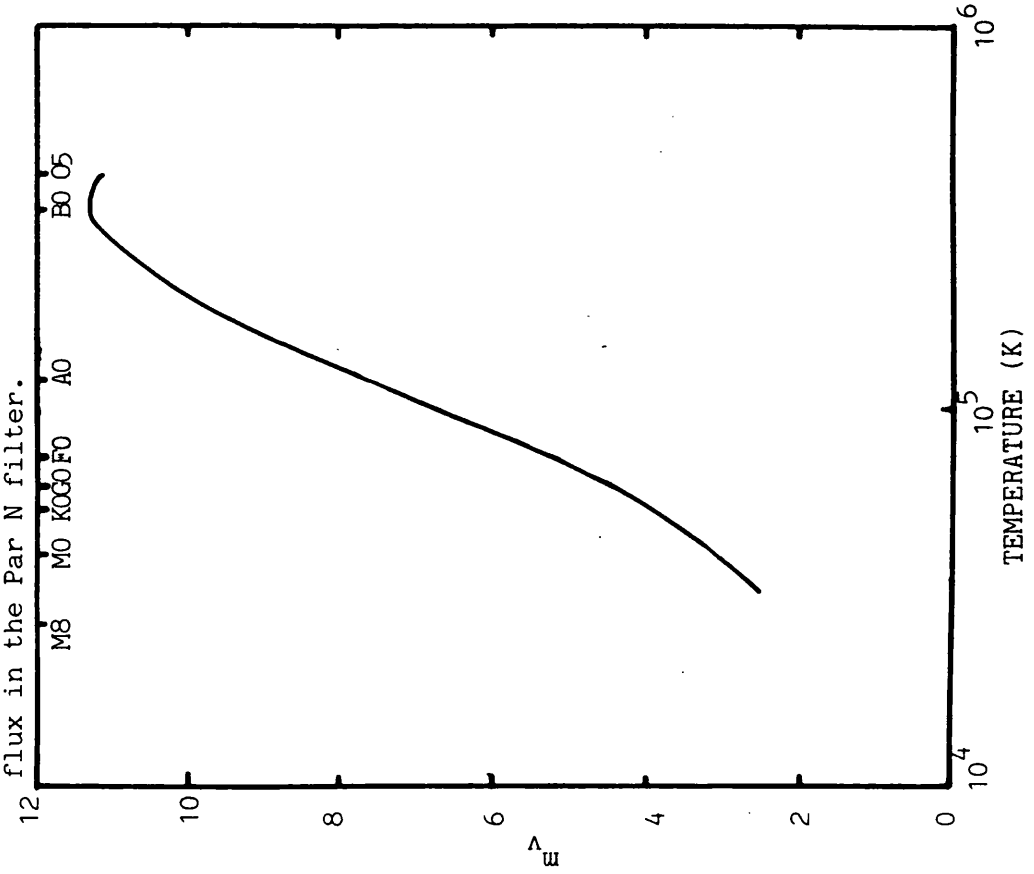

Figure 6.10 The limiting magnitude above which a star cannot be detected by its 1000-4000A flux in the Par N filter.

sphere).

Clearly the far-UV and UV transmission of the Par N filter causes a problem when coupled with a CsI photocathode. Stars with temperatures between $3x10^4$K and $8x10^4$K are indistinguishable from those above $8x10^4$K. A large number of O-B0 stars are potentially spurious detections and the brighter ones (m_v>3) will saturate the electronics.

6.5.3 The Carbon/Lexan Filter Design

From the absorption data of figure 6.3 it appears that lexan is opaque in the far-UV and from figure 6.4 that carbon is opaque in the UV. Hence, a composite filter constructed from these materials should reject the far-UV geocoronal background and O-B0 stars. As lexan and carbon have XUV absorption responses like that of Par N the composite filter should have a similar bandpass.

Flux ratios were calculated for a combination of 2000Å carbon + 1000Å lexan (figure 6.11), chosen initially as providing a good match to the 5000Å Par N XUV transmission. The temperature determination problem has been eliminated by restricting the temperature range where it occurs to $2x10^4$K-$3x10^4$K, below the temperature detection limit of the WFSXC. The magnitude limit for detection of O-B0 stars is reduced to 2.7 and 1.3 (O5 and B0 respectively). Only ~0.07 stars will now be seen in a single rocket flight. Detection of an O-B0 star will be a rare event and the star will be bright enough for easy optical identification.

Table 6.8 compares the limiting magnitudes for far-UV detection of a B0 star, the grasps (Å) of the WFSXC with the filter and the flux from the principal geocoronal lines for several carbon/lexan

Table 6.7. Number of stars of magnitude in the range $m_v \pm 1/2$

m_v	Number degree^{-2}	Number observed in one flight*
1	7.9×10^{-5}	0.079
2	3.2×10^{-4}	0.32
3	1.4×10^{-3}	1.4
4	4.9×10^{-3}	4.9
5	0.018	18.0
6	0.14	140
7	0.4	400
8	1.1	1100
9	3.3	3300
10	8.7	8700
11	21.9	21900
12	58.9	58900

* It was assumed that one flight was 1000 square degrees and that the stars are uniformly distributed on the sky.

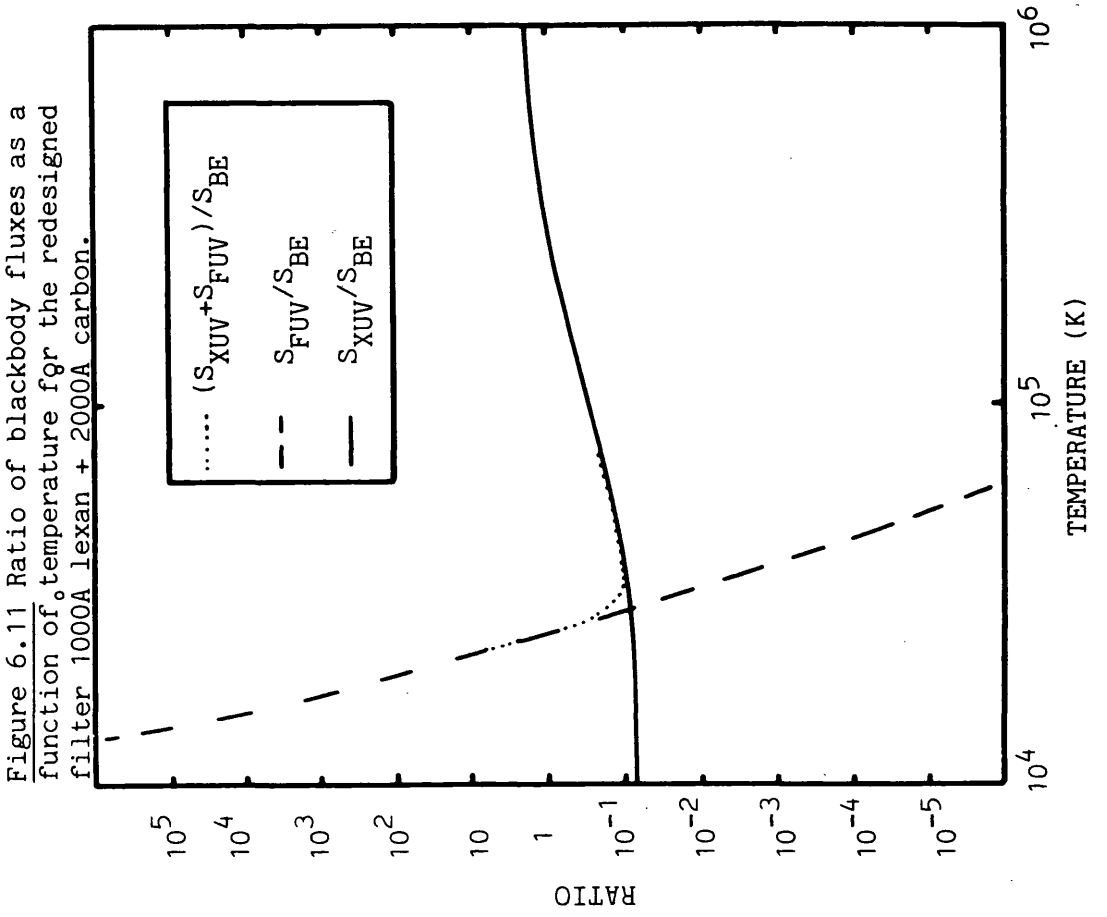

Figure 6.11 Ratio of blackbody fluxes as a function of temperature for the redesigned filter 1000A lexan + 2000A carbon.

combinations to find the optimum design. Taking minimum m_v and background as the deciding criteria the combination of 2500Å carbon + 500Å lexan is the best design. However, the grasp is <1/2 of that of any other combination and the thinnest pinhole-free lexan film that can be made is ~1000Å (B. Kent, private communication) The highest grasp combinations (500Å carbon + 2500Å lexan, 1000Å carbon + 2000Å lexan) have an unacceptably high m_v limit and background. Of the two remaining choices 2000Å carbon + 1000Å lexan was chosen for flight as the geocoronal background is reduced by a factor 2 to ~27 counts s^{-1} compared with the 1500Å/1500Å combination.

6.6 Pre-flight Calibration of Carbon/Lexan Filters

The carbon/lexan filters were manufactured by B.Kent of the Rutherford and Appleton Laboratory. The lexan composing the flight filters was deposited in 3-4 layers up to a total thickness of ~1000Å, on a highly transparent (~93%) mesh. Carbon was then deposited in the manner described by Samson and Cairns (1964). A batch of filters was produced, from which one was chosen for flight, and calibrated at 160Å and 304Å (lexan only) in the XUV and 2695Å, 2865Å and 3034Å in the UV (table 6.9).

In the UV above ~2500Å predicted lexan transmissions are high, ~0.96-0.97, hence the dominant absorber in this band is carbon. The thickness of the carbon can be derived from the UV data using the linear absorption data of Hagemann et al (1974). Assuming that variations in the calculated values are caused by experimental error the mean thickness of carbon is 1795Å±77.

Similarly the thicknesses of lexan can be derived from the 304Å data. Hatter and Hayes (Rutherford and Appleton Laboratory, private communication) have found that μ_l is $2.6 \times 10^5 cm^{-1}$ from measurements on

Table 6.8 Summary of the characteristics of different thickness combinations of carbon and lexan

Thickness (Å)		Grasp (Å)	m_v max *	Count rates (s^{-1}) in filter from brightest geocoronal lines				
carbon	lexan			304Å	1216Å	1304Å	1500Å	Total
500	2500	5.87	8.2	228	~0	~0	~0	228
1000	2000	5.22	5.9	130	~0	~0	~0	130
1500	1500	4.69	3.0	57	~0	~0	~0	57
2000	1000	4.23	2.7	27	~0	~0	~0	27
2500	500	2.37	1.4	~0	~0	~0	~0	~0

note The data of Samson and Cairns was used between 1000-2000A and that of Hagemann et al above 2000Å

* The highest magnitude at which a star of temperature 3×10^4K can be detected.

Table 6.9 Pre-flight calibrations of the carbon/lexan filters

λ(Å)	Unit I	Unit II	Unit III
160	0.11 ± 0.01	0.31 ± 0.02	0.24 ± 0.03
304*	0.10 ± 0.02	0.17 ± 0.02	0.10 ± 0.02
2526	0.001	0.002	0.001
2695	0.002	0.003	0.002
2865	0.003	0.003	0.003
3034	0.003	0.004	0.004

note all UV data accurate to ±0.001.

* measured for lexan only before deposition of the carbon.

2000Å and 3000Å thick lexan films, which compares well with the value of $2.3 \times 10^5 cm^{-1}$ measured by Huizenga et al (1979). A mean thickness ~900Å is suggested by the calibration data of table 6.9. This agrees within 10% of the quoted thickness of 1000Å which was expected to have an accuracy of ±5% (B. Kent, private communication).

6.7 Post-flight Tests of WFSXC Flight 2 Spare Filters

6.7.1 Measurements of Filter Transmission in the Far-UV

An unexpectedly high background was recorded during the second flight of the WFSXC. To assist in diagnosing the cause of the problem flight spare filters were calibrated in the far-UV.

Calibrations were performed on one Be/Par N filter and one C/lexan filter, both from the same batches as those used in flight, using the far-UV test facility at the National Physical Laboratory (NPL), Teddington, Middlesex. Initially, the transmissions of each filter were measured between 1216Å and 1540Å. After a period of 4 months the measurements were repeated and extended to 1938Å. The duplicated calibrations served as a consistency check of the measurement technique and gave a lower limit to the time variability of the transmissions.

The light source was an MgF_2 windowed deuterium lamp. A 1m normal incidence vacuum monochromator was used to obtain the required wavelength, with a band width of ~10Å. Each filter was mounted between the monochromator exit slit and a photomultiplier tube and could be swung out of the 2mm diameter beam in order to measure the incident flux (I_o). A band-pass filter, transmitting above 2000Å, was inserted between the entrance slit and the deuterium lamp, while the filter was both in and out of the beam, to measure the scattered UV

background in the apparatus (I_{TB} and I_{oB} respectively).

As a result of the high far-UV opacity (transmission (T_F) < 10^{-5}) I_o could not be measured with the same photomultiplier gain setting as the transmitted flux (I_T). A conversion factor between two gain settings ($cg_{i,i+1}$) was calculated by measuring I_T for a neutral density filter of known tranmission (10^{-3}). For any pair of gains I_o was held constant and therefore

$$cg_{i,i+1} = I_T(i+1)/I_T(i) \qquad (6.6)$$

The net conversion factor (CG) over n gain steps was

$$CG = \overline{\prod_{i=1,n}} \; cg_{i,i+1} \qquad (6.7)$$

Hence,

$$T_F = \frac{1}{CG} \cdot \frac{(I_T - I_{TB})}{(I_o - I_{oB})} \qquad (6.8)$$

A contribution ~4% to the error in T_F resulted from non-linearities in the photomultiplier response, derived by comparing the transmissions of the neutral density filter measured at each gain setting. The only other contribution to the total error in T_F was the measurement uncertainty of I_T, since by comparison the uncertainty in I_o was negligible.

The transmissions measured are presented in figures 6.12 and 6.13 for Be/Par N and C/lexan respectively. Where, in a given run, several measurements exist for a single wavelength their mean is plotted. The similarity between the transmissions on each run illustrates the reproducability of the measurement technique and shows that filter transmissions did not change within a period of 4 months.

As the behaviour of Par N is known in the far-UV (Stern and Paresce, 1975), it was possible to derive the linear absorption coefficient (μ_1) of Be in the 1216-1938Å waveband in the manner described in section 6.3.3. As before the mesh transmission was assumed to be 0.91 ± 0.03 and the tolerance in the filter thickness ~5%, the latter as quoted by the manufacturer (Lebow Company, Goleta, California). The calculated values of μ_1 are plotted in figure 6.14. As before multiple measurements at a single wavelength in a given calibration run were averaged.

The measured Be/Par N transmission is ~2-4 orders of magnitude higher than expected ($<10^{-10}$ throughout the band) and that of C/lexan (compared with the experimental data in figure 6.13) is also several orders of magnitude higher than predicted. Given the assumptions made about the far-UV absorption of Be and lexan it is not surprising that the measured transmissions are different to those predicted. However, the measured values are higher than the predictions, the latter being expected to be upper limits.

The values of μ_1 obtained for Be from the NPL data are much lower (a mean of $3.94 \times 10^5 cm^{-1}$) than that derived from the data of Toots et al ($1.45 \times 10^6 cm^{-1}$), at 1216Å, and can be seen to be constant, within the error bars, throughout the range of the calibration (figure 6.14). This behaviour would be expected if pinholes were dominating the

Figure 6.12 Transmission of 2500Å beryllium + 2000Å parylene N in the far-UV.

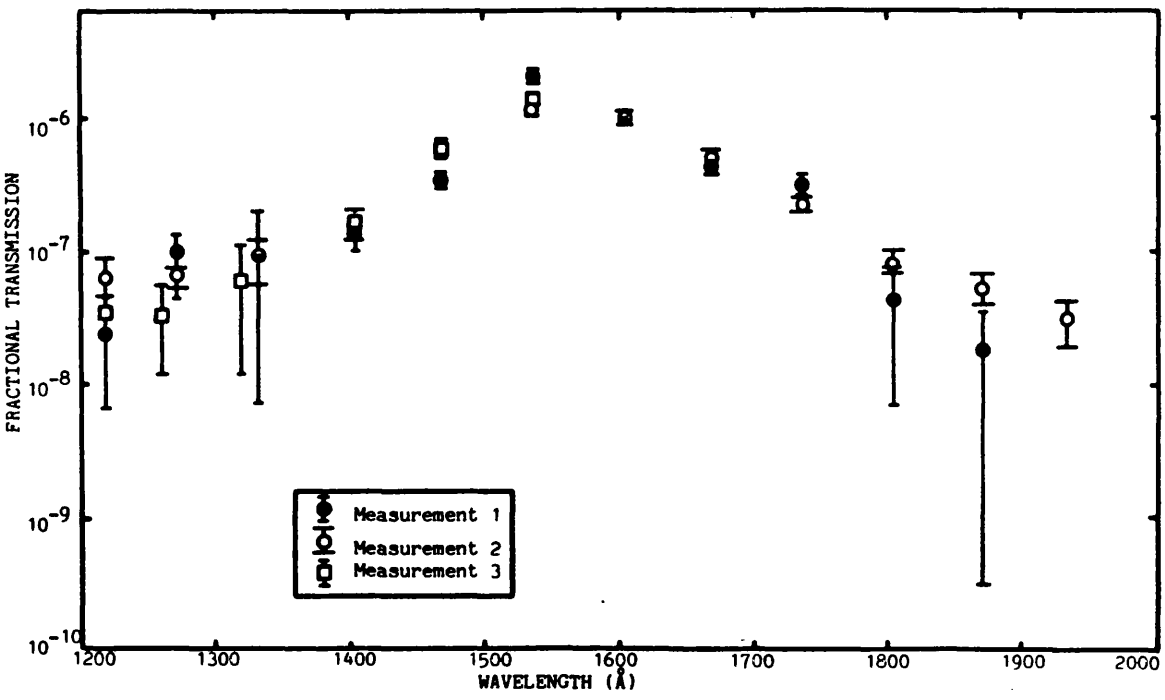

Figure 6.13 Transmissions of 1000Å lexan + 2000Å carbon in the far-UV.

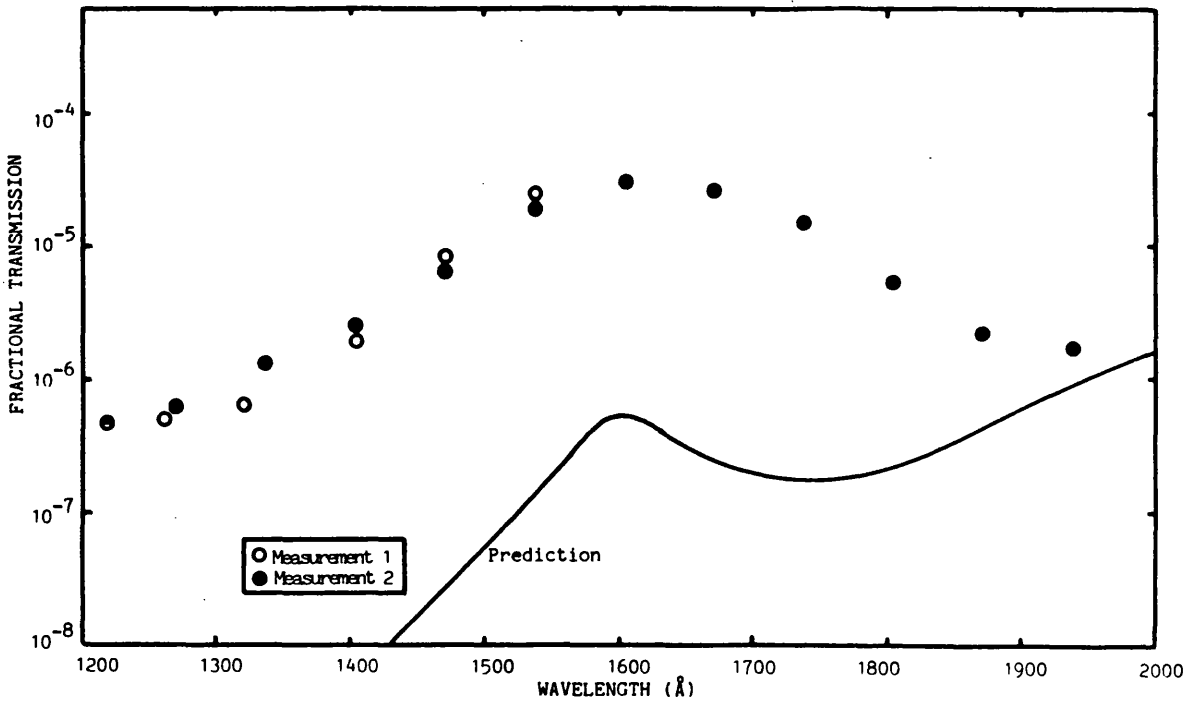

transmission of the Be foil, which is possible in view of the very low transmissions being measured and that the Be is a single layer film unlike the Par N. Consequently, the values of μ_1 derived for Be can only be taken as lower limits and imply that pinholes comprise a fractional area of $\sim 5 \times 10^{-5}$. Pinhole effects may present a fundamental difficulty in obtaining the linear absorption directly from transmission measurements in the far-UV.

The data of Samson and Cairns cannot be used to derive μ_1 for lexan from the filter transmission because at 1216Å the transmission predicted for carbon alone (2×10^{-9}) is lower than that measured. It is possible that this error is also due to pinholes, but, since there are two conflicting sets of absorption data for carbon and none for lexan in the far-UV, no firm conclusions can be drawn and further measurements are required.

6.7.2 Other Post-flight Transmission measurements

The uniformity of the C/lexan filter was tested at NPL by traversing the filter across the monochromator beam, measuring the transmission at a number of points. The limitations of the apparatus only allowed the filter to be scanned in one axis and with a maximum displacement of ~1cm. Figure 6.15 shows the transmission as a function of the displacement from the centre of the filter. The peak ~1.5mm from the centre corresponds to a crack in the carbon film, ~0.1mm wide and ~10mm long, running perpendicularly to the scan direction. The width of the peak is ~2mm, equivalent to the beam diameter.

Figure 6.14 The linear absorption coefficient of beryllium in the far-UV.

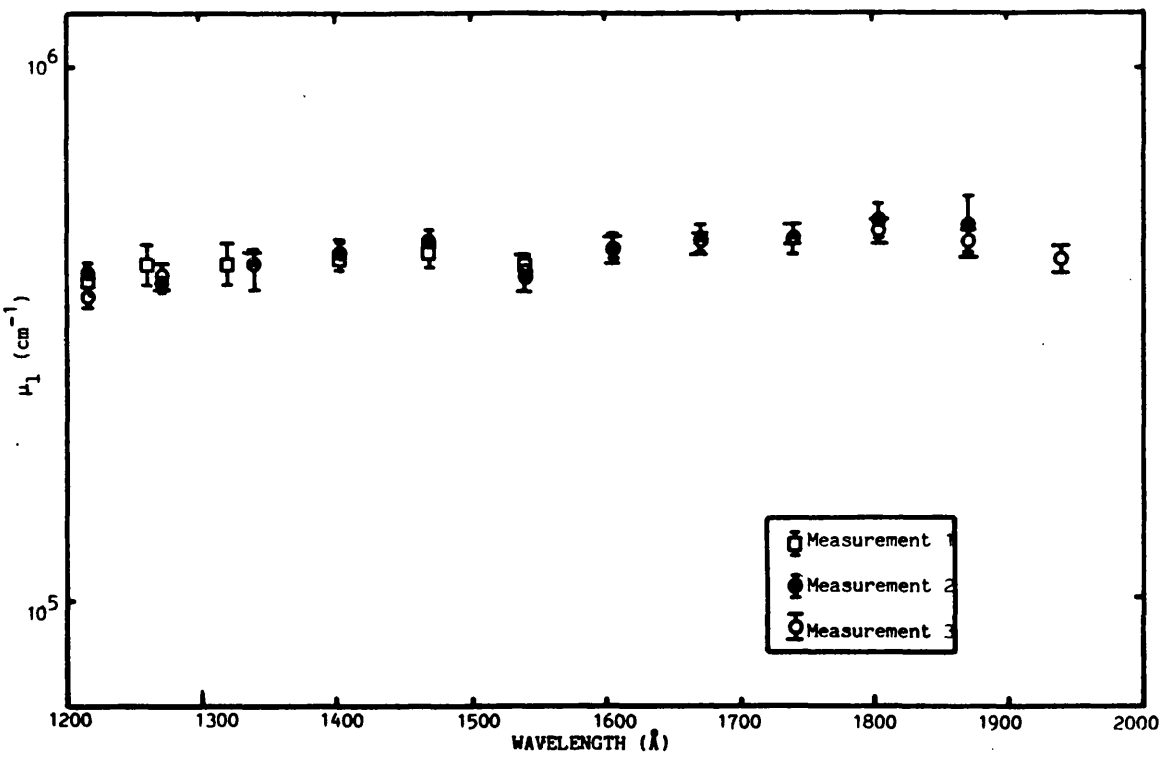

Figure 6.15 Transmission of the carbon/lexan filter as a function of position.

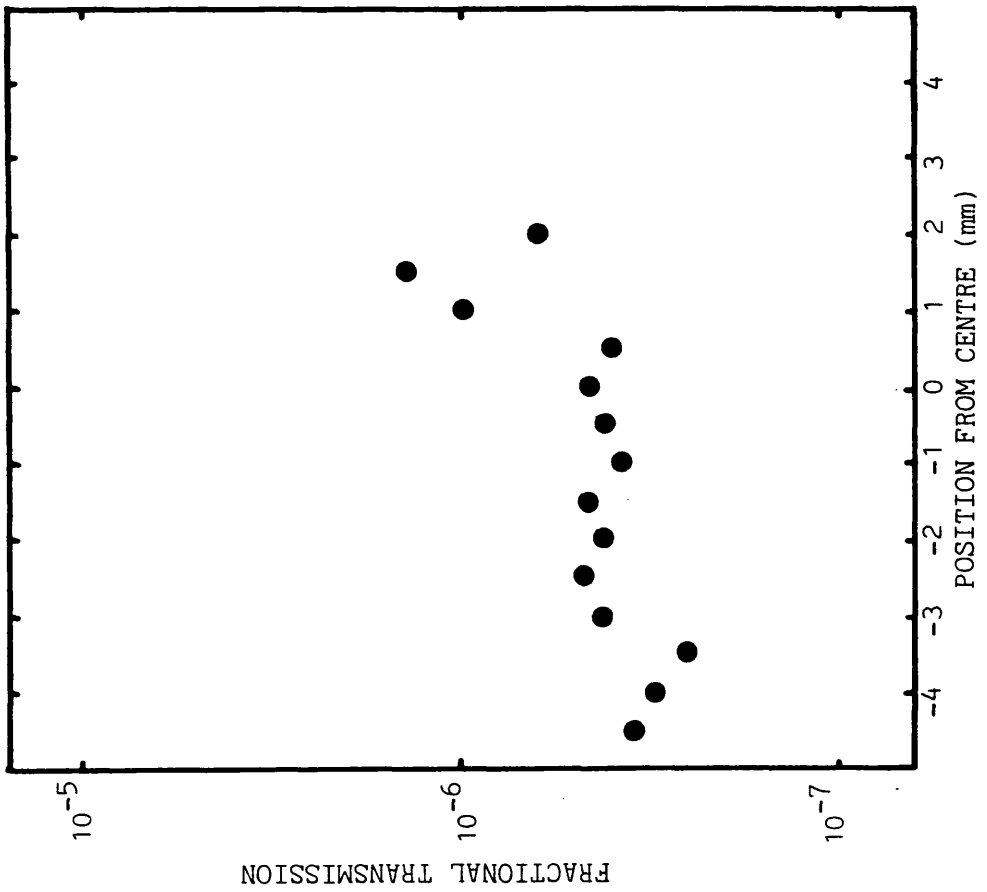

Measurements of the transmission of a Be/Par N filter were made by MIT (S. Rappaport, private communication) in the UV and far-UV bands. As the apparatus had a small dynamic range, only upper limits to the transmission could be obtained, which were 10^{-5} and 10^{-4} in 1216-2000Å and 2000-3000Å bands respectively.

6.8 Conclusion

This chapter has described the design of bandpass filters for the WFSXC with detectors having MgF_2 and CsI photocathodes. With MgF_2 the filter is principally required to reject 304Å and 584Å geocoronal lines, as the detector has a rapidly decreasing efficiency at wavelengths above 1000Å. 5000Å Par N and 2500Å Be + 2000Å Par N are the optimised thicknesses with bandpasses of 50-170Å and 114-200Å respectively. However, because of the uncertainty in the Be absorption when the filters were manufactured a filter composition of 2500Å Be + 3000Å Par N was used in flight.

The improved response of the detector in the far-UV and UV with a CsI photocathode introduced the problem of rejecting the far-UV geocoronal lines and preventing the breakthrough of far-UV and UV flux from hot stars. The Be/Par N filter was adequate, as with MgF_2, and remained optimised with the CsI photocathode. However, it was necessary to replace the Par N filter with a combination of 2000Å carbon and 1000Å lexan.

During the course of the filter design work heavy reliance was placed on a computer model based on the theoretical data of Cromer and Liberman (1970). Measurements of the absorption coefficient of beryllium and parylene N showed that the model worked well for Be up to wavelengths $\sim$300Å but showed deviations from experiment at

wavelengths >100Å with Par N. The Be data also resolved an existing discrepancy found between the absorption data of other authors. Comparison of existing data with the model at longer wavelengths (figures 6.1, 6.2, 6.3, 6.4 and 6.5), up to 1000Å, showed that above the XUV band the atomic model no longer adequately described the absorption process. Hence, the band structure of metals and the delocalisation of the outer electrons of the constituent atoms of the plastic materials (in the covalent bonds) must be taken into account in a theoretical model of far-UV absorption.

The major aim of the far-UV measurements was to determine the filter transmission for diagnosis of the cause of the high background count rate measured during the second rocket flight. Although the data did not yield any fundamental knowledge about the absorption of the filter materials, it did show that pinhole effects were significant when the filter transmissions were very low, a factor which was not taken into account when predicting the transmissions earlier. Further measurements, perhaps with single foils, are desirable to understand the absorption of the filter materials properly but in the far-UV pinhole effects may not allow μ_1 to be determined directly from transmission data.

CHAPTER 7

INTEGRATION AND CALIBRATION OF THE WFSXC PAYLOAD

7.1 Introduction

The calibration of the WFSXC detectors and the thin film filters has been described in detail in the preceding chapters (3, 4 & 5 for the detectors, 6 for the filters). MIT was mainly responsible for the production of the telescope mirrors but the author was involved in their calibration during the early stages of payload integration. This chapter deals with the calibration of the mirrors, the integration of detector 1 into the payload and the subsequent pre-flight testing.

7.2 Manufacture and Calibration of the WFSXC Mirrors

The three mirrors (figure 7.1) were machined from solid 18cm thick ingots of Reynolds 6061 aluminium alloy. As each mirror element is short, it was possible to have both reflecting surfaces of each telescope cut from a single block. A final figure was cut by a numerically-controlled lathe at the Ober Tool and Dye company, Everett, Massachusetts. However, optical tests revealed surface ripples (RMS amplitude $\sim \pm 2.5\mu m$) which, although within requested tolerances, produced an unacceptably high blur circle radius.

To improve the surface finish the mirrors were diamond turned at the Union Carbide Y-12 plant, Oak Ridge, Tennessee after being plated with 250μm of electroless nickel. The mirrors were mounted onto the payload by means of a spider bolted into slots cut in the rear of the mirrors. These slots were cut after the middle and outer mirrors were

Figure 7.1 The WFSXC grazing incidence mirrors.

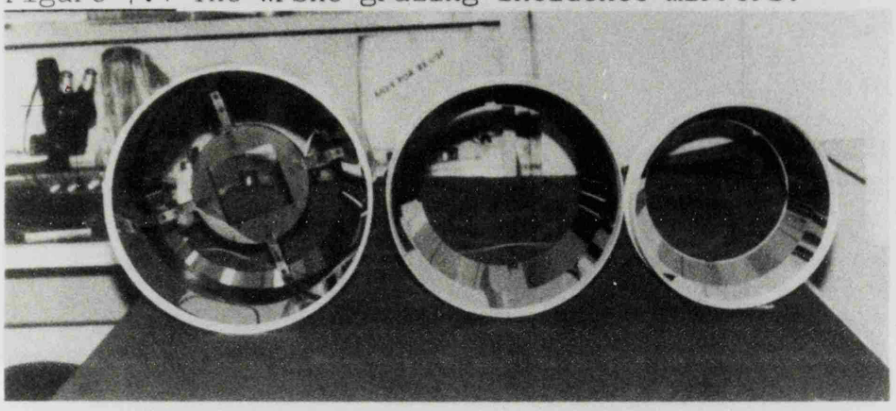

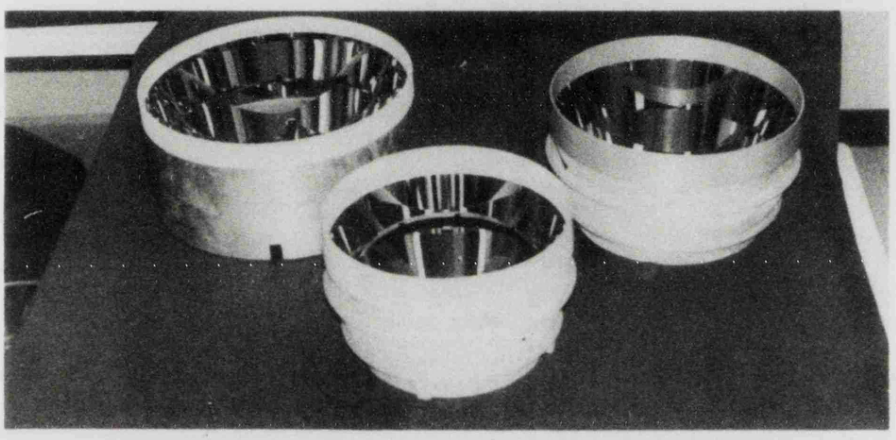

TWO VIEWS OF X-RAY MIRRORS FOR ROCKET PAYLOAD

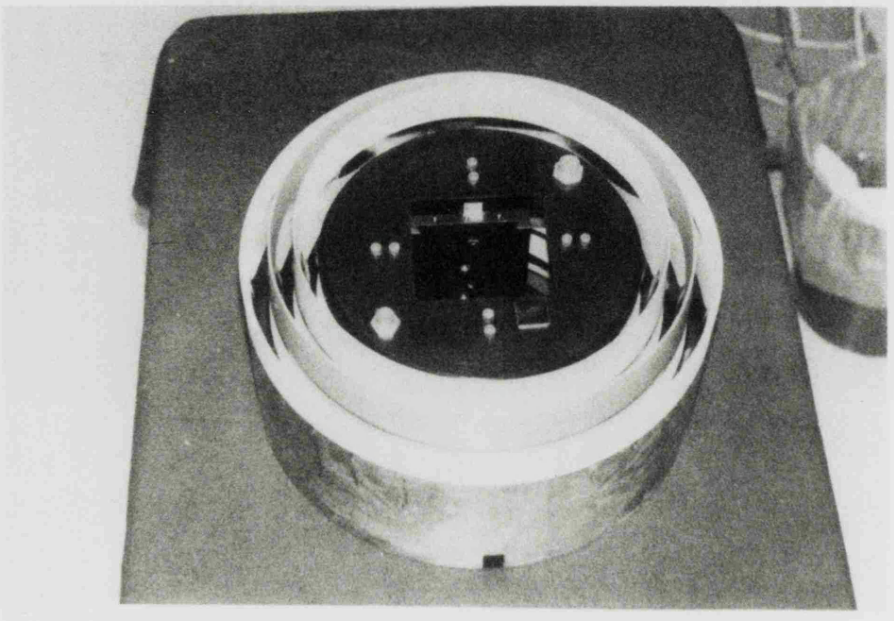

X-RAY MIRRORS NESTED IN FLIGHT CONFIGURATION

diamond turned as it was thought that a continuous cut was needed to produce a good surface figure. However, the slots were cut in the inner mirror before turning. The mirrors were then lapped and polished by the Applied Optics Centre, Burlington, Massachusetts, and were electroplated with a 1000Å thick layer of gold to provide the final surface finish.

The innermost mirror was calibrated by MIT in the 150-foot X-ray beam facility at American Science and Engineering (AS&E), in Arlington Massachusetts. An RMS blur circle radius of 2.5" was measured at 44.7Å (figure 7.2). As this wavelength represents the high energy end of the spectral range, the efficiency of the mirror was, as expected extremely low with an effective area of $0.65cm^2$, ~40% of the value calculated theoretically.

Following the X-ray calibration the mirrors were nested and placed in a collimated optical beam to measure the resolution of the individual mirrors and of the nest. The optical resolution of the inner mirror was ~2" (RMS), consistent with the X-ray image size.

However, the other two mirrors did not image properly, exhibiting four-fold symmetrical figuring errors which were in phase with the mounting notches. Figure 7.3a shows the result for the outer mirror. This distortion limited the image size to 10" and 20" (RMS) for the middle and outer mirrors respectively.

As the distortion only occurred in the outer and middle mirrors, it appeared that it was caused by cutting the mounting slots. Probably, cutting the notches allowed stresses in the mirrors to relieve themselves.

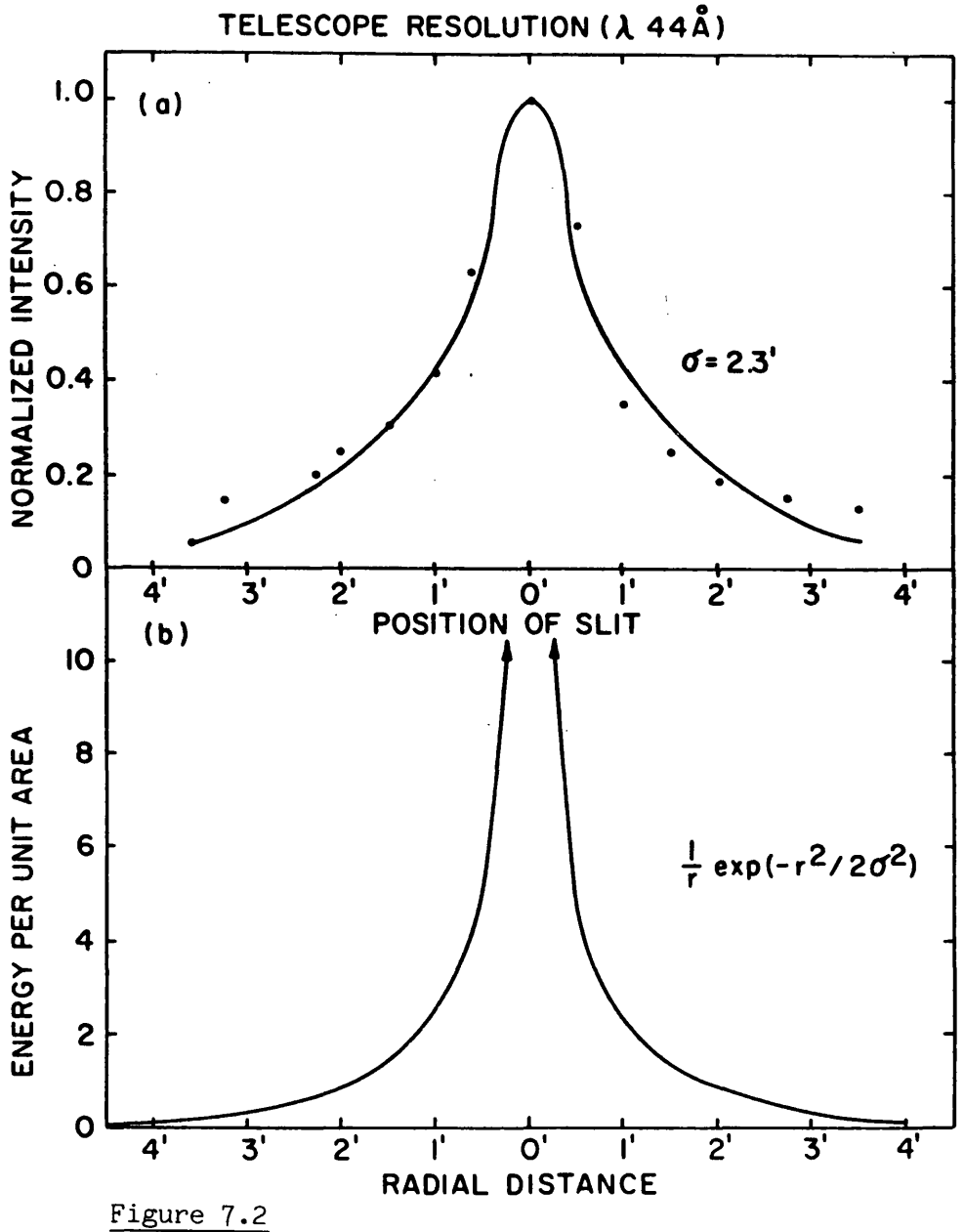

Figure 7.2

X-Ray imaging test result for inner mirror. The fitting function superposed on the data points in (a) consists of the convolution of a slit detector response to a point source with the modeled telescope resolution function shown in (b).

Much of the mirror distortion could be removed by stressing the mirrors at points corresponding to the positions of the notches. The outer mirror was stressed by means of a ring mounted against the front baffle and the middle mirror by shims between the outside edge of the base and the spider, fixed by the mounting bolts. Figure 7.3b shows that stressing the mirror concentrated the power in the defocussed image into an annulus. The defocussed image for a "perfect" telescope (the undistorted inner mirror) should be a thin annulus (figure 7.3c).

Once the distortions had been mechanically optimised and the mirrors coaligned, their optical imaging properties were measured at MIT by scanning across the image of a point source with a phototransistor having a circular aperture of diameter 0.5mm. The results of these measurements are plotted in figure 7.4, with a family of curves generated by convolving a gaussian beam response with a circular aperture. The inferred RMS radii were $1.0\hat{'}$ and $2.5\hat{'}$ for inner and middle mirrors respectively. The outer mirror had a core of $2.5\hat{'}$ RMS radius but also had a wide halo containing a significant amount of power. The composite point response of the nest had an RMS radius of $2\hat{'}$ and exhibited the halo from the outer mirror. The photograph of figure 7.3d shows the core of the image, while a longer exposure shows the extent of the halo (figure 7.3e). Because of the halo, 50% of the power lay within a circle of diameter $4.8\hat{'}$, 70% within $8\hat{'}$ diameter and 90% within $20\hat{'}$ diameter. Hence, the final telescope resolution was much larger than that of the detector ($0.4\hat{'}$ RMS radius on-axis) dominating the net resolution of the WFSXC. The point response of the inner mirror (figure 7.3f) is representative of

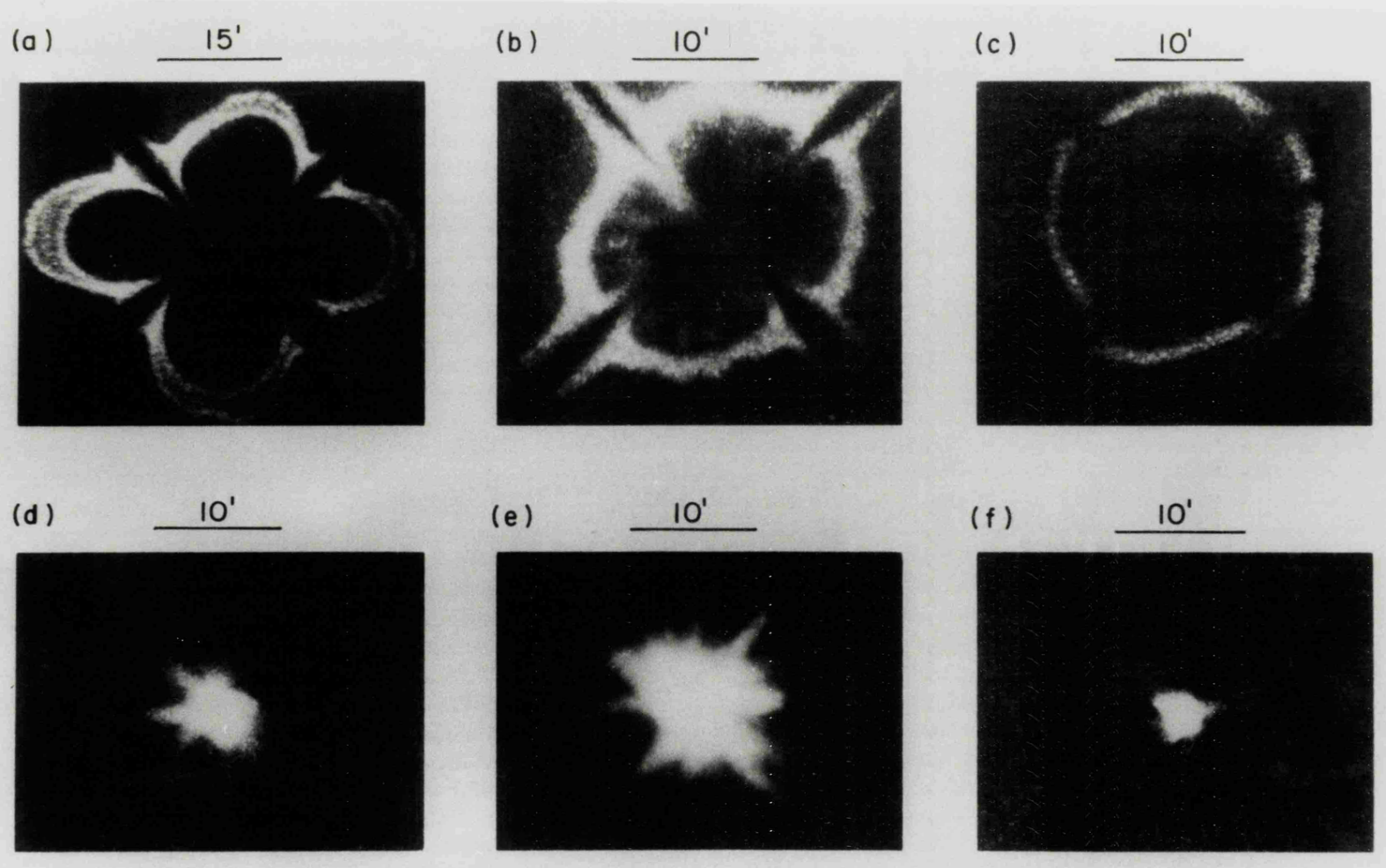

Figure 7.3 (from Petre, 1983) (a-c) Effect of mechanically stressing outer mirror. (a) Image from unstressed mirror, 3.5 mm in front of focus. (b) Image from stressed mirror, 2 mm in front of focus. (c) Image from inner mirror, 2 mm in front of focus. (d-f) Optimized image from all three mirrors at focus. (d) 100 s exposure shows mostly image core. (e) 600 s exposure demonstrates extent of tail. (f) Focused image from inner mirror. The image scale in arc minutes is indicated above each photograph.

Figure 7.4

OPTICAL MEASUREMENTS OF IMAGING QUALITY OF WFSXC MIRRORS

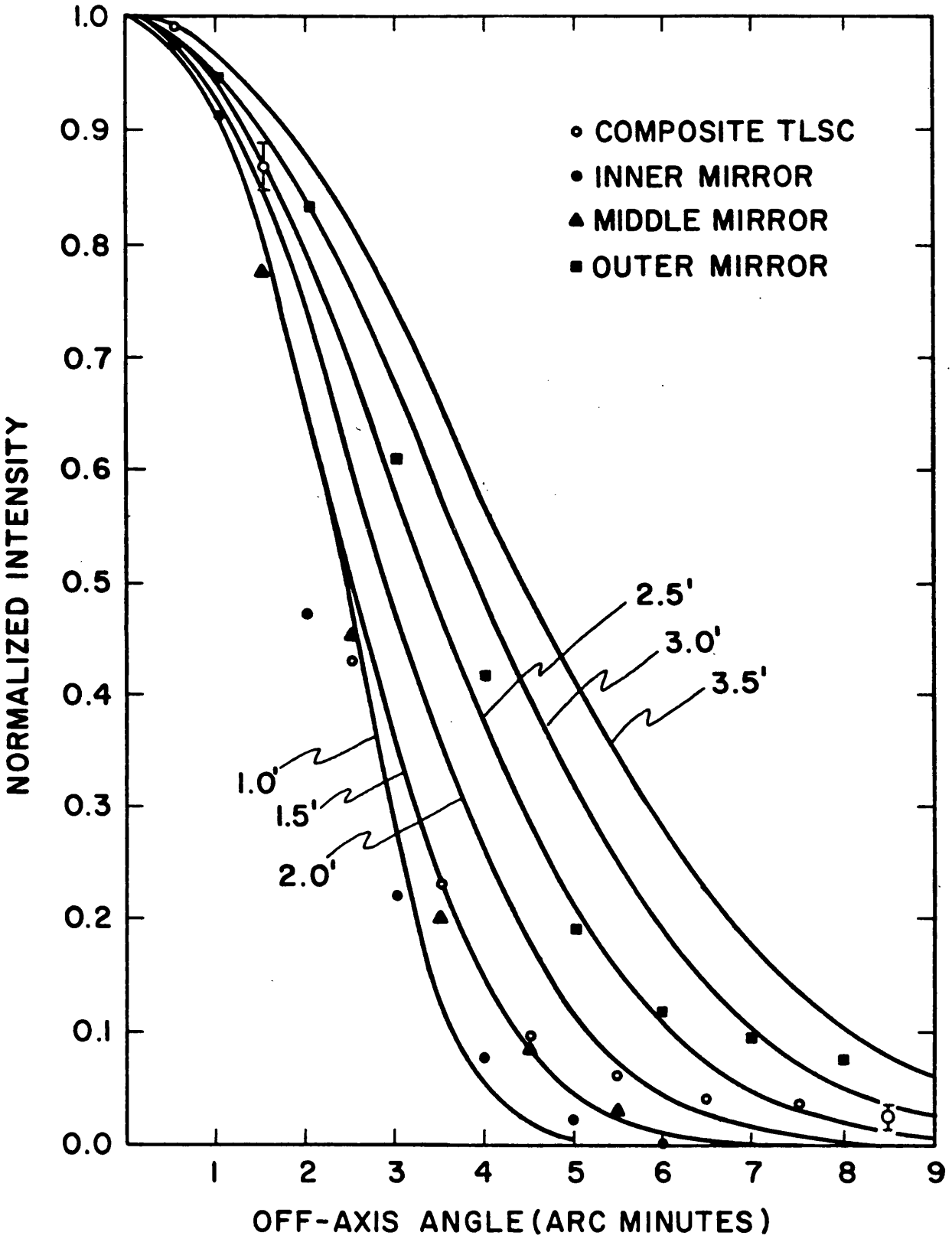

the resolution that might have been achieved had the outer mirrors not been distorted.

7.3 Integration and Testing of the Payload for Rocket 25.040

Once the mirror response had been adjusted to obtain the best possible overall resolution, the payload was assembled and the detector interfaced with the payload electronics. Some initial tests were carried out at MIT, illuminating the detector with an Fe^{55} source through a beryllium window in the lid of the vacuum housing, before the entire payload was placed in the AS&E X-ray facility. As the AS&E tube had a diameter of only 32cm it was not possible to illuminate the entire telescope. However, the whole of the inner mirror could be illuminated and substantial fractions ($\sim$1/4) of the middle and outer mirrors. The longest wavelength available was 44.7Å, lying below wavelengths for which the WFSXC was designed to operate. However, it allowed measurement of the point response function of the instrument and was the only opportunity of calibrating the telescope, detector and filters together.

In order to measure the X-ray image quality the detector was displaced from the nominal focus of the telescope to compensate for the divergence of the AS&E beam, a point source 150ft distant. Tests were performed with the inner mirror illuminated, a 1/4 section of the outer mirror illuminated and a similar section of all three mirrors illuminated together. The quantum efficiency of the payload was measured at a range of off-axis angles by comparing the WFSXC count rate with that from a monitor proportional counter (MPC) mounted in

the X-ray beam directly in front of the telescope. The MPC allowed the flux density of the beam to be measured and, knowing what fractional area of the telescope was illuminated, the input count rate derived.

Three important conclusions were drawn from the tests. First, the quantum efficiency of the payload was uniform across the detector and was as high as expected from the calibrations of the separate components. Second, the effective area of the inner mirror had not degraded from the initial calibration (effective area $0.65cm^2$) nine months previously (any degradation would be most pronounced at short wavelengths) suggesting that the reflectivity of the gold surface finish was stable. Third, the RMS blur circle radius of the image was $\sim 2.5\hat{}$ and the 90% power circle had a diameter of $25\hat{}$-$30\hat{}$, slightly worse than that measured optically ($20\hat{}$). This enlarged image size was probably due to a combination of inaccuracies in the position readout from the ground support equipment (GSE) and X-ray scattering. The latter effect should diminish at longer wavelengths.

Following the AS&E tests the payload was integrated and tested with the attitude control system (ACS), the telemetry (TM), the parachute recovery system and the nose-cone tip eject mechanism at Goddard Space Flight Center (GSFC), Greenbelt, Maryland.

The flight sequence of events was simulated with the integrated system before flight qualification tests. During the sequence the detector and imaging electronics were tested by illuminating the detector with Fe^{55} X-rays through the Be window in the vacuum housing. The data from the payload were transmitted via the TM and recorded on

magnetic tape for later analysis. The pulse height distribution (figure 7.5a) and image (figure 7.5b) from the test show that the detector and electronics were operating correctly before qualification. The image, linearised as described in chapter 5, consists only of those events of pulse height above channel 120 (~2pC).

The flight qualification comprised weighing the payload and determining the moments of inertia, spin-balancing the payload and vibration testing. During the vibration test the payload was subjected to accelerations up to 20g. No major structural faults were revealed and all components, except the ion pump, survived unharmed. The ion pump was not operated during flight, hence a failure during launch would be unimportant.

After flight qualification the ion pump was replaced and the flight sequence was repeated and the data recorded as before (figures 7.5c and 7.5d). The shadow in figure 7.5d was cast by the bar of the filter mount which was not installed during the first test. Figures 7.5c and 7.5d show that the detector and electronics were operated satisfactorily after qualification.

After integration at GSFC the payload was again tested in the AS&E facility to: i) make sure that the mirrors had not been misaligned by the vibration test; ii) determine the X-Y position of the optical axis on the detector and locate the optical axis relative to a fiducial mark on film from the aspect camera; and iii) measure the plate scale of the telescope. The mirrors had not become misaligned, the optical axis was at channels x=256 and y=267

Figure 7.5 Pulseheight distributions (a & c) and detector centred images (b & d) before flight qualification and after flight qualification respectively.

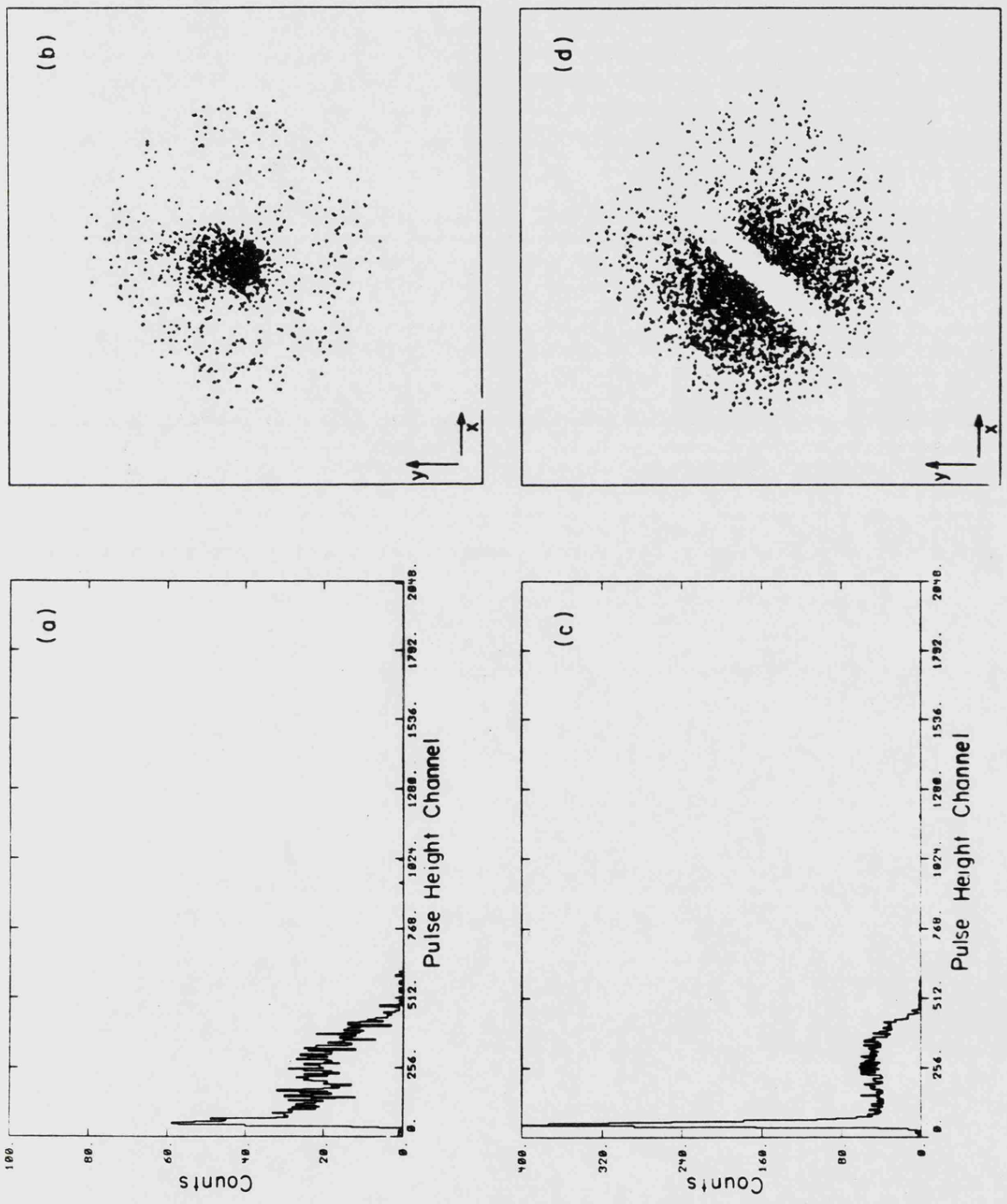

(linearised positions) and the plate scale was 0.1mm=1'.

The payload was then shipped to White Sands Missile Range for launch preparation.

7.4 The sensitivity of the WFSXC

The calibration data that was accumulated throughout the development and integration of the WFSXC allowed the final sensitivity of the WFSXC to be derived. The parameters required for the calculation (equation 2.12) are the instrument grasp, the background count rate, the bandpass and the pixel size (resolution).

The mirrors could only be tested at 44.7Å, an efficiency 40% of that predicted having been measured for the inner mirror. MIT's previous experience with grazing-incidence telescopes suggested that the ratio of measured efficiency to the theoretical value at 44.7Å was a lower limit to the ratio at longer wavelengths. Soft X-ray measurements of the detector quantum efficiency agreed very well with the values predicted by Fraser and used in chapter 2. Therefore, it was still reasonable to use the theoretical data to estimate the efficiencies at longer wavelengths. Similarly experimental measurements of the filter absorption showed good agreement with predictions of the transmissions based on the data of Stern and Paresce (1975) and Cromer and Liberman (1970) (see chapter 6). The filters finally chosen were 5000Å Par N and 2500Å Be + 3000Å Par N, the former being unchanged from the original specification. Figures 7.6a and 7.6b show the transmission of these filters calculated for an angle of incidence of 30°. A lower limit to the efficiency of the

Figure 7.6 Filter transmissions incorporating the mesh transmission (0.93) and taking into account the WFSXC angle of incidence of 30°.

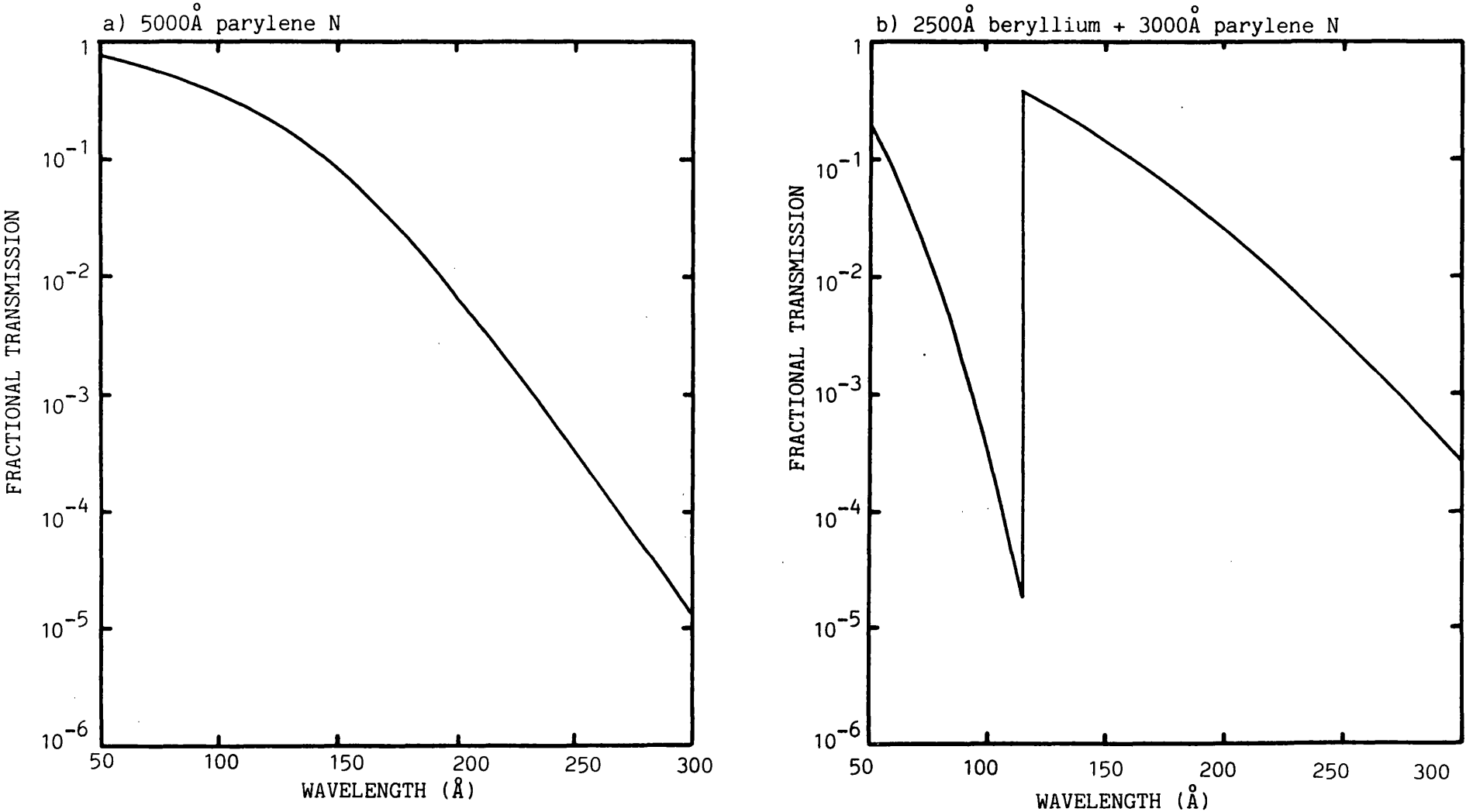

WFSXC was calculated from these filter tranmissions, the detector efficiency for the MgF_2 photocathode (figure 2.9) and 40% of the theoretical mirror efficiency (figure 2.5) and is shown in figures 7.7a and 7.7b for Par N and beryllium + Par N respectively. A grasp of 0.4Å was obtained for the Par N filter, and one of 0.19Å for the Be + Par N filter with bandpasses of 50-170Å and 114-200Å respectively.

A total detector background of ~ 5 counts s^{-1} was obtained (see chapter 3) at the detector operational voltages. As a result of stepping in the electrode diameters to eliminate noise the active area of the detector was limited to a circular field of 36mm diameter, covering a solid angle of 8.63×10^{-3}ster on the sky. Therefore the detector background referred back to the sky was 579 counts $s^{-1} ster^{-1}$. Table 7.1 summarises all the contributions to the background. It was assumed that the HeII flux had its maximum night-time value of 1 Rayleigh. A total of 2.6 counts s^{-1} in the Par N filter and 2.76 counts s^{-1} in the Be/Par N filter were expected.

Taking the 90% power circle ($\sim$25-30$\hat{}$ diameter) as an upper limit to the mirror resolution it dominated the over all resolution of the WFSXC as that of the detector was small by comparison (1-5$\hat{}$ FWHM). Therefore the pixel size (θ^2) was ~ 700 square arcminutes, corresponding to a solid angle on the sky of 6×10^{-5}ster.

Given the response of the WFSXC, the expected background and the pixel size, the sensitivity was calculated as a function of exposure time (figure 7.8). It can be seen that for observation times less than $\sim$25s the WFSXC background per pixel was effectively zero, as the

Figure 7.7 WFSXC efficiency estimated after calibration and testing of the instrument and its component parts.
a) With 5000Å parylene N filter.
b) With 2500Å beryllium + 3000Å parylene N filter.

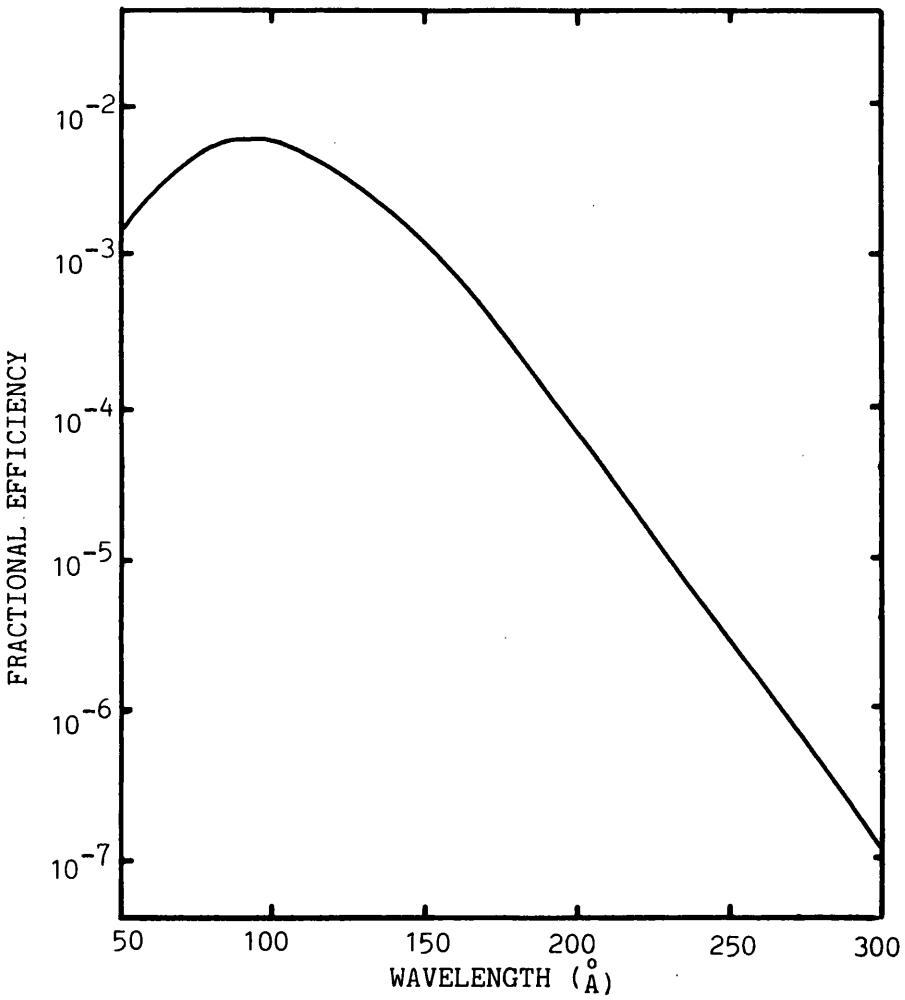

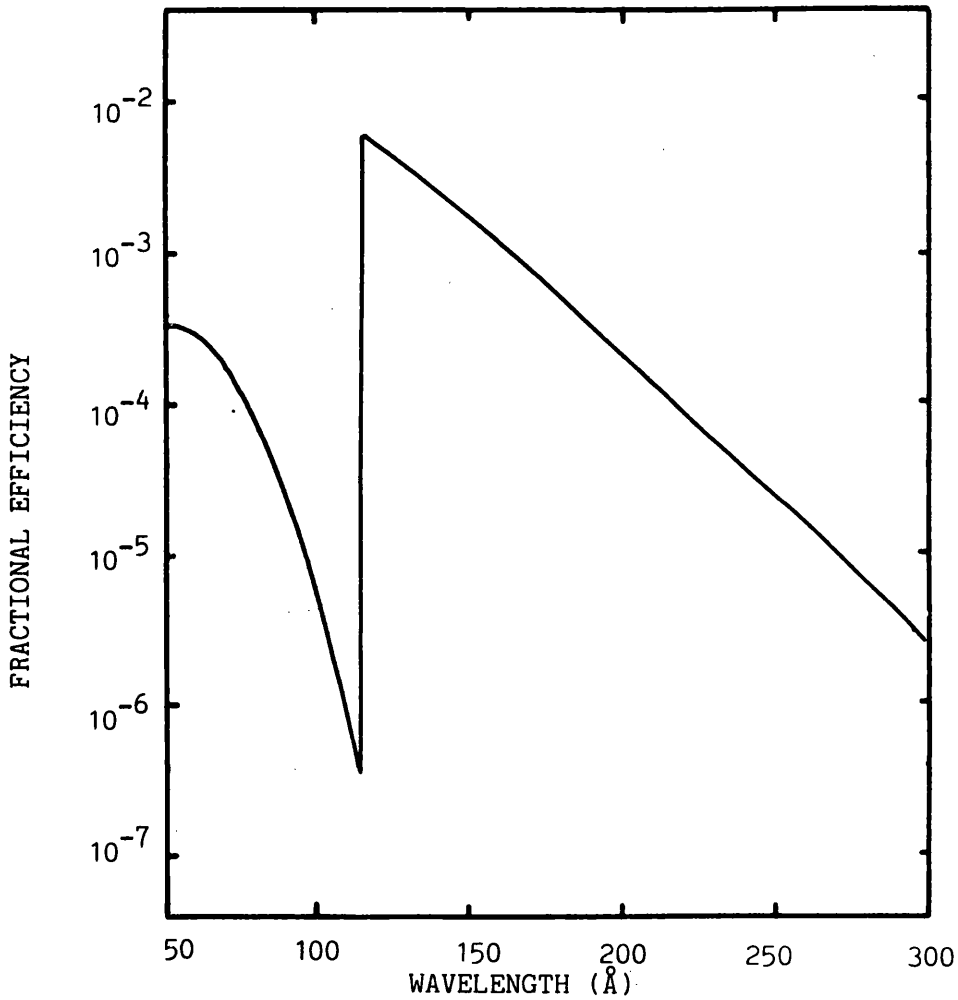

Table 7.1. WFSXC background calculated after pre-flight calibrations

Expected background in the WFSXC	Filter 5000Å Par N counts s^{-1} $ster^{-1}$	5000Å Par N total* in filter	Filter 2500Å Be + 3000Å Par N counts s^{-1} $ster^{-1}$	2500Å Be + 3000Å Par N total* in filter
Detector	579	2.5	579	2.5
Cosmic XUV	9	0.04	2.3	0.01
HeII (304Å)	8	0.03	53	0.26
Total	596	2.6	634	2.8

* it was assumed that each filter covered ~ half the field of view

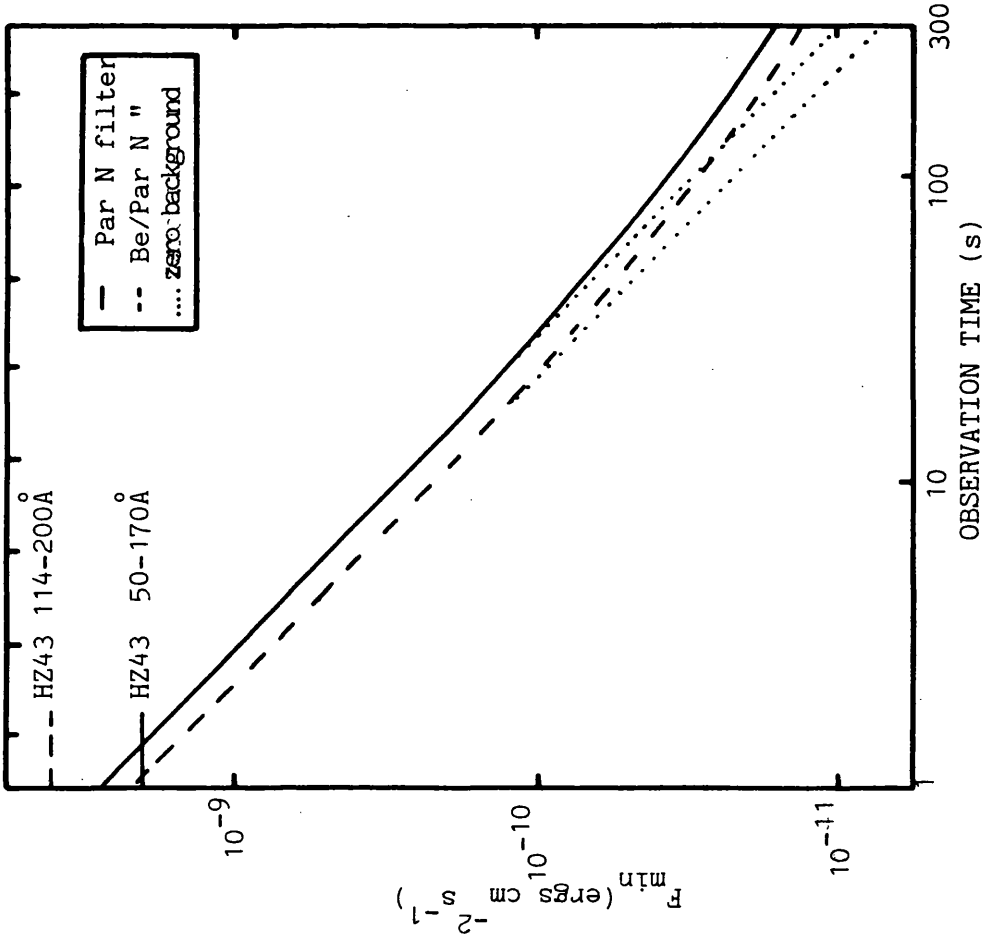

Figure 7.8 WFSXC sensitivity

sensitivity curves follow those for zero background ($F_{min} \propto 1/T$), and operated in the photon limited regime. A typical scan rate of $0.25°s^{-1}$ gave an observation time of 24s across the centre of the field of view. The resulting sensitivities for this exposure time were $1.26x10^{-10}$ergs $cm^{-2}s^{-1}$ (Par N) and $1x10^{-10}$ergs $cm^{-2}s^{-1}$ (Be/Par N).

7.5 Conclusion

Table 7.2 compares the measured performance with the design estimates, which were summarised in chapter 2. The sensitivities are compared for a scan rate of $0.25°s^{-1}$, showing that in the Par N and Be/Par N filters the sensitivity was 0.26 and 0.17 that expected, respectively. The reasons for the reduction were: i) the lower than expected mirror efficiency; ii) reduction of the field of view, reducing the observation time for a given scan rate; and iii) the addition of 2000Å of Par N to the Be/Par N filter. However, as 1/20 (Par N) and 1/70 (Be/Par N) HZ43 fluxes could be detected the final WFSXC sensitivity was adequate.

Reducing the field of view also restricted the area of sky that could be imaged in a single rocket flight. A scan rate of $0.25°s^{-1}$ allowed coverage of ~450 square degrees of sky in a single 300s flight, ~0.8% of the celestial sphere which is 0.6 times that possible with an 8° field of view.

The distortion of the middle and outer mirrors did not allow the telescope to achieve the design resolution of 1$\hat{}$ (RMS) on-axis. An RMS blur circle radius of 2.5$\hat{}$ was measured with 90% of the power

Table 7.2. Comparison of the WFSXC performance calculated after pre-flight calibrations compared with the design predictions

Parameter	Design Value		Achieved value	
Field of view (ster)	1.5×10^{-2}		8.63×10^{-3}	
Pixel size (ster)	10^{-7}		6.00×10^{-5}	
Collecting area (cm^2)	250		250	
Filter	Par N	Be/Par N	Par N	Be/Par N
Material thickness (Å)	5000	2500+1000	5000	2500+3000
Bandpass (Å)	50-170	114-230	50-170	114-200
Grasp (Å)	0.98	1.13	0.40	0.19
Total background (counts $s^{-1} ster^{-1}$)	1330	1.1×10^{4}	596	634
F_{min} ergs $cm^{-2} s^{-1}$ ($0.25°s^{-1}$ scan rate)	3.5×10^{-11}	1.6×10^{-11}	1.3×10^{-10}	1.0×10^{-10}
F_{min} as fraction of HZ43 flux in the band	1/63	1/525	1/20	1/70

lying within 25-30$\hat{}$. An on-axis resolution of 0.4$\hat{}$ (RMS) was achieved with the detector, therefore the overall resolution was dominated by the mirrors. As the WFSXC operated in the photon limited regime below exposure times of 25s the poorer than expected final upper limit to the resolution of 30$\hat{}$ (=6x10^{-5}ster pixel size) did not contribute to the lower sensitivity.

CHAPTER 8

FLIGHT PLANNING

8.1 Constraints Upon WFSXC Observations

The area of sky that is observable during a rocket flight is a hemisphere centred on the zenith of the launch site, although because of the rocket's altitude the payload can view up to 104° from the zenith at apogee (200km). The particular part of the celestial sphere that can be viewed is determined by the declination (=latitude) of the launch site and the right ascension (RA) of the zenith, the latter being a function of the time of day. White Sands Missile Range (WSMR), New Mexico, USA, the launch site for both rocket flights, has a latitude of 32.42°N allowing observations of all the northern celestial hemisphere and up to a declination of -57.58° in the southern hemisphere.

The position of the sun imposes limitations on the allowed viewing direction and thereby restricts observations of a particular area of sky to a certain time of year. First, the sun cannot be observed directly by the WFSXC as the enormous solar EUV flux will saturate the instrument. Second, geocoronal radiation (see section 1.6) is at its maximum during the daytime, the fluxes being highly dependent upon both the solar zenith angle of the line of sight and the position of the payload with respect to the sun (solar zenith angle) (see figure 1.7). In order to minimise the background the payload must be flown at night (ie. with a solar zenith angle greater than 90°) and can be reduced further by looking as far away from the sun as possible, down the earth shadow.

As a result of the above restrictions, the most useful area of sky for observation is the region bounded by both the local horizon at launch time and a solar zenith angle of 90° (figure 8.1). Solar zenith angle contours at 90°, 120° and 150° are shown as an example for the first flight (rocket 25.040) on 17th October 1981 with the horizon of WSMR at local midnight. The unshaded region represents the useful area of sky for observations at this date and time.

As explained in chapter 1 atmospheric attentuation effects are important at XUV wavelengths, therefore the WFSXC should observe as close to the local zenith as possible. An increase in the local zenith angle of a source results in a reduction of its apparent intensity. This is illustrated in figure 8.2 by the decreasing transmission of the atmosphere, with increasing zenith angle, plotted at the extremes of the XUV band (50Å and 250Å), at sounding rocket altitudes. The limits of the altitude are 120km, when the instrument turns on, and the apogee, 200km. As an example, the transmission at a zenith angle of 60° (at 250Å and 200km), and therefore the flux, is $\sim$1/3 that at the zenith. At lower altitudes the fractional reduction in the zenithal flux is larger. There is a trade-off between optimising the pointing direction for minimum geocoronal background against loss of source intensity due to increased atmospheric absorption by having to point away from the local zenith. This must be considered when planning observations.

Figure 8.1 Aitoff projection of the sky showing the useful observing area (unshaded region) for local midnight on the 17th October 1981.

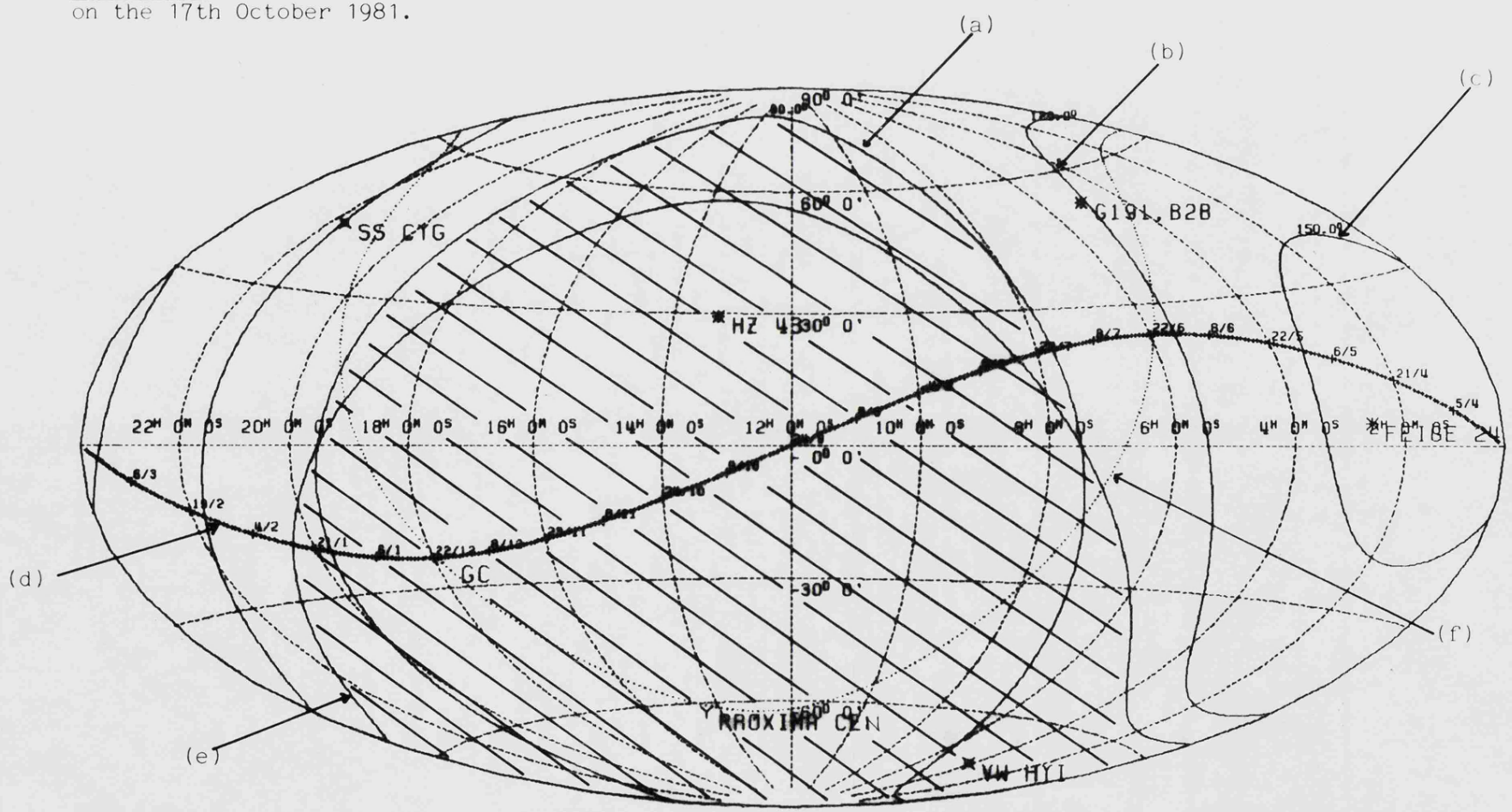

KEY: a,b & c denote contours of angular distance from the sun - a=90°, b=120°, c=150°. d is the ecliptic plane with the approximate dates on which the sun is at a given hour of right ascension. e is the horizon at WSMR at local midnight. f is the galactic plane, GC marks the galactic centre.

8.2 Rocket Manoeuvres

To survey areas of sky for EUV sources a WFSXC flight consists of a series of scans which may be executed by either pitch, yaw or roll manoeuvres (figure 8.3). The maximum rate at which individual manoeuvres can be executed is limited by the ACS to $\sim 6°s^{-1}$ with a pointing accuracy of $\sim \pm 1°$.

For simplicity the filter unit is oriented so that the dividing bar is parallel to the pitch axis. By making all scanning manoeuvres pitches objects travel through the field of view in a direction perpendicular to the filter bar, through both halves of the filter. When the scan direction is changed the payload is rolled about the optical axis to keep the filter bar perpendicular to the scan direction. If the scan direction is altered a large number of times, the time "lost" during roll manoeuvres can be a large proportion of the mission time. The chosen scan rate is determined by the required sensitivity of the observations and a trade-off exists between the sensitivity and sky coverage.

As a result of the ACS pointing accuracy, it cannot be guaranteed that an object will pass through the centre of the field of view and if it does not the observation time must be reduced. In the photon limited case the off-axis sensitivity ($F_{min}(\alpha')$) is

$$F_{min}(\alpha') = F_{min}(0).1/\sin(\cos^{-1}\alpha'/R) \qquad (8.1)$$

where: $F_{min}(0)$ is the sensitivity for a source passing through the centre of the field of view

Figure 8.2 Atmospheric transmission as a function of the angular distance from the zenith.

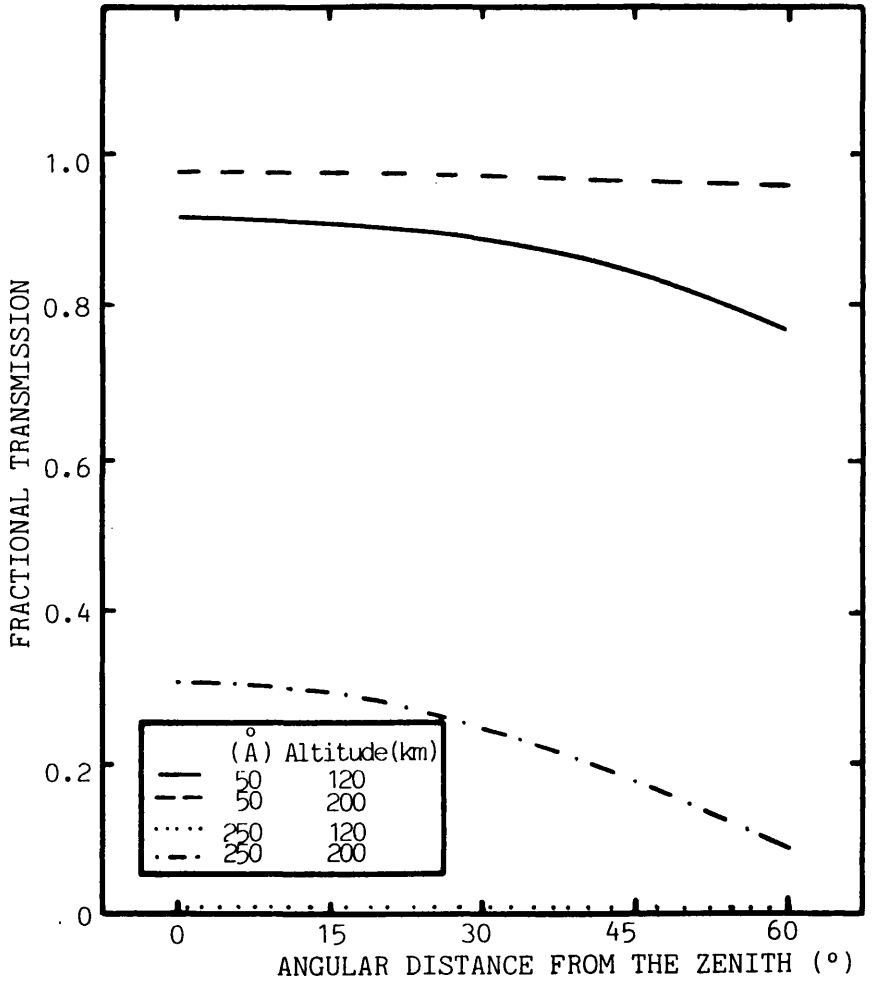

Figure 8.3 The WFSXC payload axes of manoeuvre.

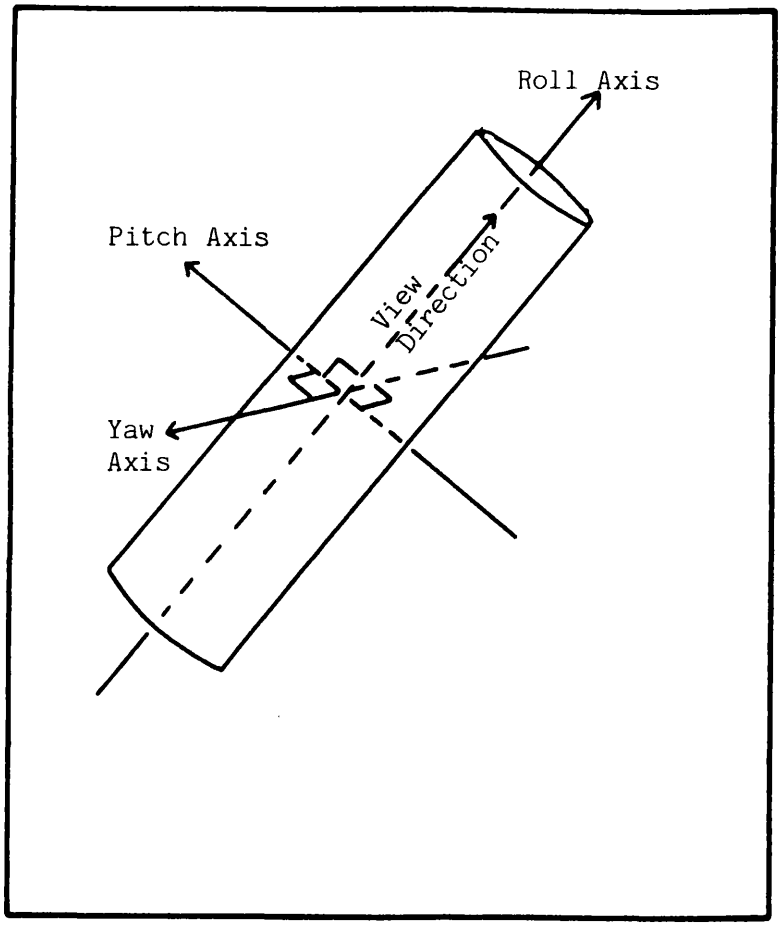

α' is the off-axis angle of the scan path (figure 8.4)

R is the angular radius of the field of view

(figure 8.4)

F_{min} increases by 1% 1° off-axis and by 50% 2° off-axis. Hence, the ACS error does not affect the sensitivity on a given target. However, when planning an observing program 2° is the maximum off-axis angle that should be allowed.

8.3 Flight Plan for Rocket 25.040

Scan rates were chosen for the flight to give minimum detectable fluxes that were much lower than the flux from HZ43 but giving a coverage of ~1% of the sky. In the Par N filter the slowest scan rate of $0.25°s^{-1}$ gave a sensitivity of ~1/20 HZ43 and a maximum rate of $1°s^{-1}$ ~1/5 HZ43. These respective scan rates gave sensitivities of ~1/70 and ~1/18 HZ43 in the Be/Par N filter.

The scientific return from a rocket flight can be maximised by careful planning so that scan paths pass over areas of sky containing potential EUV sources. The distribution of primary targets (ie. those most likely to be detected based on the discussions of chapters 1 and 2) is plotted on a skymap in figure 8.5. The galactic plane and ecliptic plane are plotted, the latter with the approximate dates on which the sun crosses each hour of right ascension.

The launch of rocket 25.040 was scheduled for late summer/autumn of 1981, hence the flight plan was based around the SS Cygni region and included the hot white dwarf EG233 as a "calibration" source to

Figure 8.4 The orientation of the filter with respect to the scan direction from above the detector.

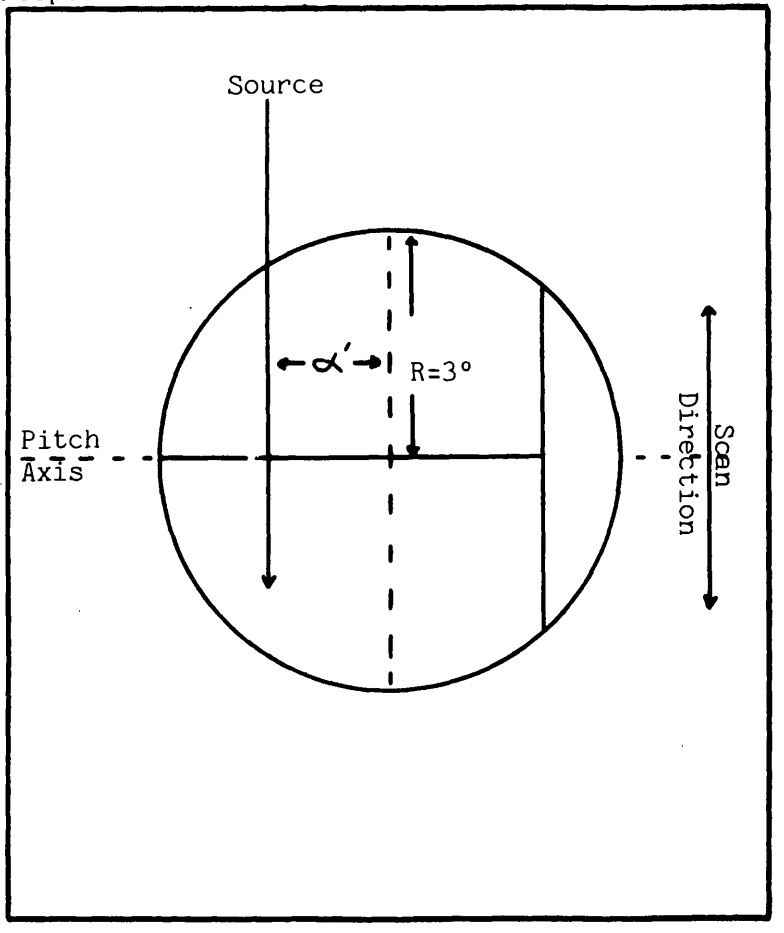

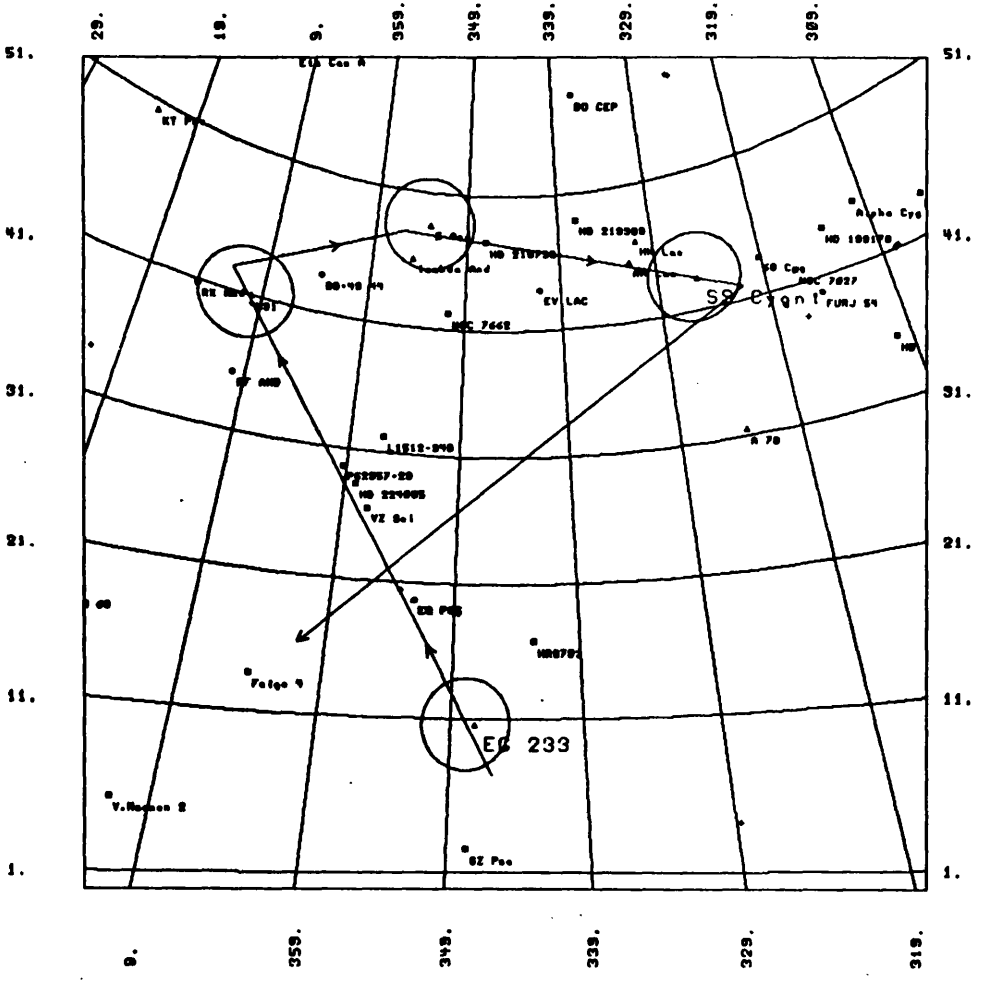

Figure 8.6 Flight plan for rocket 25.040. (note this figure is out of sequence)

Figure 8.5 Principal WFSXC targets plotted on an Aitoff projection of the sky.

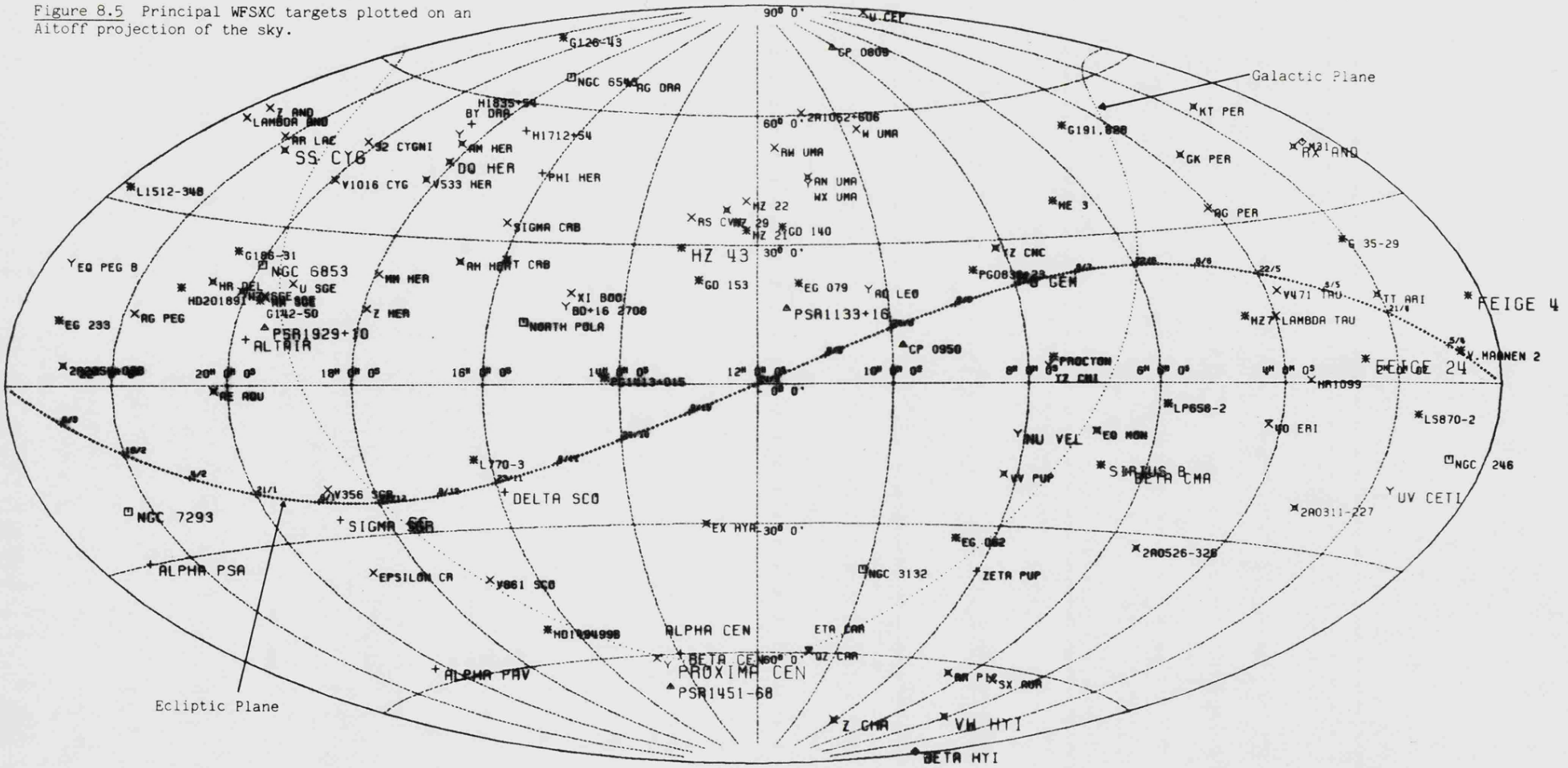

test the imaging quality and sensitivity of the WFSXC. There are also three flare stars of particular interest in this region of sky - EQ Pegasi, BD+43 44 and EV Lacertae, of which the first two have both been detected by Einstein (Vaiana et al, 1981). EV Lac was a target for ASTP (Paresce, 1977) but was not detected. Several interesting binaries, detected by Einstein, are found in this region, the RS CVn soft X-ray sources, HK Lacertae, AR Lacertae and Lambda Andromeda (Walter et al, 1980; Swank et al, 1980; Petre, private communication), with fluxes comparable to that of HR1099, and the binary Z Andromedae.

The flight plan (figure 8.6) was to commence with a $0.25°s^{-1}$ scan over EG233. To make best use of the time available the rocket was oriented so that the target would pass through the parylene filter first, as the radiation in this band would be least attenuated by the atmosphere. This was followed by a $1°s^{-1}$ scan towards M31, the scan rate being reduced to $0.25°s^{-1}$, 6° before reaching it. At this point the rocket was rolled by 80° to change the scan direction, the leading filter then being the Be/Par N. A $0.25°s^{-1}$ scan followed by a roll and then another $0.25°s^{-1}$ scan took the WFSXC past SS Cygni. A third roll, after which the leading filter was once more the Par N, was followed by a $0.25°s^{-1}$ scan towards Feige 4 obtaining maximum use from the available observing time by scanning away from the galactic plane and towards the zenith as the rocket lost altitude. The whole flight plan was expected to take ~300 seconds, the approximate observing time on an Astrobee F rocket and covered an area of sky of ~550 square degrees.

8.4 Launch Windows

The nightly window was determined by the time when the targets were at their closest approach to the local zenith. The zenith at WSMR is at a declination of 32.42°N. The right ascension of the zenith is however a function of both the time of year and the time of day.

For WSMR, the Greenwich Apparent Sidereal Time (GAST) at which the local zenith passes a given hour of right ascension (RA) is

$$GAST = (RA)+(\text{west longitude WSMR})-TF \qquad (8.2)$$

where for 1981 (HMSO, 1980)

$$TF = 6^h.6383221 + 0^h.0657098235d + E \qquad (8.3a)$$

and for 1982 (HMSO, 1981)

$$TF = 6^h.6224076 + 0^h.0657098235d + E \qquad (8.3b)$$

d is the day of the year and E is the equation of the equinoxes, the correction between mean and apparent sidereal time. E is 1s at its maximum value and can be ignored for the purposes of calculating the rocket launch windows. The launch time in the local time zone is simply (GAST-Time zone of launch site). At WSMR the time zone is 7hrs for Mountain Standard Time (MST) or 6hrs for Mountain Daylight Time

(MDT).

The best zenith position for the 25.040 flight plan occurred at an RA of ~23hrs, minimising the zenith angle at the beginning and end of the flight where atmospheric absorption is most important. An error of ±1/2hr was allowed in the position of the zenith giving a window of 22hrs 30min RA to 23hrs 30min RA. The times when the local zenith passes these points are the limits of the launch window which is shown in figure 8.7 (mountain standard time), calculated between 1st August and 31st October 1981.

Figure 8.7 The launch window for rocket 25.040 from August to October 1981 from WSMR.(Shaded region).

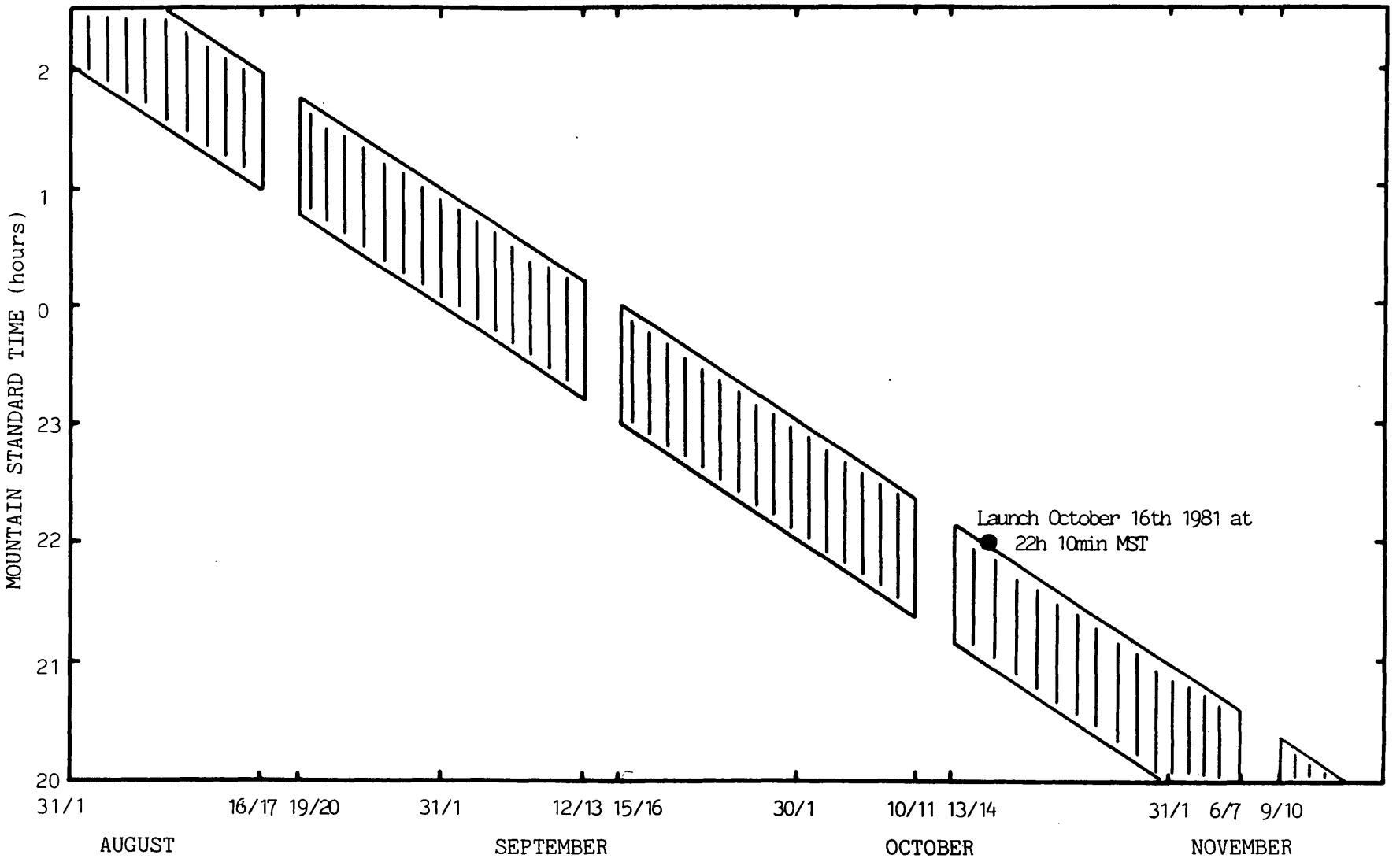

CHAPTER 9

WFSXC FLIGHT 1: ROCKET 25.040

9.1 Final Pre-launch Preparations and Flight

The WFSXC payload and Astrobee F booster were installed in the Aerobee 350 tower at launch complex 36, WSMR seven hours prior to launch on 16th October 1981 at approximately 4pm MDT. Two hours before launch a test of the payload was performed, running through the flight sequence and transmitting data via the telemetry, as in the integration tests. The detector data, recorded on a chart recorder, showed that the payload was operating normally and flash bulbs attached to the pyrotechnic firing system showed that the charges would fire at the correct time in the flight sequence, to open the vacuum housing. A test magazine was loaded into the star camera and was wound up correctly during the test, indicating that the camera drive was working properly. The flight magazine was installed after the test and a length of film wound up to ensure that the magazine was correctly loaded and would not jam. Up to the moment of launch, power was supplied to the ion pump to keep the detector and filters at as low a pressure as possible and the payload was purged with dry N_2 to minimise its water vapour content.

Rocket 25.040 was launched at $23^h10^m2.011^s$ MDT ($5^h10^m2.011^s$ 17th October UT). The rocket motor burned for 54 seconds and a peak altitude of 203.2km was attained 235s after launch. The total observing time (time at altitudes above 150km) was 220s. All events, booster separation, nose cone ejection etc., were carried out successfully at the correct times and altitudes (table 9.1) and all

Table 9.1. Times and approximate altitudes of experiment related events

Event	Time (s)	Altitude (km)
Despin	70	53
Nose cone eject	75	60
Separation	75	60
Experiment turn on	80	68
Vacuum housing open	110	109
Peak altitude	240	191
Timer, Experiment turn off	400	68
"Back up" off timer	410	53

ACS manoeuvres were completed as specified in the flight plan.

9.2 The Malfunction of the WFSXC

Data from the payload were monitored in real time during flight on the chart recorder. Figure 9.1 illustrates a sample of the output with the channel designations marked.

As soon as the payload was switched on it was apparent that it was not operating correctly. The first obvious problem involved the aspect camera electronic pulses which should have occurred at a rate of 2 pulses s^{-1}, each pulse corresponding to the exposure of a single frame of film. Instead the camera circuit generated pulses of irregular length and frequency, as can be seen in figure 9.1, averaging ~5-6 per second. Figure 9.2a shows the aspect camera pulse rate throughout the whole flight. This erratic behaviour, which began immediately the experiment was turned on, prevented the film from advancing and it was only towards the end of the flight (t>440s) that the camera began to operate correctly and advance the film.

From the real time record it appeared that most of the events from the detector were saturated (all 9 bits of the digital output triggered) in all channels, as illustrated by a group of events marked "(a)" in figure 9.1. Events marked "(b)" are unsaturated. The histogram of the total count rate (figure 9.2b) shows an average of ~40 counts s^{-1} with fluctuations up to ~100 count s^{-1} on time scales of a few seconds, somewhat higher than the expected total background of ~6 counts s^{-1} (assuming night-time HeII flux). The count rate of unsaturated events, with detector dark events rejected (events below

Figure 9.1 Sample of the real time flight record.

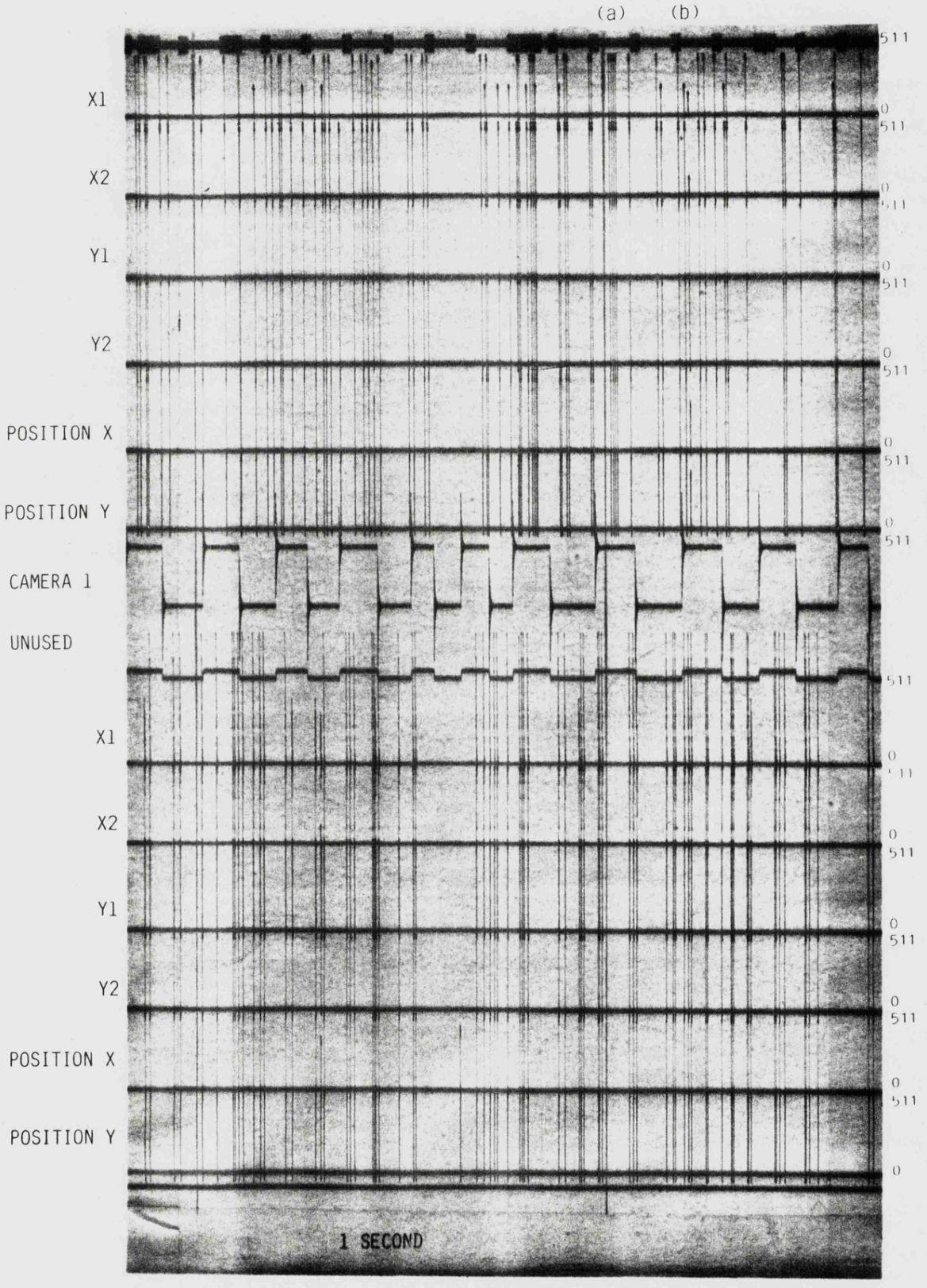

Figure 9.2 Rate histograms (count rate/elapsed time) for a) the aspect camera pulses, b) All the events detected and c) the unsaturated events alone with detector dark events (pulse height < 2pC) rejected.

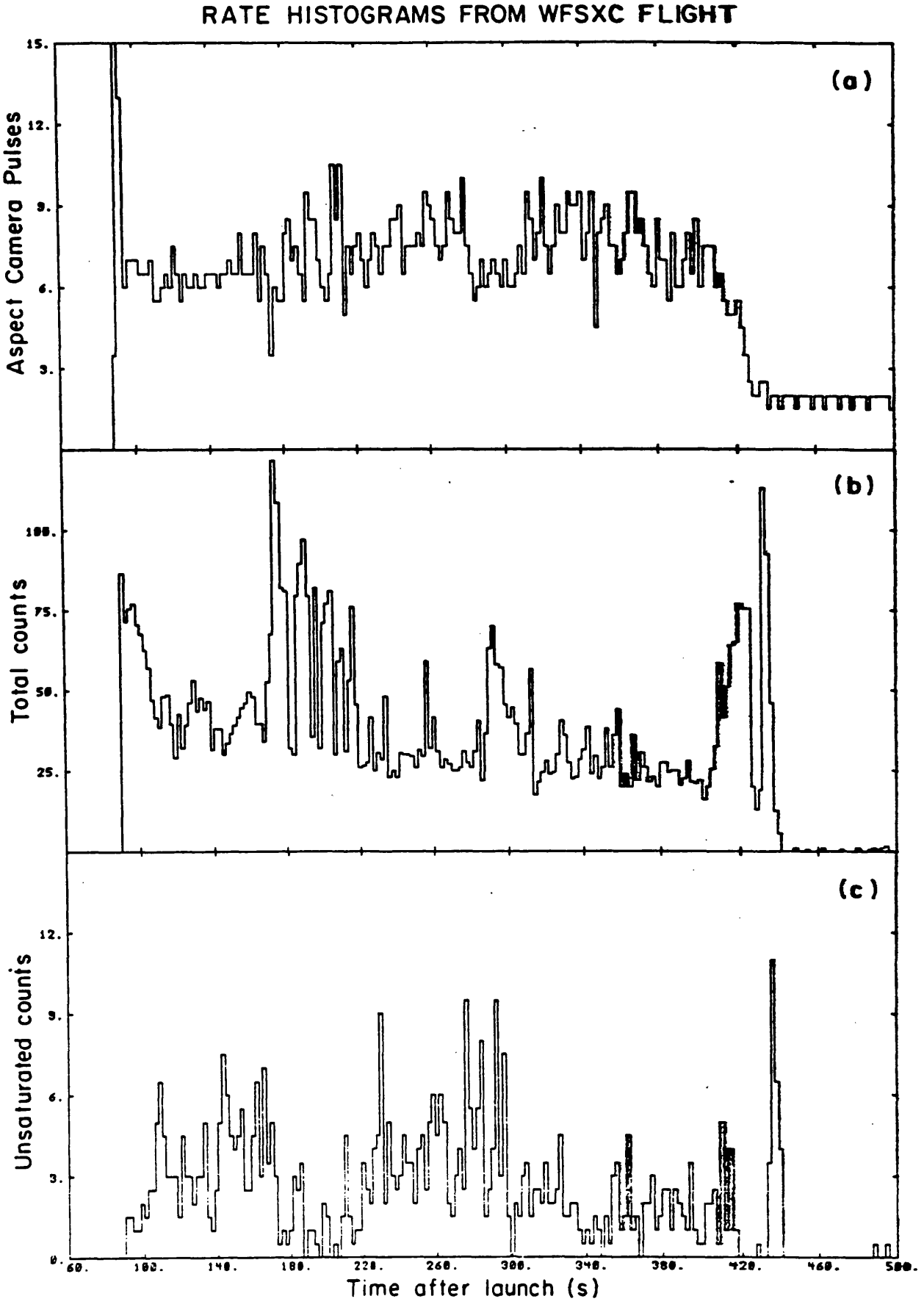

2pC), was 3-4 counts s^{-1} (figure 9.2c). Hence ~90% of the total events were saturated.

The pulse height distribution of detector events (figure 9.3a) bore very little resemblance to those measured during integration (figures 7.3a and 7.3c). Many of the pulse heights were quantised into particular channels and were generally larger than seen during integration.

The count rate during the flight should have been dominated by background events that would have been uniformly distributed over the detector image. However, the detector image of the unsaturated events above 2pC exhibited a highly non-uniform distribution (figure 9.3b). Most of the events were clumped into the centre of the image or along the saturation level of the Y-axis. Although the bright central areas resembled hot-spots in appearance their pulse heights were higher (>2pC) than would be expected for hot-spot events. The above data indicated that the detector did not operate correctly during flight.

9.3 The Determination of the Cause of the Malfunction

The payload was recovered intact after flight. However, the filter had shattered during re-entry spreading beryllium debris over the detector and a small leak had developed between the vacuum housing bulkhead and the tube leading to the ion pump. When the payload had been returned to MIT, the detector was carefully decontaminated.

Subsequent tests of the payload showed it to be in working order. The aspect camera exposed two frames per second, the detector noise was almost as low as before flight (~5 counts s^{-1}) and the proportion

Figure 9.3

ASTROBEE 25.040

(a) Pulse Height Spectrum from WFSXC Flight - All Events

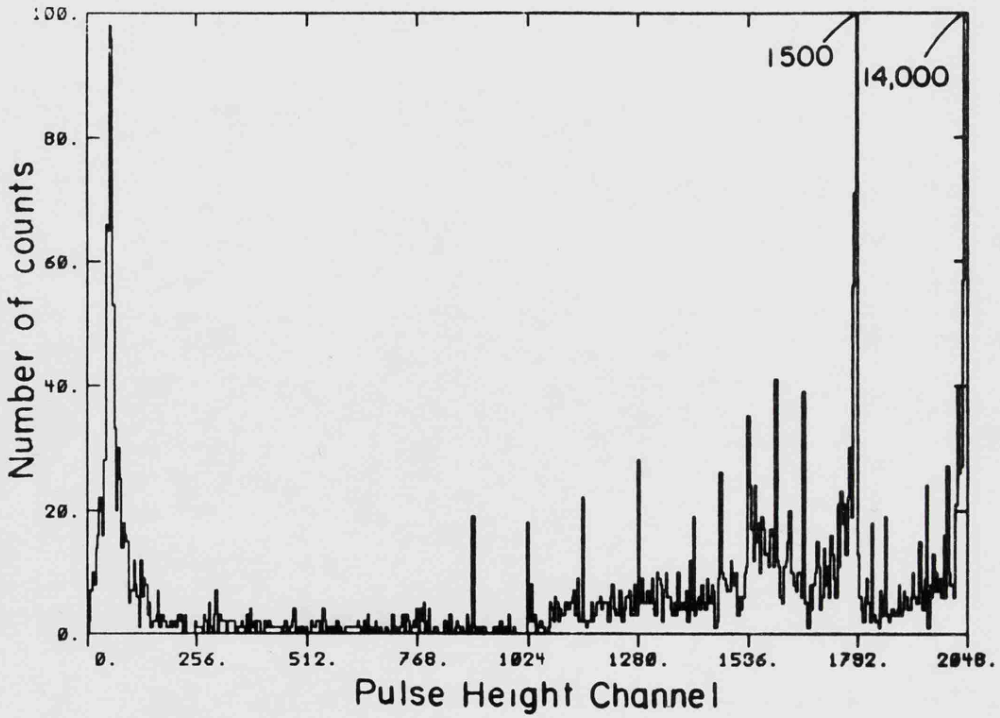

(b) Linearized Detector Image from WFSXC Flight - Unsaturated Events

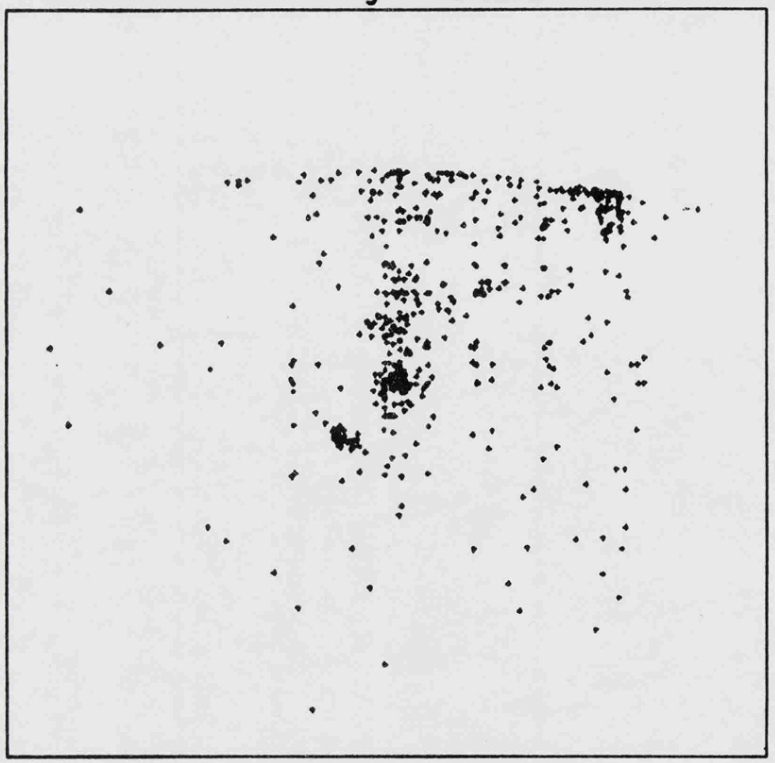

of saturated events in the detector output was less than 5% of the total.

It was found during testing that the symptoms of the malfunction could be reproduced by inducing a corona discharge between the high voltage distribution chain and the walls of the detector housing. The discharge could only be initiated at a pressure above $5x10^{-2}$Torr and sustained only above $5x10^{-4}$Torr.

It is likely that a corona discharge was the cause of the payload failure. It appeared from the data that the corona was initiated when the experiment, and therefore the high voltage supply, was switched on, which was before the detector housing was opened. The corona was sustained throughout the flight except towards the end (t>440s) when it was probably quenched by re-entering the atmosphere. The vacuum leak that was found on recovery may have occurred during launch, allowing the pressure inside the housing to rise sufficiently to initiate corona, but the housing had survived flight qualifiction with no problems. However, it was found during tests for the second flight that when the external pressure decreased below ~14Torr the vacuum housing leaked up to a corona pressure, a more satisfactory explanation of the failure. Alternatively the payload may have pumped out inefficiently leaving a residual pressure high enough to initiate a corona discharge inside the high voltage supply itself or at the HV feedthrough into the vacuum housing.

9.4 Analysis of Expected Payload Pressure During Flight

It is important to analyse the pumpout of the payload during flight to establish whether or not a pressure high enough to initiate and sustain a corona discharge could have occurred.

The only pumpout path is through the grazing incidence mirrors. Hence, until the nose cone is ejected the internal pressure inside the payload remains at 1 atmosphere (760Torr). The efficiency of pumpout after nose cone ejection depends upon the conductance of the mirror nest (C_T) and the pressure difference across the conductance (DP), the throughput being

$$Q_P = C_T.DP \text{ Torr l s}^{-1} \qquad (9.1)$$

Material will be outgassed from surfaces inside the payload. The throughput into the payload volume from outgassing effects (Q_G) acts to reduce the speed at which the payload is evacuated and the net flow of gas from the payload (Q) is

$$Q = Q_P - Q_G \qquad (9.2)$$

Analysis of the pressure inside the payload requires knowledge of C_T, Q_G and the external pressure, since DP is the difference between internal and external pressures. Each of these parameters will be estimated in the following sections and the pressure inside the payload will then be determined.

9.4.1 Outgassing Inside the Payload

The payload has a large internal surface area ($\sim 1m^2$) which is mostly aluminium. The payload was degreased and purged with dry N_2, to minimise its water vapour content, before flight. Roth (1976) quotes values of 10^{-7} to 10^{-9}Torr l s^{-1} cm^{-2} for the outgassing of degreased aluminium. Taking the higher value, an upper limit to the net outgassing rate is 10^{-3}Torr l s^{-1}. Electronics boards comprise a surface area $\sim 2000cm^2$. Roth gives an upper limit to the outgassing rates of plastic and epoxy materials of $\sim 4x10^{-7}$Torr l s^{-1} cm^{-2} when degreased. Assuming that these materials are representative of those comprising the electronics boards the expected outgassing from this source is $\sim 10^{-3}$Torr l s^{-1}. Hence, the total outgassing inside the payload is expected to have an upper limit of $\sim 2x10^{-3}$Torr l s^{-1}.

9.4.2 The External Pressure Seen by the Payload

The mean free path (MFP) of a gas molecule is determined by the number density of molecules (n, m^{-3}) and their scattering cross-section with each other ($\sigma_S{}^2$, $\sim 10^{-20}m^2$) (Sprackling, 1970)

$$MFP = \frac{1}{\pi \sigma_S{}^2 n} \qquad (9.3)$$

When the nose cone was ejected (at 83km) n was $<10^{20}m^{-3}$. Hence, the MFP was >0.3m which was $\sim$ the diameter of the payload aperture. As n decreases rapidly with increasing altitude (becoming $\sim 10^{18}m^{-3}$ at 100km) calculation of the external pressure seen by the payload must

consider the molecular flow of gas onto the telescope aperture. Therefore, the velocity (V_R, ms^{-1}) of the payload gives rise to a ram pressure (P_R) on the aperture

$$P_R = \frac{2\rho V_R^2}{1.33x10^2} \quad Torr \qquad (9.4)$$

where: ρ is the ambient gas density ($Kg\ m^{-3}$)

Assuming that the optical axis was always parallel to the velocity vector of the payload, P_R was calculated as a function of the mission time using the flight altitude and velocity profiles (figure 9.4). ρ was obtained from Jacchia (1971). The ambient external pressure (P_E), estimated from the density/altitude data of Jacchia (above 90km) and Zombeck (1981) (below 90km), is also shown in figure 9.4. When the nose cone was ejected the payload velocity was $1500ms^{-1}$ (t=75s) and the ram pressure was a significant effect, 0.3Torr compared to an ambient pressure of $\sim10^{-3}$Torr. It was not until t=200s, when the velocity of the payload was $\sim$ the molecular velocity of the gas ($\sim300ms^{-1}$) that the ram pressure was of the same order as the ambient pressure ($2x10^{-6}$Torr).

Figure 9.4 The ambient pressure (P_E), the ram pressure P_R and the estimated pressure inside the payload P as functions of the time after launch (t).

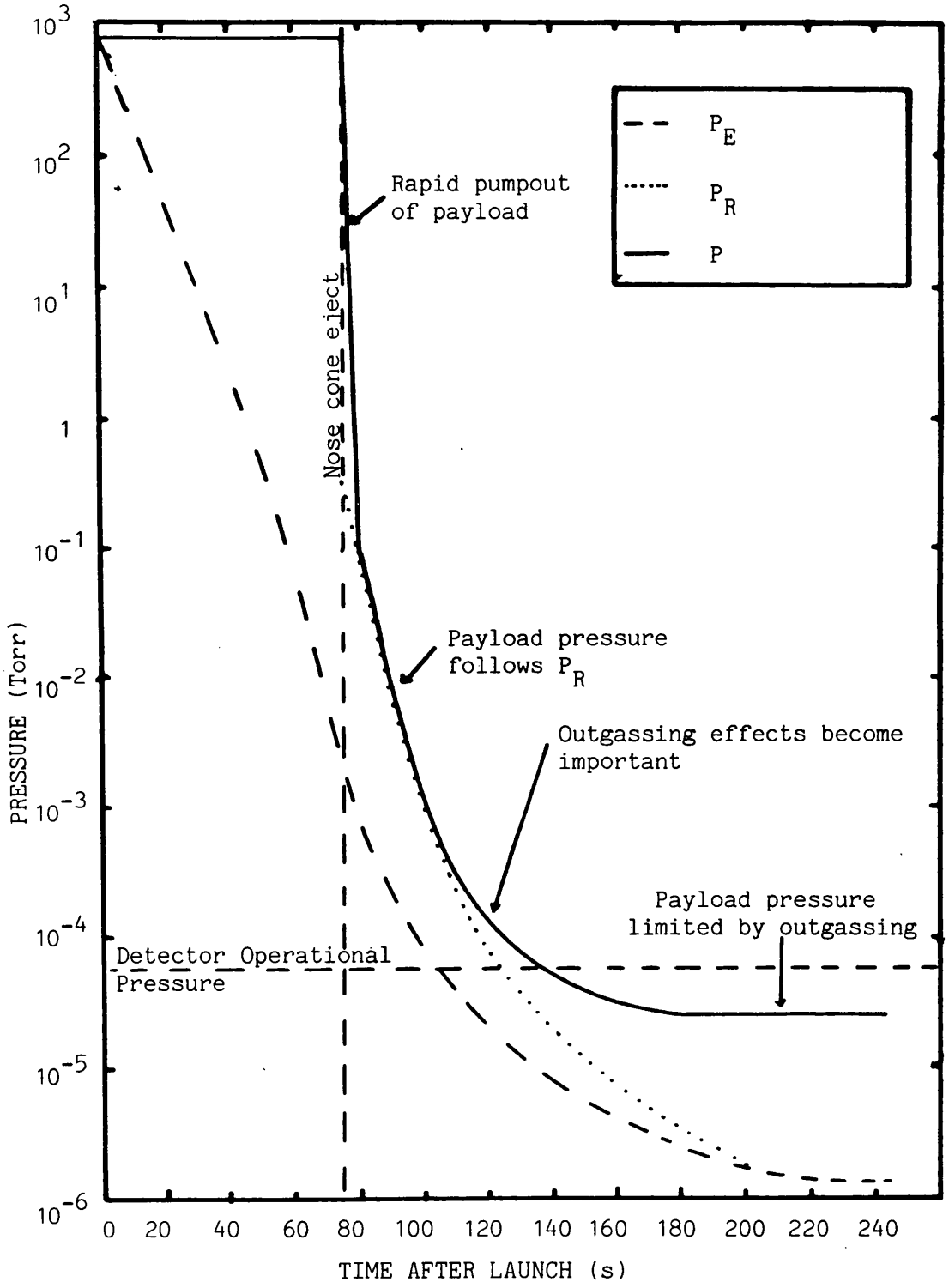

9.4.3 Pumpout of the Payload

If gas is flowing across an aperture from pressure P_A to P_B ($P_A > P_B$) the flow will be viscous if the mean free path of the molecules at P_A is small by comparison with the dimensions of the aperture. The MFP of a gas molecule is determined by equation 9.2. The spacing of the mirror shells is ~0.01m and a number density $\sim 3.2 \times 10^{22} m^{-3}$ (corresponding to a pressure of 1Torr) gives an MFP 10 times this spacing. Therefore, at pressures above 1Torr pumpout is under viscous flow conditions.

The conducting paths between the mirrors can be modelled as pipes of rectangular cross-section (bent into a circle in this case) corresponding to the annular gaps between the outer and middle mirrors, middle and inner mirrors, and the inner mirror and central baffle. The length of the longest side of the cross-section (b) is equal to the circumference of the annular gap and the shortest (a) is the width of the gap. As each gap width is ~1cm compared to a circumference of 60-100cm the difference between the inner and outer circumferences of each annular gap is small, hence the assumption of rectangular cross-section is valid, and the fact that the small sides of the pipe do not actually exist is not important.

Roth (1976) gives two equations for the conductance (C) of a pipe of rectangular cross-section. These equations agree when the ratio a/b is ~1 but at low values of a/b (<0.5) they do not. An upper limit to the pressure inside the payload will be obtained if the equation giving the lowest conductance is used. For air at 293K

$$C = 260\ Y(A^2/L)\ (P+P_R)/2\ l\ s^{-1} \qquad (9.5)$$

where: $A = a.b\ (cm^2)$

L is the length of the pipe (cm)

P is the pressure inside the payload (Torr)

Y is a correction factor which is a function of a/b

If the values of A for each conducting pipe are taken to be the areas of the annular gaps at the rear of the mirrors ($31cm^2$, $41cm^2$ and $50cm^2$), where the mirror shells have their smallest radii, a lower limit to C is obtained. L is 16 cm. a/b is ~0.005 for the mirrors hence Y is also ~0.005, estimated from the table provided by Roth. The conductance of the mirror nest is the sum of the conductances of each annular gap, since conductances add when in parallel, and is

$$C_T = 2089\ (P+P_R) \qquad (9.6)$$

It is not possible to calculate the change in the payload pressure analytically unless C_T is assumed to be constant. If a lower limit to C_T is taken as the point at which P is ~1Torr, where the assumption of viscous flow is no longer valid, an upper limit to the time taken to reach this pressure during pumpout can be estimated. When the nose cone is ejected P_R is ~0.3Torr, hence C_T is ~2700 $l\ s^{-1}$ for P=1Torr.

The pressure difference across the mirrors (DP) is $P-P_R$. Therefore, from equations 9.1 and 9.2

$$Q = 2700(P-P_R) - Q_G \qquad (9.7)$$

As P>1Torr is being considered Q_G ($2x10^{-3}$Torr l s^{-1}) is much smaller than the throughput of the mirrors (>$2x10^{3}$Torr l s^{-1}) and Q is $2700(P-P_R)$.

The amount of gas that can be pumped out of the payload is P.V (Torr l) at a given pressure P where V is the internal volume. In a small time dt_p the amount of material pumped out is Qdt_p hence the remaining material is

$$P_1V = PV-Qdt_p \qquad (9.8)$$

where: P_1 is the pressure after time dt_p

If the change in P_R in time dt_p is assumed to be small by comparison with P_1, the change in the internal pressure ($dP=P-P_1$) is then

$$dP = -C_T(P-P_R)dt_p/V \qquad (9.9)$$

The time (t_p) taken to reach a given internal pressure (P_t) can be derived by integrating equation 9.9

$$t_p = -(V/C_T)\ln[(P_t-P_R)/(P-P_R)] \qquad (9.10)$$

The payload pumps down from 760Torr and its volume is 70l. Hence, from equation 9.10, the payload evacuates to 1Torr in less than 0.2s. In this time P_R changes by less than 0.1Torr which is small in comparison with the final value of P, therefore the assumption of equation 9.9 is valid in this case.

Below a pressure of 1Torr pumpout is no longer under viscous flow conditions. An intermediate region exists between 1Torr and 10^{-2}Torr before pumpout is in the molecular flow regime. However, the molecular flow conductance is a lower limit to that in the intermediate regime and it is possible to analyse the pumpout in terms of molecular flow for all pressures below 1Torr. The conductance of a duct of rectangular aperture for air at 293K is (Roth, 1976)

$$C = 30.9(ba^2/LK) \qquad (9.11)$$

where: b>>a and L>>a

K is a correction factor for the ratio a/b

From Roth, K is estimated to be ~1.5. Using the open areas at the rear of the mirrors as before, ba^2 is $16cm^3$, $20cm^3$ and $25cm^3$ for inner, middle and rear mirrors respectively and C_T has a lower limit of 80l s^{-1}.

Using the above value of C_T in equation 9.10 it is calculated that the payload pumps down from 1Torr to 0.33Torr ($P_R+P_R/10$) in ~3s. In 3s the ram pressure decreases to ~0.2Torr. Therefore, the

assumption that the change in P_R is small by comparison with the payload pressure is no longer valid. However, calculating P iteratively using equation 9.9 for small time intervals, accounting for the decrease of P_R, shows that P converges with P_R within a few seconds after nose cone ejection.

When DP is $\sim 10^{-4}$Torr the throughput of the mirrors is of the same order as the payload outgassing. Hence, the latter makes a significant contribution to the internal payload pressure. An equilibrium condition exists where the material outgassed is equivalent to that pumped out ($Q_G = C_T.DP$). As C_T has a lower limit of 801 s^{-1} and $Q_G = 2 \times 10^{-3}$Torr l s^{-1}, the equilibrium value of DP has an upper limit of 2.5×10^{-5}Torr. Hence, the pressure inside the payload has an upper limit of $P_R + 2.5 \times 10^{-5}$Torr.

The above calculations give a clear picture of the pressure inside the payload as a function of time, summarised in figure 9.4 (solid curve).

9.5 Discussion of the Corona Hypothesis

Figure 9.4 shows that when the experiment was turned on at t=90s the pressure was 6×10^{-3}Torr, in the range where corona was observed during testing but below the pressure at which it could be initiated. At t=110s, when the vacuum box was opened the pressure was $\sim 2 \times 10^{-4}$Torr, too high for the detector to operate but below the level at which corona was seen to be extinguished. Hence, it appears that the pressure inside the payload could not have caused the corona.

Once initiated a corona discharge will not be extinguished provided a sufficiently long discharge path is available. The product of the pressure (P) and the path length required to sustain the discharge (L_p) is approximately constant (Acton and Swift, 1963). Hence, as P decreases L_p must increase. In the vacuum box the discharge was seen to be extinguished at $5x10^{-4}$Torr when the discharge path was ~15cm. Therefore, $P.L_p$ was $\sim 7.5x10^{-3}$Torr cm. The maximum path length in the payload was ~100cm. This implied a lower limit of $7.5x10^{-5}$Torr to the pressure at which a corona could be sustained, higher than the minimum pressure achieved in the payload of $2.5x10^{-5}$Torr, limited by outgassing.

The pressure inside the vacuum box could have been higher than the average value inside the payload - because of the tortuous pumpout paths around both the detector components and the filters, and possible local outgassing from them - sustaining the corona. However, this could only have occurred if the vacuum box had leaked, since it had been pumped out for a long period before launch to eliminate outgassing problems.

9.6 Conclusion

The data from postflight testing and pressure calculations suggested that the WFSXC malfunction was caused by a corona discharge. This corona must have reduced the voltages to the detector, hence it is uncertain whether it worked at all during flight. As a result of this and the anomalies in the data generated by the corona, none of the events detected during flight could be said to represent true

cosmic X-rays. Interference in the aspect camera drive circuit from the corona probably caused the erratic pulsing observed, which prevented the film from being wound up.

Analysis of the payload pressure showed that it was not high enough to cause corona and that the most likely explanation was a leak in the vacuum box. Testing of the payload for the second flight showed that when the pressure inside the payload decreased to 14Torr the vacuum box did leak up to a corona pressure.

The problem of corona could have been avoided by opening the vacuum housing and waiting until the internal pressure had fallen to an operational level ($<5 \times 10^{-5}$Torr) before turning on the experiment. In case of a recurrence of the problem in the future, the ability to stop the discharge by turning the experiment off and then on again from the ground is necessary.

CHAPTER 10

INTEGRATION AND CALIBRATION OF THE WFSXC FOR SECOND FLIGHT

10.1 Modifications to the Payload

A number of modifications were made to the payload to prevent the corona discharge experienced in the previous flight. First, the vacuum housing was rebuilt using a welded stainless steel construction to allow it to better withstand launch vibrations. Second, an additional small ion pump was added as a gauge to monitor the pressure inside the payload. Third, switches, operated by real time commands from the ground, were added to the detector high voltage and the ion gauge power supply to be switched on or off in flight. This facility would allow a corona discharge to be switched off, to let the detector assembly depressurise further before switching on again.

In addition, the detector efficiency was improved by coating the front MCP with a CsI photocathode instead of MgF_2 (see chapter 4). As CsI is a hygroscopic material strict handling procedures had to be adopted, as described in detail in section 4.3.4, to prevent contact with air of normal humidity.

The enhanced far-UV efficiency produced by the CsI necessitated the redesign of the Par N filter (chapter 6), a combination of 2000Å C + 1000Å lexan being the new choice. It was also decided to do away with the small aluminium segment so that each of the filters covered half the field of view.

It was decided not to re-figure the mirrors before the second flight as the distortions had not affected the sensitivity of the WFSXC on the first flight. Therefore, the mirrors were only polished

and replated with gold.

10.2 Integration and Testing of the Payload

As before the mirrors were stressed to remove the distortions and calibrated optically yielding a resolution very close to that measured previously, ~2.5$\hat{}$ RMS with a 30$\hat{}$ diameter 90% power circle.

No X-ray tests could be performed on the payload as the AS&E facility was unavailable. However, the enhanced UV sensitivity of the detector, produced by the CsI photocathode, allowed the position of the optical axis and the plate scale to be measured on the detector. For these tests the vacuum box lid was replaced with a quartz plate and the detector was illuminated by a mercury discharge lamp.

The new vacuum housing and ion gauge were tested by pumping the payload down to $\sim 10^{-5}$Torr in a large vacuum tank. The vacuum housing was already evacuated to 6×10^{-6}Torr before the test was begun. As the large tank was evacuated its pressure and the ion gauge supply voltage were monitored, allowing the ion gauge supply voltage to be calibrated as a function of pressure for use in flight (figure 10.1). In addition the pressure inside the vacuum housing was monitored during this test.

It was found, when the external pressure was ~14Torr, that the vacuum housing began to leak, reaching a pressure above which the ion pump could not operate ($>10^{-4}$Torr). There were two possible explanations for this problem. Either there was sufficient play in the latch securing the lid for the spring loaded hinge to lift the lid slightly, or the O-ring seal became inefficient when no longer

compressed by atmospheric pressure. A leak like this may have been responsible for the corona in the first flight. As it was intended to turn the experiment on after the vacuum housing had been opened this leak was not considered to be a problem.

After vacuum testing the payload was taken to GSFC for integration and flight qualification, as on the first flight (see section 7.3). In addition to the tests performed on the first payload the tone-ranging facility, which allowed the payload and ion gauge to be commanded on and off from the ground, was tested. Integration was completed with only two minor problems. First, a pocket of gas trapped in the potting of the high voltage distribution board caused a corona discharge. When the vacuum housing was evacuated the trapped gas would slowly leak out until the corona was extinguished. The board was replaced, without being potted this time but with all the components spot bonded, and no further problems were experienced. Second, the X_1 channel was lost after flight qualification. This was caused by a dirty connection in the electronics box. After thorough cleaning of the contact the problem was eliminated.

It was noticed during later tests, with the quartz window on the vacuum box, that the filter flexed at the beginning of venting and pumping. When the filter was removed from the vacuum housing a number of cracks, of a total length ~20mm in each half of the filter, had appeared in the metal foils, observed by backlighting the filter (figure 10.2). It is probable that the cracks were caused by the flexing observed, the plastic layers being sufficiently flexible to remain undamaged.

Figure 10.1 Calibration curve for the ion gauge. Pressure as a function of power supply voltage.

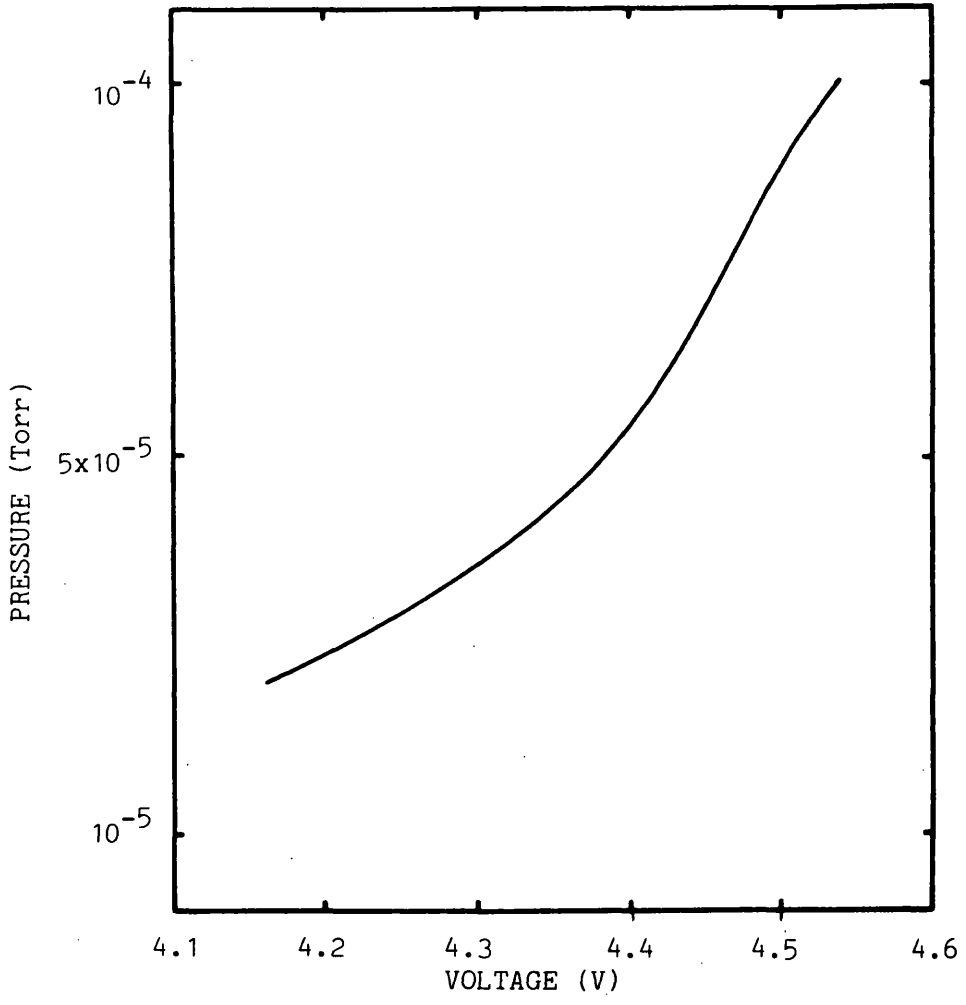

Figure 10.2 Cracks observed in the metal foils of the flight filter before flight.

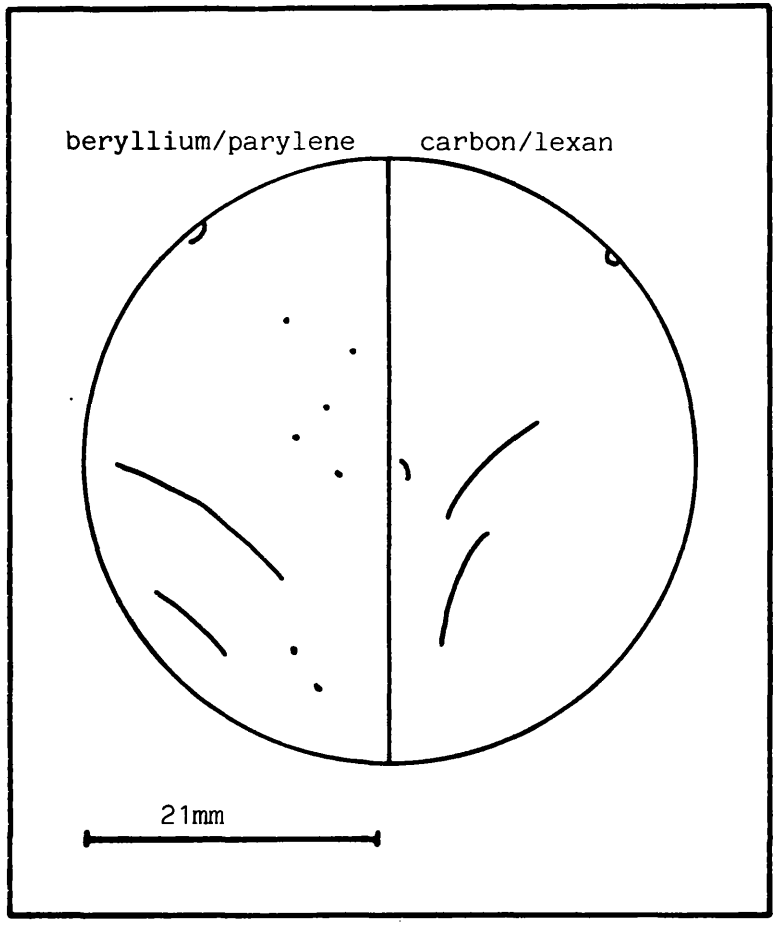

Any large cracks in the filter might have led to high background during flight. Hence, the filters was tested with the mercury vapour lamp (λ>2500Å) used for the mirror alignment. As beryllium and carbon are relatively opaque in the UV, any serious cracks in the metal foils should have been seen as bright, if out of focus, lines in the detector image. A uniform image was seen from both halves of the filter, ~100 counts s^{-1} being transmitted by the C/lexan and ~10 counts s^{-1} by the Be/Par N. Therefore, it was assumed that the cracks observed in the filter would not cause a background problem.

The payload was shipped to WSMR for pre-launch preparations. A test of the integrated payload, running through the flight sequence as for integration at GSFC, was performed before mating it with the booster (the "horizontal"). After the rocket had been installed in the tower the flight sequence was repeated (the "vertical"). During both horizontal and vertical tests the detector was tested by illuminating it with Fe^{55} (5.9keV and 6.5keV) and Co^{60} (1.2MeV and 1.3MeV gamma rays) sources. Figures 10.3a and 10.3b show the vertical pulse height distribution and linearised image respectively with Fe^{55}, which show that the detector and electronics were operating correctly before flight. An additional facility was tested which allowed the X and Y position signals from the TM to be fed into a storage oscilloscope to display the detector image in real time. This was subsequently used during the flight.

Figure 10.3a Pulse height distribution of events from the vertical test (Fe^{55})

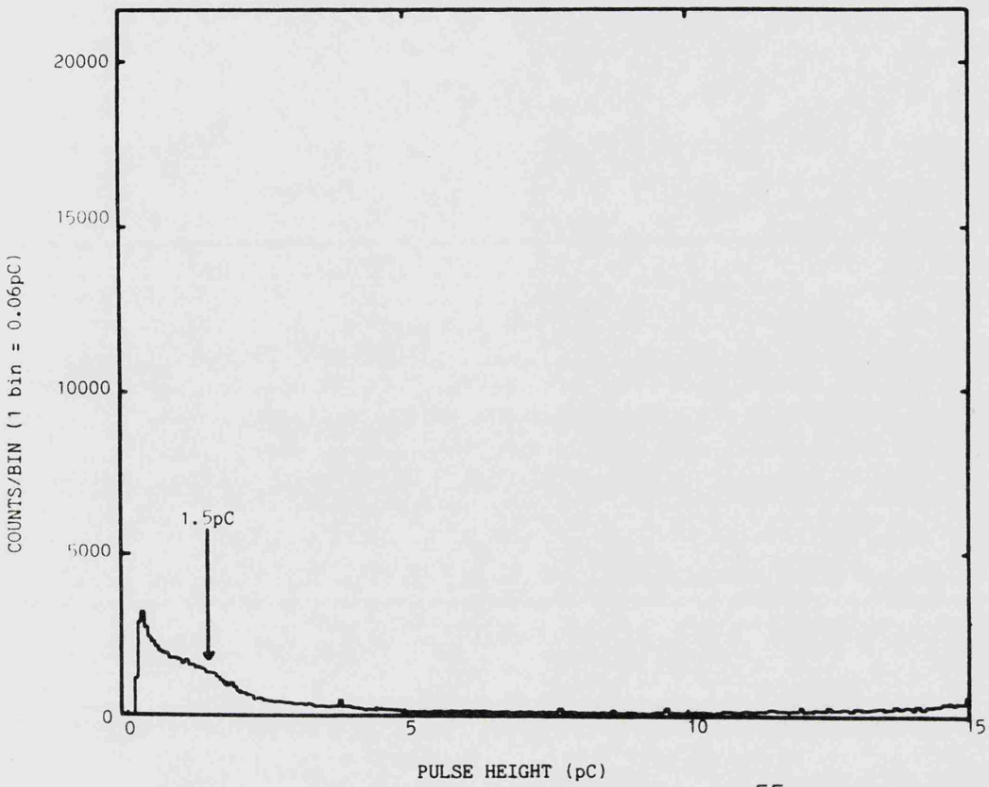

Figure 10.3b Detector image illuminated by Fe^{55} during the vertical test, the outer circle represents the field of view and the inner the Fe^{55} collimation.

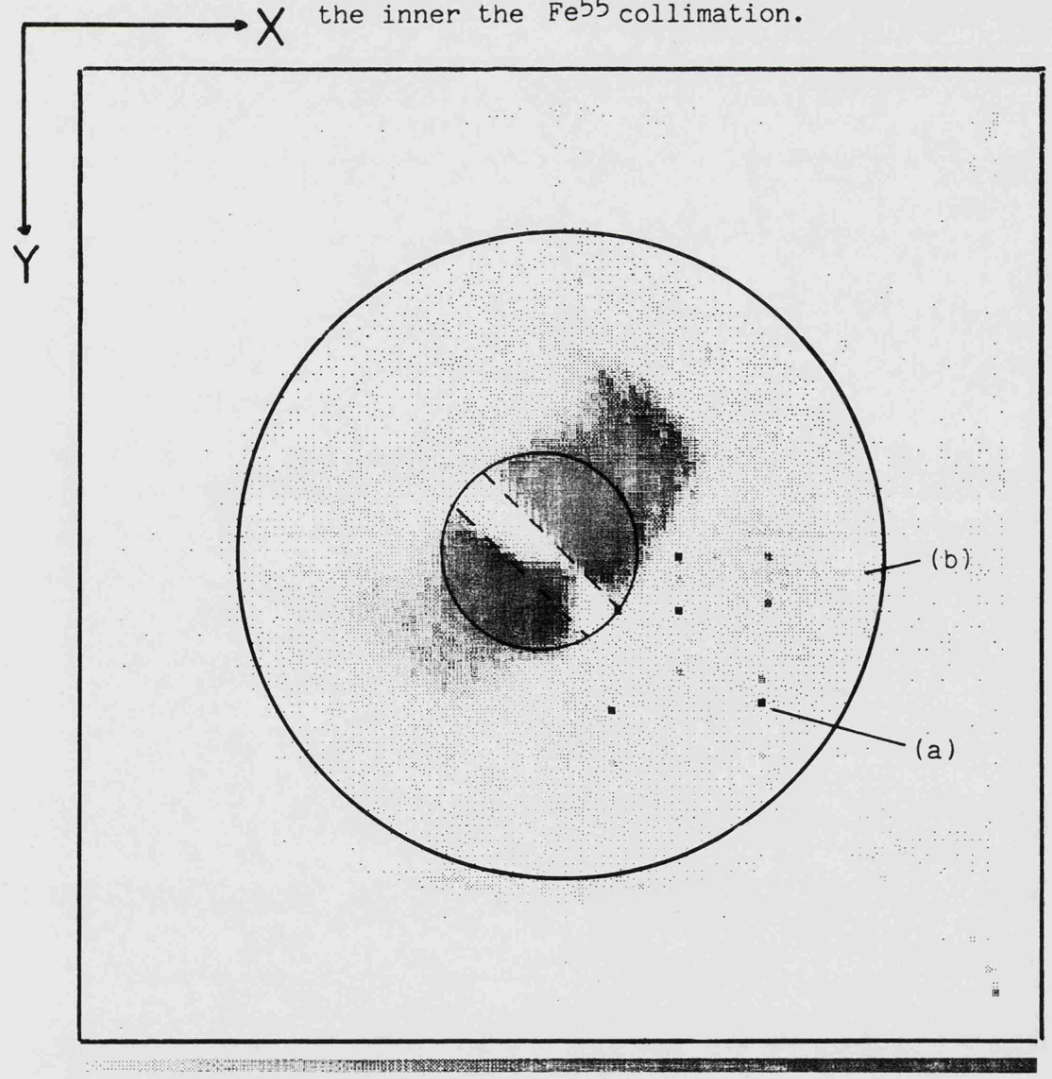

10.3 Analysis of the Pre-flight Image

The image recorded during the vertical test was analysed in some detail to assess the performance of the detector/electronics system.

Figure 10.3b shows the limit of the detector area. Events lying outside this area have saturated the position encoding electronics. The saturation levels of the filter amplifiers and stretchers correspond to a higher input charge level than the saturation level, therefore events saturate the quotient evaluator before saturating any other component. A proportion of the X-rays lie outside the nominal area of the illuminating beam (shown in figure 10.3b). This is probably incorrect positioning of low pulse height events, where the incident X-rays were near normal incidence reducing the gain as described in section 3.6.1, by the electronics.

Particular single pixels (eg. like that marked (a) in figure 10.3b) in the quadrant X>255 and Y>255 (0-511 scale, 9 bit digitisation) have a large number of events, and lines ((b) in figure 10.3b) occur across the image that contain more events than expected. The positions of the single pixels correspond to increments of 64 channels from the centre of the image. A saturated position output could give these positions if bits 7 and 8 of the digitised signal were not read out correctly or were operating intermittently. The lines can be explained in a similar manner as an incorrectly operating bit resulting in the binning of events with different positions into one particular channel. As the effects occur in both axes they are probably properties of the electronics rather than caused by a malfunction.

It is possible to obtain measurements of the resolution from the test image of figure 10.3b. The Fe^{55} X-ray source casts a shadow of the filter bar onto the detector. As the filter bar has a square profile the edge of the shadow should consitute a step in the image brightness. The profile of the step constitutes a measurement of the resolution (figure 10.4). The mathematical relationships used to calculate the spatial resolution have been derived by Thomas (1983). Thomas' analysis assumes parallel, uniform illumination and that each X-ray event falls within a gaussian profile whose width is a function of the intrinsic accuracy of the detector/electronics system. If Δd (figure 10.4) is the distance between the 1/4 and 3/4 intensity points of the slope the full width half maximum resolution is $2.36 x d x \Delta d/1.4$, where d is the plate scale of the image ($d=106\mu m$ $channel^{-1}$ for the WFSXC). The resolution measured at the centre of the field of view is $\sim 360\mu m$ ($3.6\hat{'}$). However, the illuminating X-ray beam is not a point source, and therefore not parallel at the edge of the filter bar, as assumed in the analysis. The effect of the finite source size can be modelled as in figure 10.5. The beam spread on the focal plane is $l_2 \sim d_2 . l_1/d_1$. l_1 is 1.6mm (FWHM), d_1 is 48mm and d_2 is 9mm, hence l_2 is $\sim 300\mu m$ (FWHM). Removing this contribution quadratically from the total resolution gives a final value of $190\mu m$ for the detector electronics combination, which is $\sim 80\mu m$ RMS.

Figure 10.4 Profile of the image recorded during the vertical test taken perpendicularly to the filter bar. The shadow cast by the filter bar is on the left hand side.

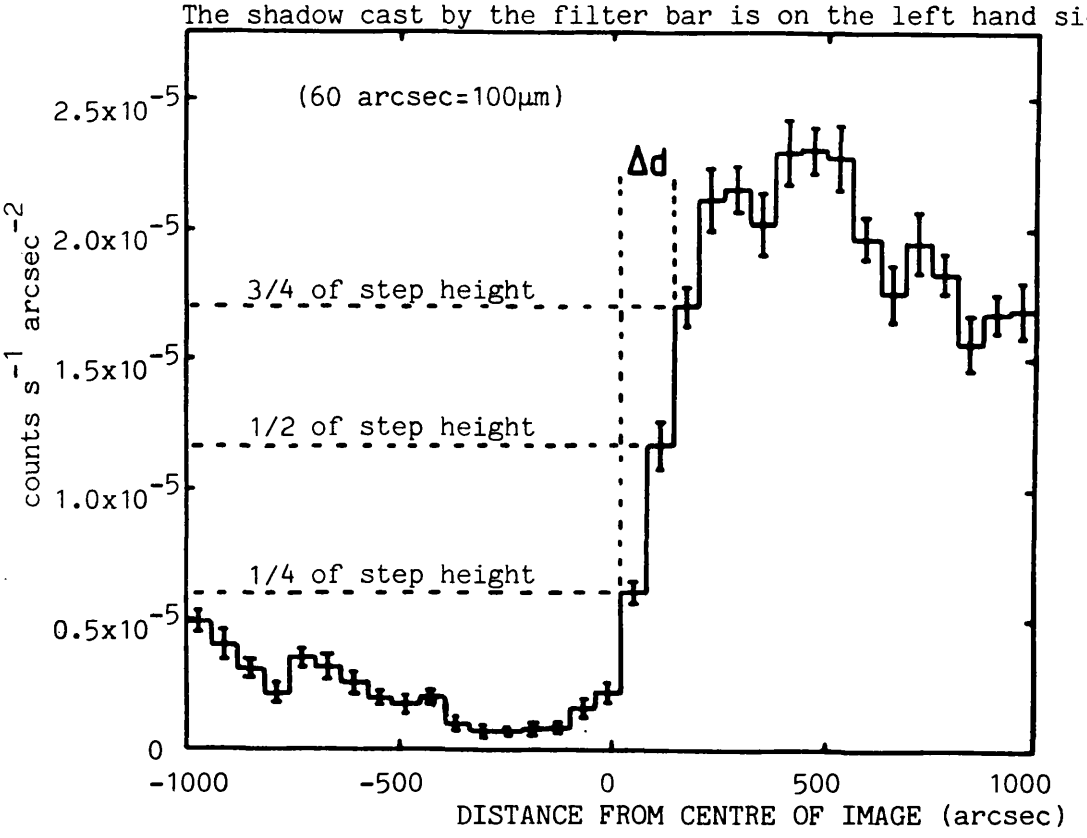

Figure 10.5 The effect of a finite source on the shadow cast by the filter bar showing that the illuminating beam is not parallel.

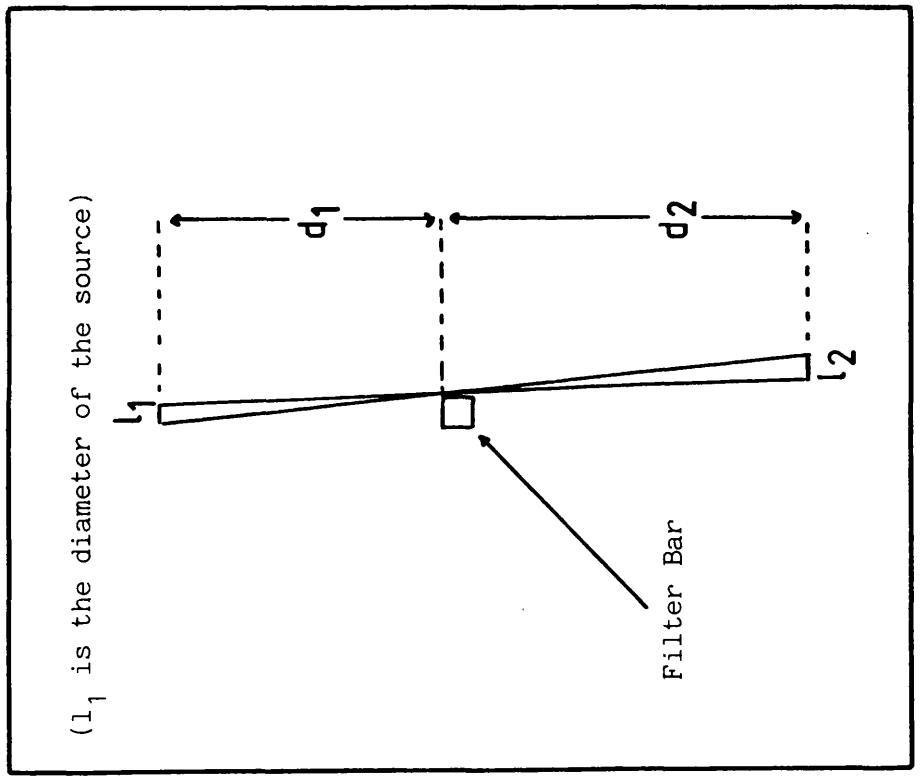

10.4 Monitoring the CsI Quantum Efficiency

It was only possible to calibrate the detector with Fe^{55} X-rays when installed in the vacuum housing. The detector had been calibrated with Fe^{55} at Leicester but it was not possible to transport the source to MIT. Subsequent tests at MIT and GSFC (during qualification) had to be performed with a different Fe^{55} source. Consequently, continuity was lost in monitoring the CsI quantum efficiency over the 4 days when the detector was in transit between Leicester and MIT. The detector was stored in a sealed container filled with dry N_2 during shipment. Tests of this procedure showed it to be suitable for storing CsI photocathodes without the quantum efficiency deteriorating by more than 5% of its original value over a period of 60 days. Therefore, the quantum efficiency of the detector should not have degraded during transit.

The MIT Fe^{55} source was collimated in a similar way to the source used at Leicester but had two interchangeable units with half angles of 4.2° and 5.9° and illuminated the detector with the axis of the beam at 0° angle of incidence. It was not possible to maintain the same geometry of illumination throughout integration and testing, because of the installation of the filter and different collimation requirements. The calibration count rates were "transferred" by comparing measurements with different geometries separated by a small time interval. The results of the Fe^{55} efficiency tests are summarised in table 10.1. This data shows that up to launch the efficiency of the photocathode at 5.9keV and 6.5keV changed by less than ~10% of its original value.

Some measurements were also made of the detector gain with Fe^{55} sources. At MIT a flat Fe^{55} source $\sim 4mm^2$ was placed directly on the Be window of the vacuum housing to illuminate the whole detector giving a range of angles of incidence from 0 to 40°. However, measurements during horizontal and vertical tests at WSMR had to use the efficiency calibration source, which when uncollimated had a maximum half angle spread of 9°. Consquently, although gain decreases were noted (table 10.2) they may have been caused by changes in the geometry of illumination rather than intrinsic changes in the detector gain.

10.5 The Sensitivity of the WFSXC with CsI Photocathode and Redesigned Filters

The sensitivity of the WFSXC was calculated as described in section 2.3.1. It was assumed that the telescope efficiency was ~40% of the theoretical prediction, as in section 7.4 for the first flight. The CsI efficiency in the XUV band was modelled from the theoretical prediction of chapter 4 (figure 4.21). Figures 10.6a and 10.6b show the WFSXC efficiency for the two filters chosen for the second flight, 2000Å carbon + 1000Å lexan and 2500Å beryllium + 2000Å parylene N respectively. A grasp of 1.7Å was obtained for the c/lexan filter, and one of 1.6Å for the Be/Par N filter with bandpasses of 50-160Å and 114-180Å respectively.

The detector background was ~5 counts s^{-1} (575 counts $s^{-1}ster^{-1}$) at the detector operational voltages, as before. The geocoronal contributions were derived as described in chapter 6, assuming a

Table 10.1. Summary of preflight tests of detector efficiency with the Fe^{55} source

Calibration number	Collimator (θ_C)	Count rate (s^{-1})	Notes
1	4.2 5.9	185 345	Initial test at MIT
2	4.2 5.9	186 357	Test after 25hrs storage in dry N_2 during payload modifications
3	4.2 5.9	169 314	After 2 further vacuum breaks
4	4.2	166	Before flight qualification
5	4.2	66	The flight filter was installed the bar occulting the source. 1 vacuum break after flight qualification.
6	4.2 no collimation	60 440	Horizontal at WSMR. Change in filter orientation
7	no collimation	480	Vertical at WSMR prior to launch

Table 10.2. Summary of preflight calibrations of detector gain using Fe^{55} illumination

Calibration number	G_C (pC)	dG_C/G_C (%)	Notes
1	4.6	66	Flat source
2	3.5	123	Flat source. After flight qualification with filter installed
3	1.5	-	WSMR horizontal. source used for efficiency test with no collimation
4	1.5	-	WSMR vertical. source as for calibration 3 above

Figure 10.6 The efficiency of the WFSXC with a CsI photocathode.

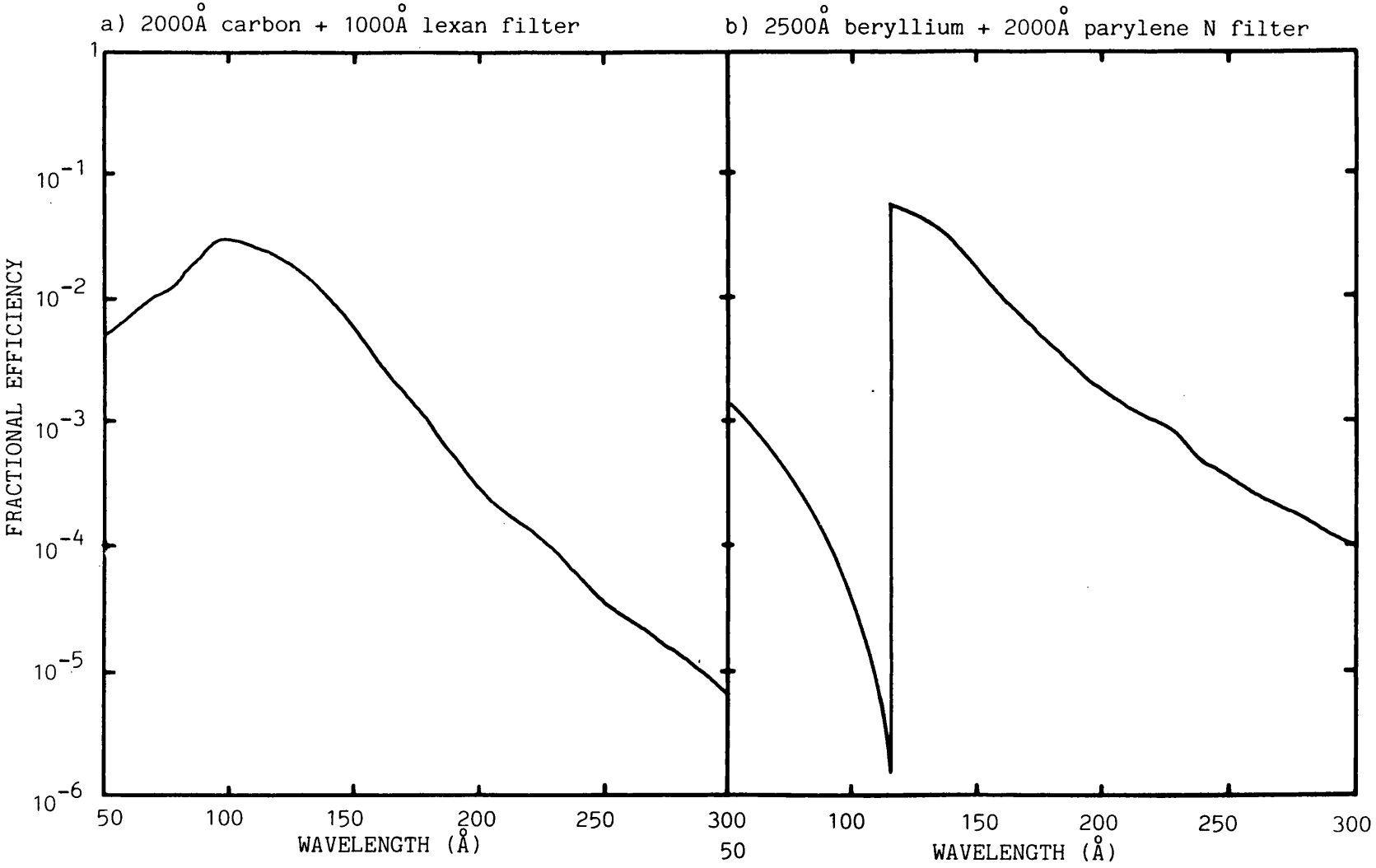

mirror efficiency of 100% at these wavelengths. A total of 30 counts s^{-1} in the c/lexan filter and 440 counts s^{-1} in the Be/Par N filter were expected.

The sensitivity of the WFSXC was calculated using the above grasps and estimates of the background with an assumed pixel size of $6x10^{-5}$ster (figure 10.7). As the background count rate was increased by the improved efficiency of the detector, the WFSXC was background limited at lower exposure times (above ~3s) than in the previous flight. For a typical 24s exposure (scan rate of $0.25°s^{-1}$) the resulting sensitivities were $4.5x10^{-11}$ergs $cm^{-2}s^{-1}$ (C/lexan) and $4.0x10^{-11}$ergs $cm^{-2}s^{-1}$ (Be/Par N).

Table 10.3 compares the performance of the WFSXC for the first (MgF_2 photocathode) and second (CsI photocathode) flights. The sensitivities are compared for a scan rate of $0.25°s^{-1}$, showing that, in the comparable filters (Par N and C/lexan; Be/Par N and Be/Par N), the use of CsI resulted in a 2.5 fold improvement in the sensitivity in both cases.

The distortion of the telescope was unchanged from the previous flight, the RMS blur circle radius being ~2.5$\hat{}$ and the 90% power circle ~30$\hat{}$ in diameter. Hence, once again the telescope dominated the WFSXC resolution as the RMS resolution of the detector/electronics system was only ~0.8$\hat{}$. As the WFSXC was background limited in the second flight because of the increased geocoronal contribution to the background count rate, the mirror distortion decreased the sensitivity below what might have been achieved. Comparing the sensitivities (24s observation) for zero background from figure 10.7, $2.7x10^{-11}$ (C/lexan)

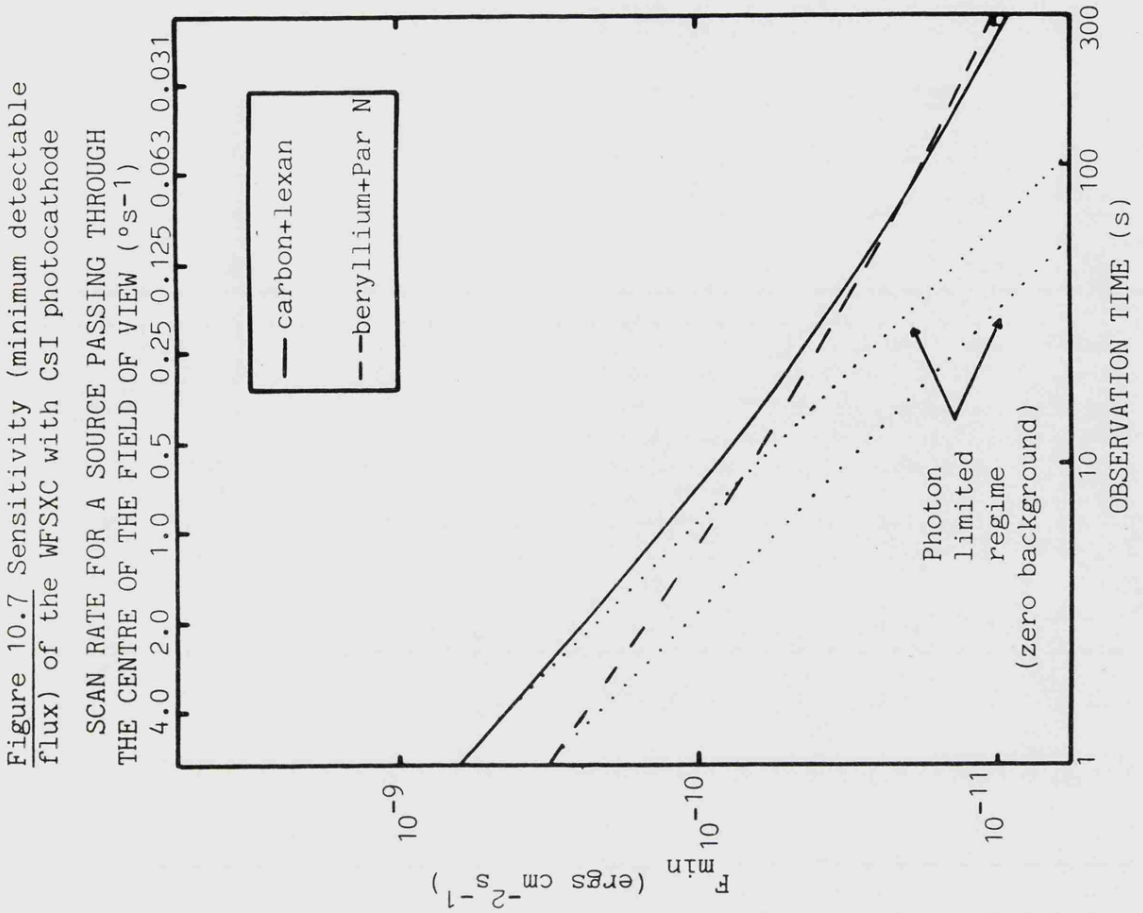

Figure 10.7 Sensitivity (minimum detectable flux) of the WFSXC with CsI photocathode

Table 10.3. Comparison of the WFSXC performance for the first and second flights

Parameter	Flight 2		Flight 1	
Field of view (ster)	8.63×10^{-3}		8.63×10^{-3}	
Pixel size (ster)	6.00×10^{-5}		6.00×10^{-5}	
Collecting area (cm^2)	250		250	
Filter	C/lexan	Be/Par N	Par N	Be/Par N
Material thickness (Å)	2000+1000	2500+2000	5000	2500+3000
Bandpass (Å)	50-160	114-180	50-170	114-200
Grasp (Å)	1.7	1.6	0.40	0.19
Total background (counts $s^{-1} ster^{-1}$)	6300	10^5	596	634
Total background in filter (counts s^{-1})	30	440	2.6	2.8
F_{min} ergs $cm^{-2}s^{-1}$ ($0.25°s^{-1}$ scan rate)	4.7×10^{-11}	2.8×10^{-11}	1.3×10^{-10}	1.0×10^{-10}

and 1.3×10^{-11} ergs $cm^{-2} s^{-1}$ (Be/Par N), with those from the previous flight shows that maximum improvements of 4.8 (Par N or C/lexan band) and 7.7 (Be/Par band) could have been achieved if the mirror resolution had been improved. Therefore, with hindsight, the decision not to have the mirrors re-figured was a mistake.

CHAPTER 11

WFSXC FLIGHT 2: ROCKET 21.069

11.1 Flight Plan and Launch Windows

As rocket 21.069 was flown in the Autumn of 1982, observations were restricted to an area of sky similar to that observed on the first WFSXC flight (25.040). EG233 was once again included in the programme. Three other hot white dwarfs were selected. Feige 24 (Margon et al, 1976) and G191-B2B (Holberg et al, 1980a) are both known to be EUV sources but the latter has only been detected at wavelengths (500-900Å) above the WFSXC band (50-180Å). Feige 4 was reported as a detection in the 600-700Å band (Sagdeev et al, 1979) but Holme and Boggess (1982) have measured a temperature cooler than that needed for EUV emission. In addition to these objects, two RS CVns were to be observed - HR 1099, which was discussed in chapter 2, and Lambda Andromedae, which has a similar soft X-ray flux to HR 1099 (Walter et al, 1980) and was a target on the previous flight. Z Andromedae, the binary system observed on the first flight was also included being close to Lambda Andromedae.

Figure 11.1 shows the flight plan, the details of the scan rates and manoeuvres being summarised in table 11.1. The launch windows (figure 11.2) were calculated as described in section 8.4. The best viewing conditions are shown in the shaded region.

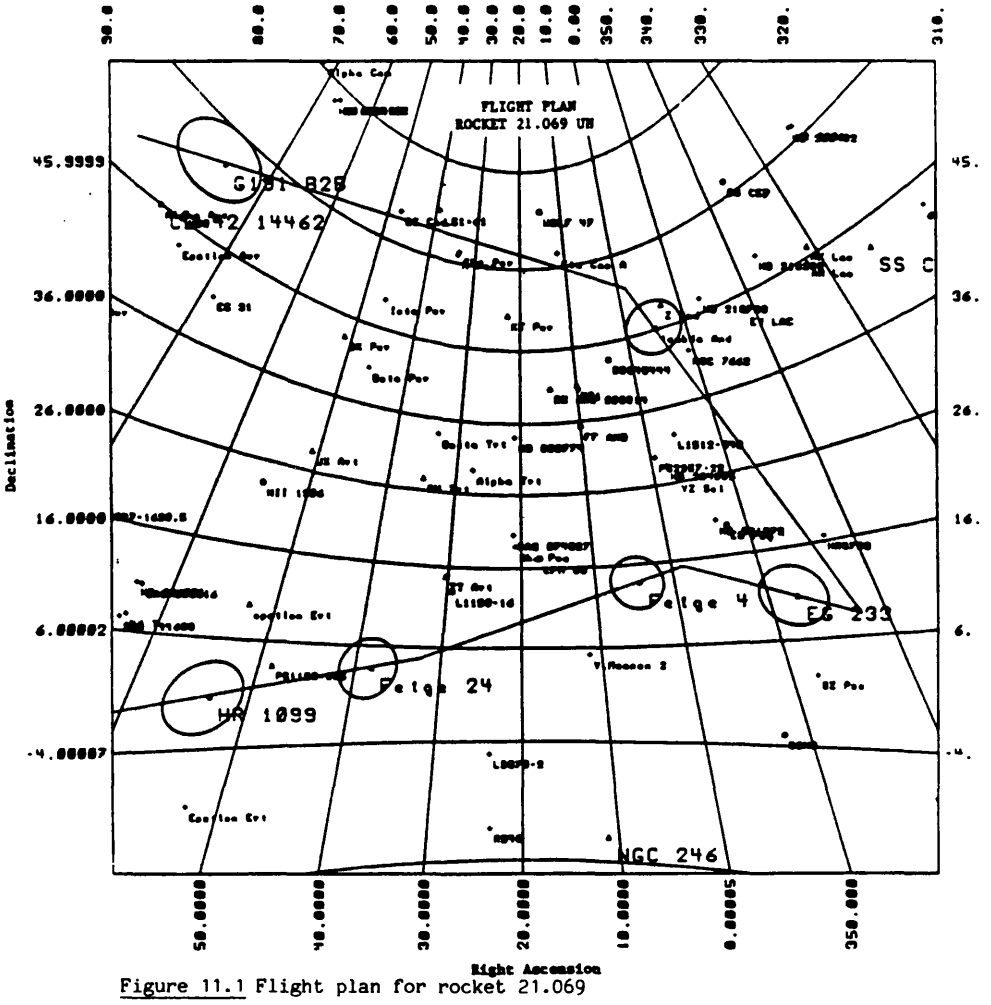

Figure 11.1 Flight plan for rocket 21.069

Table 11.1. 21.069 scan rates and manoeuvres

Manoeuvre	Distance (°)	Rate ($°s^{-1}$)	Time (s)	Target	Approximate times in field of view (s)
Pitch	28.7	0.3	96	HR1099	135-155
				Feige 24	200-225
Roll	9.3	6.0	2		
Pitch	23	2.0	11		
Pitch	12	0.3	40	Feige 4	250-270
Roll	-35.5	6.0	6		
Pitch	5	2.0	3		
Pitch	12.8	0.3	43	EG 233	290-320
Roll	-50.7	6.0	9		
Pitch	-33.8	2.0	17		
Pitch	-12	0.3	40	λ And	360-390
Roll	33.5	6.0	6		
Pitch	-39	2.0	20		
Pitch	-12	6.0	2	G191-B2B	410-420
Total			295		

11.2 The Flight of Rocket 21.069

Black Brant 21.069 was launched at 01.15 MST on 1st November 1982 (08.15 UT). All experiment related events (table 11.2) were executed successfully. However, although all the flight manoeuvres were carried out as planned, a series of manoeuvres, updated ~1 minute before launch and intended to move the payload to the initial point on the flight plan were incorrectly programmed. Hence, the wrong area of sky was scanned.

During the flight the experiment appeared to work correctly, except that the ion gauge did not work when turned on, but it was obvious, from both the real time detector image and the chart recorder data (figure 11.3), that the background event count rate was very much higher than expected. The experiment was turned off and back on again twice, in case the high count rate was caused by a corona discharge. However, no change in the count rate appeared to result from these operations, indicating that no discharge had occurred. None of the features seen in the image of the first flight were observed in either the real time image or in the post-flight reconstruction of the image, confirming this view.

When the payload was recovered it was found that the filters had been shattered and the O-ring, sealing the vacuum housing lid, had been lost. Additionally, the aspect camera magazine had become disengaged from the motor drive and no film had been wound up.

Figure 11.2

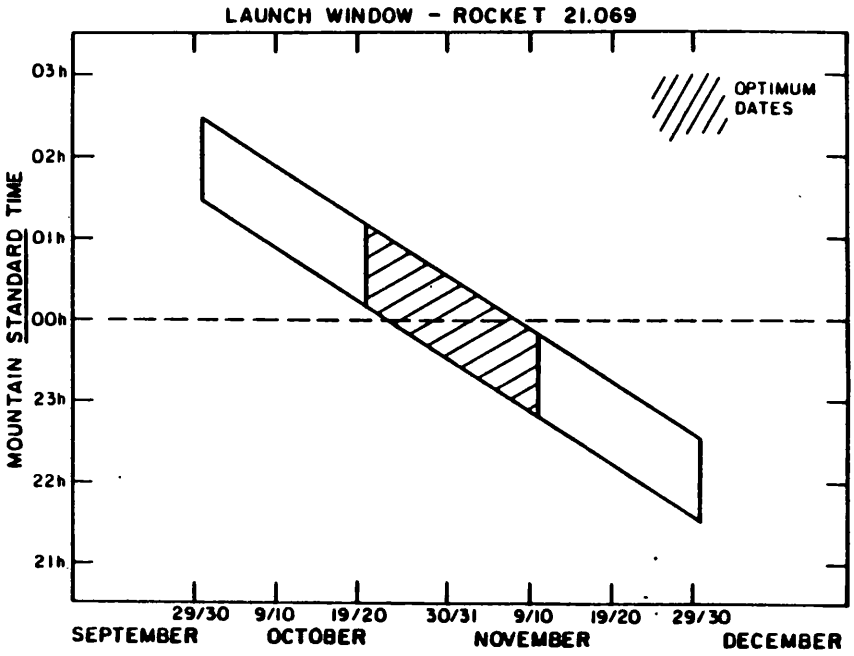

Table 11.2. Times and projected altitudes of experiment related events

Event	Time (s)	Altitude (km)
Nose cone eject	55	67
Despin	62	80
Separation	64	83
Vacuun housing open	110	152
Experiment on	125	168
Experiment off	420	72
Parachute deployed	450	24

Figure 11.3 Sample chart recorder data from rocket 21.069

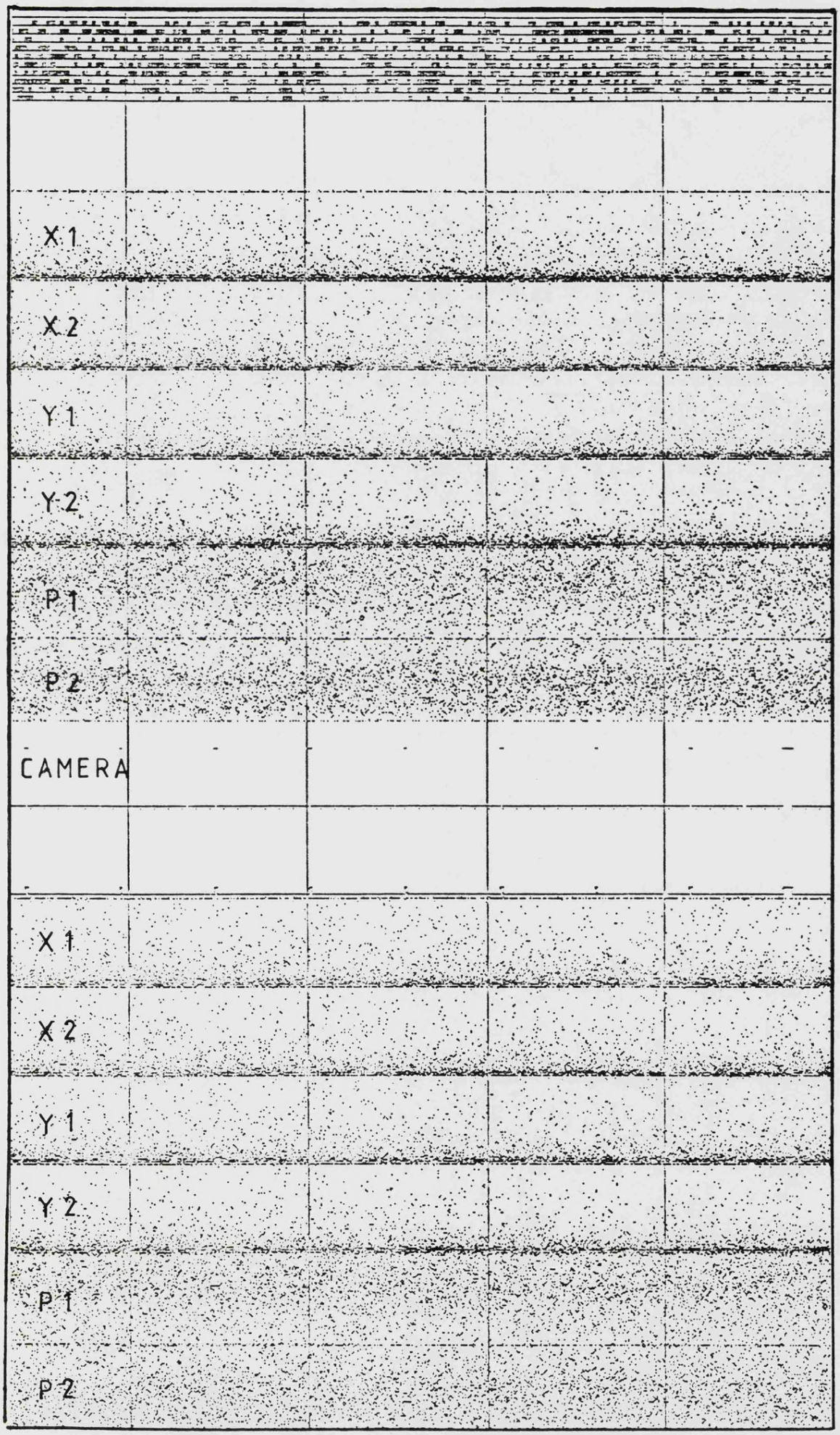

11.3 Initial Analysis of the Data

11.3.1 Count Rate Data

The telemetered data were recorded on magnetic tape for post-flight analysis. The curve of count rate versus elapsed time for the flight (figure 11.4), shows an increase from a rate of $\sim$1000 counts s^{-1} at experiment turn on (t=125s) to a maximum of 2400 counts s^{-1} at t$\sim$150. This is probably due to decreasing atmospheric absorption of the background as the rocket increases in altitude. Thereafter the count rate remains steady at 2400 counts s^{-1} except for two intervals at t=170s and t=240s when the experiment was switched off. Under these conditions, with no detector data, the output from each telemetry channel defaults to a value of 511, therefore an "event" is observed in each telemetry frame, a rate of 2500 counts s^{-1}.

Since at the high count rates observed the telemetry is close to saturation, a large dead time correction on the observed count rate (C_A) is required to give the real flux. The dead time correction is determined by the telemetry rate (T_R) and the real count rate (C_R)

$$C_A = C_R(1-\exp(-T_R/C_R)) \qquad (11.1)$$

Calculation of C_R requires an iterative solution of equation 11.1. For an apparent count rate of 2400 counts s^{-1} the corresponding real count rate is $3\text{-}4\times10^4$ counts s^{-1}, which is 100 times greater than the expected rate (470 counts s^{-1}, table 10.3). Both background and source events are equally attentuated by the telemetry dead time (by a factor of 0.06 from equation 11.1). The effective reduction in

Figure 11.4 Count rate/time after launch for rocket 21.069

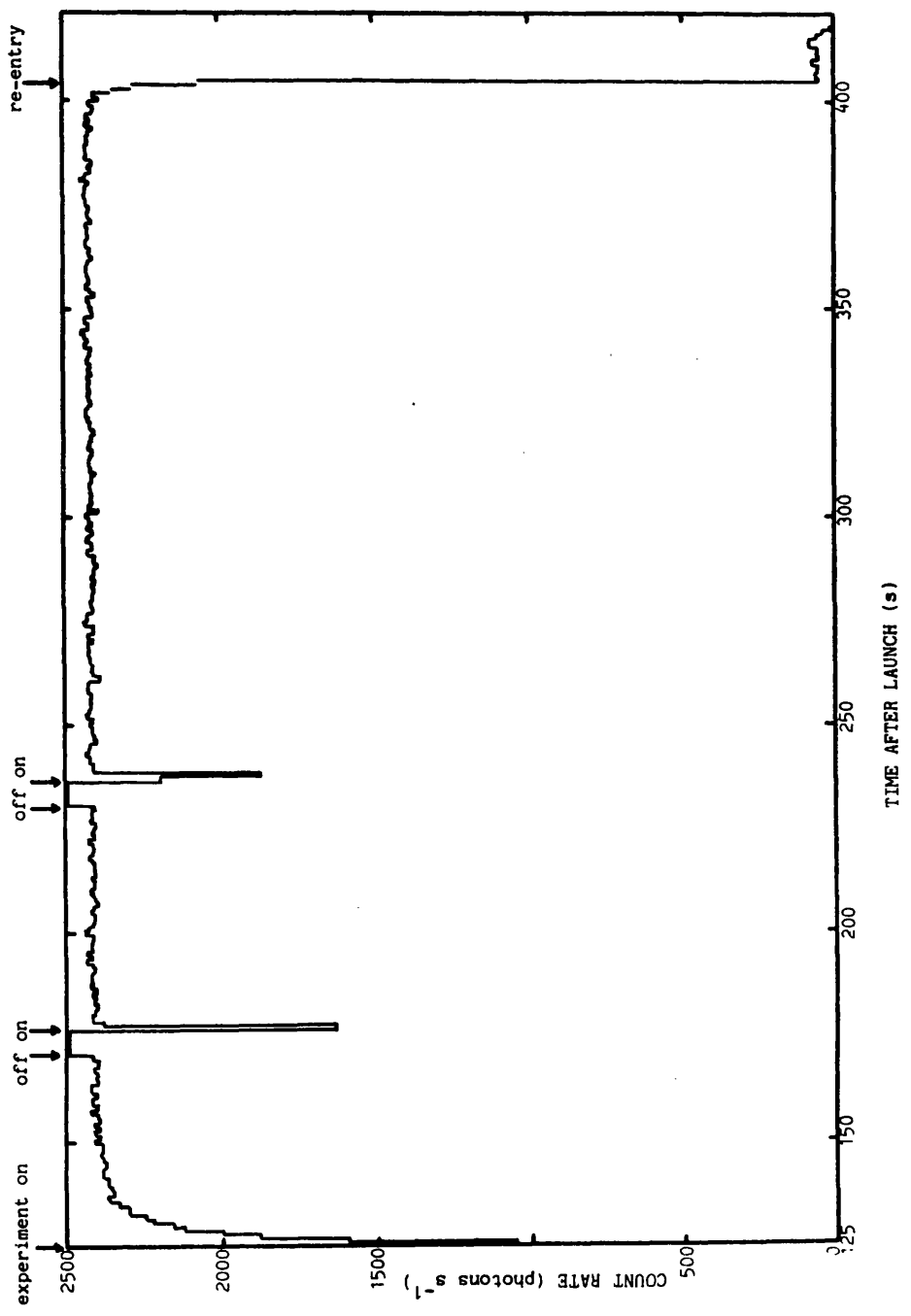

sensitivity (to ~1/2 the flux from HZ43 in each band) rendered the detection of sources weaker than HZ43 unlikely and, although a search for point sources was made in the subsequent data analysis, no positive detections were found.

11.3.2 Image Reconstruction Analysis

All (~700,000) events recorded during the flight were superimposed in an integrated detector image (figure 11.5). The image shows that that the distribution of events is not uniform over the whole field of view and that the image zone behind each filter had a different total count rate. The approximate position of the filter bar is marked but there is no shadow of the bar seen in the image. However, in a second total count image deliberately over exposing the central zone (figure 11.6), indentations caused by the vignetting by the filter bar are visible at the edges of the field of view. However, the vignetting does not extend across the image, as it should, there being no dip in the brightness at the centre. The lines that appear in the flight image were seen during integration and are a fault of the electronics, not a product of the high count rate during the flight.

A 0.3° wide intensity profile taken across the centre of the image in the direction perpendicular to the filter bar, shows a strong peak just to the left of the centre of the image (figure 11.7). The count rate density found at the peak is $\sim 1.2 \times 10^{-5}$ counts s^{-1} arcsec^{-2} falling to less than 10^{-6} counts s^{-1} arcsec^{-2} at the edge of the image. Observing the profile over shorter time intervals (~40s) at t=130s,

Figure 11.5 Integrated detector image from rocket 21.069.

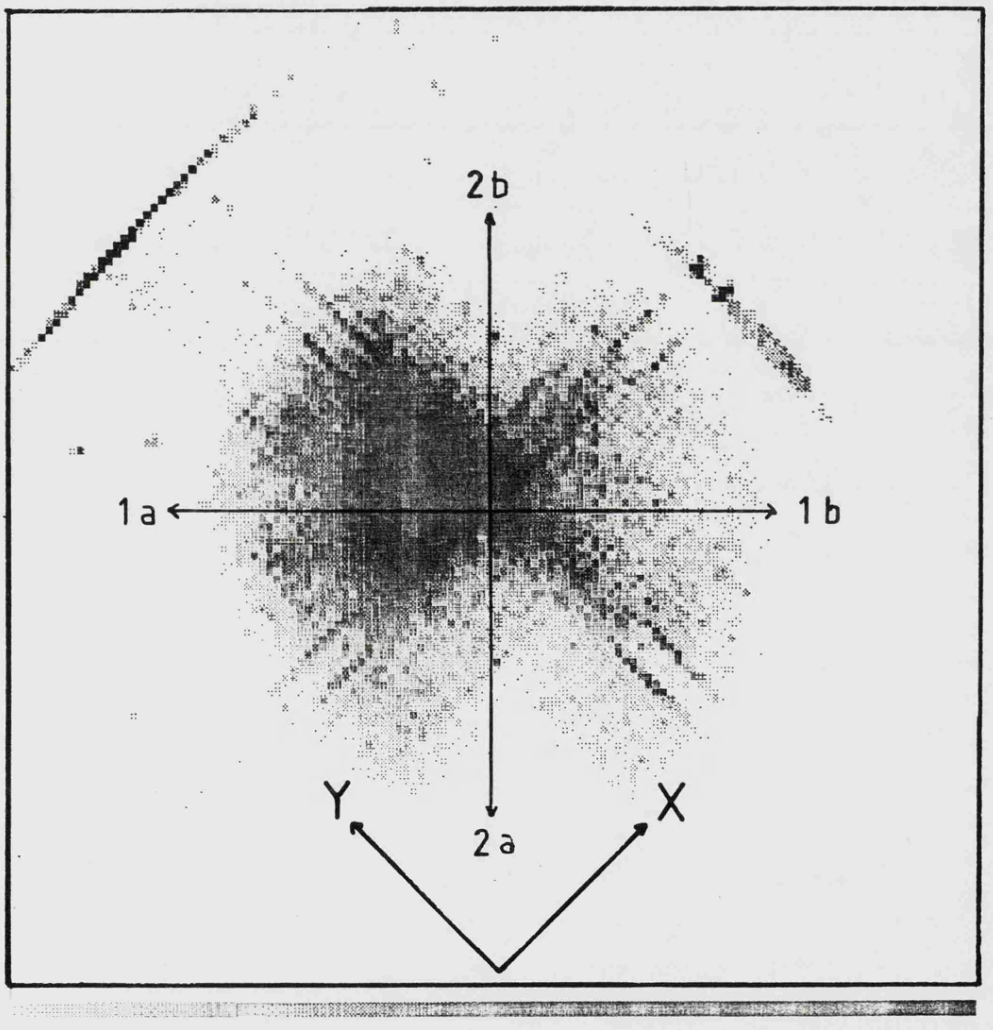

KEY: The line 1a-1b represents the profile across the image shown in figure 11.7. The line 2a-2b represents the position of the filter bar on the image

Figure 11.6 Integrated detector image deliberately over exposed.

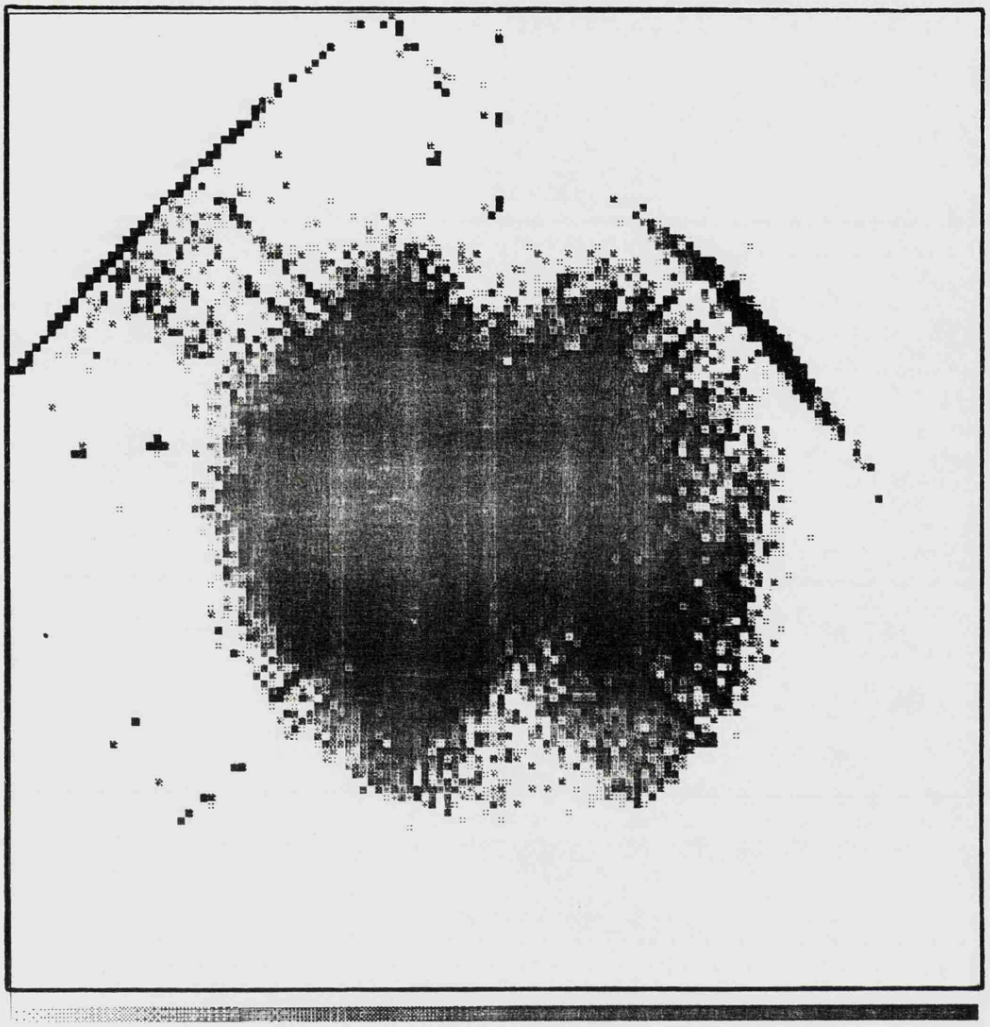

Figure 11.7 Intensity profile of the flight image perpendicular to the filter bar.

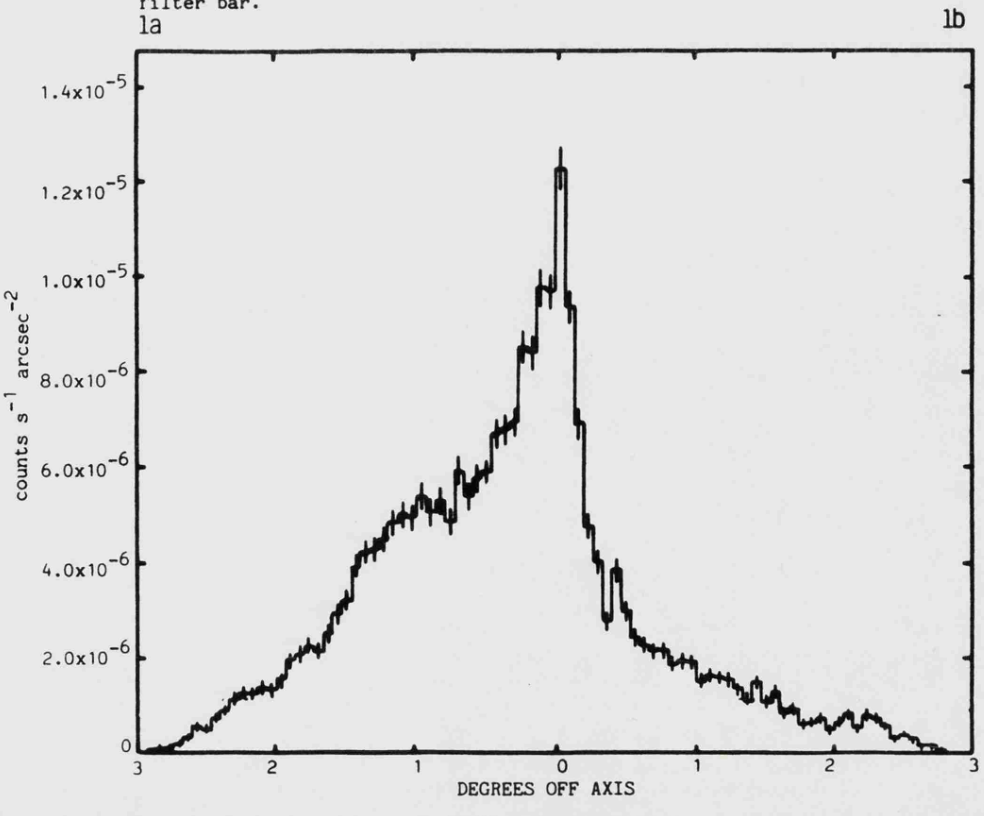

t=210s, t=280s and t=350s (figures 11.8a, 11.8b, 11.8c, 11.8d) shows that its shape does not appear to change with time and hence, as the rocket was pointing at different positions in each time interval, the area of sky viewed.

If the image were the result of a background transmitted uniformly across each filter, the intensity profile should follow the vignetting function of the telescope, shown in figure 11.9. Clearly the profile obtained from the flight image does not match that expected, in particular there is no minimum from the filter bar vignetting.

11.3.3 Pulse Height Distribution

The pulse height distribution of summed X1, X2, Y1 and Y2 signals is shown in figure 11.10. The peak of the distribution, occurs at 0.4pC which is much lower than the value obtained (1.5pC) using Fe^{55} during the vertical test (figure 10.3a). An exponential distribution is noted, contrary to the peaked distribution obtained during correct operation on the ground (figure 10.3a). Hence, the value of 0.4pC for the gain is an upper limit as the peak of the distribution is artificial, the lower fall off of the "peak" being caused by the cutoff of the low level discriminator.

Pulse height distributions (figures 11.11a, 11.11b, 11.11c, 11.11d and 11.11e) were obtained from several different areas of the flight image (shown in figure 11.11f). Towards the edge of the image, the pulse height distributions become more normal, the proportion of events in the peak decreasing in areas progressively removed from the

Figure 11.8a Image profile perpendicular to the filter bar, t=130-170s

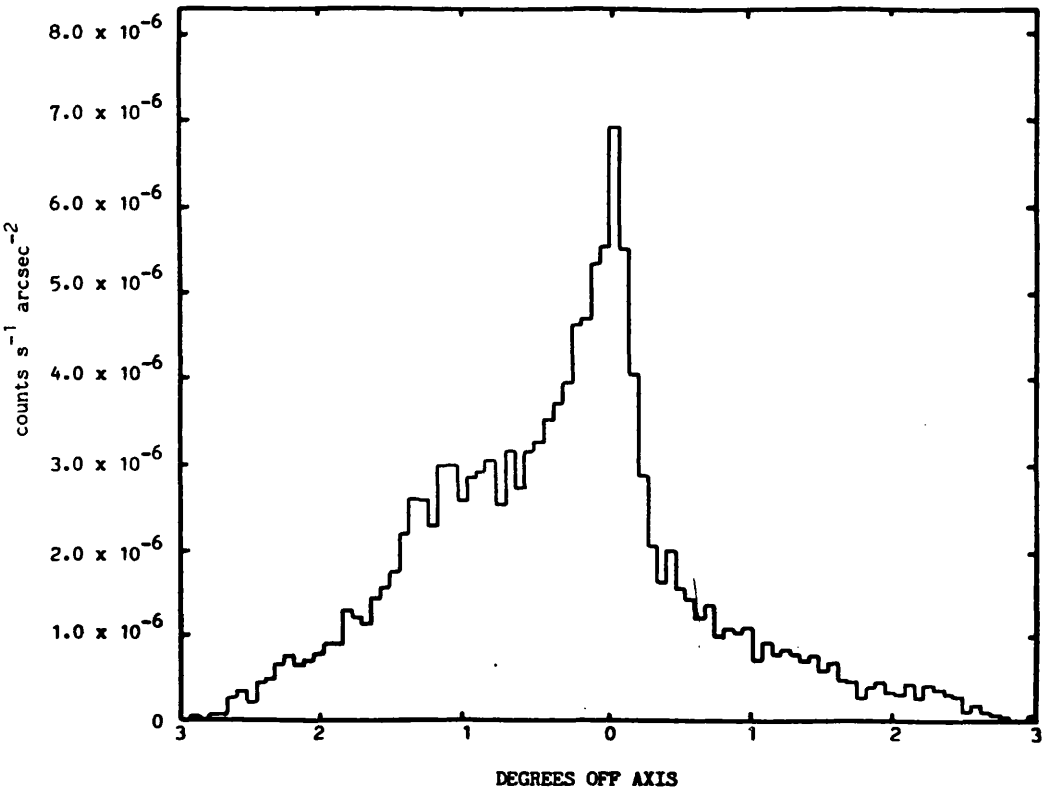

Figure 11.8b t=210-250s

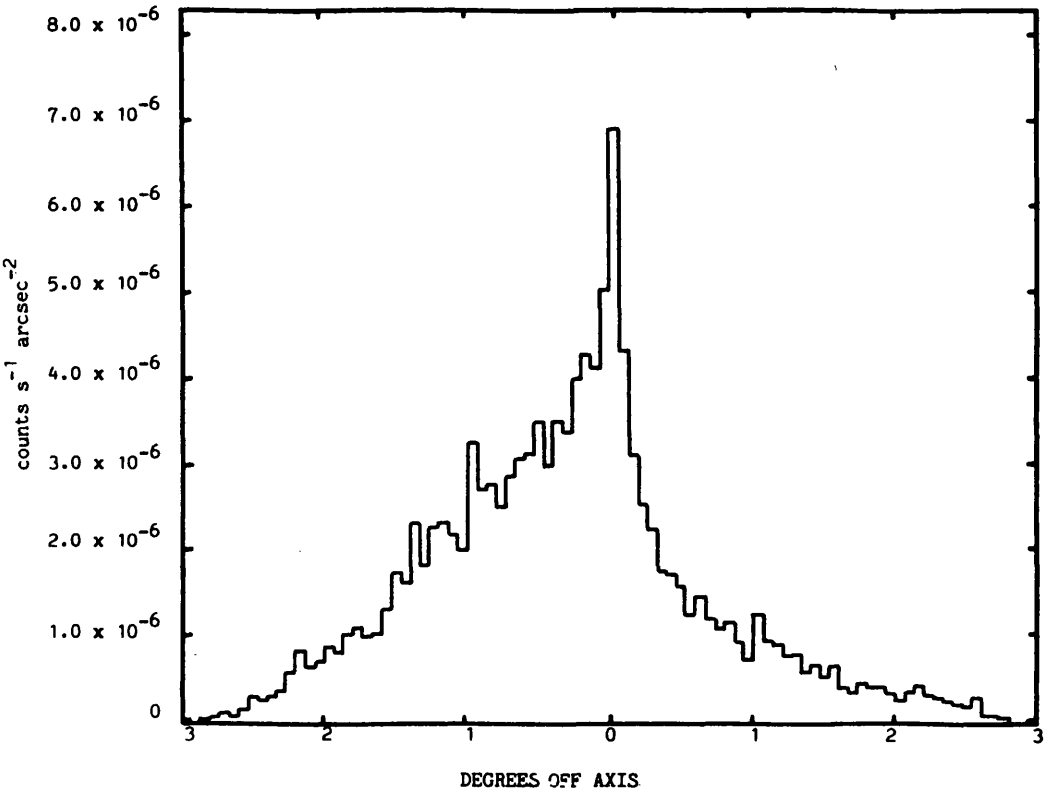

Figure 11.8c t=280-310s

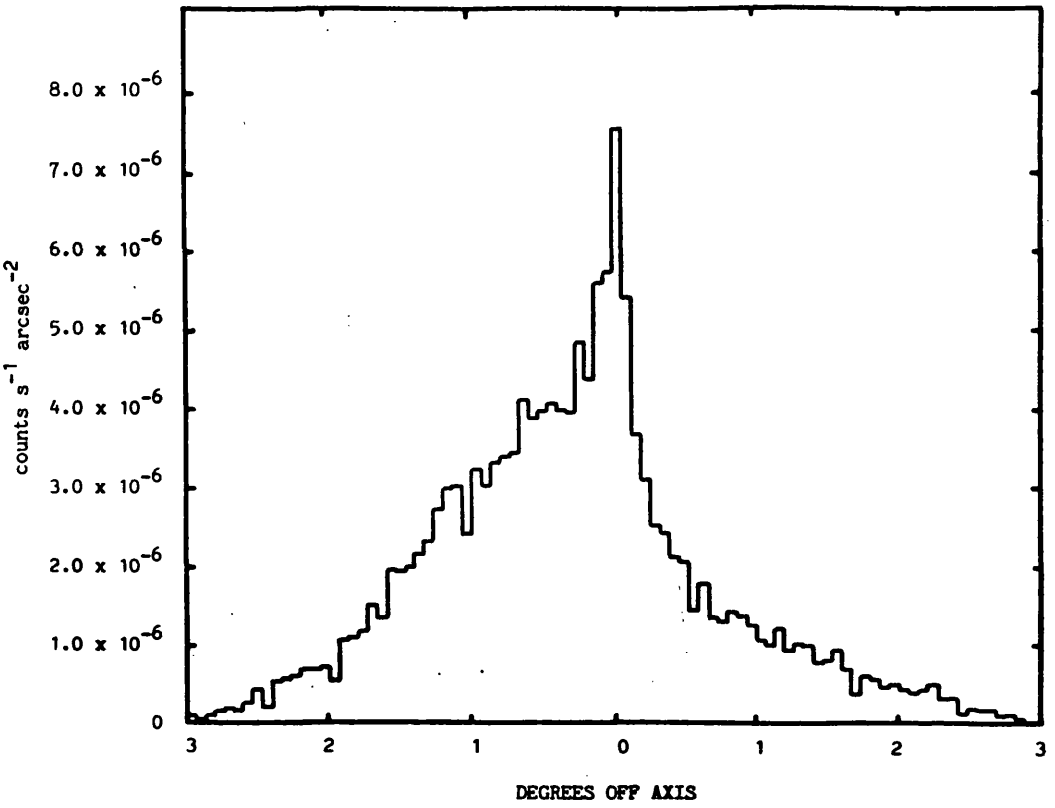

Figure 11.8d t=350-390s

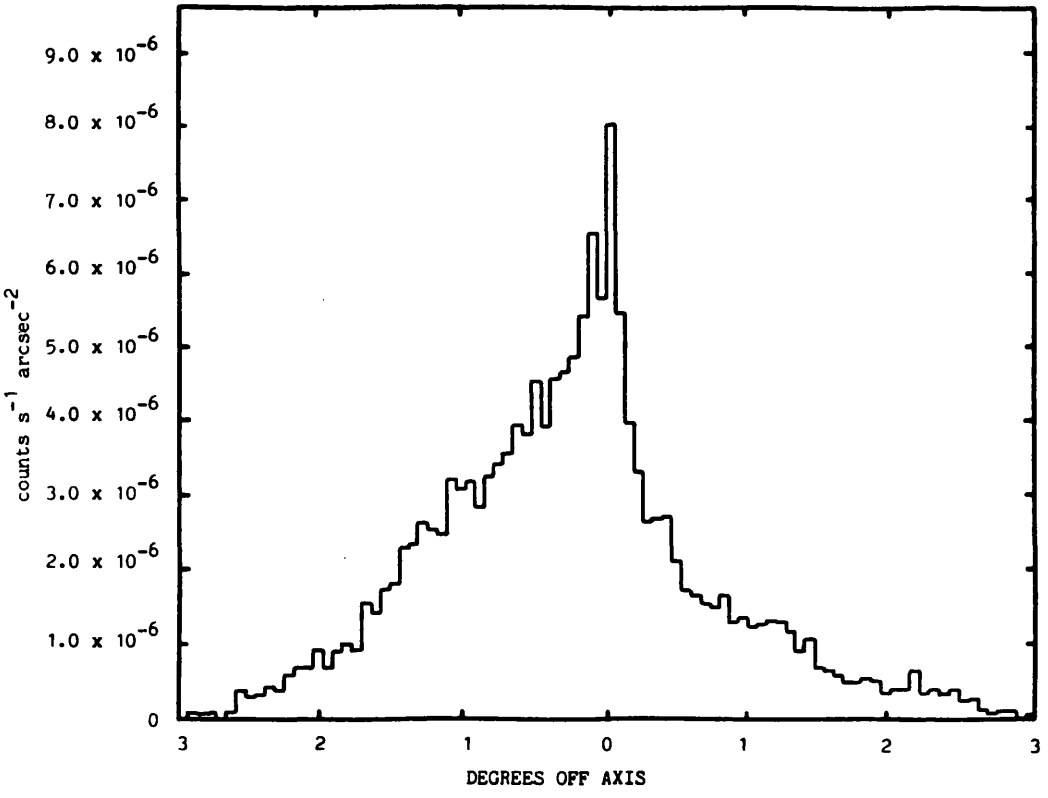

Figure 11.9 Approximate vignetting function of the WFSXC for a 1° wide cut across the image plane perpendicular to the filter bar. (assuming that a 90% power circle is 1° diameter at the edge of the field of view)

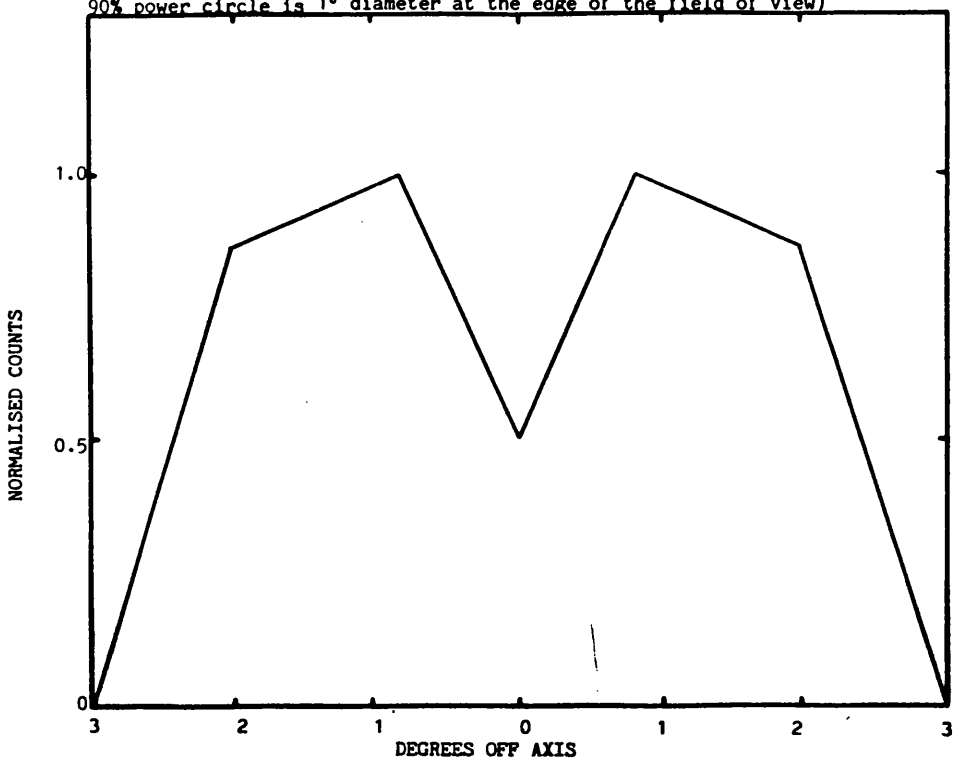

Figure 11.10 Pulse height distribution of events from rocket 21.069

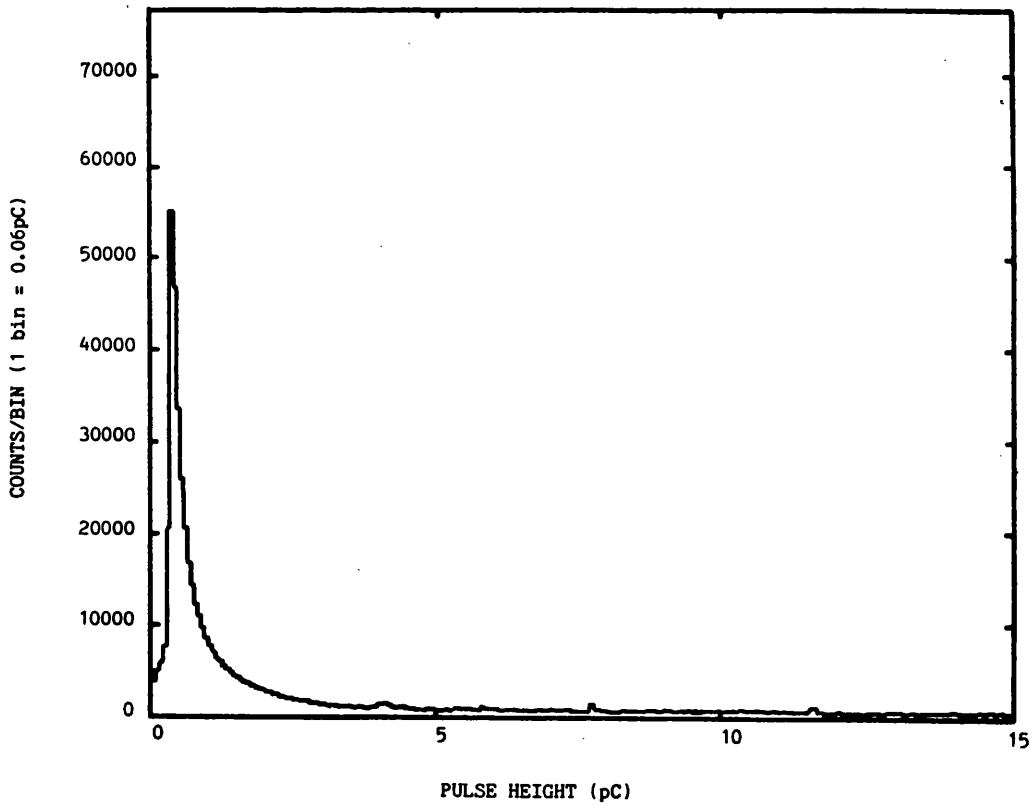

Figure 11.11 Pulse height distributions form the flight data taken from the area of the image shown in figure 11.11f.

Figure 11.11a

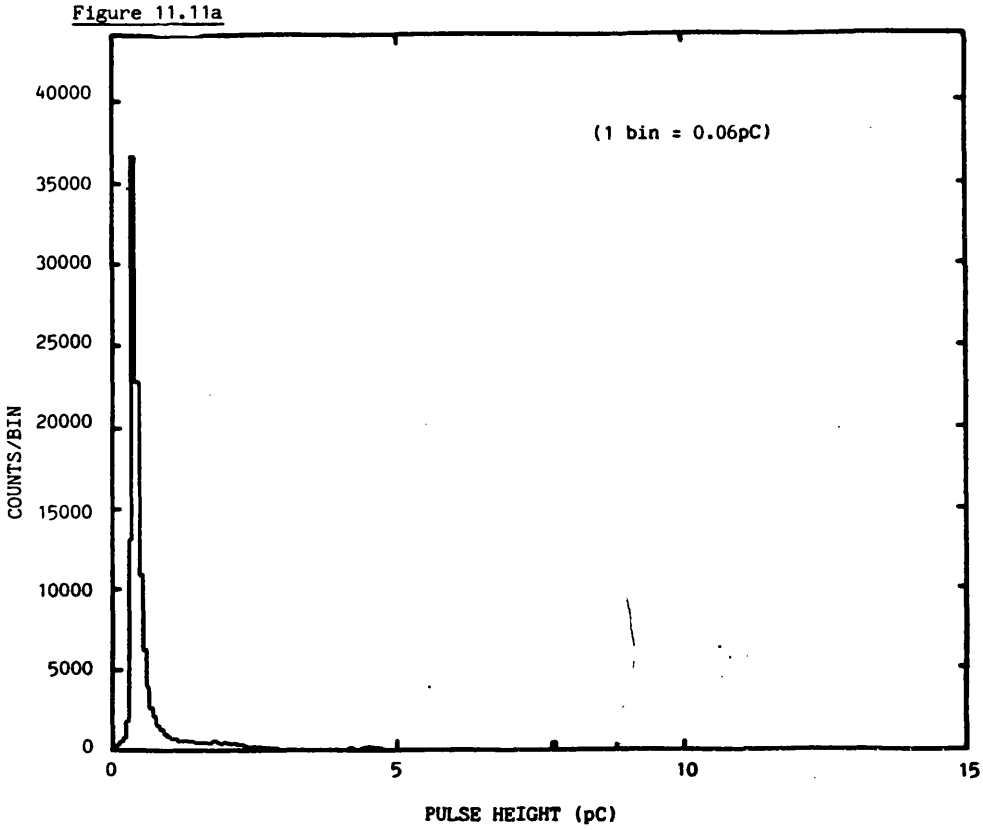

Figure 11.11b

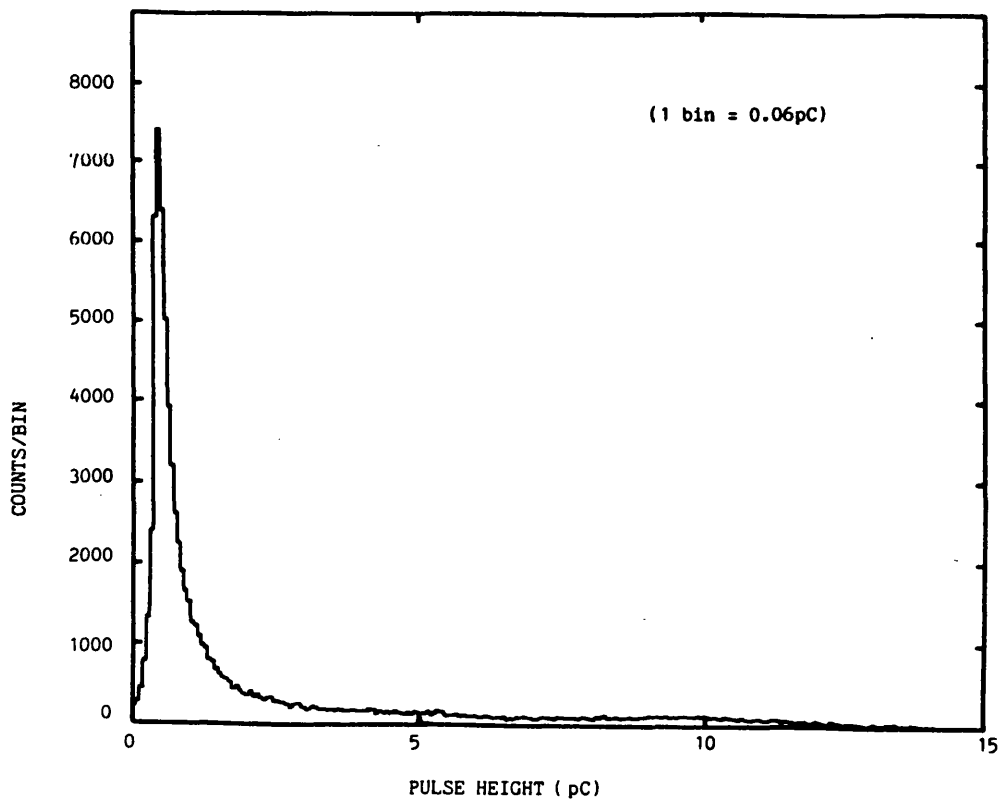

Figure 11.11c

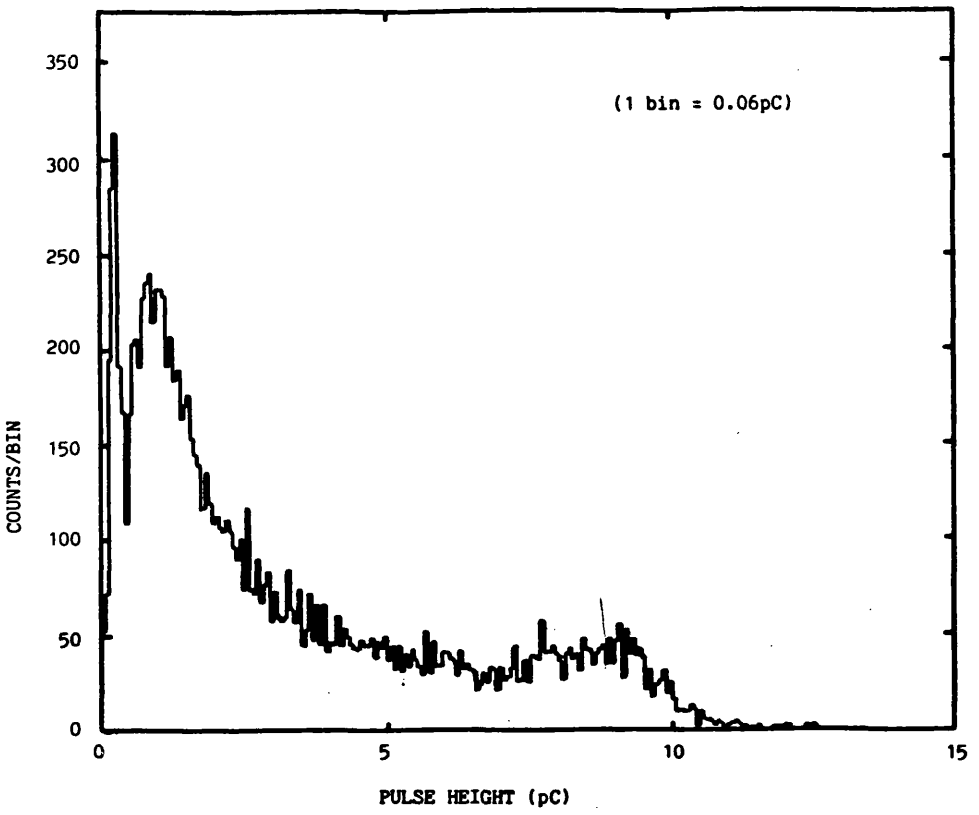

Figure 11.11d

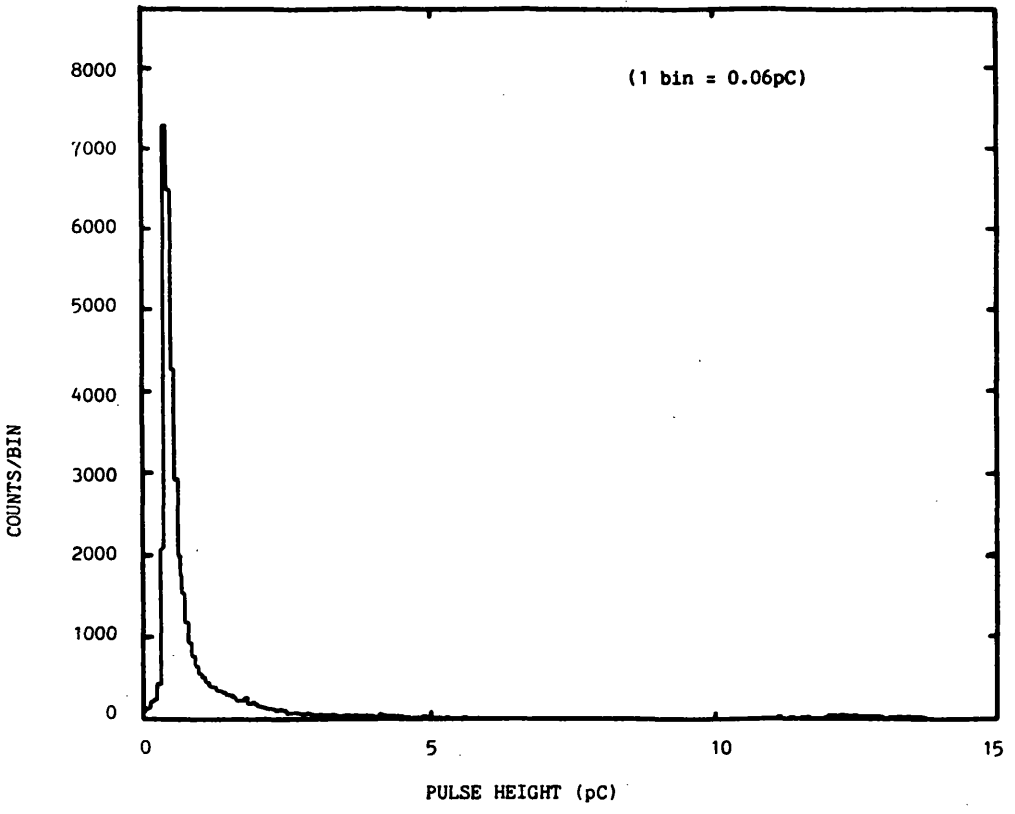

Figure 11.11e

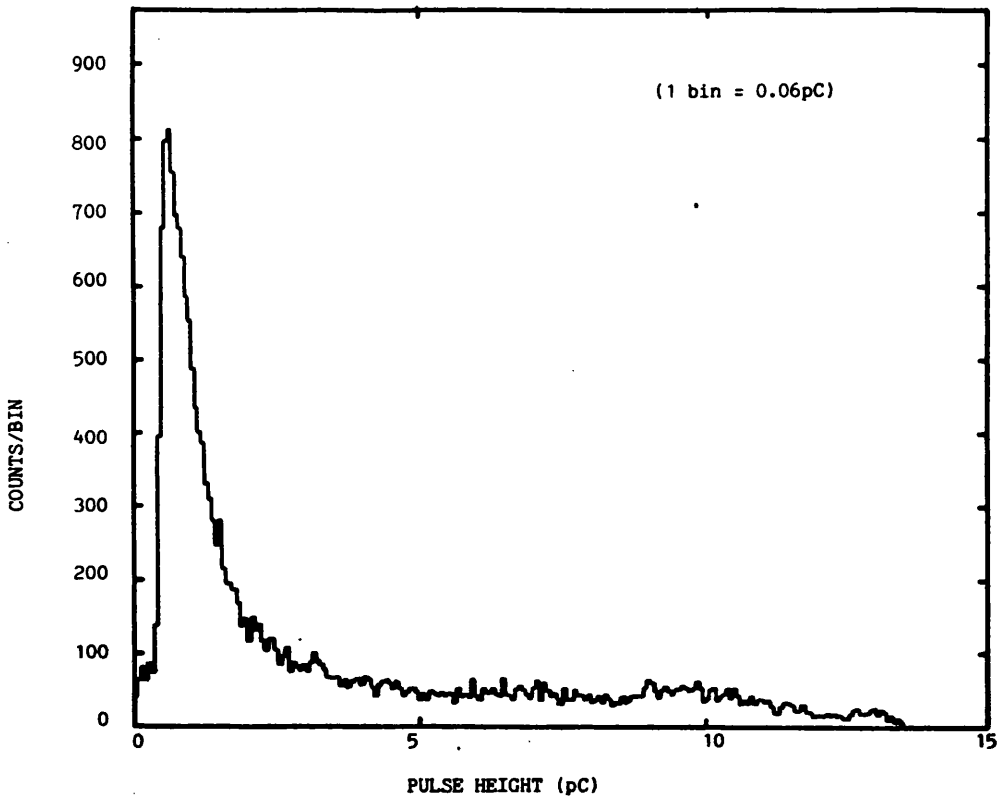

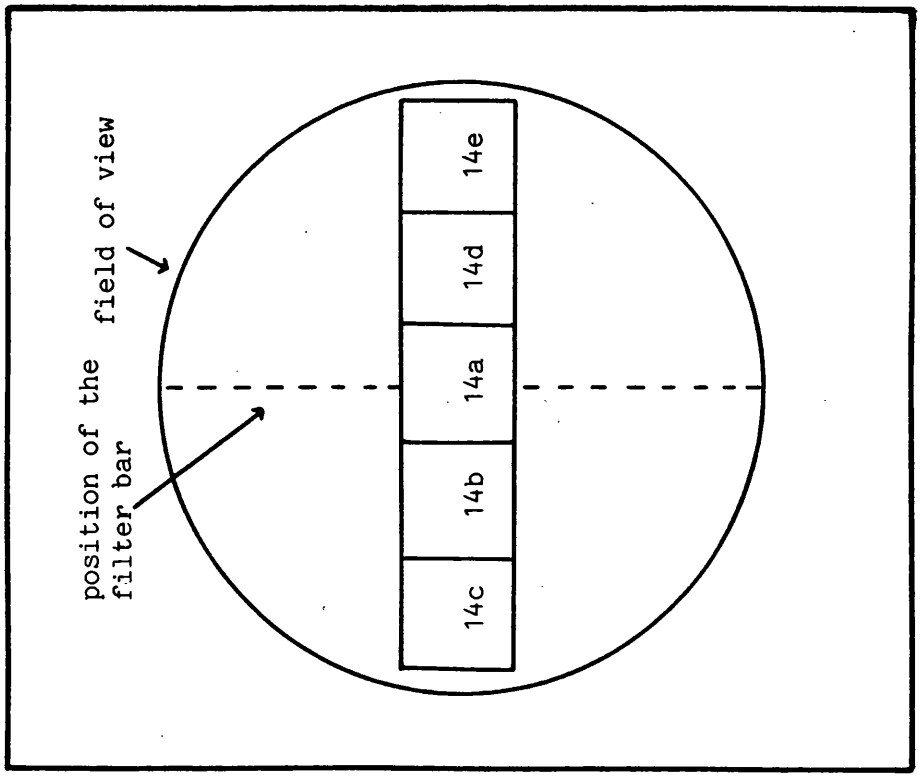

Figure 11.11f Location of pulse height distributions on the detector image

peak of the image profile. Thus the majority of events in the image peak are of low pulse height.

When the detector image is reconstructed without the low pulse height events (events below 2pC, figure 11.12), the central peak is seen to be almost completely removed and the filter bar vignetting becomes visible. The intensity profile (figure 11.13) shows that the image is similar to that expected, except for the narrow central peak, and the vignetting of the filter bar is apparent. However, the number of events of pulse height >2pC is ~1/3 of the total, implying a real count rate $\sim 10^4 s^{-1}$ if it is assumed that the dead time correction is independent of pulse height. Therefore, this "selected" event count rate is still higher than was anticipated.

11.3.4 Microchannel Plate Gain

The peak gain of an MCP pulse height distribution is independent of the wavelength of the illuminating radiation but will change with the voltage levels applied and the count rate. There is a limit to the current that can be drawn by the MCP, determined by the applied potential and the MCP resistance. At count rates where the rate of charge extraction exceeds the current limit the charge that can be extracted per event is reduced, lowering the gain of the detector. The gain suppression is restricted to the area illuminated (A_X) and the maximum attainable peak gain ($G_C(max)$) can be estimated as follows

$$G_C(max) = \frac{V_R . A_X}{R_P . A_P} \frac{1}{10.(\text{count rate})} \qquad (11.2)$$

Figure 11.12 Integrated detector image with high pulse height events (above 2pC) only

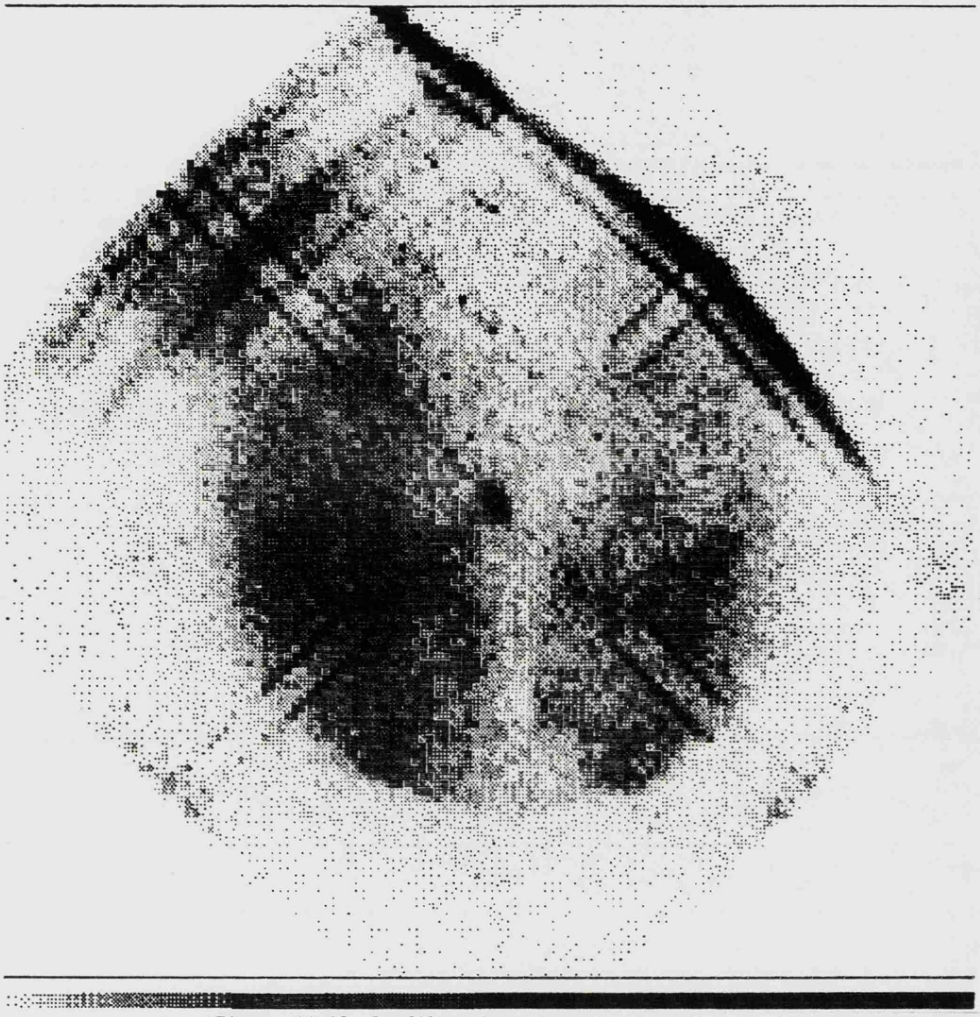

Figure 11.13 Profile taken through the high pulse height image perpendicular to the filter bar.

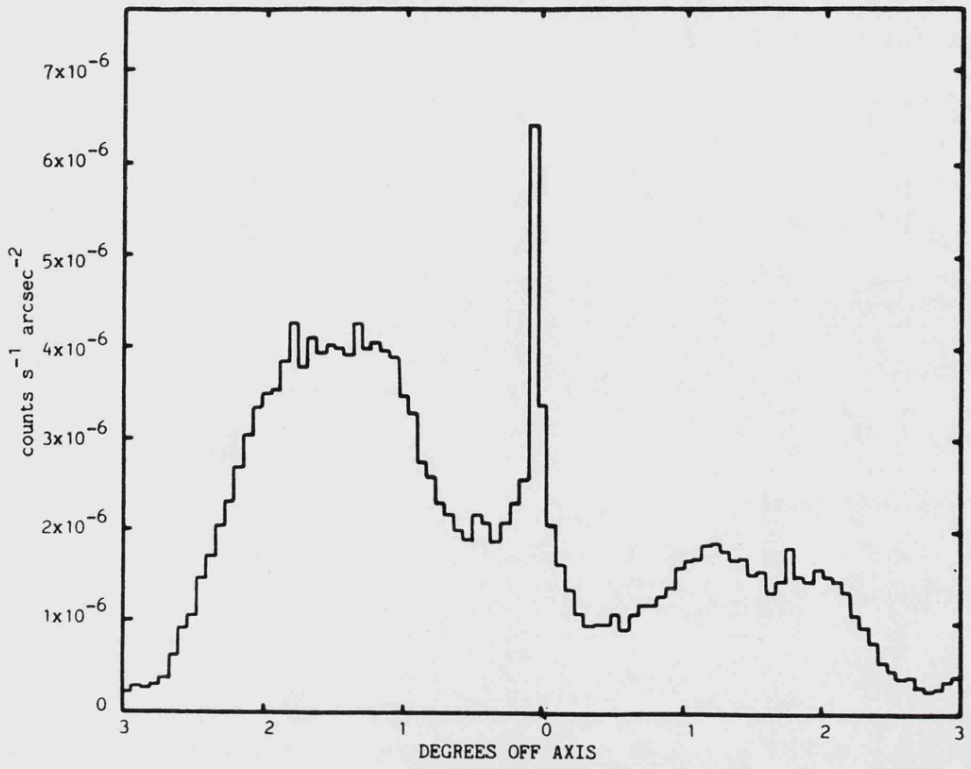

where: V_R is the potential across the rear MCP (1.6kV for the WFSXC)

R_P is the rear MCP resistance ($\sim 2 \times 10^9 \Omega$ for the WFSXC)

A_P is the area of the MCP ($2 \times 10^3 mm^2$ for the WFSXC)

Data obtained in the vertical test with an Fe^{55} source is used here to test equation 11.2. From the image of figure 10.3b it can be seen that the majority of the events fell in an area $\sim 10mm^2$, the count rate being $\sim 340 s^{-1}$. The predicted gain is $\sim$1.2pC for the above WFSXC parameters which is in reasonable agreement with the measured gain of 1.5pC.

If the very high count rate was reponsible for the low gain, equation 11.2 can also be used to estimate the area illuminated by the high count rate on the detector. Taking 0.4pC as the upper limit to G_C and the estimated input count rate to be $4 \times 10^4 s^{-1}$, suggests that the fraction of MCP illuminated must have been less than 0.2 ($400mm^2$). However, if the peak gain was below 0.4pC many events would have been rejected and the input count rate and upper limit to the illuminated area would both have been underestimated by the calculation.

11.3.5 Electronic Count Rate Limitations

During post-flight tests at MIT it was found that the detector gain could also be suppressed by the effect of a high count rate on the processing electronics. This effect was independent of the area illuminated, needing a count rate $\sim 10^5 s^{-1}$ to reproduce the pulse height distribution from the flight data.

It was observed, during pre-integration UV tests of mirror alignment, that very low pulse heights lead to a spreading of the events over a larger area on the image than is actually illuminated on the detector (figure 11.14). The spreading of the image was very much reduced when the level of the low pulse height discriminator was increased. This effect can be explained as incorrect positioning of low charge level pulses, as a result of electronic non-linearities, so that a small point image is smeared out as observed, the shape depending on the detailed behaviour of the electronics.

11.3.6 Conclusion

The count rate observed during flight was anomalously high, 100 or more times larger than expected. The high count rate resulted in a depressed detector gain and an image that did not match that expected from the known vignetting function of the WFSXC.

Two possible explanations of the observations emerge. First, the low pulse height events found in the peak could be explained if a small area of the detector ($<400mm^2$) was illuminated by a high background count rate. The shape of the image peak is consistent with the effect of low pulse heights on the imaging electronics. However, the high pulse height image, which shows very little of the central peak, needs to be explained by an additional and still anomalously large background component, which illuminates the whole detector more or less uniformly.

Figure 11.14 Image of "point" UV source

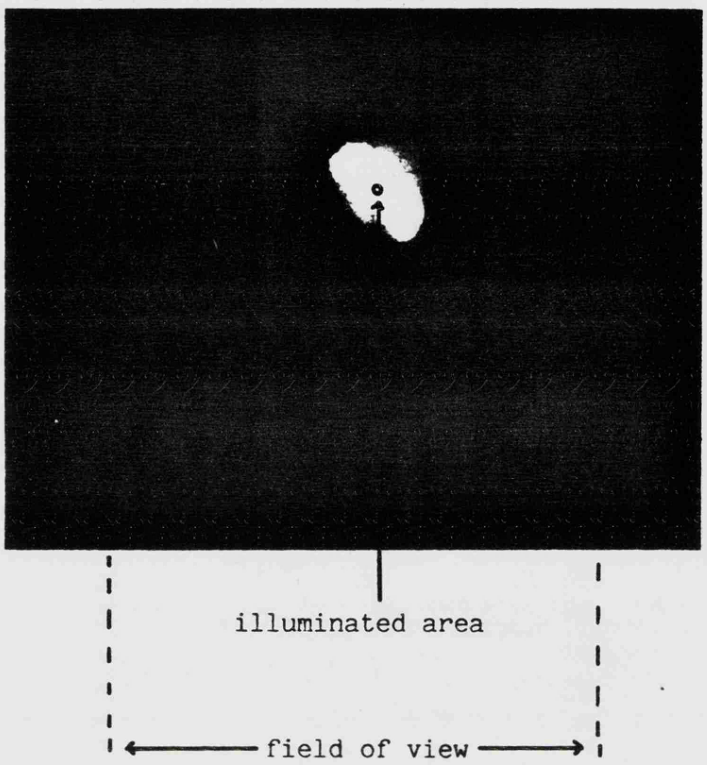

Alternatively, a single component background, uniformly illuminating the whole detector could have depressed the gain in the processing electronics. Incorrect positioning of the low pulse height events could then have produced the spurious peaked distribution of positions superimposed on the true background image.

11.4 Possible Causes of the High Background

In a further investigation of the cause of the anomalously high background and the related observations described in section 11.3 above, the following possible explanations have been considered.

1) Incorrect assumption of the CsI photocathode response

2) Incorrect assumption of the mirror response

3) High particle background

4) Unexpectedly high filter transmissions because;

either

a) Assumed linear absorption coefficients (Be and lexan) too high or filter thicknesses incorrect (too thin).

or

b) High contribution to transmission from pinholes in metal foils

or

c) Physical damage to filter during handling or launch (cracks or holes)

Each possibility will be discussed in turn in the following sections.

11.5 The Response of the CsI Photocathode and the Telescope Mirrors in the XUV and far-UV

The response of the CsI photocathode in the XUV and far-UV was discussed in detail in chapter 6 when considering the redesign of the filters. As the assumed detector efficiency was always greater than 1% at wavelengths up to 2000Å (Martin and Bowyer, 1982) a factor of $\sim 10^2$ difference between the measured background and that expected cannot be explained by an error in the assumed CsI efficiency.

Although the background calculation relies on the theoretical response of the telescope mirrors their efficiency is high, ~80-90%, throughout the EUV and far-UV. Hence the largest error in the mirror efficiency (~20%) is far too small to account for the unexpectedly high observed background.

11.6 Particle Background

A possible explanation of the unexpectedly high background observed during flight is the presence of a large soft electron flux, thought to originate in the solar wind, trapped in the earth's magnetosphere. It has been suggested that a magnetic storm produces an enhanced population of electrons which decays over a period of days. Hill et al (1970) have measured the soft particle flux (F(E)) at sounding rocket altitudes (>130km), between 0.5 to 10keV and observed a correlation between the electron flux and the magnetic

activity a few days before flight. The fluxes measured by Hill et al appear to follow an approximately E^{-1} dependence, the maximum observed flux being

$$F(E)\ cm^{-2}keV^{-1}s^{-1}ster^{-1} = 161.E^{-1} \qquad (11.3)$$

The planetary magnetic three-hour-range indices are shown in figure 11.15a with the flight date for this flux measurement marked.

To estimate the contribution that these soft electrons make to the WSFXC background it is necessary to know how efficiently they are collected by the instrument. The threshold energy of soft electrons that enter the detector is ~4keV, as electrons below this energy will be repelled by the negative potential of the front MCP. Additionally the thin film filters will reduce the energy of electrons reaching the MCP. The mechanism of energy loss is complex but to a first order the filters can be considered transparent to electrons above ~4keV.

The total expected count rate in the WFSXC (C_e) can be represented by equation 11.4.

$$C_e = A.\Omega.K.\eta.\int_{4keV} F(E).dE \qquad (11.4)$$

where: A is the geometrical collecting area ($250cm^2$)

Ω is the solid angle collected ($8.63x10^{-3}$ster)

η is the MCP electron detection efficiency

K is the collection efficiency of the mirrors

η is ~63% with a CsI photocathode. Assuming that K=1 gives an upper limit to C_e

$$C_e = 1.14 \int_{4keV} F(E).dE \qquad (11.5)$$

Extrapolating the data of Hill et al beyond 10keV and integrating between 4keV and 100keV gives a net flux of ~500 electrons $cm^{-2}s^{-1}ster^{-1}$ at the telescope. The geomagnetic activity during the period preceding the 21.069 flight (figure 11.15b) was much lower than that preceding the observations of Hill et al, hence the estimated flux is an upper limit to that occurring during the WFSXC flight. The resulting upper limit to the background in the WFSXC is 570 counts s^{-1} compared to a total of ~470 counts s^{-1} from geocoronal lines. Therefore, it can be concluded that although the electron flux could contribute significantly to the background it does not explain the level observed during flight.

11.7 Filter Transmissions

The least well understood components in the WFSXC are the focal plane filters, carbon+lexan and beryllium+parylene. All the available experimental absorption data from the XUV to UV wavebands was summarised in chapter 6 (figure 6.1 for Par N, figure 6.2 for Be, figure 6.3 for lexan and figure 6.4 for C) and a reliable theoretical model for the XUV absorption, based on the work of Cromer and Liberman

Figure 11.15

GEOMAGNETIC ACTIVITY INDICES

b) Geomagnetic activity for the months preceding the flight of rocket 21.069

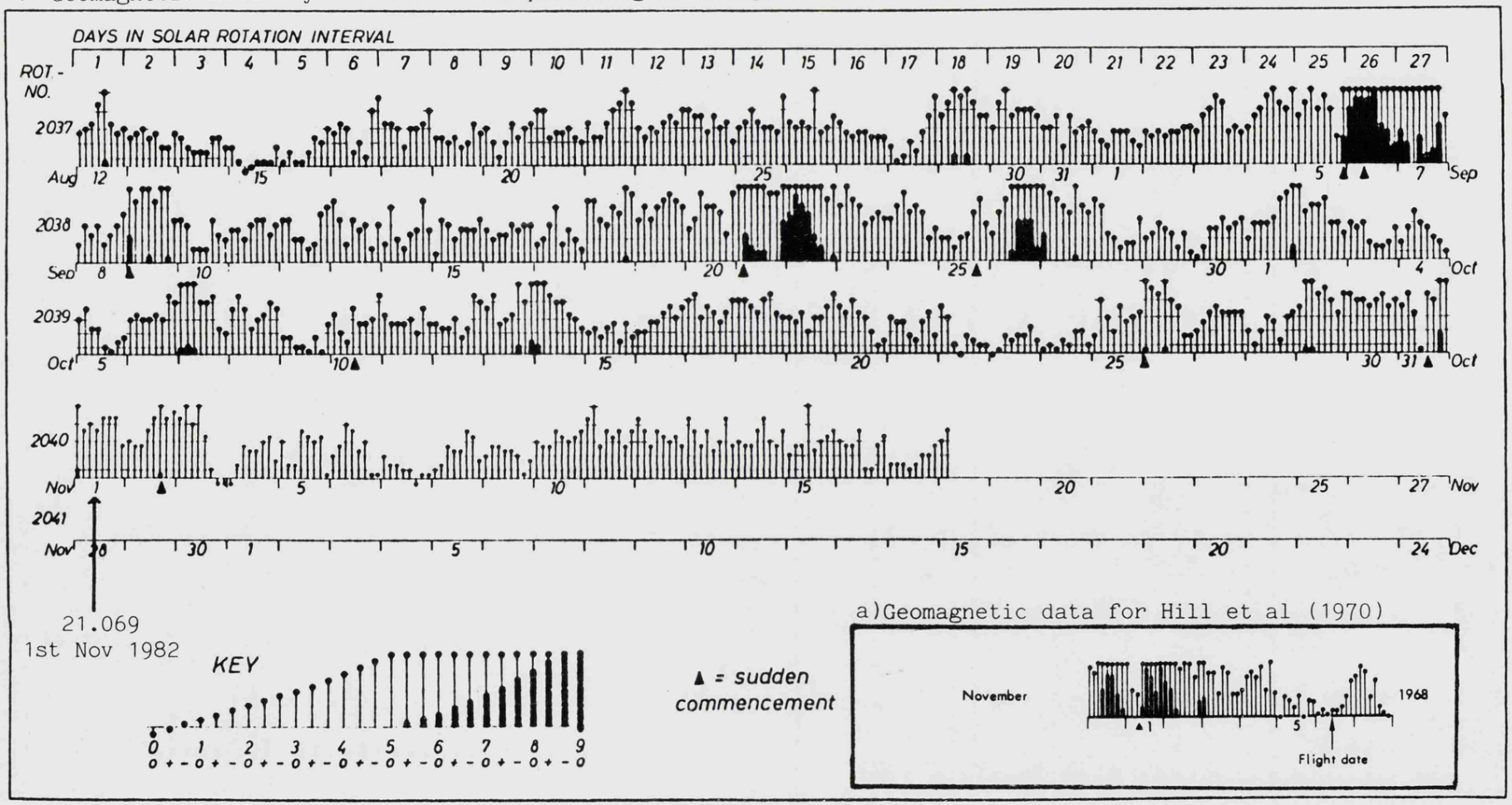

(1970), was demonstrated. However, no absorption data could be found in the literature longward of 1200Å for Be or between 304Å and ~1600Å for lexan. Also, although carbon data can be found throughout the far-UV and UV, there is a conflict between that of Samson and Cairns (1964) and Hagemann et al (1974). Therefore, there is a risk that errors in the assumed values of the absorption coefficients, used to estimate the filter transmissions in these bands, could be responsible for the anomalously high background seen during flight. In order to see if this was so, the flight filters were calibrated in the far-UV (section 6.7) at the National Physical Laboratory.

The transmissions measured at NPL were several orders of magnitude higher than predicted. Using these results to recalculate the expected geocoronal background (correcting the transmissions for 30° angle of incidence and assuming a mirror transmission of 100%) (table 11.3) gives an increase of only ~25%, from 470 counts s^{-1} to 600 counts s^{-1}.

The carbon/lexan filter appeared uniform when traversed by the far-UV beam, except for a crack in the carbon. The crack only gave a factor 2 increase in the flux, insufficient to explain the background.

Above the wavelengths at which geocoronal emission occurs (>1600Å) the only source of background is diffuse cosmic emission (see section 1.6). Using the NPL transmissions, the pre-flight calibrations of the C/lexan filter above 2000Å, the upper limit to the Be/Par N transmission above 2000Å and taking Martin and Bowyer's (1982) CsI efficiency, the calculated contribution from the cosmic UV background is negligible.

Table 11.3. Recalculated Geocoronal Background from Filter Measurements

λ(Å)	Flux (photons s^{-1}) in the filter	
	carbon/lexan	beryllium/parlyene
304	27	440
584	0	0
834	0	0
1025	0	1.9
1216	17	1.3
1304-1356	56	2.6
1356-1600	46	2.1
TOTAL	146	446

note The filter absorption was corrected for an angle of incidence of 30°.

The only area where uncertainty still remains is the transmission of the C/lexan filter between 304Å and 1216Å, because of the gap in the lexan absorption data in this range. However, even if the lexan were entirely transparent in this band the carbon alone would entirely reject the background, based on the data of either Samson and Cairns (1964) or Hagemann et al (1974), being very much less than 1 count s^{-1} over the field of view for 584Å, 834Å and 1025Å.

It can be concluded that the high background count rate was not caused by the errors in estimating the filter transmissions.

11.8 Possible Transmission of Geocoronal Radiation Through Pinholes

Pinholes in the filters, which may pass through one or both films of a filter, could cause a significant increase in the background count rate. The NPL filter calibrations suggest that the fractional area* for pinholes in the flight spare filters must be less than $\sim 10^{-7}$ (Be/Par N) and $\sim 10^{-6}$ (C/lexan). The pinhole density necessary to explain the background count rate can be estimated to test whether the above values explain the anomalously high background.

If a pinhole passes straight through a filter the background flux will only be attenuated by the efficiency of the CsI, ~20%. The count rate will be dominated by the brightest geocoronal lines, lyman α (1216Å) and oxygen 1304Å, a total $\sim 3 \times 10^{9}$ photons s^{-1} in the field of view). Therefore, the fractional area of the filter that must be occupied by pinholes in order to explain the observed background (4×10^{4} counts s^{-1}) is thus $\sim 7 \times 10^{-5}$.

* ie. the effective transmission of the filter due to pinhole effects

Where pinholes are only in one film of the filter the background will still be attenuated by the other component. Table 11.4 shows the transmission and geocoronal count rates through the separate materials comprising each filter. Assuming that ~half the net background (~2×10^4 counts s^{-1}) is transmitted by each filter, the fractional pinhole area in each film needed to explain the background count rate is ~0.6 (pinholes in Par N), ~0.02 (pinholes in Be) and ~0.0013 (pinholes in C), corresponding to effective fractional areas for the composite filters of ~6.6×10^{-6}, 5×10^{-5} and 2×10^{-5} respectively.

Consequently the pinhole areas needed to explain the background are higher than those measured at NPL. Therefore, pinholes could not have been responsible for the observed background.

11.9 Physical Damage to the Flight Filter

Several cracks in the metal foils of the filters existed before flight, as described in section 10.2. As these cracks were not imaged when illuminated by a UV lamp it was assumed that they would not contribute significantly to the instrument background. Given the transmitted count rates, ~100 counts s^{-1} for C/lexan and ~10 counts s^{-1} for Be/Par N, it is possible to derive upper limits to the size of the cracks in order to estimate the expected background and test the above assumption.

If T_F is the filter transmission, which is $<10^{-4}$ for Be/Par N and ~10^{-3} for C/lexan at the wavelength of the mercury lamp (~2500Å), and the flux incident on a filter is F(counts s^{-1} $pixel^{-1}$), then the number of background events detected in one pixel is $F.T_F$. Consider a crack

Table 11.4. Tranmissions through each filter component (corrected for 30° angle of incidence) and geocoronal fluxes after accounting for the detector efficiency

λ (Å)	2500Å beryllium		2000Å carbon*	
	Transmission	Total flux in filter (c s^{-1})	Transmission	Total flux in filter (c s^{-1})
304	0.2	3.2×10^{4}	1.0×10^{-4}	16
584	2.9×10^{-4}	53	1.3×10^{-16}	<<1
834	2.9×10^{-13}	<<1	1.3×10^{-16}	<<1
1025	3.0×10^{-35}	<<1	1.3×10^{-16}	<<1
1216	1.1×10^{-5}	1.8×10^{3}	9.0×10^{-11}	<1
1304-1356	4.8×10^{-6}	7.7×10^{2}	4.7×10^{-7}	75
1356-1600	6.8×10^{-6}	36	9.4×10^{-6}	52
TOTAL		3.5×10^{4}		143

λ(Å)	1000Å lexan**		2000Å parylene	
	Transmission	Total flux in filter (c s^{-1})	Transmission	Total flux in filter (c s^{-1})
304	0.11	1.8×10^{4}	0.012	1.9×10^{3}
584	2.3×10^{-3}	4.2×10^{2}	5.1×10^{-6}	<1
834	5.7×10^{-4}	2.7×10^{2}	3.2×10^{-7}	<1
1025	2.3×10^{-3}	8.8×10^{4}	5.1×10^{-6}	1.6×10^{2}
1216	0.0158	2.5×10^{6}	2.5×10^{-4}	4.0×10^{4}
1304-1356	0.078	1.2×10^{7}	6.1×10^{-3}	9.8×10^{5}
1356-1600	0.16	8.4×10^{5}	0.025	1.2×10^{5}
TOTAL		1.5×10^{7}		1.1×10^{6}

* Samson and Cairns (1964) data used.

** Linear absorption assumed to be the same as for parlyene.

divided into elements of 1 pixel side (p) in length and width dl. The flux through each element is F.dl/p. Assuming initially that dl<p all the flux from a crack element will lie in one pixel. If the detection of a crack is limited by the background, the required flux for a 5σ detection of a crack is then $\sim\sigma(F.T_F)^{1/2}$. Therefore the upper limit to the value of dl is

$$dl < \sigma.p(T_F/F)^{1/2} \qquad (11.6)$$

If N is the measured background count per pixel in the detector then $T_F/F=T_F^2/N$ and

$$dl < \sigma.p.T_F/N^{1/2} \qquad (11.7)$$

In the carbon/lexan filter N was ~0.09 counts $pixel^{-1}$, hence, given $T_F=10^{-3}$ and p~0.3mm (FWHM, section 10.3) dl<0.005mm. For the Be/Par N filter, N~0.009 counts $pixel^{-1}$ gives dl<0.0016mm. It should be noted that there are large errors in the above calculation as N is not well known. However, in each case the minimum values of N were chosen, which maximise the estimated upper limits of dl.

A total crack length of ~20mm was observed in each filter before flight (see section 10.2). Hence, the open areas in each metal film must be $<0.1mm^2$ (C/lexan) and $<0.03mm^2$ (Be/Par N), corresponding to $2x10^{-4}$ and $6x10^{-5}$ fractions of the area of each filter respectively. Using the flux data from table 11.4 for lexan and Par N gives expected count rates of 3000 counts s^{-1} (C/lexan) and 66 counts s^{-1} (Be/Par N),

lower than the observed background. However, if larger areas of Be (>9mm^2) or C (>0.7mm^2) were cracked, the plastic films could transmit sufficient flux to explain the background. Also, if the area of cracks measured had been through both components the expected flux in each filter would be 1.6×10^5counts s^{-1} (C/lexan) and 4.8×10^4counts s^{-1} (Be/Par N).

The cracks that existed before flight had insufficient area to explain the background, as they were observed to be only in the metal foils. However, if the cracks enlarged during launch or other damage occurred it would be possible to explain the fluxes observed.

11.10 Conclusion

Several possible causes of the high background seen during flight have been eliminated.

1) Incorrect assumption of the CsI and Mirror efficiencies
2) High electron background
3) Underestimation of the filter transmissions
4) Pinholes in the filters

Physical damage of the filter is believed to have been the cause of the high background. The flight image is consistent with damage spread over the whole filter area and possibly, if the gain suppression was caused by illuminating the detector with a high count rate in a small area, a small hole.

It is only possible to speculate about what may have caused the damage. If it was present before flight, a large number of small cracks may have existed, caused by pumping and venting the vacuum system, which were not detectable by the UV test or visual inspection. Alternatively, some undetected damage may have occurred during the final cycles of the vacuum system, before launch, when the integrity of the filter could not be checked except by visual inspection of the front of the filter. Otherwise, the filter must have become damaged during launch, by any of three possible causes. First, vibration of the filter at low pressure (~14Torr), occurring when the vacuum box seal failed, may have broken the filter. Second, loose particles, which may have been in the vacuum box or have fallen from the payload after the vacuum box lid opened, may have punctured the filter. Third, the O-ring seal between the vacuum box and the lid, which had fallen out of the box some time during flight, may have fallen across the filter and damaged it when the lid opened.

It is especially disappointing to conclude that, although the detector and filters developed for this flight both appeared to function during all pre-flight tests and the detector continued to work to specification in all the post-flight diagnostic tests at MIT, a technical malfunction once again prevented the achievement of any astronomical result.

CHAPTER 12

CONCLUSION

12.1 Achievements of the WFSXC Programme

As both flights of the WFSXC payload experienced severe problems, it was not possible to obtain any astronomical data. However, during the course of the development of the WFSXC a certain amount of useful science was obtained.

Experimental measurements of the detector quantum efficiency (chapter 4) gave excellent agreement with theoretical predictions calculated for a photocathode wall thickness determined from a detailed geometrical analysis of photocathode deposition (section 4.3.3 and Appendix A). This showed two things: first, the geometrical analysis was a useful means of characterising the photocathode for an MCP and second that the theoretical model of Fraser (described in section 4.2) - which considered the emission of both primary and secondary electrons when a photon is absorbed - was a good description of photocathode behaviour in the soft X-ray band.

The photocathode model predicted that the best choice of material for the WFSXC band was CsI. CsI was used on the WFSXC detector for rocket 21.069 yielding improvements in the detector efficiency of between 5 and 10 times (depending upon the incident angle) the uncoated efficiency at 44.7Å. Special handling techniques were devised to cope with the hygroscopic nature of CsI (section 4.3.4) which were successfully applied under field conditions to obtain stable photocathode operation.

The linearity of the resistive anode image readout was measured experimentally, the results agreeing very closely with the theoretical predictions of Fraser (1980) and showing that the model was a good description of the anode behaviour. Two techniques were developed, from the theory, to remove the distortion from anode images. Low residual distortions were obtained after applying these methods, effectively eliminating the distortion problem, which would otherwise only have been possible by detailed calibration of the anode.

Thin film bandpass filters were developed for the WSFXC yielding some useful data concerning the absorption of the constituent materials. Calibrations of the filters showed that the atomic model of absorption of Cromer and Liberman (1970) could be applied in the XUV, up to wavelengths ~300Å for Be and ~100Å for Par N (section 6.3). It was seen, by comparing the model with data from other authors that at longer wavelengths the atomic model did not adequately describe the behaviour requiring other mechanisms to be taken into account. The measured Be data also resolved a serious discrepancy between other sets of absorption data (Johnston and Tomboulian, 1954; Henke and Elgin, 1970).

Far-UV measurements of absorption were made on carbon/lexan and beryllium/parylene filters, the transmissions appearing to be determined by pinhole effects. However, useful lower limits to the linear absorption coefficient of Be were obtained between 1216Å and 1938Å. The problem of pinholes was noted as an effect that should be taken into account when modelling filter transmissions in bands where absorption coefficients are high.

12.2 Discussion of the Failures of the WFSXC

The causes of the problems experienced on the flights of the WFSXC have been discussed extensively in chapters 9 and 11 for rockets 25.040 and 21.069 respectively. However, the success or failure of any flight is dependent upon how well a payload has been tested beforehand and it is necessary to discuss the WFSXC problems in this context.

Although damage to the vacuum housing (caused by launch) cannot be completely ruled out as the cause of the corona seen on the first flight, the leaking of the lid when the external pressure decreased below ~14Torr was the most likely explanation. This phenomenon was not detected during either pre-flight or post-flight testing of the payload for rocket 25.040 and was a serendipitous discovery during tests for rocket 21.069. A serious omission was made in that, while the whole payload was run in a vacuum several times (to test the telescope), the pressure inside the vacuum housing was never monitored before the lid was opened. Had this test been made and the problem detected, the corona could have been avoided by simply switching on the detector after the housing was opened. This was done on the second flight and no corona occurred.

The problem experienced in the second flight can also be ascribed to inadequate mechanical testing. However, the reasons for this were somewhat different, inadequate test equipment and procedures being part of the problem. Only the carbon/lexan filters were tested - at 160Å, 304Å and a range of UV wavelengths - before flight and although

post-flight calibrations of the flight spares vindicated the filter design, there may have been a fault in the filters flown that was not present in the spares. Only a crude method of testing the filter integrity before flight (section 10.2) was available, relying on detecting images of cracks or damaged areas, which would have been out of focus since the illumination was divergent. Also, as a UV source was used, only damage in the carbon or beryllium could have been detected (the plastic films were transparent in the UV). There was no means of detecting unexpectedly high transmissions, which would occur if damage was a large number of small cracks or pinholes, with the UV test. Furthermore, at WSMR the filter could only be checked before launch by visual inspection of the front of the filter prior to sealing the vacuum housing for the final time and, as the vacuum housing could not be closed at the end of the flight, the filters were inevitably damaged by reentry. Consequently, it could not be determined when the filters were damaged (ie. before or after launch) and therefore what was the cause of the damage.

A third flight of the WFSXC is planned and it is necessary to learn from the experiences of the previous two to ensure its success. Two modifications will be made to the payload itself.

i) The vacuum housing lid will be motorised so that it will maintain a positive seal and prevent air leaking in during ascent and will be extensively tested under vacuum to ensure that it will operate correctly. Also, the motor will enable the housing to be closed prior to re-entry, preventing the destruction of the filter.

ii) The WFSXC detector will be coated half with CsI and half uncoated. The dividing line will lie perpendicular to the filter bar so that each filter covers a segment of each photocathode. As MCP glass is a factor ~10-100 less efficient than CsI at the far-UV geocoronal line wavelengths, this arrangement will assist diagnosis of the source of the background if the failure recurred.

In addition it is hoped to make several improvements to the pre-flight calibration and testing.

i) Calibration of all filters before flight, in the bands 50-584Å and 1216-3000Å, to ensure that there are no errors in the filter specification or any signs of pinholes or cracks.

ii) Testing of the filter integrity, at intervals during payload integration and testing, by visual microscopic inspection and UV illumination (with a parallel beam) through a quartz window in the vacuum housing lid to image cracks and monitor the filter transmissions.

iii) Improved cleanliness in and around the vacuum housing

iv) Improved handling and transportation of filters to minise the risk of damage.

v) The use of a micro computer as part of the ground support equipment to allow storage and detailed anaylsis of payload data before flight.

12.3 Future Developments

MIT has commenced design studies for a SPARTAN payload utilising the WFSXC as an extension of the sounding rocket programme. SPARTAN is a self contained payload, with an ACS system and an on-board tape recorder for data storage, able to operate in space for several days. Deployed from the Space Shuttle it will fly free for the duration of a Shuttle mission and be recovered before the Shuttle returns to earth. Some changes will have to be made to the WFSXC design to make the instrument compatible with a longer duration mission. For example, a CCD aspect camera, thermal shielding and an interface to a tape recorder rather than a telemetry unit.

It is envisioned that construction of the SPARTAN payload will commence in 1985, with flight in 1986/87 after at least one and preferably two successful flights of the sounding rocket payload. The increase in mission time will allow an increase in the WFSXC sensitivity and the area of the sky covered by the experiment.

Finally, an upgraded version of the WFSXC is to be flown as an ancillary experiment on the German satellite ROSAT, by a consortium of British X-ray astronomy groups headed by Leicester University. ROSAT is an X-ray telescope, similar to the Einstein observatory, whose mission is to perform an all-sky survey. The WFSXC is the perfect complement to ROSAT, because of its design as a sky survey instrument and its lower energy band. ROSAT is scheduled for launch in mid-1987 and will carry out the sky survey in the first six months of its life, followed by at least 12 months source and field studies. The sensitivity (5σ) of the WFSXC sky survey (exposures of $\sim$5000s) will be

$\sim 6 \times 10^{-12}$ ergs $cm^{-2} s^{-1}$ (60-170Å) and $\sim 8 \times 10^{-12}$ ergs $cm^{-2} s^{-1}$ (114-230Å) representing improvements of 20x and 14x respectively over the equivalent sounding rocket sensitivities. With ROSAT, the original WFSXC concept of high sensitivity coupled with all-sky coverage will be fulfilled.

APPENDIX A

DEPOSITION PHOTOCATHODE GEOMETRY

This model of photocathode deposition considers evaporation onto a rotating MCP, mounted in relation to a source of material and a crystal thickness monitor as shown in figure 4.3 where the nominal coating angle is $\theta_C = Tan^{-1}(l/h')$. In this treatment it is assumed that -

i) Evaporation is from a point source

ii) The molecules travel in straight lines

iii) Deposition occurs with no reflection from the channel walls

iv) The flux of molecules is uniform and constant

v) The MCP rotates at a constant rate

If the channel diameter (D) is small compared to the distance to the source, then the beam of molecules can be considered parallel across a channel, and thus the profile of the photocathode deposit is simply the projection of the circular channel entrance onto the channel wall at a deposition angle θ' (D=25μm and the source distance is ~200mm therefore this assumption is valid). The geometry is exactly the same as that for illumination by parallel X-rays (see figure 4.1). The depth that the coating reaches along a channel is

$$Y_C = D.Cos\Psi.Cot\theta' \qquad (A.1)$$

The thickness of the deposit around the channel will not be uniform as the projection of the beam is onto a curved surface. Unless the source is at a large distance from the MCP with respect to the MCP

diameter, θ' will not be constant across the MCP.

Let the flux of atoms/molecules at a particular channel have a deposition rate normal to the beam F_C $\dot{A}s^{-1}$. Consider a small area of channel wall, $ds=Y_C.dz$ (figure A.1) which represents the projection of a small slice through the beam. The area of the slice normal to the beam is $Y_C Sin\theta'.dzCos\psi$. Thus the rate of deposition, calculated from the ratio of the two elemental areas at polar angle ψ, is

$$F(\psi) = F_C.Sin\theta'.Cos\psi \qquad (A.2)$$

and is independent of Y up to a maximum of Y_C. If $Y>Y_C$, $F(\psi)=0$.

The angle γ can be defined as a polar angle in the channel relative to a fixed point on the MCP (see figure 4.4). γ can be measured from an arbitrary point but for convenience $\gamma=0$ is the closest point in the channel to the MCP centre. In order to obtain a coating at all values of γ it is necessary to rotate the MCP during deposition, as described in chapter 4. Under these conditions the coating thickness at ψ will no longer be a function of ψ alone and $F(\psi)$ will be a periodic function of time/orientation of the MCP. Rotating the MCP by angle ϕ scans the locus of points defined by γ through a range of values of ψ.

The source of photocathode is at a lateral distance l from the centre of the MCP in the plane parallel to the MCP and r_C is the distance of the channel from the MCP centre. ϕ is measured from an arbitrary but fixed point on the MCP. ψ can then be defined in terms of the other parameters

Figure A.1 The elemental area (ds) on a channel wall.

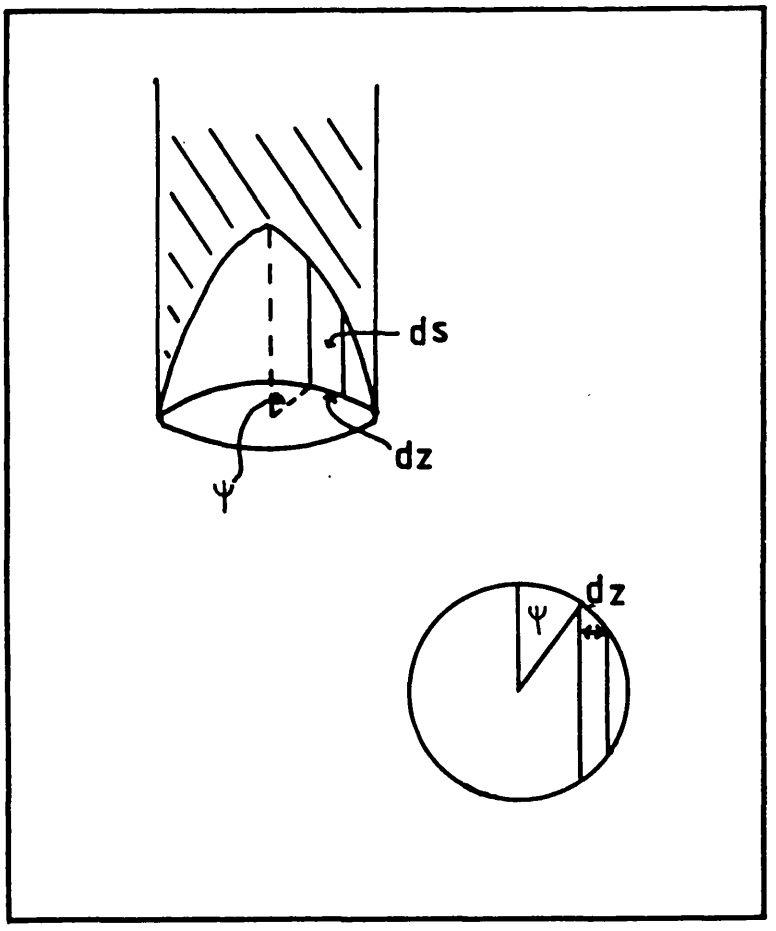

$$\mathrm{Cos}\psi = \mathrm{Cos}\left[\mathrm{Sin}^{-1}\left(\frac{l.\mathrm{Sin}\phi}{x}\right)-\gamma\right] \qquad (A.3)$$

where: $x^2=r_c^2+l^2-2r_c.l.\mathrm{Cos}\phi$ ($\mathrm{Tan}\theta'=x/h'$)

As $h'/x=\mathrm{Cot}(\theta')$, combining equations A.1 and A.3

$$Y_c = \frac{D.h'.\mathrm{Cos}}{x}\left[\mathrm{Sin}^{-1}\left(\frac{l.\mathrm{Sin}\phi}{x}\right)-\gamma\right] \qquad (A.4)$$

Hence, Y_c is expressed in terms of the parameters of the MCP-source arrangement, h' and l and the MCP-channel coordinate system r_c, ϕ and γ. For each value of γ Y_c has a maximum value Y_0 when $\mathrm{Cos}\psi=1$ (ie. $(1/x)\mathrm{Sin}\phi=\gamma$).

Consider an arbitrary position (Y,γ) in a channel at radius r_c. The coating rate at this point can be derived from equation A.2 by substituting for $\mathrm{Sin}\theta'$ ($\mathrm{Sin}\theta'=x/(x^2+h'^2)^{1/2}$) and $\mathrm{Cos}\psi$ (equation A.3)

$$F(\phi) = \frac{F_c.\ x.\ \mathrm{Cos}}{(x^2+h'^2)^{1/2}}\left[\mathrm{Sin}^{-1}\left(\frac{l.\mathrm{Sin}\phi}{x}\right)-\gamma\right] \qquad (A.5)$$

if $0 < Y < Y_c$.

Unless the source of material is a long way from the MCP by comparison with r_c, F_c is as function of position and rotation. Assuming that the source radiates symmetrically into a hemisphere the

inverse square law holds for the flux from the source. If F_0 is the coating rate measured at the crystal

$$F_C = F_0.\text{Cos}^2\theta' = \frac{F_0.h'^2}{(h'^2+x^2)} \qquad (A.6)$$

Hence,

$$F(\phi) = F_0.\frac{h'^2}{(h'^2+x^2)^{3/2}}.x.\ \text{Cos}\left[\text{Sin}^{-1}\left(\frac{l.\text{Sin}\phi}{x}\right)-\gamma\right] \qquad (A.7)$$

The mean coating rate per revolution at point (Y,γ,r_C) is given by

$$F = \frac{1}{2\pi}\int_{\phi_1}^{\phi_2} F(\phi).d\phi \qquad (A.8)$$

where: ϕ_1 and ϕ_2 are limits determined by Y and γ defining the period when the point (Y,γ,r_C) is illuminated by the coating source.

The thickness of coating at a given point $(T'(Y,\gamma,r_C))$ accumulated in a time t is

$$T'(Y,\gamma,r_C) = F.t \qquad (A.9)$$

provided the number of revolutions in t (n_r=w.t/2π, where w is the angular frequency of the rotation) is large so that the "end effects" of part rotations are negligible. The periodic nature of the coating rate allows $T'(Y,\gamma,r_c)$ to be independent of n_r or w. t is determined by the required thickness on the monitor crystal (T'_0) and the coating rate the crystal the crystal measures, $t=T'_0/F_0$. Thus

$$T'(Y,\gamma,r_c) = T'_0.F/F_0 \qquad (A.10)$$

Substituting into equation A.8 for $F(\phi)$ (equation A.7), from equation A.10

$$T'(Y,\gamma,r_c) = \frac{T'_0}{2\pi}\int_{\phi_1}^{\phi_2} \frac{h'^2.x}{(h'^2+x^2)^{3/2}} \cos\left[\sin^{-1}\left(\frac{1.\sin\phi}{x}\right)-\gamma\right] d\phi \qquad (A.11)$$

Therefore the thickness of coating at a given point can be related to the nominal thickness on the front MCP face by a geometric parameter ($G'(Y,\gamma,r_c)$).

$$T'(Y,\gamma,r_c) = T'_0.G'(Y,\gamma,r_c) \qquad (A.12)$$

where:

$$G'(Y,\gamma,r_c) = \frac{1}{2\pi}\int_{\phi_1}^{\phi_2} \frac{h'^2.x}{(h'^2+x^2)^{3/2}} \cos\left[\sin^{-1}\left(\frac{1.\sin\phi}{x}\right)-\gamma\right] d\phi \qquad (A.13)$$

In an ideal situation G' will be constant for any value of γ in any channel, r_c, but will not be constant for Y, the depth along the channel. This ideal occurs if $r_c/l \sim 0$ and $r_c/h' \sim 0$. Whatever value of l or h' these conditions hold when $r_c=0$. Therefore the geometry at the centre of the MCP is in fact the ideal coating geometry.

In this geometry x becomes equal to l and G' (equation A.13) reduces to

$$G_p = \frac{1}{2\pi} \int_{\phi_1}^{\phi_2} \frac{h'^2.l}{(h'^2+l^2)^{3/2}} \cos(\phi-\gamma).d\phi \qquad (A.14)$$

The limits of ϕ can then be calculated very simply from equation A.4

$$\gamma - \cos^{-1} \frac{l.Y}{D.h'} < \phi < \gamma + \cos^{-1} \frac{l.Y}{D.h'}$$

Therefore,

$$G_p(Y) = \frac{1}{\pi} \frac{(h'/l)^2}{[(h'/l)^2+1]^{3/2}} \sin \cos^{-1}\left(\frac{Y.l}{D.h'}\right) \qquad (A.15)$$

A useful parameter is $G_p(0)$ as it allows computation of the wall

thickness at the channel entrance

$$G_p(0) = \frac{1}{\pi} \frac{(h'/l)^2}{[(h'/l)^2+1]^{3/2}} = \frac{1}{\pi}.\mathrm{Cos}^2\theta_c.\mathrm{Sin}\theta_c \qquad (A.16)$$

REFERENCE ABBREVIATIONS

Adv.Electron.Electron Phys. - Advances in Electronics and Electron Physics.

Ann. Rev. Astr. and Ap. - Annual Review of Astronomy and Astrophysics.

Ap.J. - Astrophysical Journal.

Astr. and. Ap. - Astronomy and Astrophysics.

Bull.A.A.S. - Bulletin of the American Astronomical Society.

ESA - European Space Agency

IAU - International Astronomical Union.

IEEE Trans.Nuc.Sci. - Institute of Electrical and Electronic Engineers Transactions on Nuclear Science.

JGR - Journal of Geophysical Research.

JOSA - Journal of the Optical Society of America.

J.Phys.E: Sci.Instrum. - Journal of Physics E: Scientific Instrumentation.

MNRAS - Monthly Notices of the Royal Astronomical Society.

NASA Tech.Mem. - NASA Technical Memorandum.

Nuc.Instrum.Meth. - Nuclear Instruments and Methods.

Nuc.Instrum.Meth.Phys.Res. - Nuclear Instruments and Methods in Physics Research.

Phil.Trans.R.Soc.Lond.A. - Philosophical Transactions of the Royal Society of London A.

Planet.Space.Sci. - Planetary and Space Science.

Pub A.S.P. - Publications of the Astronomical Society of the Pacific.

Phys.Rev. - Physical Review.

Rev.Sci.Instrum. - Review of Scientific Instruments.

SAO - Smithsonian Astrophysical Observatory.

SPIE - Society of Photo-optical Instrumentation Engineers.

REFERENCES

Acton,J.R., and Swift,J.D., "Cold Cathode Discharge Tubes", Academic Press (1963).

Allen,C.W., "Astrophysical Quantities", The Athlone Press, University of London (1973).

Aller,L.H., Pub. A.S.P. 71(1959), 324.

Authinarayanan,A. and Dudding,R.W., Adv.Electron.Electron Phys., 40A(1976), 167.

Baliunas,S.L., and Dupree,A.K., Ap.J. 227(1979), 870.

Barry,D.C., Sandel,B.R., Holberg,J.B., Forrester,W.T. and Broadfoot,A.L., Nature 285(1980), 210.

Bevington,P.R., "Data Reduction and Error Analysis for the Physical Sciences", McGraw Hill (1969).

Bleeker.,J.A.M., Davelaar,J., Deerenberg,A.J.M., Huizenga,S., Brinkman,A.C., Heise,J., Tanaka,Y., Hayakawa,S., and Yamashita,K., Astr. and Ap. 69(1978), 145.

Bleeker,J.A.M., Huizenga,H., den Boggende,A.J.F., and Brinkman,A.C. IEEE Trans.Nuc.Sci., NS-27(1980), 176.

Bohlin,R.C., Ap.J. 182(1973), 139.

Bowyer,S., Kimble,R., Paresce,F., Lampton,M., and Penegor,G., Applied Optics, 20(1981), 477.

Burke,E.A., IEEE Trans.Nuc.Sci., NS-24(1977), 2505.

Burstein,P., Borken,R.J., Kraushaar,W.L., and Sanders,W.T., Ap.J 213(1977), 405.

Capriotti,E.R., from "Planetary Nebula, Observations and Theory", IAU Symposium No76 (1978), 263.

Carnochan,D.J., Dworetsky,M.M., Todd,J.J., Willis,A.J., and Wilson,R., Phil.Trans.R.Soc.Lond.A, 279(1975), 479.

Carruthers,G.R., SPIE 279(1981), 112.

Cash,W., Bowyer,S., Freeman,J., Lampton,M., and Paresce,F., Ap.J., 219(1978a), 585.

Cash,W., Bowyer,S., and Lampton,M., Ap.J. Letters 221(1978b), L87.

Cash,W., Bowyer.S., and Lampton,M., Astr. and Ap. 80(1979), 67.

Cash.W., Malina.R., and Stern,R., Ap.J. Letters 204(1976), L119.

Catura,R.C., Acton,L.W., and Johnson,H.M., Ap.J. Letters, 196(1975), L47.

Chase,R.C., and VanSpeybroeck,L.P., Applied Optics, 12(1973), 1042.

Clark,D.H., and Culhane,J.L., MNRAS 175(1976), 573.

Cromer,D.T., and Liberman,D., Los Alamos report LA 4403,(1970).

Cruddace,R., Paresce,F., Bowyer,S., and Lampton,M., Ap.J. 187(1974), 497.

Cowie,L.L., Jenkins,E.B., Songaila,A., and York,D.B., Ap.J. 232(1979), 467.

Cox,D.P., and Smith,B.W., Ap.J. 218(1977), 148.

Dupree,A.K., Ap.J. Letters, 200(1975), L27.

Eng,W., and Landecker,P.B., Nuc.Instrum.Meth., 190(1981), 149.

ESA Extreme Ultraviolet/X-ray Sky Survey (EXUV) Mission, Report on the Phase A Study SCI(79)9, (1979).

Fabian,A.C., Willingale,R., Pye,J.P., Murray,S.S. and Fabbiano,G., MNRAS, 193(1980), 175.

Fabbiano,G., Hartmann,L., Raymond,J., Steiner,J., Branduardi-Raymont, G., and Matilsky,T., Ap.J. 243(1981), 911.

Fabricant,D.G., Goddard,R.E., Harnden,F.R., and Gorenstein,P., Rev.Sci.Intrum. 50(1979), 727.

Fraser,G.W., PhD Thesis (1980).

Fraser,G.W., Nuc.Instrum.Meth.Phys.Res., 195(1982), 523.

Fraser,G.W., Nuc.Instrum.Meth.Phys.Res., 206(1983a), 251.

Fraser,G.W., Nuc.Instrum.Meth.Phys.Res., 206(1983b), 265.

Fraser,G.W., Barstow,M.A., Whiteley,M.J. and Wells,A., Nature, 300(1982), 509.

Fraser,G.W., and Mathieson,E., Nuc.Instrum.Meth., 179(1981), 591.

Fraser,G.W., Mathieson,E., Lewis,M., and Barstow,M., Nuc.Instrum.Meth.Phys.Res., 190(1981), 53.

Fraser,G.W., and Pearson,J.F., Nuc.Instrum.Meth.Phys.Res., in press (1983).

Giacconi,R., and 30 coauthors, Ap.J., 230(1979), 540.

Giacconi,R., Reidy,W.P., Vaiana,G.S., Van Speybroeck,L.P., and Zehnpfennig,T., Space Science Reviews 9(1969), 3.

Gott,R., Parkes,W. and Pounds,K.A., IEEE Trans.Nuc.Sci., NS-17 (1970), 367.

Greenstein,G., Ap.J., 200(1975), 281.

Greenstein,G., and McClintock,J.E., Science, 185(1974), 487.

Greenstein,G., Margon,B., Bowyer,S., Lampton,M., Paresce,F., Stern,R., and Gordon,K., Astr.and Ap. 54(1977), 623.

Greenstein,J.L., and Sargent,A., Ap.J. Supplement 28(1974), 157.

Grewing,M., Astr. and Ap., 38(1975), 399.

Griffiths,R., Lamb,D.Q., Ward,M.J., Wilson,A.S., Charles,P.A., Thorstensen,J., McHardy,I.M., and Lawrence,A., MNRAS 193(1980), 25p.

Hagemann,H.-J., Gudat,W., and Kunz,C. DESY report SR-74/7 May(1974).

Haisch,B.M., Linsky,J.L., Lampton,M., Paresce,F., Margon,B., and Stern,R., Ap.J. Letters, 213(1977), L119.

Hall, R., PhD Thesis, Leicester University, (1982).

Harman,R.J., and Seaton,M.J., Ap.J., 140(1964), 824.

Hearn.D.R., and Marshall,F.J., Ap.J. Letters 232(1979), 21L.

Heise,J., Brinkman,A.C., Schrivjer,J., Mewe,R., Gronenschild,E., and Den Boggende,A., Cospar/IAU Symposium "Fast transients in X and Gamma rays" (1975).

Henke,B.L. and Elgin,R.L., Advances in X-ray Analysis, 13(1970), 639.

Henry,J.P., Kellogg,E., Briel,U.G., Murray,S.S., VanSpeybroeck,L.P., and Bjorkholm,P.J., SPIE 106(1977), 176.

Henry,P., Bowyer,S., Lampton,M., Paresce,F., and Cruddace,R., Ap.J. 205(1976a), 426

Henry,P., Bowyer,S., Rapley,C.G., and Culhane,J.L., Ap.J. Letters 209(1976b), L29.

Henry,P., Cruddace,R., Lampton,M., and Paresce,F., Ap.J. Letters (1975a), L117.

Henry,P., Cruddace,R., Paresce,F., Bowyer,S., and Lampton,M., Ap.J. 195(1975b), 107.

Hill,G.E., Adv.Electron.Electron Phys. 40A(1976), 153.

Hill,R.W., Grader,R.J., Seward,F.D., and Stoering,J.P., JGR 75(1970), 7267.

Hills,J., Astr.and.Ap., 12(1971), 1.

Hills,J., Astr.and.Ap., 18(1972), 155.

HMSO, "The Astronomical Almanac 1981", (1980).

HMSO, "The Astronimical Almanac 1982", (1981).

Holberg,J.B., Forrester,W.T. and Broadfoot, A.L., Bull.A.A.S. 12(1980a), 872.

Holberg,J.B., Forrester,W.T., Shemansky,D.E., and Barry,D.C., Ap.J., 257(1982), 656.

Holberg,J.B., Sandel,B.R., Forrester,W.T., Broadfoot,A.L., Shipman H.L., and Barry,D.C., Ap.J. Letters 242(1980b), L119.

Holland,L., "Vacuum Deposition of Thin Films", Chapman and Hall (1956).

Holme,A.V., and Boggess,A., Pub A.S.P. 94(1982), 553.

Huizenga,H., Bleeker,J.A.M., Diemer,W.H., and Huben,A.P., Rev.Sci.Instrum., 52(1980), 176.

Jacchia,L.G., SAO Special Report 332(1971).

Jenkins,E.B., Ap.J. 210(1978), 845.

Jenkins,E.B., Silk,J., and Wallerstein,G., Ap.J. Letters, 209(1976), L87.

Johnston,R.W. and Tomboulian,D.H., Phys.Rev 94(1954), 1585.

Kayat,M.A., PhD Thesis (1980).

Kellogg,E., Henry,P., Murray,S., VanSpeybroeck,L., and Bjorkholm,P., Rev.Sci.Instrum., 47(1976), 282.

deKorte,P.A.J., Bleeker,J.A.M., Deerenberg,A.J.M, Hayakawa,S., Yamashita,K., and Tanaka,Y., Astr. and Ap. 48(1976), 235.

Lampton,M., Margon,B., Paresce,F., Stern,R., and Bowyer,S., Ap.J. Letters, 203(1976), L71.

Lampton,M., and Paresce,F., Rev.Sci.Instrum., 45(1974), 1098.

Lang,K.R., "Astrophysical Formulae" Springer,
Berlin-Heidelberg-New York (1974)

Lapson,L.B., and Timothy,J.G., Applied Optics, 12(1973), 388.

Lapson,L.B., and Timothy,J.G., Applied Optics, 15(1976), 1218.

Lecomte,P., and Perez-Mendez,V., IEEE Trans.Nuc.Sci., NS-25(1978),
964.

Leibert,J., Ann.Rev.Astr.and.Ap., 18(1980), 363.

Levine,A., Petre,R., Rappaport,S., Smith,G., Evans,K., and Rolf,D.,
Ap.J. Letters, 228(1979), L99.

Levine,A., Rappaport,S., Doxsey,R., and Jernigan,G., Ap.J.,
205(1976), 215.

Levine,A., Rappaport,S., Halpern,J., and Walter,F., Ap.J.,
211(1977), 215.

Margon,B., Lampton,M., Bowyer,S., Stern,R., and Paresce,F., Ap.J.
Letters, 210(1976), L79.

Margon,B., Szkody,P., Bowyer,S., Lampton,M., and Paresce,F., Ap.J.,
224(1978), 167.

Marshall,F., PhD Thesis, Massachusetts Institute of Technology
(1982).

Martin,C and Bowyer,S., Applied Optics, 21(1982), 4206.

McClintock,W.E., Barth,C.A., Steele,R.E., Lawrence,G.M., and
Timothy,J.G., Applied Optics 21(1982), 3071.

McKee,C.F., Ap.J., 188(1974), 355.

McKee,C.F., and Ostriker,J.A., Ap.J. 218(1977), 148.

Meier,R.R., and Mange,P., Planet.Space.Sci 18(1970), 803.

Meier,R.R., and Prinz,D.K., JGR. 76(1971), 4608.

Meier,R.R., and Weller,C.S., JGR. 79(1974), 1575.

Mewe,R., Heise,J., Gronenschild,E.H.B.M., Brinkman,A.C., Schrivjer,J., and Den Boggende,A.J.F., Ap.J. Letters, 202(1975), L67.

Morton,J.M., and Parkes,W., Acta Electronica, 16(1973), 85.

Mulder,B.J., and Vrakking,J.J., J.Phys.E: Sci.Instrum., 11(1978), 743.

Mullard Technical Information 31, TP1561 (1976).

Oba,K., Sugyama,M., Suzuki,Y., and Yoshimura,Y., IEEE Trans.Nuc.Sci., NS-26(1979), 346.

Paresce,F., Appl. Opt. 14(1975), 2823.

Paresce,F., Earth and Extraterrestrial Sciences 3(1977), 55.

Paresce,F., Kumar,S., and Bowyer,S., Planet.Space.Sci 20(1972), 297.

Paresce,F., and Stern,R., Ap.J. 247(1981), 89.

Parkes,W., PhD Thesis (1974).

Parkes,W., Evans,K.D., and Mathieson,E., Nuc.Instrum.Meth. 121(1974), 151.

Parkes,W., and Gott.R., Nuc.Intrum.Meth., 95(1971), 487.

Parkes,W., Gott,R., and Pounds,K.A., IEEE Trans.Nuc.Sci., NS-17(1970), 360.

Petre,R., PhD Thesis, Massachusetts Institute of Technology (1982).

Pye,J.P., Pounds,K.A., Rolf,D.P., Seward,F.P., Smith,A., and Willingale,R., MNRAS, 194(1981), 569.

Rager,J.P., and Renaud,J.F., Rev.Sci.Instrum., 45(1974), 922.

Rappaport,S., Petre,R., Kayat,M., Evans,K., Smith,G., and Levine,A.,

Ap.J., 227(1979), 285.

Reigler,G.R., and Garmire,G., Astr. and Ap. 45(1975), 213.

Rogers,D., Space Sciences Laboratory Berkeley, Space Astrophysics Group internal report DR/EUVE/302/80 (1980).

Rogerson,J.B., York,D.G., Drake,J.F., Jenkins,E.B., Morton,D.C., and Spitzer,L., Ap.J. Letters 181(1973), L110.

Roth, A. "Vacuum Technology", North-Holland Publishing Company, (1976).

Rustgi,O.P., JOSA., 55(1965), 630.

Sagdeev,R., Kurt,V., and Bertaux,J., IAU Circular No 3261 (1979).

Saloman,E.B., Pearlman,J.S. and Henke,B.L., Applied Optics, 19(1980), 749.

Salpeter,E.E., Ann.Rev.Ast.and.Ap. 9(1971), 127.

Samson,J.A.R., and Cairns,R.B., Applied Optics 4(1965), 915.

Sanders,W.T., Kraushaar,W.L., Nousek,J.A., and Fried,P.M., Ap.J. Lett. 217(1977), L87.

Savage,B.D., and Jenkins,E.B., Ap.J. 172(1972), 491.

Seward,F.P., Burginyon,G.A., Grader,R.J., Hill,R.W., Palmieri,T.M., and Stoering,J.P., Ap.J., 169(1971), 515.

Shipman,H.L., Margon,B., Bowyer,S., Lampton,M., Paresce,F., and Stern,R., Ap.J. Letters, 213(1977), L25.

Sims,M.R., PhD Thesis, Leicester University (1981).

Smith,D.G. and Pounds,K.A., IEEE Trans.Nuc.Sci., NS-15(1968), 541.

Smith,G.C., Pearson,J.F., and Mathieson,E., Nuc.Instrum.Meth.Phys.Res., 192(1982), 383.

Spitzer,L., Drake.J.F., Jenkins,E.B., Morton,D.C., Rogerson,J.B.,

and York,D.G., Ap.J. Letters 181(1973), L116.

Sprackling,M.T., "The Mechanical Properties of Matter", English Universities Press (1970).

Stern,R., and Bowyer,S., Ap.J. 230(1979), 755.

Stern,R., and Paresce,F., JOSA., 65(1975), 1515.

Swank,J.H., White,N.E., Holt,S.S., and Becker,R.H., NASA Tech.Mem. 82045 (1980).

Tabata,T., Ito,R., and Okabe,S., Nucl.Instrum.Meth., 103(1972), 85.

Thomas,G.E., and Anderson,D.E., Planet.Space.Sci. 20(1972), 297.

Thomas,H.D., PhD Thesis in preparation (1983).

Thorstensen,J.R., Charles,P.A., Margon,B., and BowyerS., Ap.J. 223(1978), 260.

Timothy,J.G., Rev.Sci.Instrum., 52(1981), 1131.

Timothy,J.G., and Bybee,R.L., Rev.Sci.Instrum., 46(1975), 1615.

Timothy,J.G., Mount,G.H., and Bybee,R.L., SPIE "Space Optics", 183(1979), 169.

Toots,J. Fowler,H.A., and Marton,L., Phys.Rev. 172(1968), 172.

Tsuruta,S., IAU Symposium 53, "Physics of Dense Matter" (1974), 209.

Tsuruta,S., IAU Symposium 95, "Pulsars" (1981), 331.

Vaiana,G.S., Cassellini,J.P., Fabbiano,G., Giacconi,R., Golub,L., Gorenstein, P., Haisch,B.M., Harnden,F.R.,Jr., Johnson,H.M., Linsky J.L., Maxson,C.W., Mewe,R., Rosner,R., Seward,F., Topka,K., and Zwaan,C., Ap.J., 245(1981), 163.

Walter,F.M., Cash,W., Charles,P.A., and Bowyer,C.S., Ap.J., 236(1980), 212.

Washington,D., Duchenois,V., Polaert,R., and Beasley,R.M., Acta Electronica, 14(1971), 201.

Webster, B.L., MNRAS 143(1969), 113.

Weidemann,V., Ann.Rev.Astr.and.Ap., 6(1968), 351.

Weiser,H., Vitz,R.C., Moos,H.W., and Weinstein,A., Applied Optics 15(1976), 3123.

Weller,C.S., SPIE 279(1981), 216.

Weller,C.S., and Meier,R.R., JGR. 79(1974), 1572.

Williamson,F., and Maxson,C.W.,Rev.Sci.Instrum. 46(1975), 50.

Willingale,R., PhD Thesis, Leicester University (1979).

Wiza,J.L., Nuc.Instrum.Meth., 162(1979), 587.

Wiza,J.L., Henkel,P.R. and Roy,R.L., Rev.Sci.Instrum., 48(1977), 1217.

Wolter,H., Annalen Der Physik 10(1952a), 94.

Wolter,H., Annalen Der Physik 10(1952b), 286.

Yentis,D.J., Novick,R., and Vanden Bout,P., Ap.J., 177(1972), 365.

Young,J.M., Weller,C.S., Johnson,C.Y., and Holmes,J.C., JGR 76(1971), 3710.

Zombeck,M., SAO Special Report 386(1981).